



# Contribution to the Modelling of Fission Gas Release in Light Water Reactor Fuel

**Paul Van Uffelen**

Promotor Prof. C. Vandenberg
Mentor Ir. K. van der Meer

A dissertation submitted in partial satisfaction of the requirements for the degree of Doctor in Applied Sciences

January 2002

BLG-907

# Contribution à la modélisation du relâchement des gaz de fission dans le combustible nucléaire des réacteurs à eau légère

Thèse présentée en vue de l'obtention du grade de Docteur en Sciences Appliquées

de

l'Université de Liège
Faculté des Sciences Appliquées
Département des centrales nucléaires

par

**Paul Van Uffelen**

Burgerlijk werktuigkundig-electrotechnisch ingenieur, Vrije Universiteit Brussel (1992)
Ingénieur en sciences nucléaires appliquées, Université Libre de Bruxelles (1994)

Soutenue le 8 Janvier 2002 devant le Jury de thèse:

| | |
|---|---|
| P. Mathieu | Professeur à l'Université de Liège (Président) |
| C. Vandenberg | Chargé de cours à l'Université de Liège (Promoteur) |
| J. Lecomte-Beckers | Chargé de cours à l'Université de Liège |
| D. Baron | Professeur à l'Ecole Centrale de Nantes et<br>Manager, R&D combustible nucléaire, EdF, Les Renardières (FRA) |
| P. D'hondt | Director, Reactor Safety, CEN•SCK, Mol |
| M. Lippens | Manager, Fuel Studies, S.A. BELGONUCLEAIRE, Bruxelles |
| D.R. Olander | Professor at the University of California at Berkeley (USA) |
| J.A. Turnbull | Nuclear Fuel and Materials Specialist, Bristol (UK) |

# Executive summary

Despite the excellent safety records of nuclear fuel rods, efforts to enhance the predictive capabilities of the fuel performance codes are still necessary in view of economic driving forces. These tendencies might have implications for fuel integrity and, accordingly, this could be in conflict with safety requirements. In order to address these questions, it is necessary to identify the safety issues and to understand the basic underlying mechanisms. Fission gas release (FGR) is among the topics of primary interest since it is considered as one of the possible mechanisms that restricts the upper limit of burnup in nuclear fuel rods.

The general objective of this work is to improve the predictive capabilities of the FGR model in fuel performance codes for light water reactors. More precisely, a FGR model has to be developed that must be able to cope with the incubation behaviour, especially with the reduction of the release threshold at high burnup, as well as with the burst phenomenon during smooth power variations in $UO_2$ fuel. These objectives are achieved by means of two complementary contributions; (a) by elucidating underlying basic mechanisms, in particular those governing the intergranular behaviour, and (b) by improving the mathematical description of the FGR process as a whole.

A model for the precipitation of fission products in a grain boundary, which embodies a variable reaction rate on the precipitate surface, has been developed. This enables one to account for modifications of the local fuel chemistry, or to distinguish between the behaviour of different migrating species. In addition, the influence of the trapping parameters on the precipitation rate has been assessed according to different models from the open literature, which have been extended in order to incorporate the variable intrinsic reaction rate. The interrelationships among the models have been established while their limitations and range of validity have been discussed. The results reveal that there is a critical value above which the influence of the intrinsic reaction rate coefficient, between a fission product and an intergranular trap, on the global precipitation rate coefficient becomes negligible. This justifies the assumption of an infinite intrinsic reaction rate coefficient for intergranular bubbles in fission gas release models, and it could explain the similar behaviour of different species for which the reduced intrinsic reaction rate coefficient is larger than 1.

There appeared to be a contradiction about the role of grain boundaries in fission gas release. Either they operate as a sink where fission gases form bubbles, or they serve as a high diffusivity pathway for release. Both points of view are reconciled by considering grain boundary diffusion plus trapping and re-solution. With these competing processes, there is a switch from grain boundary diffusion to growth and interlinkage of intergranular bubbles in controlling intergranular fission gas migration. This idea, however, raises several questions. In order to address these questions, experimental data on Xe release in trace-irradiated $UO_2$ have been re-analysed. The measurements indicated that the data are consistent with sequential lattice and grain boundary diffusion unimpeded by intergranular traps. The fitting procedure also provided rough estimates of the grain boundary diffusion coefficient in $UO_2$. Furthermore, the mean migration distance of a fission gas atom in a grain boundary decorated with a population of circular traps has been assessed. From the computations, it is concluded that for values of the geometric parameters that roughly encompass the intergranular bubble populations observed in irradiated fuel, a fission gas atom will be trapped after a migration distance in the grain boundary equal to the size of a grain or less. This result simply provides a theoretical justification for the universal rejection of grain

boundary transport as a release mechanism for fission gas in irradiated $UO_2$. The calculations also offer a qualitative explanation for the dissimilar release rates observed in trace-irradiated $UO_2$ for Te and I in comparison with Xe.

A new model for fission gas release has been developed. The mathematical concept is based on that of Kogai but includes the necessary improvements brought up in the analysis of the existing models: the kinetics of the intra- and intergranular behaviour of the gas atoms are coupled in both directions; the intergranular precipitation rate constant accounts for the competition effect between neighbouring traps; grain boundary bubble sweeping is accounted for during bubble growth; the influence of the hydrostatic pressure on the thermal release component has been corrected; the model accounts for two important fabrication parameters, namely the grain size distribution and the open porosity fraction.

According to the present model, the release of fission gas is determined by two different components. The thermal release component is controlled by the formation of an interconnected tunnel network of grain boundary bubbles, and is able to handle burst release due to the lowering of the pellet clad mechanical interaction and/or the thermal stress distribution during power reductions. The athermal release component provides an alternative explanation for the decrease of the release threshold at high burnup, rather than introducing an increase of the bulk diffusion coefficient, or a reduction of the re-solution rate at the grain boundaries.

A new programme has been written for the numerical implementation of the FGR model. The key issue for the implementation is the reduction of the calculation time while assuring sufficient precision. Most of the efforts have been devoted to the implementation of the intragranular module. The optimisation involves several steps and relies on the Taguchi technique. From the optimisation procedure, the dichotomic grid emerges as the best choice in terms of precision and running time. In addition, it allows an elegant implementation of the re-solution process near the grain boundary.

The new FGR model can be coupled with any fuel performance code. This is demonstrated by the successful coupling of the FGR model with the FTEMP2 code of the OECD Halden Reactor Project, as well as with the COMETHE-IV code from BELGONUCLEAIRE.

A parametric study of the empirical threshold for fission gas release not only underlines the crucial parameters, it also shows that the FGR model provides an excellent tool to analyse the contribution of each mechanism to the overall release process. Furthermore, it revealed that the model reproduces the decrease of the incubation period with burnup fairly well, although it is extremely difficult to predict accurately. In addition, the outward shift of the onset of release in the pellets with increasing burnup, as well as the saturation concentration or the bubble pressures at the grain boundaries correspond very well with experimental observations.

The model predictions have been compared with the data-set of Zimmermann, which has been used by many others for their model qualification. Nevertheless, all of them erroneously compared their predictions with those of Zimmermann, rather than with the experimental data. In addition, they applied average values for several sensitive parameters. The simulation of the individual data points with the new FGR model is better, and takes into account the temperature fluctuations. In addition, the temperature threshold at which the release begins lies between 1000 °C and 1100 °C and corresponds very well with that reported in the literature.

In order to extend the model validation by means of in-pile observations, the first FUMEX case has been reproduced. This case was part of the round robin exercise organised by the IAEA and is difficult for accurate predictions as the fractional release is close to the onset of release. The simulation is satisfactory and points out the importance of the open porosity fraction for the athermal release.

It is thus fair to conclude that the comparison of the new FGR model with experimental data, characterising normal steady state conditions, is satisfactory when applying for all the parameters a combination of the values that are reported in the literature.

*To my parents in gratitude.*

# Acknowledgements

I am greatly indebted to SCK•CEN and BELGONUCLEAIRE for giving me the opportunity to prepare this dissertation under excellent conditions. In this respect, a special word of thanks goes to P. D'hondt and K. van der Meer of SCK•CEN for their confidence and continuous support throughout my PhD-work.

Without the experience and precious advice of M. Lippens from BELGONUCLEAIRE, D.R. Olander from the University of California at Berkeley, J.A.T. Turnbull formerly with Nuclear Electric, and C. Vandenberg from the University of Liège, it would have been impossible to end this project successfully. Their kindness and openness were extremely stimulating too.

I also wish to acknowledge my indebtedness to D. Baron from Electricité de France and T. Kogai of Japan Nuclear Fuel, for the fruitful and enjoyable discussions, as well as for the exchange of valuable information.

It is a great pleasure to thank V. Sobolev from the Moscow Engineering Physics Institute and M. Verwerft of SCK•CEN for their interest, constructive criticism and support, especially in difficult situations. There are still a lot of other persons that I should show gratitude to for various reasons. Yet, they are too numerous to mention.

Finally, the largest measure of thanks and my deepest appreciation is due to my wife and my son for their encouragements and indulgence. They share my happiness to see the end of this PhD-work, albeit for different reasons.

# Contents

# Abbreviations

| | |
|---|---|
| BNFL | British Nuclear Fuels (United Kingdom) |
| BWR | Boiling Water Reactor |
| CANDU | CANadian Deuterium Uranium |
| CEA | Commissariat á l'Energie Atomique (France) |
| CPU | Central Processing Unit |
| FGR | Fission Gas Release |
| FUMEX | FUel Modelling at EXtended burnup |
| HRP | OECD-Halden Reactor Project (Norway) |
| IAEA | International Atomic Energy Agency |
| IFA | Instrumented Fuel Assembly |
| JAERI | Japanese Atomic Energy Research Institute |
| LHR | Linear Heat generating Rate |
| LWR | Light Water Reactor |
| MEPhI | Moscow Engineering Physics Institute |
| MOX | Mixed OXide fuel, more precisely a mixture of $UO_2$ and $PuO_2$ |
| ODE | Ordinary Differential Equations |
| OECD | Organisation for Economic Cooperation and Development |
| OMICO | Oxide fuels: MIcrostructure and COmposition variations |
| PWR | Pressurised Water Reactor |
| RBC | Radiation Boundary Condition |

SBC Smoluchowsky Boundary Condition

SCK•CEN StudieCentrum voor Kernenergie • Centre d'étude de l'Energie Nucléaire (Belgium)

TD Theoretical Density

# Nomenclature

## Physical constants

| | |
|---|---|
| $A_{gb}$ | grain boundary surface ($\mu m^2$) |
| $C_{bl}$ | concentration of intergranular gas-filled bubbles ($\#/\mu m^{-2}$) |
| $c_{gb}$ | local areal concentration of fission products in the grain boundary ($\#/\mu m^{-2}$) |
| $C_{gbv}$ | concentration of fission gas atoms dissolved in the grain boundary volume ($\#/\mu m^{-3}$) |
| $C_{gbb}$ | concentration of fission gas atoms accumulated in grain boundary bubbles ($\#/\mu m^{-3}$) |
| $C_{klm}$ | concentration of fission gas atoms in a grain of class $(k,l,m)$ ($\mu m^3_{gas}/\mu m^3_{ox}$) |
| $C_{tr}$ | concentration of traps in a grain boundary ($\#/\mu m^{-2}$) |
| $D$ | volume diffusion coefficient for fission gas atoms ($\mu m^2/s$) |
| $D_v^{'}$ | reduced volume diffusion coefficient for fission gas atoms ($s^{-1}$) |
| $D_{klm}$ | volume diffusion coefficient for fission gas atoms in a grain of class $(k,l,m)$ ($\mu m^2/s$) |
| $D_{gb}$ | grain boundary diffusion coefficient for inert gas atoms in $UO_2$ ($\mu m^2/s$) |
| $D_{gb}^v$ | grain boundary diffusion coefficient for U-vacancies in $UO_2$ ($\mu m^2/s$) |
| $DT$ | microscopic time-step length employed in the numerical routine for diffusion equation in the spherical grains ($s$) |
| $\Delta t_{macr}$ | macroscopic time-step length ($\Delta t_{macr} = DT \cdot NT$), i.e. period of time in the irradiation history during which the temperature and fission rate density are assumed to remain constant, ($s$) |
| $\left(\frac{\Delta V}{V}\right)^0_{open}$ | volume fraction of initial open porosity |
| $\delta_{gb}$ | grain boundary thickness ($\mu m$) |
| $\delta_R$ | half-width of the re-solution layer near the grain face ($\mu m$) |

| | |
|---|---|
| $\delta_0$ | range around a fission fragment track where intragranular bubbles are destroyed ($\mu m$) |
| $\eta$ | viscosity of the fission gas ($sN/\mu m^2$) |
| $f_{dens}$ | fraction of the original porosity which has annealed out |
| $f_{klm}$ | volume fraction of the grains in group $k$ of the discretised grain size distribution |
| $\dot{F}$ | the fission rate density ($\sharp/\mu m^3_{ox}/s$) |
| $\phi$ | fraction of the grain boundary surface occupied by bubbles (or traps), sometimes referred to as $\phi_{bl}$ |
| $\phi_{eff}$ | effective coverage fraction of the intergranular traps |
| $\phi_{af}$ | athermal open porosity fraction due to the fabrication process |
| $\phi_{at}$ | athermal open porosity fraction due to the establishment of fine grain edge tunnels as a result of grain boundary segregation effects at temperatures between $\sim 600\,^{\circ}$C and $\sim 1000\,^{\circ}$C |
| $\gamma$ | surface tension of the intergranular bubbles in $UO_2$ ($1\,J/m^2$ [1, 2]) |
| $\Gamma_r$ | re-solution rate, i.e. the probability per unit of time for a fission product accumulated in the grain boundary to be re-dissolved in one of the adjacent grains ($s^{-1}$) |
| $J_g$ | flux of fission products leaving the grains ($\#/\mu m^2 \cdot s$) |
| $k_{in}$ | intrinsic reaction rate coefficient between an intergranular trap and a fission product migrating along the grain boundary ($\mu m^2/s$) |
| $k_{in}^{'}$ | dimensionless intrinsic reaction rate coefficient between an intergranular trap and a fission product migrating along the grain boundary ($k_{in}^{'} = k_{in}/(2\pi D_{gb})$) |
| $k$ | global capture rate coefficient at all the grain boundary traps ($\mu m^2/s$) |
| $k_B$ | Boltzmann constant ($1.38066\times10^{-23}$ J/K) |
| $k_{ss}$ | steady-state rate constant: $k_{ss} = lim_{t\to\infty} k(t)$ ($\mu m^2/s$) |
| $k_{qs}$ | quasi-steady-state rate constant ($\mu m^2/s$) |
| $\lambda$ | radioactive decay constant ($s^{-1}$) |
| $L$ | intergranular diffusion length for fission gas atoms ($\mu m$) |

| | |
|---|---|
| $L_{on}$ | Onsager radius associated with an intergranular trap in the case of ionic species ($\mu m$) |
| $l$ | reduced (dimensionless) intergranular diffusion length |
| $\mu$ | conversion factor for the concentration from atoms/$\mu m^3_{ox}$ to $\mu m^3_{gas}/\mu m^3_{ox}$ ($22.4 \times 10^{-8}/6.023$ $\mu m^3_{gas}$ / atom) |
| $n_{bl}$ | number density of intragranular bubbles ($\mu m^{-3}$) |
| $N_{sat}$ | saturation concentration of gas atoms at the grain boundary ($\#/\mu m^{-2}$) |
| $N_{bl}$ | number of gas atoms in a grain boundary bubble |
| $\omega$ | the van der Waals constant for Xe atoms ($8.5\times10^{-29}$ m$^3$per atom) |
| $\Omega$ | U-vacancy volume in the $UO_2$-matrix ($4.09\times10^{-29}$ m$^3$) |
| $P_h$ | hydrostatic pressure ($N/\mu m^2$) |
| $Q_{ex,num}$ | total number of fission gas atoms in a spherical grain, according to the exact/ analytical expression or the numerical solution, respectively ($\mu m^3_{gas}/\mu m^3_{ox}$) |
| $R_B$ | radius of the equivalent Booth sphere ($\mu m$) |
| $R_{gr}$ | grain radius ($\mu m$) |
| $R_{klm}$ | radius of a grain of class $(k, l, m)$ ($\mu m$) |
| $R_{bl}$ | projected radius of an intergranular bubble on the grain face ($\mu m$) |
| $\rho_{bl}$ | radius of curvature of an intergranular bubble ($\mu m$) |
| $r_{bl}$ | radius of an intragranular bubble ($\mu m$) |
| $R_{tr}$ | Projected radius of an intergranular trap on the grain face ($\mu m$) |
| $R_{eff}$ | effective trapping radius of an intergranular trap ($\mu m$) |
| $R_s$ | radius of the equivalent unit (Wigner-Seitz) cell around each intergranular trap, in the event of a regular distribution of traps ($\mu m$) |
| $s$ | segregation coefficient of the grain boundaries |
| $S_{gb}$ | specific surface of the grain boundaries ($\mu m^{-1}$) |
| $S_v$ | intragranular source term ($\mu m^3_{gas}/(\mu m^3_{ox} \cdot s)$) |
| $S_{fis}$ | uniform intragranular source term due to the fission process ($\mu m^3_{gas}/(\mu m^3_{ox} \cdot s)$) |

$S_{res}$ non-uniform intragranular source term due to the re-solution process at the grain boundaries ($\mu m^3_{gas}/(\mu m^3_{ox} \cdot s)$)

$\tau$ dimensionless time

$\theta$ half dihedral angle, i.e. the angle between the intergranular bubble surface and the grain boundary ($\theta = 50^\circ$ [1])

$\theta_v$ uniform initial concentration of fission gas atoms in a grain, employed in the analytical solution for the numerical parameter optimisation ($\mu m^3_{gas}/\mu m^3_{ox}$)

$y$ cumulative yield of fission gas atoms per fission event ($\sim 29$/fission)

## Mathematical constants

$CRIT_{conv}$ convergence criterion for the grain boundary concentrations

$\delta_s$ width of the imaginary supplementary layer at the grain face ($\mu m$)

$\Delta\hat{C}_{gbb}$ margin on the critical concentration for the switch between the nucleation and the growth phase of the intergranular module

$\Delta\rho_{bl}$ margin on the lower radius of curvature of the grain boundary bubbles for the switch between the growth and the nucleation phase of the intergranular module

$\lambda_0, \lambda_1$ first and second eigenvalues in the eigenvalue expansion of $C_{gb}$ in a Wigner-Seitz cell when the bubbles are regularly arranged ($\mu m^{-1}$)

$NT$ number of microscopic time-steps ($\Delta t_{macr} = NT \cdot DT$)

$P$ precision of the numerical solution of the diffusion equation in each spherical grain

# Part I

# State of the art

# Chapter 1

# Background

At present, the share of the electricity produced worldwide by nuclear power plants amounts to 17 %. Light water reactors (LWR) contribute to 85 % of this electricity production. They rely on uranium dioxide ($UO_2$), or a mixture of uranium and plutonium dioxide (MOX), for fuel. The fuel is prepared in the form of sintered pellets, which are piled-up in a metallic cladding material. The fuel pellets and the cladding are the main components of the fuel rod, as illustrated in Figure 1.1.

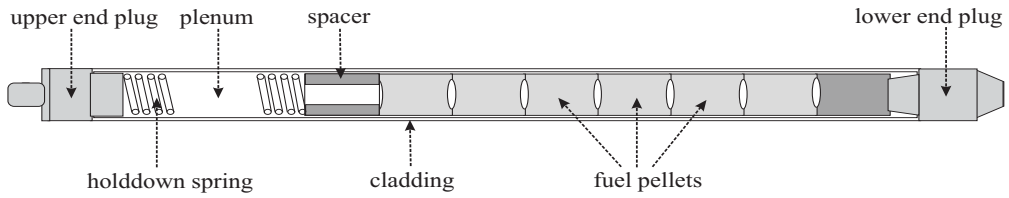


Figure 1.1: Schematic representation of a fuel rod for light water reactors

The fission process not only generates heat in the pellets, it also produces a broad spectrum of fission products, most of which are radioactive and should not be released to the environment. The pellets and the cladding thus play an important safety role, since the pellets inhibit the release, while the cladding constitutes the first barrier against the release of radioactive fission products.

In order to ensure the safe and economic operation of the fuel rods, it is necessary to be able to predict their behaviour and life-time. The accurate description of the fuel rod's behaviour, however, involves various disciplines ranging from chemistry, nuclear and solid state physics, metallurgy, ceramics, and applied mechanics. The strong interrelationship between these disciplines calls for the development of computer codes describing the general fuel behaviour. Fuel designers and safety authorities rely heavily on this type of codes since they require minimal costs in comparison with the costs of an experiment or an unexpected fuel rod failure.

The development as well as the validation of the codes, in turn, relies on data both from in-pile and out-of-pile experiments.

Despite the excellent safety records of nuclear fuel rods, efforts to enhance the predictive capabilities of the codes are still necessary in view of the following economic driving forces:

- Utilities pledge for improving the general availability of nuclear power plants in terms of load following and extended operation at reduced power, with subsequent restoration of nominal power.
- New products (nuclear fuel, cladding materials, new concepts, etc.) are explored by fuel designers and cladding manufacturers.
- Economics and prudent utilisation of natural resources provide strong incentives for extending both the fuel cycle length up to 24 month and the average discharge burnup in commercial reactors beyond 60 MWd/kgU.

These tendencies might have implications for fuel integrity and, accordingly, this could be in conflict with safety requirements. In order to address these questions, it is necessary to identify the safety issues and to understand the basic underlying mechanisms. The topics of primary interest include the fission product release, fuel swelling, fuel thermal conductivity degradation, fuel specific heat, the size (relocation) and the thermal conductance of the fuel pellet gap, fuel cladding interaction (chemical and mechanical), cladding corrosion, etc. .

The present study focuses on the behaviour of inert gas atoms, mainly Xe and Kr, in $UO_2$ fuel. On one hand, their release can lead to a variety of unwelcome effects, to such an extent that it is considered as one of the possible mechanisms that restricts the upper limit of burnup. In addition to the build-up of the rod internal pressure, the release deteriorates the thermal conductivity of the gas between the cladding and the pellets. Since the fission gas release process is strongly temperature dependent, any increase in the fuel temperature may exacerbate the situation and eventually lead to cladding failure. Perhaps a more important problem from the viewpoint of radiological safety is the content of radioactive gases and volatile solids present in the free volume of the rod at any time.
On the other hand, gas atoms and solid fission products remaining in the pellets engender swelling, which in turn can boost the mechanical interaction between the pellets and the cladding at high burnup. It is therefore essential to be able to predict the behaviour of fission gas atoms, especially at high burnup where their number increases. This of course requires a detailed knowledge of the entire fuel pin history in terms of temperature, linear heat rate, etc., a history which, for the purposes of this thesis, is assumed to be well characterised.

Before defining the objectives of my research more precisely, it is necessary to review the large number of investigations dedicated to this issue over the last four decades. These studies covered both the elucidation of basic underlying mechanisms as well as the mathematical analysis of the release process.

# Chapter 2

# Fission gas release mechanisms

## Contents

The process of fission product release in nuclear fuel involves a large number of basic mechanisms. The present chapter aims at describing briefly those phenomena that have been identified, along with their main properties and, more importantly, their domain of application. (A more detailed report has been published earlier [3]). Based on this review we will determine the mechanisms which have to be incorporated in a model for fission gas release in LWR fuel.

## 2.1 Recoil

### 2.1.1 Description

In general, a fission event entails - among others - two fission fragments that convey their kinetic energy to the fuel lattice primarily by interaction with the electrons of the material. When the kinetic energy has been expended by the stopping power of the medium, the fragment comes to rest as a fission product. However, a fission fragment, close enough to a free surface ($< 6$ to $7\ \mu m$), can escape from the fuel due to its high kinetic energy (60 to 100 MeV) [4–7], as illustrated in Figure 2.1.

### 2.1.2 Properties

Release by recoil is considered to be an athermal mechanism, i.e. independent of the local fuel temperature and temperature gradient, but proportional to the fission rate $\dot{f}$ (fissions / s) and independent of the decay constant for radioactive species [4, 6]:

$$R_i^{recoil} = \frac{1}{4} y_i \, \dot{f} \, \mu_{ff} \, \left(\frac{S}{V}\right)_g \tag{2.1}$$

where $R_i^{recoil}$ is the recoil release rate $(atoms/s)$, $y_i$ is the fission yield of the fission product of type $i$, $\mu_{ff}$ is the range of the fission fragment $(cm)$ and $\left(\frac{S}{V}\right)_g$is the geometric surface to volume ratio of the solid $(cm^{-1})$.

### 2.1.3 Domain of application

Recoil can only be observed in-pile at temperatures below 1000 °C [4, 5], when the thermally activated processes do not dominate. It can play an important role in the release of short-lived radioactive nuclides in failed rods and in low level release experiments in which a relatively high density of gas surrounds the fuel [5, 6, 8, 9].

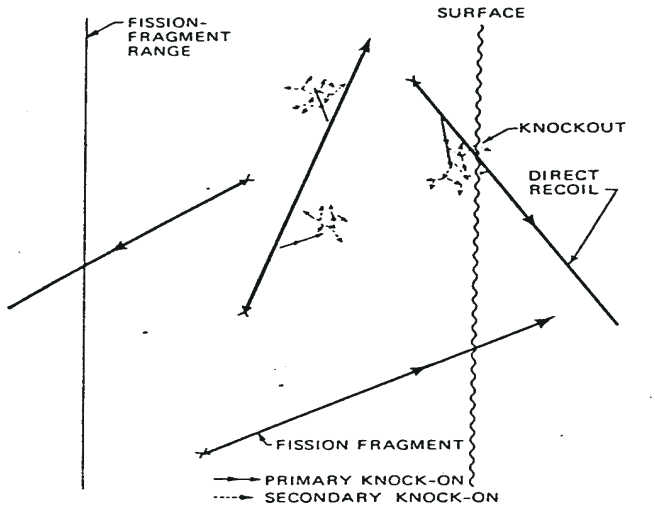


Figure 2.1: Schematic representation of the recoil and knock-out mechansism for fission gas release [4].

## 2.2 Knock-out and sputtering

### 2.2.1 Description

When fission fragments make elastic collisions with the nuclei of atoms of the lattice, the latter also become energetic particles called primary knock-ons (mean energy 100 keV [10]). These can be released, or transfer part of their energy to neighbouring atoms thereby creating higher order knock-ons (mean energy 200 eV [10]). The interaction of a fission fragment, a collision cascade or a fission spike with a stationary gas atom near the surface can cause the latter to leave the fuel if it happens within a distance close enough to the surface (Figure 2.1).

The fission fragment travelling through the oxide looses its energy by "electronic" and "nuclear" interactions with $UO_2$ at a rate of $dE/dx \sim 1keV/\text{Å}$ leading to a high local heat pulse along its path [7]. When it leaves or enters a free $UO_2$ surface, the heated zone will evaporate or sputter. For the time being, there is no definite quantitative description available for the release by sputtering.

### 2.2.2 Properties

Assuming that the fission products can be knocked-on in the same way as the uranium atoms, Olander [4] and Lewis [6] quantified the knock-out release for short-lived isotopes with the following relationship:

$$\left(\frac{R}{B}\right)_i^{knock} = \frac{\alpha_u \, \mu_{ff} \, \dot{F}}{4 N_U \, \lambda_i} \left(\frac{S}{V}\right)_t \tag{2.2}$$

where $R$ corresponds to the release rate by knock-out for species $i$ ($s^{-1}$), $B = y_i \dot{F} V$ is the birth rate for species $i$ ($s^{-1}$), $\dot{F}$ is the fission rate density ($fissions/cm^3 s$), $\lambda_i$ is the radioactive decay constant of the fission product of type $i$, $N_U$ is the concentration of U atoms ($atom/cm^3$), $\alpha_U$ represents the number of uranium atoms emitted per escaping fission fragment ($\alpha_U \simeq 5$ in sintered $UO_2$ [6]), and $\left(\frac{S}{V}\right)_t$ is the total surface to volume ratio of the fuel ($cm^{-1}$).

It should be pointed out that knock-out is proportional to the total (microscopic) surface area of fuel, whilst recoil is proportional to the geometrical surface area since a recoiling fission product is liable to re-enter any fuel it encounters whereas a higher order knock-on possesses sufficiently low energy to be stopped in the porosity or cracks [4, 6, 11].

The two athermal release processes, recoil and knock-out, lead to different release rates for the various radioactive species :

$$\begin{aligned} R_{recoil} &\propto \lambda^0 \\ R_{knock} &\propto \lambda^{-1} \end{aligned}$$

In general, the experimentally observed expression for the athermal FGR reads as follows:

$$R_{\exp} \propto \lambda^{-0.7}$$

and corresponds to a combination of the two mechanisms.

### 2.2.3 Domain of application

Knock-out and sputtering are only observable in-pile and at temperatures below 1000 °C, i.e. under conditions where the thermally activated processes do not dominate. In addition, the release by knock-out is negligible compared with that of recoil for the short-lived isotopes [5, 6, 8, 9]. Accordingly, the athermal release for these species is independent of the decay constant.

The release of stable fission gas atoms by direct recoil and knock-out is generally of little importance in reactor fuel-element performance at intermediate burnup levels [4]. The fraction of athermal release is roughly under 1% for rod burnups below 45 MWd/kgU while this released fraction accelerates to roughly 3% when the rod burnup reaches about 60 MWd/kgU [12]. Nevertheless, the athermal release component can become more important in the event of a large fraction of open porosity resulting from the fabrication process [13, 14].

## 2.3 Lattice diffusion of single gas atoms

### 2.3.1 Description

The first and basic step in the fission gas release process is single gas atom diffusion in the lattice. Possible mechanisms by which the inert gas atoms migrate through the fuel have been studied by Grimes [15] by considering low energy migration pathways between solution sites as well as the stability of gas atoms at a variety of solution sites within a defective $UO_{2\pm x}$ lattice ($x = \left|\frac{O}{M} - 2\right|$, the deviation of the stoichiometry). He postulates a cation vacancy controlled migration pathway for Xe and Kr atoms. Indeed, according to his calculations, Xe is trapped at a uranium vacancy in $UO_{2+x}$, at a tri-vacancy cluster in $UO_{2-x}$ and at a di- or tri-vacancy in $UO_2$. Since the local environment of the migrating Xe atoms is supposed to become the charged tetra-vacancy for all stoichiometries, the mechanism for diffusion only considers the association of a cation vacancy to the trap sites. (Uranium vacancies as the slower moving species are rate-controlling for most diffusion related processes in $UO_2$). The migration energy for Kr is also limited by uranium vacancy migration, considering the most stable sites for Kr in $UO_2$ (where the di-vacancy is favoured over the tri-vacancy site for Kr) and in $UO_{2\pm x}$ (same as for Xe) and assuming that the diffusion occurs through vacancy assisted pathways.
The calculational work of Grimes is partly supported by the experimental results of Matzke [16–18].

### 2.3.2 Properties

The lattice diffusion coefficient for inert gas atoms in ceramic oxide fuels like $UO_2$ is influenced by several factors.

**Temperature** Matzke [17] recommended the following Arrhenius law above 1000K for the single gas atom diffusion coefficient in $UO_2$:

$$D_{UO_2}^{Xe} = D_0 \exp\left(-\frac{\Delta H}{RT}\right) \tag{2.3}$$

where $D_0$ is the pre-exponential factor ( $= 0.5 cm^2/s$), $\Delta H$ represents the activation enthalpy ( = 375 kJ/mole = 3.9 eV/atom), and $R$ is the universal gas constant (=8.314 J/mole K). The temperature dependence is depicted in Figure 2.2. The diffusion coefficient below 1000K, referred to as the athermal diffusion coefficient, is described below.

**Deviation from stoichiometry** It has long been postulated that due to the different oxidation states of fission products and fuel, the average oxygen to metal ratio increases with burnup, in particular for fissioning Pu [16, 19–21]. This subject is still open to debate [22]. In contrast, there is no doubt that fuel oxidation by steam occurs in normal operation of a

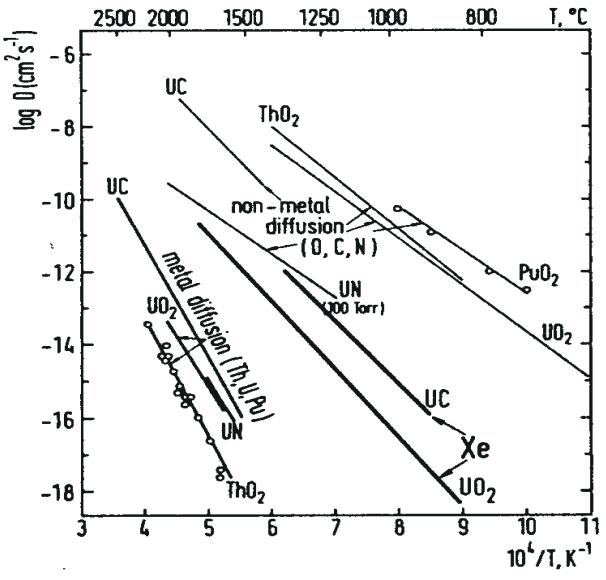


Figure 2.2: Schematic Arrhenius diagram showing non-metal atom diffusion in nuclear oxides, carbides, and nitrides. The thick lines show the recommended temperature dependences for diffusion of single Xe atoms in $UO_2$ and UC after Matzke [18] .

defective fuel rod as well as during a severe accident [23–25].

Although there is general agreement on the fact that Xe-release from $UO_{2+x}$ is faster than release from $UO_2$, and, conversely that Xe-release is inhibited in $UO_{2-x}$, there is essential disagreement on the details [16, 17, 24, 26–32]. This stems from the lack of knowledge on the diffusion mechanism of the inert gases in the fluorite-type oxide fuels. Nevertheless, three different approaches can be adopted to explain the influence of stoichiometry deviations in uranium dioxide. The first one is based on the strong correlation, irrespective of the migration mechanism, between cation vacancy diffusion enhancement [16–18] and fission gas release enhancement [16, 33]. In hyperstoichiometric fuel, Matzke [17] advocates that cations migrate by means of a vacancy mechanism. For self-diffusion by a vacancy mechanism, the diffusion coefficient is proportional to the concentration of vacant sites. The latter may be intrinsic defects, i.e. they are activated thermally as in pure stoichiometric $UO_2$, or extrinsic in nature, i.e. they are chemically induced by rendering the fuel non stoichiometric or by doping the fuel with heterovalent impurities (cf. Additives). In accordance with the model of Lidiard [34] for the concentration of uranium vacancies in non-stoichiometric fuel, some authors [27, 33, 35] have therefore taken the diffusion coefficient proportional to $x^2$, where $x$ is the deviation from stoichiometry. However, for high deviations from stoichiometry defect clustering will occur [17, 36, 37]. Consequently, one might expect a saturation of the stoichiometric effect on the diffusion coefficient of the single gas atoms as it is observed for cations [17] in $UO_{2-x}$.

The second explanation is based on the calculations of Catlow [38] and Grimes [15]. In their work, the local environment of the migrating Xe atoms is supposed to become the charged tetra-vacancy for all stoichiometries [15]. The influence of the stoichiometry deviation on the lattice diffusivity is therefore twofold. First, the formation energy of the tetra-vacancy depends on the initial trap site which in turn depends on the stoichiometry (cf. § 2.3.1). Secondly, the migration energy for Xe and Kr is limited by uranium vacancy migration, which is affected by $x$ as well.
The third explanation for the diffusion enhancement in hyperstoichiometric fuel has been suggested by Miekeley [26] and, more recently, by Shiba [39]. According to their theory, the Xe atoms trapped in vacancy clusters can be released when oxygen interstitials decompose the cluster. Increasing the number of anion interstitials can therefore inhibit the trapping of the migrating inert gas atoms and promote their diffusion.

**Additives** Several types of dopants have been added to $UO_2$ fuel in order to improve different aspects of fuel performance. Gadolonia is being used as a burnable neutron absorber in high enriched fuel rods which in turn enables to increase the discharge burnup [33] although it slightly decreases the thermal conductivity of the fuel. Several additives such as magnesia, titania, niobia and chromia have been shown to produce large-grained material in order to reduce the release of fission products [40–44]. The present understanding is that doping $UO_2$ with foreign cations can simulate the non-stoichiometry, hence it affects the defect structure as well. Finally, alumino-silicates are introduced in order to improve the sinter-ability of the powder [41] or the grain boundary retention of some volatile fission products [45].

**Phase changes** Diffusion processes can proceed at different rates and with different dependencies in different phases despite an identical composition. This fact normally leads to a knee or to two separate lines in the Arrhenius diagram [17, 46]. A further possibility is a peak in D, although this would not be expected for equilibrium processes, but may be due to temperature fluctuations during the diffusion anneal around the temperature of the phase change [17].

Matzke [17] enumerated some experimental observations which suggest the existence of a dynamic disorder in both anion and cation lattices at about 2400 °C in $UO_2$ (and about 2700 °C in $ThO_2$, etc.). Therefore, cation diffusion - including fission product diffusion - should also be affected. This is in agreement with the theory of high-temperature phase transitions in actinide oxides of Tam et al. [47]. They advocate that Schottky defects should be included in the theory to account for anomalous behaviour in mass-transport properties for these processes are controlled by the slowest-moving species, that is the cations. There is a natural coupling of the anion Frenkel defect to the Schottky defect primarily through the oxygen vacancies. A concurrent increase in the metal defects near the transition temperature would account for the observed large increases in both the creep rate and fission gas release

leading to massive plastic swelling in fluorite-structured actinide oxides.

Phase changes of potential second phases may be examined as well. In the steady state, the oxygen liberated by the fission process could combine with the fission products by reducing them (e.g. formation of cesium uranates [48]), provided that pellet-cladding contact is not yet established. The entailing departure from stoichiometry will be small [21]. However, during transient heating the precipitated fission products can decompose, thereby releasing oxygen. The stoichiometry can therefore increase locally and temporarily, leading to fission gas release enhancement (cf. Deviation from stoichiometry).

**Burnup** Two fission products are produced per fission event, creating impurity atoms of about 30 different elements. As a consequence, the defect structure of the fuel will change due to chemical doping. Moreover, due to the different oxidation states of fission products and the fuel, the average O/M ratio can increase slightly with burnup (cf. § 2.3.2). Both chemical modifications can affect the location of fission products, hence their lattice diffusivity, as was confirmed by Nicoll and Catlow [38]. Their calculations indicate that the preferential solution sites of the xenon atoms are not only sensitive to the stoichiometry of the fuel but also to the xenon concentration.
In addition to chemical modifications, the fission event generates a high rate of defects. The radiation damage interacts with the migrating fission products, entailing trapping (cf. § 2.4), re-solution of fission gas atoms from bubbles (cf. § 2.5) and fission enhanced diffusion (cf. Radiation enhanced diffusion). Accordingly, most fission gas release models make use of an effective diffusion coefficient which accounts for those mechanisms [49].

**Radiation enhanced diffusion** There is a constant slowing down process of fission products in the fuel causing fission spikes or tracks to be formed. The spikes have a length in the order of 7 $\mu m$ wherein about $1.5\,10^4$ $U$-Frenkel pairs are produced instantaneously [16]. Only 5000 pairs remain after direct annihilation [16]. The width of the permanently disturbed zone is approximately 7 nm [18]. Significant temperature increases along the axis occur causing large hydrostatic pressure gradients leading e.g. to a separation of vacancies from interstitials and hence a largely temperature-independent, athermal radiation-enhanced diffusion, as well as re-solution of inert gas atoms from bubbles or even complete destruction of bubble nuclei or small bubbles. Each atom is affected by a fission spike at a rate of once in a few hours to once in a day, depending on the reactor type [18].

A consistent set of radiation enhanced diffusion coefficients ($D^*$) is available for metal self-diffusion [16, 17]. In as far as these data may be due to a mixing of atoms in the course of fission spikes, the $D^*$ values will apply for gases as well. However, no firm conclusions emerge as to the mechanism. Despite this, $D^*$ has been shown to be directly proportional to the fission rate density ($\dot{F}$): $D^* = A\dot{F}$ where $A = 1.2\,10^{-29} cm^5$ for oxide fuels.

Since $D^{Xe} > D^U$, the thermally activated temperature-regime for fission gas diffusion

extends to lower temperatures than $D^U$ [18]. A radiation enhanced diffusion coefficient will therefore only be operative in the cold outer rim of the fuel where gas release is low and swelling is small [35]. (At low temperatures, recoil, knock-out and radiation enhanced diffusion dominate). However, at temperatures between 1000 °C and 1400 °C [17], there appears to be some influence of the irradiation as well, leading to a lower activation enthalpy of the single gas atom diffusion coefficient. This has been modelled by Turnbull et al. [9] who considered three mechanisms dominant in different temperature regimes (cf. Fig. 2.3):

$$\begin{aligned} D &= D_a + D_b + D_c \\ &= 7.6\ 10^{-10} \exp\left(-\frac{35000}{T}\right) + 5.64\ 10^{-25}\sqrt{\dot{F}} \exp\left(-\frac{13800}{T}\right) + 8\ 10^{-40}\dot{F} \end{aligned} \quad (2.4)$$

where the single gas atom diffusion coefficient ($D$) is expressed in $m^2/s$, $D_a$ denotes the intrinsic diffusion which depends only on the fuel temperature and is dominant above 1400 °C, $D_b$ describes diffusion via thermal and irradiation induced cation vacancies which depends both on the fuel temperature and the fission rate density and dominates when 1000 °C$\leq T \leq$1400 °C, $D_c$ ($= D^*$) corresponds to the athermal term and dominates down to 250 °$C$. $D_b$ can also be expressed as an explicit function of the uranium vacancies, using standard random walk arguments [1]:

$$D_b = s^2 j_v C_v^0 = s^2 j_v \left[\frac{k_I s^2}{2Z}\left(\sqrt{1 + \frac{4KZ}{j_v k_V^2 k_I^2 s^4}} - 1\right)\right] \quad (2.5)$$

where $s$ is the atomic jump distance (3.868 Å ), $j_v$ represents the jump frequency of the vacancy ($=10^{13} \exp(-2.39/kT)$), $k_I, k_V$ are the interstitial and vacancy sink strength respectively, $Z$ is the number of sites around a defect from which mutual recombination is inevitable ($\approx$100), $C_v^0$ refers to the steady-state vacancy concentration, and $K$ is the damage rate or displacement rate of atoms from their lattice sites during irradiation ($10^4 \dot{F}\Omega \leq K \leq 5 \times 10^5 \dot{F}\Omega$, where $\Omega$ = atomic volume).

**Diffusion of precursors** The inert gases Kr and Xe are practically not formed directly by fission, but originate by $\beta$-decays from the precursor [18] (Se and Br in the case of Kr, Te and I in the case of Xe). Many of such precursors have a half-life long enough to allow diffusional mobility of the precursor, thus the gas to be studied may be located at a site some distance away from where it was formed. Complications arise particularly for short-lived nuclides, i.e. when the precursor half-life is comparable to or longer than that of the rare gas nuclide, or if the diffusion coefficient of the precursor is much larger than that of the gas [16] (e.g. I and in particular Te diffuse faster than Xe [18, 30, 49] while Br diffuses faster than Kr [49]). For instance, at temperatures above 1000 °C, thermally activated lattice diffusion, and at lower

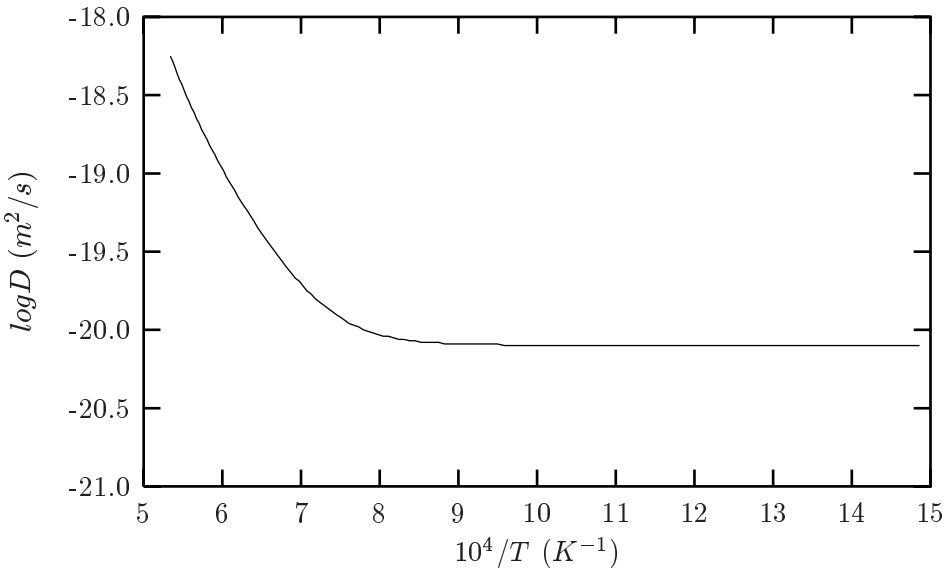


Figure 2.3: The volume diffusion coefficient of inert gas atoms in $UO_2$ between 400 $^\circ C$ and 1600 $^\circ C$ at a fission rate density of $10^{19} m^{-3} s^{-1}$ according to Eq.(2.4)

temperatures, radiation enhanced diffusion enable the precursors to migrate typically 10 nm (for $^{133}$Xe) before decaying to the rare gas [16]. However, in general the precursor enhancement is less then 30 % for most isotopes [50], and is incorporated in an effective diffusion coefficient (cf. chapter 3).

### 2.3.3 Domain of application

There is a general consensus to consider three diffusion mechanisms dominant in different temperature regimes ($D = D_a + D_b + D_c$) as illustrated in Figure 2.3. Intrinsic diffusion ($D_a$) depends only on the fuel temperature and is dominant above 1400 °C. Diffusion via thermal and irradiation induced cation vacancies ($D_b$) depends both on the fuel temperature and the fission rate density and dominates when 1000 °C $\leq T \leq$ 1400 °C. Finally, the athermal term ($D_c$) dominates down to 250 °C. Unperturbed (intrinsic) diffusion of single inert gas atoms (Xe, Kr) can be observed at low damage and gas concentration ($\leq 10^{-5}$ at%) [17]. At higher gas and damage concentrations other effects should be taken into account (cf. § 2.4 and § 2.5).

## 2.4 Trapping of fission products

In this section we will deal with trapping in the bulk material. Trapping in the grain boundaries will be treated separately in chapter 5.

### 2.4.1 Description

Gas atom migration in nuclear fuels involves more than simple lattice diffusion. Shewmon [46] indicated the large effect that trapping at defects can have on diffusion in solids of solute with a low equilibrium solubility (e.g. H in iron, Xe in $UO_2$). In nuclear fuels, either natural (e.g. impurities, closed pores, dislocation lines, etc.) or radiation produced imperfections in the solid (e.g. vacancy clusters in fission tracks, fission gas bubbles, solid fission-product precipitates, etc.) depress the release rate by temporarily or permanently trapping the migrating atoms. The experiments show that for burnups characteristic in power reactors, gas atom trapping due to fission produced defects should be very much more important than trapping at natural defects in the as-fabricated fuel [4]. The most likely deep trap is the population of fission gas bubbles, in agreement with electron microscopy observations [51]. Volatile fission products such as Cs, I, and Rb can also form bubble-like structures in the bulk when the temperature exceeds $\sim 0.33\,T_m$ ($T_m$ = absolute melting temperature), although to a lesser extent, and depending on the chemical nature of the impurity [52–54]. The absence of retarded release for these precursors (of Xe and Kr) mentioned by Matzke [17] has been attributed to distortions of the profiles in ion-implanted samples [55].

### 2.4.2 Properties

The interaction of a gas atom with each trapping site is characterised by a binding energy. According to Matzke [17, 18], the trapping increases the activation enthalpy of inert gas diffusion by about 0.5 to 0.8 eV, hence a value of about 4.4 eV is reached for $UO_2$ and UC in instead of 3.9 eV (cf. § 2.3).

The capture rate of gas atoms ($\Gamma_{tr}$) is an important characteristic of trapping. The reactions of point defects with traps are usually described in terms of phenomenological rate equations of chemical kinetics. Accordingly, the trapping rate is linearly proportional to both the trap density in the solid ($C_{lattice}^{traps}$) and the concentration of free gas atoms in the lattice ($C_{lattice}^{gas}$):

$$\Gamma_{tr} = k C_{lattice}^{traps} C_{lattice}^{gas} \tag{2.6}$$

where $k$ represents the rate constant for trapping ($cm^3/s$). At present, several diffusion-controlled reaction rate coefficients are in use, derived basically from the Smoluchowsky theory of coagulation [56]:

$$k = 4\pi R_{tr} D \tag{2.7}$$

where $R_{tr}$ corresponds to the trap radius and $D$ is the lattice diffusion coefficient. When the particle growth is reaction-rate-limited, the expression for $k$ reads [4]:

$$k = \frac{4\pi R_{tr}^2 D}{a_0} \tag{2.8}$$

where $a_0$ is the lattice constant. This value of $k$ is larger than that obtained from Eq.(2.7) by a factor $R_{tr}/a_0$, hence diffusion control is much more likely for spherical sinks on the order of a few nm in diameter.

Another important aspect related to the trapping phenomenon is the saturation of the sinks, that is when the concentration of the atoms in the traps ($C^{gas}_{traps}$) is constant:

$$\frac{\partial C^{gas}_{trap}}{\partial t} = 0 \tag{2.9}$$

During irradiation, a re-solution mechanism is operative, hence the trapping and the re-solution rates can be balanced. Accordingly, the migrating atoms are at equilibrium between the lattice and the traps, in other words there will be an equilibrium relationship between $C^{gas}_{traps}$ and $C^{gas}_{lattice}$:

$$gC^{gas}_{lattice} = bC^{gas}_{trap} \tag{2.10}$$

where $g = kC^{traps}_{lattice}$ is the capture rate and $b$ corresponds to the re-solution rate, defined as a probability per unit time (cf. § 2.5). Speight [57] has shown that saturation of the intragranular bubbles occurs relatively fast. As a result, many models for fission gas release define an effective volume diffusion coefficient [1, 49, 58, 59]:

$$D_{eff} = D\frac{b}{b+g}\,, \tag{2.11}$$

which applies to all the fission gas atoms in the grains ($C^{gas}_{trap} + C^{gas}_{lattice}$). In reality, the free, untrapped gas atoms still diffuse with their intrinsic $D$, but the fraction of them migrating to the grain boundaries decreases.

Based on the expression for the trapping rate in Eq. (2.6), one can enumerate the most important parameters affecting the trapping of migrating fission products in nuclear fuels:

**Fission density** Experiments on single crystals and sinters of nominally stoichiometric $UO_2$ indicate that the diffusion coefficient of Xe is dramatically decreased once the fission dose exceeded $10^{15}$ fissions/cm$^3$ [16,60]. This has been attributed to trapping by irradiation induced defects, and is also reflected in Eq. (2.6). The experimental results also indicate a saturation of the trapping effect [16]. This is in accordance with the conclusions of Lawrence [11] who suggested that after a low burnup, in the region of 0.07 to 0.4 MWd/kgU, the reduction mechanisms saturate. However, in view of some ion implantation work, Matzke [18] recalls that a more complicated behaviour could be prevailing.

**Gas concentration** From Eq. (2.6), it can clearly be seen that the trapping of gas atoms is more pronounced at high gas concentrations, where the probability of an encounter with other gas atoms or vacancy clusters increases. This is a consequence of the insolubility of the gases

in nuclear fuels and of the stability of the gas-gas cluster [61]. Nicoll et al. [38] provided a complementary explanation to the sharp decrease in the diffusion coefficient once a threshold burnup is exceeded. The decrease in the diffusion coefficient of Xe is explained in terms of a change in the stable site of single Xe atoms not trapped by radiation damage: from di- to tri-vacancies when the Xe concentration surpassed $10^{-6}$ at% (percent of U + O atoms).

**Fission rate** When the fission rate increases, the number of radiation induced defects first grow larger and cannot anneal out. The trapping is therefore enhanced. Olander [4] indicates that when fission rates exceed $2 \times 10^{13}$ fissions/(cm$^3$·s), the entailing annealing of defects will increase the effective diffusion coefficient. However, this could also be due to an increase of the irradiation induced re-solution effect (cf. § 2.5).

**Oxygen potential** If the tri-vacancy is granted a higher binding energy than di-vacancies with respect to trapping of single gas atoms, hyperstoichiometric fuel will have a smaller activation enthalpy for migration in comparison with hypostoichiometric fuel. This conclusion can be drawn from the computational study of Nicoll et al. [38] since they showed a shift of the most probable site for Xe atoms from di- to tri-vacancies when the fuel becomes hypostoichiometric.

### 2.4.3 Domain of application

Trapping of migrating gas atoms in the matrix occurs at very low burnup values, corresponding to a fission density of $10^{15}$ fissions/cm$^3$. Speight [57] has indicated that traps can be considered to be saturated for irradiation times of practical interest. Experimental results [11] indicate a saturation of the trapping effect in the region of 0.07 to 0.4 MWd/kgU. Finally, it should be stressed that the amount of trapping will depend on the number density and size of the traps (bubbles), hence on the temperature and the fission rate.

## 2.5 Irradiation induced re-solution

It is well known that the high energy of solution of inert gas atoms and volatile fission products in metals and most solids (e.g. $\sim$ 10 eV for Xe in $UO_2$) provides a strong driving force for precipitation in bubbles. This section deals with a re-solution route through which gas atoms can leave these traps.

### 2.5.1 Description

**Relevance** It has been recognized that the amount of fission gas arriving at grain boundaries through the high density of intragranular traps would be very small, far below the steady-state experimental gas release measurements. Early experimental investigations [62–67] have shown

that irradiation induced re-solution of the gas from bubbles during the irradiation significantly increases the gas population in the matrix (i.e. the dynamic solubility of the inert gases) which is capable of diffusing out of the grains.

Another important consequence of re-solution is its ability to moderate the build-up of gas in grain boundary bubbles. Hence, the incubation period, i.e. the time before which no significant fission gas release can be observed, increases because the grain boundary capacity for gas atoms must be exceeded such that the porosity there grows and interlinks to form pathways to the free surface (cf. § 2.11).

**Mechanisms for re-solution** Although $\gamma$-rays, neutrons and fission fragments are all capable of causing re-solution of fission gases from bubbles, it is only the fission fragment that can account for the high efficiency of the process as observed experimentally. Fission fragments not only have a higher initial kinetic energy (50-100 MeV) than fast neutrons (2 MeV), but they are also charged and consequently have a higher cross-section for transferring energy either to lattice, or to gas atoms.

Turnbull [67] and Olander [68] have reviewed plausible mechanisms of re-solution that could be induced by fission fragments. The first model for the re-solution process was a microscopic model. It considers simple knock-out of one gas atom at a time from bubbles when the gas atom is struck directly by a fission fragment or by a primary knock-on uranium atom. This model does not predict complete bubble destruction - as suggested from experimental observations [67, 69] - since only about 10 % of the initial fission fragment energy is lost in direct collisions with lattice ions while the rest is first dissipated in the electronic structure of the material through which it passes by means of Rutherford collisions. Ronchi et al. [70] confirmed these findings with their calculations.

Also several macroscopic models have been proposed. They have in common the feature of partial or complete destruction of a bubble by a fission fragment. Although the actual mechanism remains uncertain, the balance of opinion favours a mechanism based on fission fragment energy loss via electron excitation leading to a cylindrical heat distribution around the fission fragment track along with a compressive thermoelastic stress pulse [67–70].

### 2.5.2 Properties

The irradiation induced re-solution rate depends on the number of fission gas atoms and the fission rate. In addition, the re-solution mechanism based on the energy loss via electron excitation implies that the re-solution efficiency is likely to be dependent on bubble size. The re-solution causing complete destruction of small intragranular bubbles may not have the same efficiency when applied to larger grain boundary bubbles [67,69]. A further implication is that the efficiency of re-solution is dependent on the electron-lattice coupling of the nuclear fuel [69, 70]. For example in the case of $UO_2$, which has a mixed covalent-ionic character, the coupling

is much stronger in comparison with UC, which has a metallic character. As a consequence, the lattice immediately surrounding the fission fragment track in $UO_2$ experiences a more severe temperature and pressure pulse which can result in permanent damage to this lattice.

One should be careful in applying the re-solution parameters in the fuel behaviour calculations because the form of the term representing re-solution generally depends on whether the macroscopic ($b'$) or microscopic model ($b$) of the phenomenon is used. However, in the expressions for the rate at which single gas atoms appear in the matrix as a result of re-solution from all bubbles per unit volume ($\Gamma_{res}$), the parameters $b'$ and $b$ can be used interchangeably:

$$\begin{aligned} \Gamma_{res} &= b\, n_{bl}\, m_{bl} = b'\, m_{bl}\, n_{bl} \\ &= b\, M_{bl} = b'\, M_{bl} \end{aligned} \tag{2.12}$$

where $b'$ and $b$ are defined as the probability per second that a bubble in the fuel is destroyed and the rate at which gas atoms are redissolved from a bubble respectively [68], $n_{bl}$ corresponds to the bubble density of the fuel ($bubbles/m^3$), $m_{bl}$ is the number of gas atoms in a bubble and $M_{bl}$ is the total number of gas atoms per unit volume contained in the bubbles. Consequently, several models [1, 58] account for the re-solution effect at intragranular bubbles by means of the macroscopic model [67]

$$b' = 2\pi\,(r_{bl} + \delta_0)^2\,\mu_{ff}\dot{F} \tag{2.13}$$

according to which a bubble can be destroyed if its centre lies within a distance $(r_{bl} + \delta_0)$ of the fission fragment. For the larger grain boundary bubbles the same mechanism is operative but its ferocity is likely to be tamed by their large size [1, 71]. The re-solution event is therefore more likely to be a "whittling away" process than the wholesale destruction of the bubbles envisaged for intragranular porosity.

### 2.5.3 Domain of application

The re-solution mechanisms driven by the fission spikes is considered to operate during all in-pile conditions.

## 2.6 Thermal re-solution

### 2.6.1 Description

For a trapped gas atom to be redissolved requires a potential barrier to be crossed. The thermally activated re-solution of a second phase, whether a precipitate or a bubble, within a matrix is clearly linked up with both the solubility of the second phase constituent (or the solution energy) and the binding energy of the migrating atom to the trap. [a]

[a] Volatile fission products could be "trapped" by the formation of immobile compounds, hence the thermally activated dissociation of these compounds can be considered as thermal re-solution as well.

### 2.6.2 Properties

As indicated by White [71], the equilibrium gas concentration resulting from thermal re-solution in the vicinity of a bubble can be expressed by:

$$C = C_0 \exp\left(\frac{bp}{kT}\right) \tag{2.14}$$

where $C_0$ represents the thermal re-solution pre-multiplier, $\gamma$ is the surface energy of a small bubble, $k$ is Boltzmann's constant, $T$ is the absolute temperature, $p$ corresponds to the internal gas pressure and $b$ is the Van der Waal's gas volume. According to Eq. (2.14) the main parameters influencing thermal re-solution are the temperature and the internal gas pressure. As a result, small bubbles with a high internal pressure will sustain thermal re-solution with a higher probability, in accordance with computations of Jackson et al. [61, 72].

### 2.6.3 Domain of application

Olander [68] predicts a thermal re-solution parameter a factor 10 to 100 times lower than the irradiation induced re-solution factor. According to ion-implantation studies of Kr in $UO_2$ [73], thermal re-solution should be disregarded. Calculations also rule out any thermal dissolution of gas from underpressurised bubbles, since the predicted solution energy is very high [61] ($\sim$ 10 eV). As a result, thermal re-solution has generally been considered not to be too important. Neverteless, small overpressurised bubbles are predicted to lose gas rather easily, typically with energies in the range of 2-8 eV [72]. Theoretical considerations of Veshchunov [74] corroborate the importance of thermal re-solution from small intragranular bubbles at temperatures in excess of 1500 °C. In line with this, Brearly et al. [75] explain the high release rates observed during isothermal transient heating of fuel. Also White [71] applies thermal re-solution from overpressurised bubbles, both during post-irradiation annealing experiments and under in-pile conditions.

## 2.7 Thermal diffusion

### 2.7.1 Description

It is an empirical fact that, if a homogeneous two-component phase is placed in a temperature gradient, an unmixing occurs since one component diffuses preferentially to the hot (or the cold) end. This effect is called thermal diffusion or the Soret effect. The simplified flux equation that will fit this empirical observation can be written as [18, 46]:

$$J_i = -D_i\left(\nabla c_i + \frac{Q_i c_i}{RT^2}\nabla T\right) \tag{2.15}$$

where $J_i$ corresponds to the flux of atoms of type $i$, $c_i$ represents the concentration of the species $i$, $Q_i$ is the heat of transport for the considered species and $R$ is the universal gas constant. This expression can be derived from the principles of irreversible thermodynamics [46, 76]. According to this theory, a particular flux is the result of a combination of all forces present and the fluxes of various types are related to all forces in a linear manner. In particular, the temperature gradient induces a mass flux. If $D/RT$ is taken to be the mobility of the component, $-(Q/T)\nabla T$ is the effective "force" exerted by the temperature gradient on each solute atom.

### 2.7.2 Properties

The simplified equation above shows that the flux $J_i$ is proportional to $D$ and to $Q$. The latter quantity is called the heat of transport, since it physically represents the quantity of heat transported by a mole of diffusing material in the absence of a temperature gradient or the heat flow due to a unit of matter flow. The sign of the experimentally determined parameter $Q$ determines the magnitude and direction of the migration: a positive (negative) value corresponds to a flow of matter down (up) the thermal gradient.

The thermal gradient induces a higher probability for the migrating species to move up or down the gradient. This small biasing of the jump direction will change neither the jump mechanism nor the jump frequency at any given temperature. Therefore, the matter flow induced by the thermal biasing will be proportional with $D$, or the chemical diffusion coefficient [17] in the case of metal atoms in (U,Pu)$O_2$.

### 2.7.3 Domain of application

Pronounced temperature gradients exist in operating nuclear fuels, especially fast breeder oxide pins where the power density is the highest. Several redistribution phenomena, related to thermal diffusion in nuclear fuels, have been observed, among which the redistribution of oxygen [12, 77–79], the actinides [80, 81] and the constituents in U-Zr alloys [82].

Thermal diffusion of oxygen in $UO_{2\pm x}$, (U,Pu)$O_{2\pm x}$ and $PuO_{2\pm x}$ is very pronounced [17], but there is a minimum in the heat of transport in the vicinity of the stoichiometric composition [79]. Kleykamp [20] concluded that $UO_2$ fuels operated at high power, hence at high temperatures, remain essentially stoichiometric since any excess oxygen due to possible hyperstoichiometry of the starting fuel or due to the formation of excess oxygen by fission would diffuse to the clad and be gettered in a reaction layer. This was confirmed by Matzke [22], who assessed the oxygen potential in the rim region of high burnup $UO_2$ fuel. Accordingly, thermal diffusion of oxygen and the potential influence of the stoichiometric deviations on the fission product release (cf. § 2.3) can be neglected in LWR fuels, except for accident conditions [25].

## 2.8 Grain boundary diffusion

### 2.8.1 Description

Grain boundary diffusion is the most commonly observed route for solute migration in polycrystalline materials. It is generally accepted that diffusion in crystalline solids proceeds more rapidly along grain boundaries than through the lattice [46, 83, 84]. This is due to the atomic jump frequency in these planar defects which is about a million times greater than the jump frequency of regular lattice atoms in stoichiometric materials at 0.6 $T_m$ ($T_m$ is the melting temperature expressed in Kelvin). The dominant atomic jump mechanism by which the atoms move along grain boundaries appears to be a vacancy mechanism [83–85].

Several observations in nuclear fuels such as creep [86], intergranular swelling [87, 88], the dispersion of oxygen [89], burnable poisons [90] and plutonium [91], have been attributed to grain boundary diffusion as well. In a similar way, Turnbull et al. [92–94] have considered grain boundary diffusion in the model for in-pile release of volatile fission products and inert gas atoms in trace irradiated $UO_2$ fuels. Olander and co-workers [95, 96] followed the same idea in their post-irradiation analysis of low burnup $UO_2$ samples, as did Akabori et al. [97] for $ThO_2$. More recently, post irradiation examinations [98] have indicated that fission gases may migrate long distances on the grain boundaries in (U,Pu)$O_2$ fuels and be released.

### 2.8.2 Properties

The majority of experimental investigations regarding grain boundary diffusion mechanisms has been performed on metals and more specifically dealt with self-diffusion [83, 84]. Unfortunately, there are no experimental data available at present for the grain boundary diffusion coefficient of inert gas atoms in LWR fuel. Therefore, one can merely summarise the qualitative effects of several parameters on the grain boundary diffusion in this material:

**Temperature** In general the grain boundary is a much more open medium for the atomic movements than the adjoining grains. The energy to form a vacancy or move an atom into a vacancy will therefore be lower than in the lattice. Thus, considering a vacancy mechanism for self-diffusion, it is easy to see qualitatively that the activation energy in the boundary will be appreciably less than in the lattice. As a result, grain-boundary diffusion will be more important at lower temperatures.

**Grain boundary structure and orientation** For the small-angle grain boundaries a "pipe" model has been proposed [46, 83, 84], where the grain boundary is replaced by a planar array of dislocation cores or pipes. According to this model, diffusion in small-angle tilt boundaries should be highly anisotropic, diffusion along the dislocation pipes being much larger than that perpendicular to the pipes. In addition, the model predicts a dependency on

the mis-orientation axes as it affects the distance between dislocations. On the other hand, the activation energy is predicted to be independent of the mis-orientation angle.
For large-angle boundaries, experimental results [46, 84] indicate that the anisotropy varies very smoothly from the small-angle to the large-angle grain boundaries. It persists to angles up to 45 °, where the dislocation model is no longer applicable. Furthermore, there is evidence that the activation energy depends on the mis-orientation angle, with maxima occurring at the coincident site lattice mis-orientations [83].

Finally, it appears that grain boundary diffusion coefficients of all the metals with the same crystalline structure can be represented by a single Arrhenius line on a reduced temperature scale ($T_m/T$), indicating that diffusion in structurally similar metals must occur by the same mechanism [83].

**Composition and burnup** A number of factors is responsible for hindering a clear understanding of the phenomenon of grain boundary diffusion in non-metals, especially oxides and ceramics. One major practical problem with these materials is the difficulty in controlling their purity as well as stoichiometry. Even their volume diffusion characteristics are known to be extremely sensitive to the presence of impurities (cf. § 2.3). Furthermore, distinction should be made between self-diffusion and impurity migration. The latter may be subject to strong segregation effects since interactions of impurity atoms with the boundaries may stabilize different structures, produce precipitates, and therefore significantly influence grain boundary diffusion. Trapping or precipitation of fission products can occur at different types of traps such as structural defects, gas filled bubbles and pores, and metallic precipitates. In addition, volatile fission products such as Cs and I can be immobilised by means of a chemical interaction with the fuel (e.g. uranates) or other fission products (e.g. CsI). As a result, the precipitation or trapping of fission products is dependent on the temperature and burnup [99–104], on the species under consideration [52, 93, 103, 105], on stoichiometry deviations and additives [45, 106], as well as on the geometrical parameters such as the number density and the size of the trapping centers.

**Ionic charge** The extrapolation of the properties for grain boundary diffusion in metals to ceramics also warrants special care because of the ionic character of the structure. This leads to the formation of an electrostatic potential at the grain boundaries, and may affect the diffusivity of charged ions (e.g. Cs or I) along the grain boundaries in oxides [83]. Common ceramic oxides usually contain relatively large concentrations of aliovalent impurities. Consequently, electrical charge effects should make grain boundaries in the oxides particularly susceptible to strong segregation effects [84].

### 2.8.3 Domain of application

In view of the lower activation energy, grain boundary diffusion should be perceptible at temperatures [84] $T \leq 2/3T_m$, e.g. below 1800 °C for $UO_2$. However, there appears to be a contradiction about the role of the grain boundary in fission gas release. Some authors advocated that it serves as a high diffusivity pathway for the release of fission products in trace irradiated fuel [92–97], while most present day models in high burnup $UO_2$ [1, 7, 58, 59, 71, 107, 108] consider it to be a perfect sink where gas atoms are immobile and precipitate to form bubbles, which eventually will interconnect and form a tunnel network . This is mainly based on the presence of grain boundary bubbles in high burnup fuel [109–113] which appears to be inconsistent with rapid grain boundary diffusion. I have reconciled the two contradictory roles of the grain boundaries (cf. Chapter 6) by considering a switch from release assisted by grain boundary diffusion in trace irradiated $UO_2$ to trapping and eventual interlinkage of the intergranular bubbles in high burnup fuel (cf. § 2.11).

## 2.9 Grain boundary sweeping

### 2.9.1 Description

In this section we will only deal with normal (or equiaxed) grain growth. Columnar grain growth mainly occurs under fast reactor fuel conditions and is related to bubble migration by means of the evaporation/condensation mechanism, which will be discussed in § 2.10.

During normal grain growth, large grains spontaneously grow at the expense of smaller ones. On a microscopic scale the process involves movement of matrix atoms from the convex to the concave side of a curved grain boundary, where the atoms are surrounded by a somewhat larger number of neighboring atoms. Consequently, the grain boundary, which moves in the direction opposite the net flow of atoms, is displaced toward the center of curvature of the grain on the convex side of the boundary [4].
From a macroscopic point of view, the driving force for grain growth is the reduction of the free energy of the solid that accompanies the decrease of the area of the grain boundaries it contains.

The grain growth phenomenon affects the fission product release in two ways. First of all, grain boundary sweeping provides another mechanism for the collection of fission gas at these internal surfaces from which release can occur [114]. The collection results from the fact that fission gas is most insoluble in the fuel matrix, hence the sweeping grain boundary does not redeposit any gas in the newly-formed crystal behind it. The moving grain boundary acts as a fission gas filter.
Secondly, the diffusion distance for the fission products created in the grain increases. Unlike the first consequence this tends to reduce the release rate. Therefore an inadequacy in grain growth modelling is rapidly reflected in inaccuracies in calculated fission gas inventories.

### 2.9.2 Properties

In general, the kinetics of grain growth in $UO_2$ are written in the following form [115–121]:

$$R_{gr}^n = R_{gr,0}^n + Kt \tag{2.16}$$

where $R_{gr,0}$ and $R_{gr}$ stand for the initial and current grain size respectively, $n$ is the grain growth exponent, and $K$ corresponds to a rate constant. The grain growth exponent varies between 2 and 4, depending on the factors controlling grain growth, i.e. on the growth mechanisms [120]. The difficulty of deriving one single grain growth law for the whole range of operating conditions in reactor fuel stems from the variety of parameters affecting grain growth :

**Temperature** The grain growth rate is determined either by the mobility of the grain boundaries, either by the mobility of the pores or the fission product accumulations exerting a retarding force on the boundary movement. In any case, the transfer is thermally activated and the rate constant varies exponentially with the temperature according to the Arrhenius function. The activation energy is directly related to the transport mechanism determining the grain boundary motion, i.e. it can vary from about 267 kJ/mole for curvature driven forces [120] up to 570 kJ/mole for evaporation mechanisms [115].

**Grain radius** The influence of the grain radius on its growth can best be explained from the following analysis [120]. Each grain is treated as an isolated entity and it is assumed that the inward force ($F$) on an element of grain boundary is inversely proportional to its radius of curvature and proportional to the grain boundary energy ($\gamma_{gb}$):

$$v \propto \frac{dR_{gr}}{dt} \propto M_{gb}F \propto \frac{D_{gb}}{kT}\frac{\gamma_{gb}}{R_{gr}} \tag{2.17}$$

where $v$ corresponds to the grain boundary velocity, and $M_{gb}$ represents the grain boundary mobility which is related to the diffusion coefficient of the boundary ($D_{gb}$) through the Nernst-Einstein equation: $M_{gb} = D_{gb}/kT$. Eq.(2.17) is equivalent to the assumption that the velocity of a grain boundary is proportional to the pressure difference caused by its curvature [115, 116, 118, 120]. This approach leads to a parabolic kinetics like equation (i.e. $n = 2$). However, many experimental investigations of $UO_2$ grain growth indicate that $n$ is rather between 2 and 3 suggesting that the derivation given is overly simplistic.

As already mentioned before grain growth is a far more complex process than simply the expansion of the average grain size in a single-phase material with second-phase particles. The sum of the individual grain sizes is constant and the increase in average grain size is thus connected with a disappearance of some grains. This process may be viewed as the change of the grain size distribution with time. The mean field theories have been developed in order to

determine this distribution function $f\left(R_{gr}, t\right)$ as a function of time and the grain radius [120]. The mean field approach deals with the change in size of an isolated grain embedded in an environment which represents the average effect of the whole array of grains. They provide a continuity equation for the flux of grains through grain size space :

$$\frac{\partial f}{\partial t} = \frac{\partial}{\partial R_{gr}}\left(\widehat{D}\frac{\partial f}{\partial R_{gr}}\right) - \frac{\partial f}{\partial R_{gr}}\left(vf\right) \tag{2.18}$$

where $\widehat{D}$ can be identified with a diffusion coefficient which only depends on the specific grain boundary mobility. According to this equation, the flux of grains through grain size space consists of two contributions : a diffusion-like process (the physical basis of which is not clear) and a curvature-driven drift term. Hillert [118] assumed that the latter term dominates and suggested an expression for the drift velocity, seen as equivalent to the boundary velocity and proportional to $dR_{gr}/dt$:

$$\frac{dR_{gr}}{dt} = M^{'}\left(\frac{1}{R_{cr}} - \frac{1}{R_{gr}}\right) \tag{2.19}$$

where $M^{'}$ represents the growth rate constant which is proportional to both the mobility and the surface energy of the grain boundary. The critical grain radius ($R_{cr}$) is such that grains with radii less than $R_{cr}$ tend to shrink initially and those with larger radii tend to grow. The mean field theories predict parabolic growth kinetics as well. Another criticism of all these theories is the lack of concern regarding topological constraints and their role in grain growth.

**Grain shape** Rhines and Craig have proposed a grain growth model which accounts for the changes in topological parameters [117, 120]. They obtain a value of 3 for the grain growth exponent. According to Vandermeer [117], this arises from an improper consideration of the driving force for grain growth: the force is distributed over every atom in the volume of the material rather than over just the grain boundary atoms. Accordingly, he asserts that a parabolic time behaviour should prevail provided that the average grain shape does not change during growth. Grain shape modifications could be caused by the grain boundary segregations and fabrication pores.

**Pores and second-phase particles** A bubble located on a grain boundary exerts a force on the latter, either because the bubble is driven to move by an external force (e.g. the temperature gradient) or because the grain boundary has a tendency to move in response to the tension contained in its curved surface. Small bubbles in the path of a moving grain boundary are swept along with the boundary but they retard the speed of it. However, a moving grain boundary can pass right through large bubbles. One can calculate a critical bubble radius marking the border between the smaller bubbles which are collected by the moving grain boundary and the larger ones which are detached from the grain boundary [4].

In order to take into account the effect of second-phase particles, referred to as the Zener

pinning effect, one introduces a back stress and assumes that the geometry is unaffected [119]. This additional force term ($K_r^{'}$) in Eq.(2.17) leads to an equation similar to Eq. (2.19):

$$\frac{dR_{gr}}{dt} = \frac{K}{R_{gr}} - K^{'} = K\left(\frac{1}{R_{gr}} - \frac{1}{R_{max}}\right) \tag{2.20}$$

where $R_{max} = K/K^{'} = 1.12\,10^3 exp\,(-7620/T)\,\mu m$ according to Ainscough et al. [119]. Hillert [118] predicts a more gradual retardation of the growth rate of the average radius:

$$\frac{dR_{gr}}{dt} = \frac{K^{'}}{R_{gr}}\left(1 - \frac{R_{gr}}{R_{max}}\right)^2 \tag{2.21}$$

These equations indicate that grain growth may be retarded and even terminated when a maximum grain size is attained. In the empirical relation of Ainscough et al. [119], $R_{max}$ depends on the burnup and the temperature. More recently, Khoruzhii et al. [122] introduced an additional but similar retarding effect on grain growth due to the defect areas arising on the grain faces as a result of interaction with fission tracks.

### 2.9.3 Domain of application

Grain boundary sweeping occurs at temperatures at which grain growth is significant. According to Olander [115], the temperature range for equi-axed grain growth is between 1900 K and 2100 K (Above these temperatures, columnar grain growth can be observed). Consequently, this process is not operative in LWR fuel under normal operating conditions, probably because of the combination of low temperatures and the retarding effect of fission products on grain boundaries. However, the influence of retarding forces due to pores, second phase particles, and possibly the fission tracks, is still under investigation.

## 2.10 Bubble migration

### 2.10.1 Description

Before going into detail, one should distinguish between fission gas bubbles, fabrication pores and solid inclusions of fission products for their respective mobility and behaviour are quite different. The first kind of bubble results from precipitation of fission gases and is quite small (radius $\leq 1\,\mu m$) due to re-solution effects. It contains mainly xenon and some krypton at relatively high pressure. The second type of closed pore results from incomplete densification of the fuel during manufacture. These pores are usually large (radius $\geq 1\,\mu m$) and contain a low-pressure gas that is composed primarily of a cover gas (e.g. He or Ar) used during fuel-element assembly. According to Kleykamp [123], the solid inclusions of fission products are mainly composed of metallic precipitates (Mo, Tc, Ru, Rh, Pd, ...) or oxide precipitates

(Rb, Cs, Ba, Zr, Nb, Mo, Te). In the following we will use "bubble" to denote all these three types of inclusions unless specified otherwise.

The migration of fission gas bubbles and solid inclusions provides an alternative to the sequence "bubble formation / re-solution / gas atom diffusion" in order to describe fission product release from nuclear fuels [68, 123–129]. Migration of bubbles has two other important consequences, namely the columnar grain growth with the concomitant central void formation [68, 126], and the coalescence of the bubbles entailing fuel swelling [68, 127].

### 2.10.2 Properties

In the absence of a driving force (e.g. during post-irradiation annealing experiments), the molecules that determine the bubble motion move about randomly. As a result, the bubble performs a form of Brownian motion in three dimensions. When the individual molecules are moving under the influence of a potential gradient, the bubbles move in the direction of that gradient. Nichols [125, 127] has developed a general analysis of bubble mobility that can be applied to any force acting on a bubble or to any microscopic mechanism by which bubble motion occurs. Mobility ($M_b$) is defined as the velocity ($v_b$) when a unit force ($F_b$) is applied: $v_b = M_b F_b$. The mobility can be related to the bubble diffusion coefficient by the Nernst-Einstein equation. The force on the entire bubble ($F_b$) can be directly associated with a macroscopic potential gradient (e.g. stress gradient). Alternatively, this force can be expressed in terms of the forces on individual molecular species ($f$) which are actually responsible for bubble motion [68, 125]:

$$F_b = -\frac{4\pi R_{bl}^3}{3\Omega} f \tag{2.22}$$

where $R_{bl}$ is the bubble radius and $\Omega$ represents the molecular volume "deposited" on the surface for each diffusing (rate-controlling) species.

Different forces may affect the bubble motion [68, 127], such as the thermal gradient, the stress gradient, the electric potential gradient in ionic crystals, moving dislocations and shifting grain boundaries. In the absence of a detailed analysis, one can assume the very large thermal gradients to dominate [127]. (The other gradients are supposed only to alter the magnitude of the effective heat of transport). More recently, Evans et al. [73, 129–131] proposed another driving force which is even operative under thermal annealing conditions. Their approach invokes the presence of a thermal vacancy concentration gradient between a vacancy source (e.g. a grain boundary) and intragranular bubbles. A large directed diffusion component is therefore imposed on the bubble population up this gradient.

There are several rate-controlling mechanisms by which bubbles migrate in a solid. The motion of a bubble through a solid requires the transfer of atoms around the bubble, either by direct surface diffusion, either by mass transfer (via vacancies) through the volume of the

solid near the bubble or by vapour diffusion (evaporation and condensation) of the matrix material within the bubble volume. One can derive an expression for the bubble diffusivity ($D_b$), or equivalently the mobility, for each of these mechanisms [68, 127, 132]:

- surface diffusion: $D_b = \frac{3\lambda\Omega}{2\pi R_{bl}^4} D_s$
- volume diffusion: $D_b = \frac{3\Omega}{4\pi R_{bl}^3} D_v$
- vapour diffusion: $D_b = \frac{3\Omega^2 \alpha_v p_v}{4\pi kT R_{bl}^3} D_g$

where $D_{s,v,g}$ denotes the surface, volume, or gas diffusion coefficient of the rate-controlling species, $\lambda$ represents the normal spacing in the lattice between diffusing (rate-controlling) species, $p_v$ is the equilibrium vapour pressure of the rate-controlling species, and $\alpha_v$ measures the departure from equilibrium ($\alpha \leq 1$): $p_v \alpha_v \Omega = kT$. The approach presented above enables to predict the drift velocity of the bubbles as a function of several parameters (local temperature, temperature gradient, bubble radius, grain boundary energy, etc.) given a particular driving force and a migration mechanism [127]. We will limit ourselves to the case where the force exerted on the bubble is determined by the thermal gradient:

$$F_b = \frac{4\pi R_{bl}^3}{3\Omega} \frac{Q}{T} \nabla T_b \tag{2.23}$$

where $Q$ is the heat of transport for the rate-controlling mechanism and $\nabla T_b$ is the temperature gradient in the bubble.

**Temperature** The dominant mechanism for migration depends on the temperature, due to the different activation energies involved : usually $Q_{vapour} > Q_v > Q_s$. As the temperature increases, the dominant mechanism could thus shift from surface diffusion to volume diffusion to vapour transport.

**Temperature gradient** From formula (2.23) for $F_b$ above it is possible to explain why in an operating fuel element much larger pores will be restrained from moving in the regions of low $\nabla T_b$ even though the temperatures in these regions will be the highest. This is of course because the driving force is itself proportional to $\nabla T_b$. Conversely, in the colder regions where $\nabla T_b$ is higher (e.g. at fractional radii $> 0.7$ [68]) the critical sizes will be smaller but the mobility may be so low that no significant motion occurs.

**Bubble radius** The mechanism responsible for motion for any cavity is simply the one yielding the highest migration velocity. In the case of a temperature gradient, surface diffusion control leads to $V_b \propto R_{bl}^{-1}$ and volume diffusion leads to a velocity which is independent of $R_{bl}$. Vapour transport likewise yields a velocity independent of $R_{bl}$ if $D_g$ remains constant

($D_g \propto p_v^{-1}$) but when the pressure in the pore is assumed to be dictated by surface tension forces ($2\gamma/R_{bl}$), then $V_b \propto R_{bl}$. Accordingly, it is clear that surface diffusion must dominate at sufficiently small size ($R_{bl} \leq 1\,\mu m$). As $R_{bl}$ increases ($R_{bl} \geq 1\,\mu m$), either volume diffusion or vapour transport eventually becomes dominant. However, according to Olander [68] and Nichols et al. [128], the vapour transport mechanism is only likely to be significant for fabrication pores with a diameter in the order of $10\,\mu m$ but not for fission gas bubble migration.

**Impurities and defects** Several authors [127, 129, 133, 134] have explained the suppression of predicted surface diffusion controlled diffusivity by interface control for pore migration, also referred to as the bubble facetting effect for very smooth surfaces in the absence of external driving forces.
Evans [129] mentioned two other possible mechanisms for surface diffusion suppression. The first considers the inhibiting effect of gas atoms when they occupy the space needed for the surface ad-atoms to perform the jump-step. A second suppression mechanisms is attributed to the effects of impurities coating or partially coating bubble surfaces [124]. This was also argued by Manley [63], Nichols [127] and Matzke [18] who mention the association of bubbles with small precipitates (e.g. "5-metal particles") which are thought to be less mobile.

Finally, reactor fuels contain a variety of crystal defects (cf. § 2.4) which are responsible for the pinning of bubbles. The critical size at which a bubble can pull free from an obstacle occurs when the driving force due to the temperature gradient is equal to the restraining force due to the bubble-defect interaction. Olander [68] and Nichols [127] have derived an expression and estimated this radius for dislocations and grain boundaries in $UO_2$ and $UC$: a few 100 to 1000 Å for dislocations and 5000 to 10000 Å for a grain boundary.

### 2.10.3 Domain of application

According to Matzke [16], fission gas bubbles in $UO_2$ remain small ($\leq 20\,nm$) due to the effective fission induced re-solution, and they show irregular and small mobility, at least up to $T \sim 1800°C$. Furthermore, according to Olander [68], bubbles of radii less than 50 nm are pinned by dislocation lines, and other crystal defects, too small to be observed by an electron microscope, could very well immobilise bubbles in the 10 nm size range. Accordingly, for LWR fuel gas atom diffusion is still thought to dominate fission gas release [16, 135, 136].
Despite this, Evans and co-workers [129] have suggested both a new driving force for bubble migration (cf. p. 29), and that volume diffusion plays a dominant role in $UO_2$ for the intragranular bubble sizes and temperatures considered in transient annealing experiments. However, they have only performed annealing experiments where inclusions, inhibiting bubble migration, were missing [137]. Accordingly, their ideas are open to debate [136–140].

## 2.11 Bubble interconnection

### 2.11.1 Description

Fission gas bubbles appear along grain faces and grain edges after a certain burnup, depending on the temperature history [102, 109–113]. When bubbles interconnect, they form a so-called tunnel network through which the gas can be released. The bubble interconnection is a reversible process, for the tunnel network can close again under the influence of the surface tension when the outgoing flux of gas atoms outweighs their supply.

The interconnection of grain boundary bubbles has two important consequences. First of all, it determines the onset of release as the release remains small (due to athermal release) before grain boundary bubbles interconnect with open grain edge tunnels. This incubation period is reflected in the Vitanza threshold for fission gas release [141] (cf. § 3.3.1). The ensuing release corresponds to a seepage process. Secondly, when grain face bubbles interconnect and form snake-like tunnels, there will be a sudden release of the gas accumulated in these bubbles, referred to as burst release [11, 16, 68, 112, 142–148] (cf. § 3.3.3). Burst release can also be interpreted as a sudden "interconnection" or opening of grain face bubbles due to micro-cracking along grain boundaries during abrupt power variations [14, 112, 149–151]. Cracking entails the sudden opening of a fraction of the grain boundaries with the instantaneous venting of the corresponding fraction of accumulated gas atoms. Nevertheless, burst release due to micro-cracking upon sudden power changes is not part of the model presented later.

### 2.11.2 Properties

The interconnection of bubbles is very often treated in a simplified manner; either the bubbles are assumed to be closed, either they are considered to form an open tunnel network (other treatments will be summarised in the following chapter). The interconnection occurs when the grain boundary concentration of gas atoms reaches a saturation concentration ($N_{sat}$), determined by [1]

$$N_{sat} = \frac{4\rho_{bl} f(\theta)}{3kT \sin\theta^2} \phi \left( \frac{2\gamma}{\rho_{bl}} + P_h \right) \tag{2.24}$$

where (Fig. 2.4) $\rho_{bl}$ corresponds to the radius of curvature of the grain face bubbles, $2\theta = \arccos(\gamma_{gb}/2\gamma)$ is the dihedral angle between the bubble surface and the grain boundary, $\gamma$ and $\gamma_{gb}$ designate respectively the free surface energy and the grain boundary energy, $f(\theta) = 1 - 1.5\cos\theta + 0.5cos^3\theta$, $P_h$ is the hydrostatic pressure in the surrounding bulk material, and $\phi$ stands for the fraction of the grain face occupied by the bubbles at interconnection.
Eq. (2.24) is based on two assumptions. First, it is assumed that the (lenticular) bubbles are in mechanical equilibrium, i.e. the gas pressure in the bubble balances the grain boundary energy and the hydrostatic pressure. Secondly, one assumes that the gas behaves like a perfect gas.

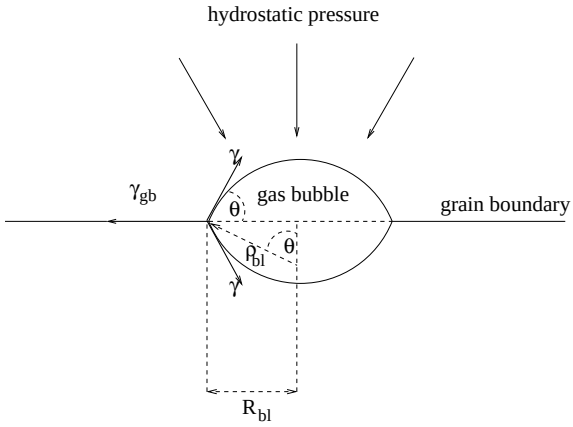


Figure 2.4: Schematic representation of a lenticular grain boundary bubble subjected to a hydrostatic pressure.

Irrespective of the validity of these assumptions, Eq.(2.24) enables us to infer the influence of the different factors on the onset of release due to bubble interconnection:

- the re-solution at the grain boundary bubbles impedes the build-up of the saturation concentration and increases the incubation time for release;
- the (compressive) hydrostatic pressure increases the amount of gas atoms necessary to obtain the saturation or opening of the tunnel network, hence it defers the onset of release;
- when the grain boundary energy increases, the storage capacity of the grain face bubbles will increase, entailing extended incubation periods;
- a temperature increase will raise the pressure of the gas in the bubbles and boost the interconnection.

### 2.11.3 Domain of application

Interconnection of gas filled bubbles takes place in general where diffusion controlled precipitation occurs at the grain boundaries, i.e when both the T and the burnup are high enough [102]. The conditions correspond roughly to the Vitanza threshold. Indeed, before grain boundary tunnels are established, only athermal release can occur through the open surface resulting from the fabrication porosity [13, 14, 152] and small grain edge tunnels [102].

The modelling of burst release due to micro-cracking along grain boundaries during abrupt power variations would require the precise knowledge of the local conditions (e.g. stress, temperature, etc.). Given the uncertainties pertaining to some of those parameters, most authors accounted for the cracking phenomenon in an empirical manner [152–155].

## 2.12 Sublimation or vaporisation

It is possible for some of the surface layers of a $UO_2$ specimen to sublime during an anneal. Fission gas atoms and small bubbles situated in the surface layers will be released when the $UO_2$ sublimes. This component of gas release must be subtracted before true values of the diffusion coefficient can be obtained. If no correction is made, one obtains a higher value of the diffusion coefficient. Furthermore, if vaporisation is dominant, the apparent activation energy for diffusion could reach a value near to the heat of sublimation [11] of $UO_2$ (= 147 kcal/mole). Lawrence [11] concluded that at temperatures greater than 1600 °C vaporisation effects become an important contributor to fission gas release rates.

The layer lost by evaporation increases linearly with time ($t$) and is exceeding the mean diffusion distance (which increases with $\sqrt{t}$) for $UO_2$ and typical durations of diffusion experiments already at relatively low temperatures (expressed as a fraction of the melting point) in contrast to the behaviour of most metals [16]. The different time dependences can a priori be used to differentiate between evaporative and diffusional release.

## 2.13 Conclusions

Considering the domain of application of the mechanisms described above, we can define those which have to be included in a model for fission gas release in LWR fuel under normal operating conditions, more precisely steady state conditions:

- single gas atom diffusion in the grains (§ 2.3);
- irradiation induced re-solution and trapping associated with intragranular bubbles (§ 2.5 and § 2.4);
- diffusion-controlled precipitation of gas atoms into intergranular bubbles (chapter 5);
- irradiation induced re-solution of the gas atoms accumulated in the grain boundaries (§ 2.5);
- interconnection of grain boundary bubbles entailing a gaseous flow through the tunnel network (§ 2.11);
- recoil and knock-out at the open surface (§ 2.1 and § 2.2).

The relationship between the different phenomena is schematically represented in Figure 2.5. Since the validity domain of the model is limited to normal steady state conditions in light water reactors, I have disregarded grain growth, micro-cracking and bubble migration. These phenomena should only be considered under transient conditions: grain growth only occurs at temperatures in excess of 1900 K; micro-cracking only takes place during abrupt power

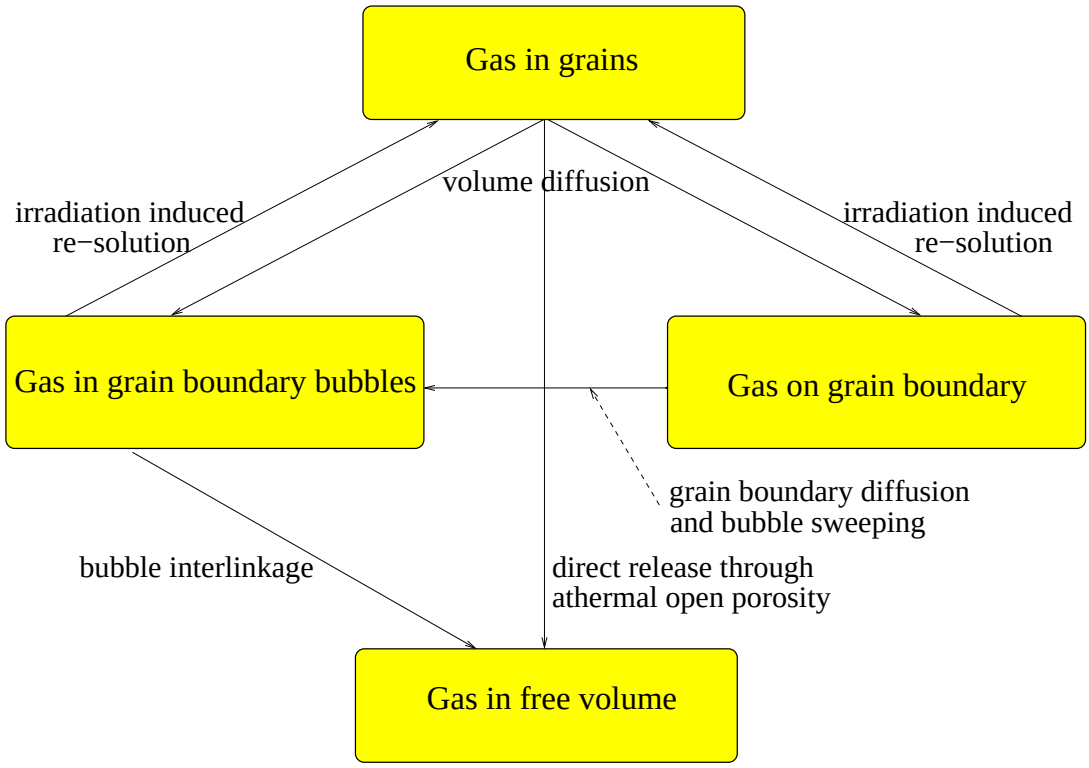


Figure 2.5: The relationship between the various processes involved in fission gas release in LWR fuel under normal steady state conditions

changes; and bubble migration is not expected to contribute significantly below 2000 K, except during annealing experiments, which is still open to debate.

The precipitation or trapping of fission products is dependent on the temperature and burnup, on the species under consideration, on stoichiometry deviations and additives, as well as on the geometrical parameters such as the number density and the size of the trapping centres. The existing models for the precipitation of volatile fission products, however, consider the traps to be perfect absorbers or black spheres. Accordingly, they do not account for the variable efficiency of the traps at trapping fission products impinging on their surface. It is thus necessary to develop a model for intergranular precipitation of fission products that accounts for the variable trap efficiency. At the same time, there is a need to analyse the effect of the various parameters on the precipitation rate in grain boundaries.

In addition to the mechanisms listed above, one should also account for grain boundary bubble sweeping. By similarity with the sweeping effect of growing grains on fission products dissolved in the bulk of the grains, grain boundary bubble sweeping will enhance their expansion by capturing gas atoms dissolved in the grain boundary. Bubble sweeping thus constitutes a necessary correction factor to the diffusion controlled precipitation process, since the model for the latter assumes a fixed bubble radius during each time step (cf. Chapter 5).

The properties and/or domain of application of several other mechanisms are not well characterised at present and require further research. Such is the case of grain boundary diffusion. There is a general consensus to disregard grain boundary diffusion in fission gas release models for medium and high burnup values. However, some observations in trace-irradiated fuels indicate a contribution from grain boundary diffusion to the release and require further clarification.

# Chapter 3

# Fission gas release models

## Contents

Having analysed the underlying mechanisms of fission gas release, I will briefly review how they are accounted for in the corresponding models from the open literature. Subsequently, I will establish interrelationships among the different concepts and discuss their main advantages and drawbacks in order to highlight the need for further improvements.

There are various approaches in fission gas release modelling. They can be classified in two categories. On one hand there are purely empirical models [152, 156], including those based on soft computing techniques such as neural networks [157]. These models are inexpensive in use and provide an efficient tool for the design of fuel rods within a limited range of application. However, they are not suitable for gaining knowledge about the underlying mechanisms, nor do they enable us to extend their range of application to higher discharge burnup values as required by the industry.
On the other hand, there are mechanistic models which aim at the physical description of the underlying phenomena. Despite their great data needs, such models provide an excellent basis, both for the analysis of the mechanisms as well as for the extension of the models beyond their range of calibration. Accordingly, only the latest category of models will be considered in the framework of the present thesis.

## 3.1 The Booth model

Most of the mechanistic fission gas release models for LWR fuel rely on the pioneering work of Booth [158, 159] who proposed the equivalent sphere model. This theory considers a polycrystalline sinter as a collection of uniform spheres with an equivalent radius in order to simplify the mathematical problem. The hypothetical sphere radius ($R_B$) is defined so that the effective surface-to-volume ratio of the fuel, $(S/V)_t$, is preserved:

$$R_B = 3 \left( \frac{V}{S} \right)_t , \tag{3.1}$$

where $(S/V)_t$ accounts for the sum of the geometric surface of the pellets as well as the surface due to open porosity. The two limiting values of the Booth radius are therefore associated with 0 % and 100 % open porosity, respectively:

$$3 \left( \frac{V}{S} \right)_g \geq R_B \geq R_{gr} , \tag{3.2}$$

where $(S/V)_g$ only contains the geometric pellet surface, i.e. corresponds to 0 % open porosity.

As irradiation proceeds, fission gases are generated within the Booth sphere and migrate to the surface, where the concentration is taken to be zero. Consequently, single gas atom diffusion is postulated to be the rate controlling step for the release of the fission products as they are supposed to be vented once they have reached the sphere boundary.

## 3.2 Extensions of the Booth concept

The original Booth approach has been improved by several workers ever since in order to account for some effects neglected in the former model. In the present survey, I will focus on the evolution of the physical concepts involved in the models, rather than distinguishing the numerical methods applied to solve the diffusion problem, such as the finite element method [160, 161], the finite volume method [59], the finite difference technique [58] or other approximations [162–166].

### 3.2.1 Applying an effective volume diffusion coefficient

A fine intragranular dispersion of small bubbles (a few nanometer in size) appears after a short irradiation period and stabilizes rapidly, both in size and in number density. The bubbles hamper the diffusion of gas atoms towards the grain faces. Speight [57] provided an analytical solution for the migration problem in the Booth sphere incorporating the effects of both trapping and irradiation induced re-solution at a fixed number of intragranular traps. From these expressions he inferred an approximation in the case of saturated traps that enables one to use the Booth-formulas with an effective diffusion coefficient (cf. Eq.(2.11)).

The influence of precursors on the release rate of radioactive gases can be treated analytically [167–170], but it is usually incorporated in the simplified expression for the release to birth rate ratio $(R/B)$ of radioactive species [8, 9, 159]. If the predominant mode of release is via a diffusion mechanism, this ratio is expressed by:

$$\frac{R}{B} = \frac{S}{V}\sqrt{\frac{\alpha D}{\lambda}}, \tag{3.3}$$

where $D$ is the single gas atom diffusion coefficient, $\lambda$ represents the decay constant, $S/V$ is the surface to volume ratio of the specimen, and $\alpha$ denotes the diffusion enhancement term [8]. The influence of precursors can therefore be incorporated in the effective volume diffusion coefficient for each decay chain of interest [169].

The original Booth approach disregards the athermal release due to recoil and knock-out at open surfaces. Some codes have circumvented this restriction by introducing an empirical release term as a function of burnup [12, 171] and, in some cases, of the initial open porosity fraction [172]. Other codes introduced an effective diffusion coefficient depending on the burnup and the local fission rate, and/or an equivalent sphere radius which is a function of the open porosity fraction resulting from the fabrication process [173].

### 3.2.2 Coupling with the intergranular behaviour of gas atoms

Fission gas release starts at the beginning of irradiation according to the Booth theory. However, in general the onset of fission gas release has been observed to be delayed [141]. This

incubation period has been ascribed to the saturation process of the intergranular bubbles, which is affected by irradiation induced re-solution. As a result, it was necessary (a) to model the intergranular behaviour of the fission gas atoms and (b) to couple this with the Booth model.

#### 3.2.2.1 Modelling the intergranular behaviour of fission gas

There are different approaches to describe the behaviour of the gas atoms along the grain boundaries. Most models do not describe the kinetics, they merely serve to determine the conditions for the saturation of the intergranular bubble population. As soon as this saturation criterion is fulfilled, the excess gas atoms arriving at the grain boundaries are deemed free.
In order to assess the saturation concentration of gas atoms at the grain boundaries, it is assumed that all the gas atoms are accumulated in spherical bubbles with a fixed radius of curvature ($\rho_{bl}$). The bubbles can vent their content when their number density is such that they cover a certain areal fraction of the grain faces ($\phi$). The corresponding concentration of gas atoms ($N_{sat}$) is inferred from the equation of state, generally the ideal gas law, and the bubble pressure. The latter is supposed to balance the capillary forces restraining the bubble in addition to any external hydrostatic pressure ($P_h$).
Several models improved this description by accounting for the non-spherical character of the bubbles due to the difference between the grain boundary energy and the free surface energy ($\gamma$). This results in equation (2.24) [174]:

$$N_{sat} = \frac{4\rho_{bl} f(\theta)}{3kT \sin\theta^2} \phi \left( \frac{2\gamma}{\rho_{bl}} + P_h \right)$$

More recently, White [71] neglected the influence of the hydrostatic pressure and proposed the concept of "quasi-crystalline" lenticular cavities as an alternative for the equation of state. He suggested that the number of gas atoms per unit area ($N_{gb}$) is proportional with the ratio of the bubble radius and the van der Waal's volume for a fission gas atom ($b_v$)

$$N_f = \epsilon' \frac{\rho_{bl}}{b_v} \tag{3.4}$$

where $\epsilon'$ is the so-called cavity packing fraction, a tunable parameter. His idea is motivated by experimental evidence, indicating that the fission gas inventory of the bubbles is well above the theoretical value inferred from the equilibrium condition for a perfect gas [109, 110, 113] (cf. § 3.3.3). The subsequent underestimation of the grain boundary storage capacity for fission gas entails a depreciated incubation period, unless a significant compressive stress is applied to the bubbles [59].

Only a few models describe the kinetics of the intergranular behaviour of fission gas atoms. Turnbull et al. [93] developed a model for the interpretation of their in-pile experiments with

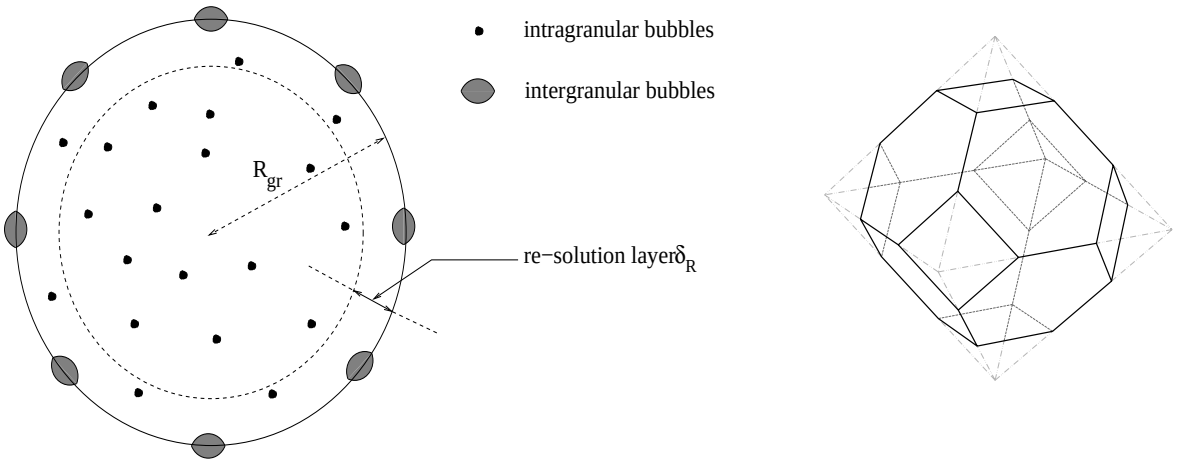


(a) Spherical (b) Tetrakaidecahedral

Figure 3.1: Simplified representations of a grain

very low burnup fuel. They identified the equivalent sphere with the average grain ($R_B = R_{gr}$: Figure 3.1) rather than with the quantity defined in Eq. (3.1).

Furthermore, they considered two diffusion processes to operate in series, that is, the fission products formed uniformly within the grains diffuse to the grain boundaries, then along the grain boundaries to the free surface by grain boundary diffusion. The model has been extended by Speight and Turnbull [92] in order to account for the decrease of the bulk concentrations at higher release rates, along with the contribution of direct release by lattice diffusion to the free surface from those grains forming the outermost layer of the sample. Olander [95] followed the same idea in his analysis of post-irradiation annealing experiments with trace-irradiated $UO_2$ samples.

In high burnup fuel, fission gas bubbles appear along grain boundaries after a certain burnup, depending on the temperature history [102, 109–113]. The interconnection of these bubbles is a reversible process, as the tunnel network can close again under the influence of the surface tension when the outgoing flux of gas atoms outweighs their supply. White and Tucker [1] represented the gaseous flow along this intermittently open intergranular porosity by a diffusion process in the equivalent Booth sphere. As a result, they presumed release to occur from the outer surface of this sphere by two parallel processes: the standard intragranular diffusion process, in addition to the gaseous diffusion process through the tunnel network. Their approach enabled them to obtain analytical approximations in which each term is identical in form to the original Booth calculation, though with "effective" values for both diffusion coefficients as well as for the source term in the tunnel network. The effective grain boundary diffusion coefficient is defined on random walk grounds in terms of the frequency of opening

(and closing) of the tunnel network, and the mean square flight distance travelled by any individual gas atom during the period in which the tunnel is open. The effective source term in the tunnels arises directly from the intragranular diffusion process, and from the seepage mechanism between the grain faces and edges.

Koo et al. [107] followed the ideas of White and Tucker in that they described the grains of the polygranular aggregate as tetrakaidecahedra (Figure 3.1), and they assumed that bubble interlinkage at grain corners was the rate-controlling step in the release process. However, rather than considering two different processes in the equivalent sphere, they considered two contributions to the effective open surface to volume ratio ($S/V$), which is required to compute the equivalent sphere radius according to Eq. (3.1). The released fraction of fission products is calculated by means of the Booth equation for bulk diffusion in the equivalent sphere.
The primary contribution to the effective $S/V$ stems from macroscopic crack surfaces and is based on two assumptions. First, they assume that only grains in direct contact with cracks can liberate unstable fission products by bulk diffusion. Furthermore, Koo and co-workers take on a particular geometry of the cracked pellet in order to compute the corresponding $S/V$ value. More precisely, they consider an inner plastic cylinder in the pellet whose temperature is greater than 1000 $^{\circ}C$, and an outer region containing a number of radial cracks proportional to the fuel rod power [175].
The second contribution to the open surface fraction is determined by the tunnel network along grain boundaries. Koo et al. assess the fraction of interconnected grain corner bubbles with the use of a site percolation simulation, i.e. a Monte Carlo technique, in two dimensions. They multiply this fraction by the surface to volume ratio of the grain corner bubbles in order to compute the second contribution to the total $S/V$ value.

Hoffman and Meek [176] described the gas transport through the interconnected porosity in fast breeder fuel pellets by means of Darcy's law [177, 178]. The migration of fission gas in the grains appeared as a source term in this equation. In order to reduce the dimensions of the equation in the cylindrical pellet, they assumed circumferential symmetry and neglected axial pressure gradients in the porosity. In addition, they disregarded body forces ($P_h$), applied the perfect gas law and assumed that gas and fuel are in thermal equilibrium. The resulting non-linear partial differential equation in cylindrical geometry was solved by means of finite differences. O'Caroll et al. [179] assessed several numerical solution schemes for the same problem, whereas Ivanov [180] proposed an analytical solution in Cartesian geometry.

The model of Kogai [181] for the intergranular kinetics combines features of the previous concepts in LWR fuel. In line with the proposals of Matthews et al. [182], Une et al. [112], Dehaudt et al. [102], and Charles et al. [183], Kogai considers gas on the grain boundary in atomic form which is available to nucleate boundary bubbles immediately on heating. The separate treatment of single gas atoms and bubbles at the grain boundaries is consistent with the approach generally adopted within the grains following the idea of Speight [57].

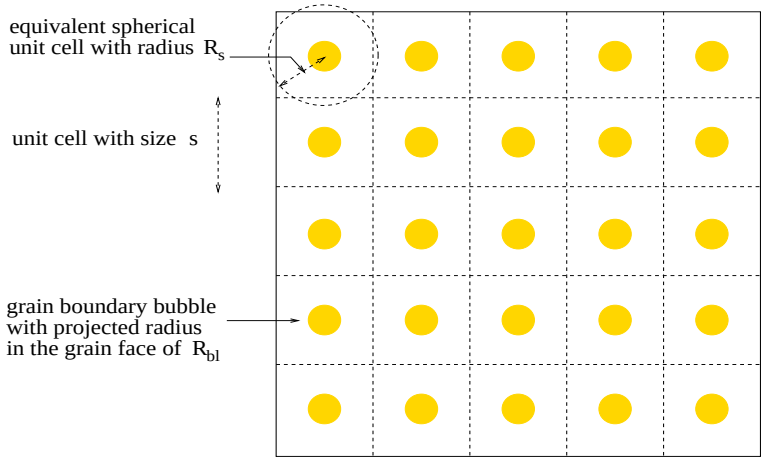


Figure 3.2: Schematic representation of a grain boundary covered by a regular distribution of bubbles according to Kogai [181]

Kogai invoked a combination of bulk diffusion in spherical grains and grain boundary diffusion, though only on a local scale since the gas atoms migrate towards neighbouring bubbles on the grain boundary (Figure 3.2). In accordance with White, Kogai predicts the onset of release when these bubbles interconnect. However, in contrast with the theory of White and in line with experimental observations [184], the bubble number density remains constant before the onset of interlinkage while they grow by means of a flux of vacancies along the grain boundary. The balance between the bubble internal pressure, the hydrostatic pressure and the surface tension constitutes the driving force for the growth (or shrinkage) of the bubbles, which is in contrast with the thermal equilibrium assumption of Hoffmann et al. [176].
When the interconnection starts, the release from the porous medium is represented by a flow through a fine tube, connecting the average bubble with the free volume (Figure 3.3), according to the equation of Poiseuille [177, 185], or equivalently, Darcy's law under stationary conditions. Both the extent of bubble interconnection as well as the stress distribution determine the tube conductivity (cf. § 3.3.3 and § 3.3.4).

#### 3.2.2.2 Coupling of the intergranular with the intragranular model

The coupling between the intra- and intergranular modules is two-directional. On one hand, the flux of gas atoms leaving the grains forms the source term for the intergranular module. This aspect is accounted for by all the models that incorporate the intergranular behaviour of fission products (cf. previous section). On the other hand, the grain boundary concentration affects the intragranular module in two ways. First of all, the concentration of gas atoms dissolved in the grain face determines the boundary condition for the diffusion equation in the

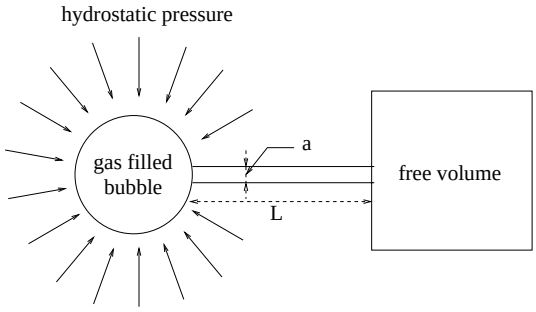


Figure 3.3: Schematic representation of the gaseous flow through the interconnected tunnel network along the grain boundaries by a tube connecting the average grain boundary bubble with the free volume in the fuel rod [186]

grains. Secondly, the irradiation induced re-solution induces a flux of gas atoms back into the adjacent grains, which constitutes a supplementary source term near the grain face.

Turnbull and co-workers [92, 93] as well as Olander [95] applied a non-zero boundary condition at the surface of the grains in order to account for the boundary concentration in the intragranular module. More precisely, they introduced a segregation factor, defined as the ratio of the solute concentration in the grain boundary to that in the bulk near the boundary [83], which reflects the interaction energy between the solute atoms and the grain boundary. All the other models regarded the Booth sphere boundary as a thermodynamic perfect sink, corresponding to the limiting case of an infinite segregation coefficient, and applied a zero boundary concentration.

With respect to the influence of the irradiation induced re-solution at the grain boundary, White et al. [1] as well as Hargreaves et al. [114] applied a correction factor to the Booth flux in accordance with Speight [57]. Although the grain boundary concentration was still taken to be zero in the Booth flux calculation, their basic idea was to introduce a diffusion barrier at a distance $\delta_R$ away from the grain face (cf. Fig. 3.1a). This barrier is generated by the re-solution process and attenuates the net flux to the grain face. The correction factor was obtained by means of a linear interpolation of the flux between two limiting cases. The first case corresponds to the Booth flux, i.e. the maximum flux when the grain face concentration is zero ($N_{gb} = 0$). The other limiting case corresponds to an equilibrium between the re-solution flux and the diffusion flux when the grain boundary concentration is saturated ($N_{gb} = N_{sat}$), hence the net flux towards the grain face is annihilated.
Rather than reducing the Booth flux with a correction term, Forsberg and Massih [187] generalised the idea of Speight to a time varying boundary condition. They provided analytical approximations of the resulting integro-differential equation for short and long times.

Olander [4], and later also Dowling et al. [188] embodied the re-solution effect in the intragranular module by means of a supplementary source term adjacent to the grain face.

Olander considered all the re-dissolved fission products to reappear at a fixed distance ($\delta_R$) from the grain boundary, whereas Dowling et al. smeared out the amount of re-dissolved fission products between $R_{gr}$ and $R_{gr} - 2\delta_R$, referred to as the re-solution layer. Yet, both models still considered a zero boundary concentration. Despite this limitation, the smeared model has been applied by Ito et al. [161], Nakajima et al. [189] and Denis et al. [58]. However, except for Denis et al., they have smeared out the re-dissolved gas atoms in one single layer near the grain face. The thickness of this layer ($2\delta_R$) is too large from the numerical point of view; the large concentration gradients in this area require a much more refined mesh (cf. § 8.4.2.2 p. 159). Accordingly, in the present model the re-dissolved gas atoms have been smeared out in several layers adjacent to the grain face (cf. § 7.1.4).

### 3.2.3 Accounting for grain growth

As mentioned in section 2.9, the influence of grain growth on the gas release process is twofold. Grain boundary sweeping provides a mechanism for the collection of fission gas at these internal surfaces from which release can occur. Conversely, the diffusion distance for the fission products created in the grain increases. Accounting for both phenomena simultaneously requires the solution of a diffusion equation in a sphere with a moving boundary. In addition, the restructuring affects the intergranular module itself, since an increase of the average grain size reduces the specific surface of the fuel.

Some models only took into consideration the sweeping effect. Such is the case of Hargreaves and Collins [114] who brought up the role of grain growth in gas release. According to them, the amount of fission products accumulated by the moving boundary was proportional with its velocity. Kogai [181] followed the same idea. On the other hand, Malen [190] has taken the idea one step further and proposed that all solute within the volume fraction swept by the mean-size grain during its growth is released to the free volume. Notley et al. [191] extended the idea of Malen to columnar grain growth. However, except for the model of Hargreaves et al., they all disregarded the re-solution effect. In addition, they all fail to properly incorporate boundary motion into the intragranular diffusion equation and artificially separate the two aspects of grain growth on fission gas release.

In an attempt to include grain boundary sweeping in the intragranular diffusion equation, Ito et al. [161], Nakajima et al. [189] and Denis et al. [58] have artificially separated the two processes. Forsberg et al. [12] on the other hand solved the moving-boundary diffusion equation with a source term to model in-pile release. They accounted for the re-solution effect by applying a time varying boundary condition. They did not consider, however, the details of the grain boundary behaviour of the gas atoms.

None of the models treated solute transport processes in a grain-size distribution. This is an important fabrication parameter that affects release after establishment of the tunnel network at the grain boundaries. Furthermore, Olander and co-workers [30, 96] have shown that

neglecting the grain size-distribution may lead to overpredicted release fractions. Therefore, they considered a combination of bulk diffusion in a distribution of growing or shrinking grains and grain boundary diffusion on the macroscopic scale. However, Olander et al. have omitted the source term in their post-irradiation analysis of trace-irradiated fuel. Furthermore, unlike Paraschiv et al. [169], the re-solution effect at the grain boundaries has not been included, and a zero boundary concentration has been applied. In line with Forsberg et al., Paraschiv and co-workers introduced a time-varying boundary condition containing a correction factor and derived analytical solutions. Moreover, they included the precursor effect explicitly in the set of equations. Yet, the kinetics of gas diffusion depended strongly on the correction factor at the grain boundaries which could vary by three orders of magnitude. In addition, they did not model the intergranular kinetics of the release process.

## 3.3 Main challenges for the models

Following the survey of the concepts employed in fission gas release models from the open literature, I will now discuss their capabilities to account for several important experimental observations.

### 3.3.1 The incubation behaviour

As pointed out previously (cf. § 2.11), one generally observes a period of time at the beginning of irradiation during which the release is negligible, typically below 1 %. Vitanza and co-workers [141] have determined an empirical relationship between the burnup ($bu$ in MWd/kg$UO_2$) and the peak central temperature ($T_c$ in °C) which divides the high ($\geq$1%) and low gas release rods[a]:

$$T_c = \frac{9800}{ln\left(\frac{bu}{0.005}\right)} \tag{3.5}$$

The data points from which this criterion has been inferred, along with more recent experimental points at higher burnup values [192] are depicted in Figure 3.4.

At present there are still difficulties to properly simulate (not only) the onset of the fission gas release process in LWR fuel rods. This has been underlined in one of the conclusions drawn from the recent round-robin exercise organised by the IAEA [13]. With regard to fission gas release it was concluded that "being a highly non-linear process, strongly influenced by temperature and feedback effects, accurate modelling is difficult over the whole range of release values from 0 to 100 %. In particular, the region around 1 % is extremely difficult to predict accurately and this happens to be *the* most important region above which gas release and rod internal pressure can run away." These difficulties are reflected in Fig. 3.5, where the cumulative released fractions predicted by the 19 codes (cf. Appendix A) are shown versus

[a] This correlation is also referred to as the empirical Halden threshold.

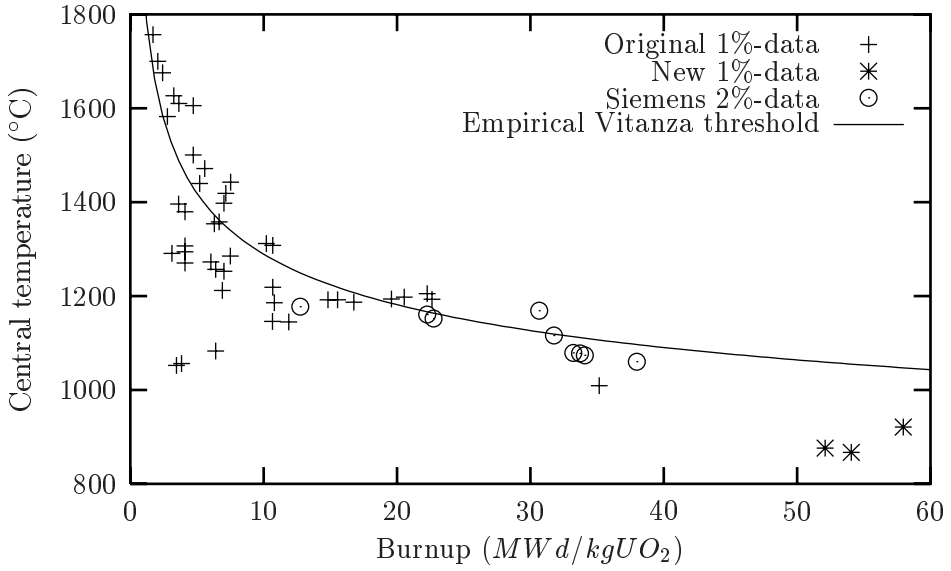


Figure 3.4: Original Vitanza criterion for the onset of fission gas release and supporting data [192].

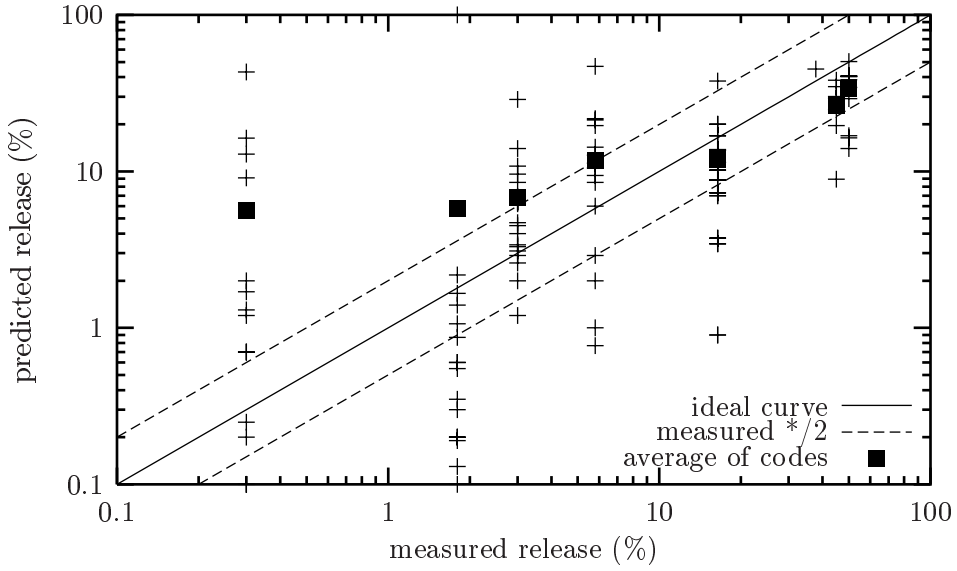


Figure 3.5: Measured versus predicted release fractions in the FUMEX exercice [13].

the experimental results[b]. Despite the overall discrepancies, however, it should be emphasised that some of the codes involved in the exercise have proven more reliable in comparison with the "average" code. For instance, some versions of the ENIGMA code or the TRANSURANUS code provided better predictions of the released fractions under certain circumstances. The diversity of the predictive capabilities among the codes has been attributed in part to the varying complexity of the models, and partly to the divergence of both the quality as well as the extensiveness of the data base used for the development and the validation of the models.

The onset of release has generally been ascribed to the saturation process of the grain boundaries. More specifically, it is interpreted as the time necessary to achieve interconnection of the intergranular bubbles. I have already underlined the reversible character of this tunnel formation (cf. p. 32). Accordingly, I will only talk about models considering the kinetics of the intergranular processes in the following discussion.

The models of Turnbull et al. [92–94] and Olander et al. [95, 96] were only applied to very low burnup fuel because they were based on rapid grain boundary diffusion, hence they are incompatible with the appearance of grain boundary bubbles and the associated incubation period.

Several theories for fission gas release [58, 107] are derived from the model of White and Tucker [1]. They consider a particular sequence of bubble formation and interconnection based on the qualitative description of Tucker [111]. According to this theory, bubbles along the grain edges can only form after grain face bubbles developed and grow into contact with as yet unoccupied grain edges, and in turn, bubbles at grain corners can only develop after successive interlinkage and pinch-off of the grain edge tunnels. As a result, they consider the interconnection of grain corner bubbles as the rate-controlling step for the onset of fission gas release. However, this sequence of events is not always valid. It is in contradiction, both with some experimental data [102] and with theoretical considerations, according to which grain edge tunnels can form before grain face bubbles are established under certain circumstances. This is because four-grain junctions are the most favored nucleation sites, three-grain junctions next most favored followed by two-grain junctions [193, 194].
Furthermore, in a more recent model, White [71, 116, 195] considers non-equilibrium bubbles or "quasi-crystallites" nucleating with a fixed radius of 0.5 $\mu m$ and an increasing number density. However, this is not in line with experimental observations.

Hoffman et al. [176], O'Caroll et al. [179] and Ivanov [180] consider the non-stationary gas transport through the porous pellet only in the radial direction. Furthermore, while the gas transport equation embodies the source term associated with the flux of atoms leaving the grains, their model disregards entirely the coupling with the intragranular module in the other direction. Finally, they do not touch on the bubble growth or shrinkage. Consequently, their concepts are inadequate to describe the onset of release.

[b] When you encounter difficulties in predicting a result accurately, try plotting the predictions versus experimental results in a logarithmic plot, or look at the results of others and you will feel much more comfortable...

In view of the preceding, it seems that the concept proposed by Kogai [181] is the most appropriate. It enables us to predict the reversible kinetics of the bubble evolution in a physical way, rather than introducing an effective grain boundary diffusion coefficient [1], or an effective surface to volume ratio [107]. The separate treatment of single gas atoms and bubbles at the grain boundaries, and the inclusion of the hydrostatic pressure in the equation for the bubble evolution also provides an alternative explanation for the "quasi-crystallites" invoked by White [71]. The constant number density of grain boundary bubbles before the onset of interlinkage is in accordance with experimental observations [109, 147, 184], while the constant surface fraction of bubbles after the onset of interlinkage reflects the further growth of bubbles by coalescence [109, 147]. The stochastic nature of the interlinkage process is accounted for by means of a sigmoidal curve for the permeability of the porous medium as a function of the surface covered by bubbles. Finally, the approach of Kogai implicitly assumes that the interconnection of bubbles on the grain faces is the rate-controlling step, implying that grain edge tunnels are already established when the grain face bubbles start to interconnect. This is in line with the concepts of Hering [152] and Tayal et al. [155] and is understandable, both in view of the fact that grain edges are part of a grain face, and because of the different energy required to form the various types of bubbles as indicated above.

Nevertheless, Kogai's approach contains restrictions affecting the incubation behaviour. For instance, the sweeping effect of growing bubbles at the grain boundaries is disregarded. More importantly, the coupling between the intra- and intergranular kinetics is a one-way approach, that is, Kogai only accounts for the flux of gas atoms leaving the grains as the source term for the intergranular module. He disregards the dual impact of the grain boundary concentration on the intragranular module (cf. § 3.2.2.2).

### 3.3.2 The release at high burnup

Economics and prudent utilisation of natural resources have provided strong incentives for extending the average discharge burnup levels of LWR fuel in commercial power plants. Figure 3.4 reveals that there is a possible stronger decrease of the release threshold than predicted by means of Eq.(3.5) at burnup values between 50 and 60 MWd/kg$UO_2$, which is way in excess of the burnup range on which the expression was originally based. Similar indications were reported by Forat et al. [196] and Bagger et al. [197], in contrast with previous experimental findings in Halden [198].

Several explanations have been put forward for the increased release in high burnup fuel [14, 196, 199, 200]. At first it has been realised that the thermal conductivity degradation of the fuel, due to an increasing number of defects and impurities, contributed to an enhancement of the release.

Several people have advocated the direct and indirect contribution of the so-called "rim structure". This structure arises at the outer part of the pellets when the local burnup values

exceed $\sim 65$ MWd/kg$UO_2$, as a result of the resonance capture of epithermal neutrons by $U^{238}$, leading to a build-up of $Pu^{239}$. Although the structure is relatively well characterised, there are still research programs ongoing, aiming at a better understanding of both the development as well as the consequences of this structure on the fuel behaviour [201–204]. The investigations revealed a large porosity fraction (up to 15 - 20 %) accompanied by a depletion of Xe in the $UO_2$ matrix. In view of this, two possible consequences on the release were suggested. First, the rim was assumed to contribute directly to the athermal release [12]. Nevertheless, it appears to be limited [205], only takes place beyond a local burnup $\sim 75$ MWd/kg$UO_2$ [206–208], and depends on the hydrostatic pressure [209]. Second, there is an indirect bearing on the thermal release, since the porous structure constitutes a thermal barrier at the pellet periphery [154].

Finally, some individuals claimed that the initial open porosity [14], and/or fine grain edge tunnels appearing above $\sim 600$ °C and burnup levels above 10 MWd/kg$UO_2$ [102], may promote athermal release.

Ideally, one would need a mechanistic model encompassing the various phenomena enumerated above, in order to assess each contribution properly. However, in view of the complexity as well as the uncertainties pertaining to some of the phenomena at high burnup, several codes have introduced a burnup dependent diffusion coefficient [171,173], and/or they considered an empirical dependence of the athermal released fraction on the burnup [12,108,171,210]. Turnbull [192] also proposed the reduction of the re-solution probability at the grain boundaries as a mechanism to lower the release threshold at high burnup. Yet, there are models that do not predict release at temperatures below $\sim 1200^\circ$ C, for instance the concepts of Koo et al. [107] and Kogai [181], hence they can not account for the observed low temperature release at high burnup.

### 3.3.3 Burst release

The most prominent feature of the release curves in post-irradiation annealing experiments is the rapid initial rate followed by a nearly linear (with $\sqrt{t}$) slower rise due to classical diffusion processes [112,142,143,147,148]. Cooling as well as heating bursts have also been reported in some in-pile experiments [11,142,145,148,183,211].

Various explanations on the mechanisms of this burst release have been proposed. Earlier experiments conducted by Stevens et al. [142] showed that burst release during annealing experiments was due to oxygen enriched surface layers in which the mobility of the fission gases was much higher. Barnes et al. [143] extended this concept. They argued that during irradiation and heating an oxygen enriched surface layer, if it is heavy enough, separated from the sample. During an anneal an initial "burst" occurs from this surface layer. Gas is then released at the normal rate from exposed surfaces of the un-oxidised $UO_2$. However, it has been found that chemical attack of the surface is not responsible for the burst in $UO_2$ post irradiation anneals and that it is unnecessary to attribute special properties to the surface

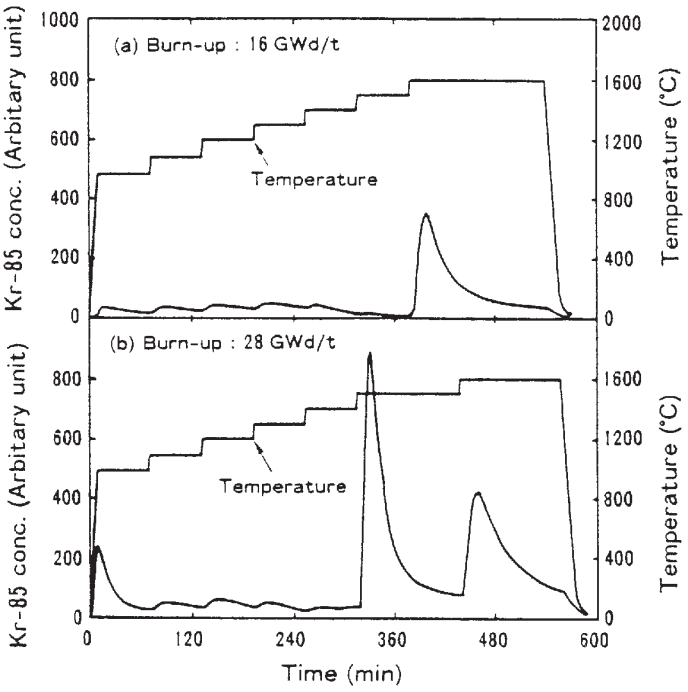


Figure 3.6: Burst release of $^{85}$Kr during a stepwise temperature ramp [112]

layer as a result of preferential radiation damage [4].

In-pile experiments by Caroll et al. [144] enabled the isotopic composition of the burst to be investigated. They observed changes in the isotopic composition which could not be explained by classical diffusion since a cooling "dip" would be expected. Instead they proposed a defect-trap model for a heating burst. According to this model, the "burst" can be interpreted as an increase in the probability of escape of the fission gas atoms from the traps due to an increase in the temperature. For the cooling burst they have put forward microcracking due to bubble overpressure.

According to Olander [4], the diffusion-trapping model shows that the initial slope of the release fraction versus $\sqrt{t}$ plot is identical to that for simple diffusion in the absence of trapping. Early release was believed to be due to gas so near to the surface that the probability of encountering a trap before reaching the surface of the specimen and escaping is very small, i.e. unperturbed diffusion. Trapping should be evident in the release kinetics only later when the surface flux arises from gas drawn from deep within the particle. Matzke has put forward a similar explanation. He presented a system of stages in gas release [16] and ascribed the fast initial burst to release from gas fortuitously located in some unspecified fast mobility sites (e.g. in an interstitial position, surface layers, grain boundaries, etc.). The subsequent slow release was supposed to be affected by trapping as well.

More recent destructive examinations of Walker et al. [109] unveiled important additional

information regarding fission gas release, in particular for burst release. By comparing the signals of two different techniques, namely X-ray fluorescence and electron microprobe analysis, they concluded that a large amount of gas was stored on the grain boundaries. Other crucial information was obtained from the annealing tests of Une et al. [112]. They analysed the influence of the temperature and the burnup on the burst release. The critical temperature for the onset of burst release decreased while the fractional release was enhanced with increasing burnup. In line with the conclusions drawn by Walker et al., they attributed these observations in annealing experiments to an increase of the grain boundary inventory. The assessment of the large fraction of gas released during the initial burst by Une et al., along with the results of Walker et al. has often been taken as evidence for the overpressurisation of the grain boundary bubbles.

Rather than considering that burst release was due to the venting of gas accumulated at the grain boundaries, Cayet [145] explained the increase of the internal gas pressure during a power drop by the opening of the gap and the cracks where gas, previously released during the high power operation, was held up and could not be detected. This explanation, however, does not hold under post-irradiation annealing conditions where pellet-cladding mechanical interaction is missing. Moreover, Nakamura et al. [211] interpreted burst release during a power drop as the venting of gas accumulated at the grain boundaries, which is in line with the observations of Walker et al. and Une et al. . The sudden release was attributed to the reduction of the thermal stress in the pellet. Pellet-clad mechanical interaction was absent in view of the large initial fuel-cladding gap (310 $\mu m$) and the medium burnup (22 MWd/kgU).

Having located the gas inventory, two main questions remain unanswered. The first question relates to the state of the fission gas inventory and has already been touched on in section 3.2.2. Walker and co-workers [109, 110, 113] advocated the formation of overpressurised bubbles due to a large hydrostatic pressure (cf. section 3.3.4). White neglected the hydrostatic stress but introduced artificial "quasi-crystallites" [116]. Une et al. on the other hand followed the idea of Matthews et al. [182] and Charles et al. [183], suggesting that the fission gases in the grain boundaries not only precipitate in the bubbles, but also dissolve in the grain boundaries having many defects.

The second question concerns the mechanisms of burst release from the grain boundaries. The promptness can not be explained by bulk diffusion. Instead bubble interlinkage and micro-cracking along grain boundaries [14, 147, 183, 195, 211, 212] have been put forward as the most plausible mechanisms, although both are characterised by a different time constant.
Micro-cracking due to thermal shocks entails the sudden opening of a fraction of the grain boundaries and the instantaneous venting of the corresponding fraction of accumulated gas atoms [151, 183]. Ideally, modelling this brittle process would require the knowledge of the local conditions such as the stress, the temperature, the strain rate, etc. However, most authors accounted for the cracking phenomenon in an empirical manner, given the uncertainties

pertaining to some of those parameters [152–155].

White [195] modelled burst release by means of bubble interconnection, which corresponds to a more ductile behaviour. He distinguished grain face from grain edge bubble interlinkage. The latter causes a partial venting of gas following initial saturation according to an orderly growth and spillage process of grain face bubbles to grain edges as described above. The grain face interconnection is assumed to cause the rapid venting at high ramp rates. It is supposed to occur when the arrival rate of gas at the grain faces causes a rapid bubble growth rate, such as to prevent the orderly spillage process to grain edges. More precisely, White introduced an empirical criterion, that is a limit for the growth rate of the grain face bubbles above which they are supposed to interlink and vent their entire inventory instantaneously. However, it should be underlined that the bubble growth rate is entirely determined by the arrival rate of gas atoms at the grain faces according to White. Consequently, the onset of burst release is implicitly assumed to be controlled by bulk diffusion (and/or grain growth). Obviously, this does not apply to cooling bursts.

MacDonald et al. [213] adopted a combined approach. They supposed that if the grain face bubbles grew large enough to touch, they would interlink and vent their content to the free voidage through the tunnel network when the applied stress is compressive (negative). Conversely, in the event of a tensile (positive) stress, they supposed grain face separation caused a burst release of fission products. They did not, however, describe the crucial stress calculation (cf. § 3.3.4).

Originally, Kogai [212] proposed a similar approach as MacDonald et al. To this end, he modelled gas release from the grain boundary to the free voidage to take place through a thin tube connecting both regions. This concept relies on experimental observations indicating release kinetics proportional with the square of the bubble pressure [186]. Ivanov [180] corroborated the approach more recently, showing that the time constant of gas leakage through a porous medium matches the experimental time constant.
In the initial model of Kogai, the tube conductivity was determined by the maximum of a "bubble interlinkage" factor and a "pellet cracking" factor. The first factor was determined by the areal fraction of the grain boundary covered by the bubbles, while the latter was proportional with the effective tensile stress. More recently, Kogai [181] accounted for both phenomena simultaneously since the tube conductivity is governed by the product of two sigmoidal functions. The first was similar with the former "bubble interlinkage" factor, while the second function depends on the effective tensile stress exerted on the grain boundary. His model is thus able to account for both heating and cooling bursts. Unlike the model of White, the onset of a heating burst will be controlled by rapid grain boundary diffusion, i.e. by the precipitation of gas atoms dissolved in the grain boundary. Finally, the combination of interlinkage and cracking seems to be in accordance with the experimental spread of the burst duration (from one minute to an hour [148]).

### 3.3.4 The effect of the hydrostatic pressure

In view of the preceding sections, it comes into view that the proper prediction of gas release is dependent on the stress distribution in the fuel pellets. The stress has different contributions:

- There can be a mechanical interaction with the cladding due to the combined effects of the fuel expansion and cladding creep-down;
- The differential thermal expansion in the temperature gradient of the pellets produces large stresses that cause pellet cracking during the first startup of the reactor;
- Gaseous and solid fission product swelling induce mainly normal stresses;
- Both thermal and irradiation induced creep provide stress relaxation.

The hydrostatic stress is defined in a solid as the average normal stress [178, 214]

$$P_h = -\frac{\sigma_{rr} + \sigma_{\theta\theta} + \sigma_{zz}}{3} \tag{3.6}$$

and affects the mechanical equilibrium of gas filled bubbles at grain boundaries, as shown in Eq.(2.24).

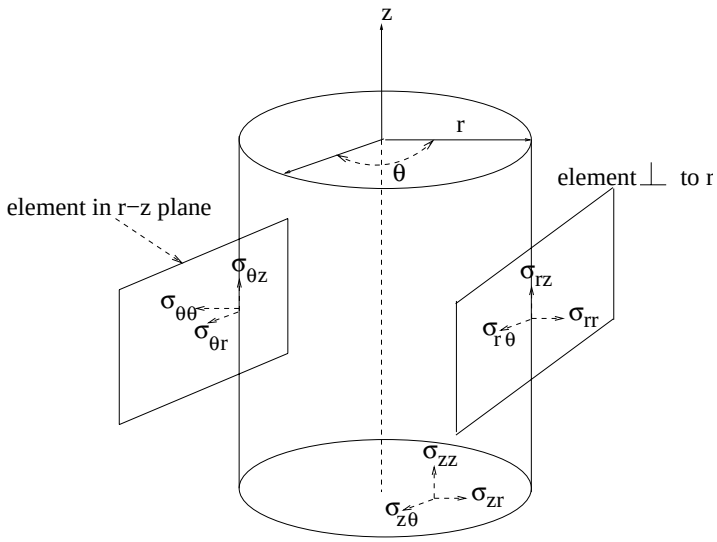


Figure 3.7: Components of the stress tensor ($\sigma$) in the cylindrical coordinate sytem.

There are data, both from in-pile and out-of-pile experiments, indicating an important effect of the hydrostatic stress on the fission gas release and the concomitant gaseous swelling behaviour [113, 186, 211, 215, 216]. In contrast, Tempest and White [217] concluded that there was no delaying effect on interlinkage from internally pressurizing the rods to 40 atm. White

therefore disregarded the effect of $P_h$ in his model [71], as did Denis et al. [58] and Ito et al. [161]. Yet, White advocates that the bubble pressure is above the equilibrium pressure and introduces the "quasi-crystallites". This concept is based on the idea that there is a lack of vacancies in the grain boundary, which is in contradiction with the idea that the grain boundary is a source of vacancies [87, 129, 216, 218]. Moreover, the conclusion drawn by Tempest and White was due to the range of the hydrostatic pressure applied in their experiments, which is more than an order of magnitude smaller in comparison with the range of $P_h$ in the aforementioned experiments (up to 200 MPa).

In line with the general awareness of the importance of $P_h$ [219] most models account for it, though only in the saturation criterion at the grain boundary [59, 169, 171]. Consequently, $P_h$ will merely affect the onset of release and not the release kinetics once the saturation is achieved. According to Kogai et al. [186] there is also a clear effect of the hydrostatic pressure on the release kinetics. Therefore he applied an intergranular bubble growth law like Matthews et al. [220] and Hayns et al. [221]. This formula is derived from the model for void growth on grain boundaries developed by Speight et al. [218], which has been verified by means of small angle neutron scattering [222]. Matthews et al. [220], as well as Hayns et al. [221] have extended the idea of Speight and co-workers by considering gas filled bubbles rather than voids. To include the presence of gas within the cavity, they simply included the gas pressure into the chemical potential of the cavity

$$\frac{\partial \rho_{bl}}{\partial t} = \frac{\delta_{gb} D^v_{gb} \Omega}{4 f(\theta) \rho^2_{bl} k_B T} \left( P_{bl} + P_h - \frac{2\gamma}{\rho_{bl}} \right) k(\phi) \tag{3.7}$$

where $\delta_{gb}$ represents the grain boundary thickness ( $= 0.5\ nm$), $D^v_{gb}$ is the vacancy diffusion coefficient on the grain boundary, $\Omega$ corresponds to the U-vacancy volume in the $UO_2$-matrix ( $= 4.09 \times 10^{-29} m^3$), $\gamma$ is the surface tension of the intergranular bubble, $\theta$ is the half-dihedral angle between the intergranular bubble and the grain boundary ( $= 50°$), $f(\theta) = 1 - 1.5\cos\theta + 0.5\cos^3\theta$ corresponds to the ratio between a spherical and a lenticular bubble with the same radius of curvature, and

$$k(\phi) = \frac{8(1-\phi)}{(\phi-1)(3-\phi) - 2\ln\phi}, \tag{3.8}$$

where $\phi$ is the fraction of the grain boundary surface covered by bubbles. Matthews et al. [220] have compared their results on swelling in nuclear fuel successfully with the experimental data of Zimmermann [215]. Kashibe and Une [216, 223, 224], as well as White [225] have confirmed these findings more recently.

In addition to the influence of $P_h$ on the bubble growth law in Eq. (3.7), Kogai considered the tube conductivity to be proportional with the sigmoidal curve

$$1 - \exp\left[-\left(\frac{\sigma_{eff}}{\sigma_{ref}}\right)^{10}\right] \tag{3.9}$$

where $\sigma_{ref}$ represents a reference value, and the effective tensile stress acting on the grain boundary ($\sigma_{eff}$) is defined as a function of the hydrostatic pressure and the gas pressure in the bubble ($P_{bl}$):

$$\sigma_{eff} = \frac{(P_h + \phi P_{bl})}{(1-\phi)} \tag{3.10}$$

As a result, the effect of $P_h$ is accounted for twice in the model of Kogai: once in the bubble growth law (Eq.(3.7)), and a second time in the tube conductivity (Eq.(3.9)), which seems to be redundant. Moreover, according to Eq.(3.9) the release will also be boosted in the case of a compressive (negative) stress, which is physically unacceptable.

### 3.3.5 The effect of the fabrication parameters

The fractional release is dependent, of course, on the fabrication process of the fuel pellets. The parameters affecting the release directly are the fraction of open porosity along with the grain and the pore size distributions. The influence of the grain size distribution has already been touched upon previously (cf. § 2.9 and § 3.2.3).

The open porosity provides an easy escape route for the gas atoms. It is generally accepted that, at high temperatures, the gas liberation mainly occurs through the interconnected tunnels along grain boundaries. At low temperatures such bubbles are absent, hence athermal release takes place at the open surface unintentionally left after imperfect manufacturing techniques [13, 14, 152]. The contribution of as fabricated open porosity is expected to be less important with increasing burnup because in-pile densification reduces the total porosity and therefore also the open porosity [152]. Nevertheless, densification may be strongly reduced at low temperatures [226], hence open porosity could still promote gas liberation during low power irradiation [13, 14].
The initial open porosity fraction is only empirically accounted for in the models for fission gas release. Either by means of an empirical contribution of athermal release [152, 172, 210], either through the equivalent Booth sphere radius [1, 173].

Several fuel design parameters have an indirect effect on the release [186]. For example, we have verified experimentally the influence of the cladding-gap width on the release through the temperature distribution [227]. Nevertheless, the consequences of these fuel design parameters, such as the temperature or the hydrostatic stress distribution, are provided as input parameters for the fission gas release model. Their proper assessment is beyond the scope of the present investigation.

## 3.4 Conclusions

Fission gas release modelling in nuclear fuels has received much interest for several decades. At present, there is a general consensus regarding the application of the Booth approach with an effective diffusion coefficient for the intragranular behaviour of fission products. Main differences among the concepts relate to the behaviour at the grain boundaries as well as to the coupling between the intra-and intergranular modules.

Despite all the efforts, there is still room for improvement. Two of the most important issues models should be able to cope with from an industrial point of view are the incubation behaviour and the burst phenomenon during power variations, especially at high burnup. This requires a proper description of the release kinetics, both in the grains and along the grain boundaries. To this end, the recent model of Kogai [181] provides the most appropriate basis. Nevertheless, some limitations of this model have been highlighted and need to be tackled:

- The bulk diffusion coefficient does not account explicitly for the trapping and re-solution processes associated with intragranular bubbles.
- There is only a one-way coupling between the intra- and intergranular modules. The intragranular module disregards the presence of the fission products in grain boundaries entirely.
- The formalism adopted by Kogai for the grain boundary precipitation underpredicts the capture rate by an order of magnitude, as will be pointed out later (cf. chapter 5).
- The model for precipitation ignored the contribution of grain boundary bubble sweeping to bubble growth.
- The influence of the hydrostatic stress on the tube conductivity in the intergranular module is redundant and physically unacceptable.
- The concept of precipitation and subsequent grain boundary bubble interconnection in the intergranular module can not reproduce the gas release observed at high burnup and low temperatures.
- The model does not enable to account for two important fabrication parameters, namely the grain size distribution and the open porosity fraction.

# Chapter 4

# Objectives and outline of the dissertation

The general objective of this work is to improve the predictive capabilities of the fission gas release model in fuel performance codes for light water reactors under normal operating conditions. More precisely, a FGR model must be developed that should be able to cope with the incubation behaviour, especially with the reduction of the release threshold at high burnup, as well as with the burst phenomenon during smooth power variations in $UO_2$ fuel. These objectives can be achieved by means of two complementary contributions; (a) by elucidating the underlying basic mechanisms, in particular those governing the intergranular behaviour, and (b) by improving the mathematical description of the FGR process as a whole.

In this **first part**, it was necessary to review the literature on the fission gas release mechanisms and the corresponding models. This survey not only underlines the complexity of the initial situation, it highlights the importance of the intergranular behaviour of fission products, and, most importantly, it delineates the issues I should address in more detail (cf. § 2.13 and § 3.4).

The **second part** deals with the analysis of basic mechanisms involved in the fission gas release process at the grain boundaries. In chapter 5, I develop a model for the precipitation of fission products in a grain boundary, which embodies a variable reaction rate on the precipitate surface. This enables one to account for modifications of the local fuel chemistry, or to distinguish between the behaviour of different migrating species.
In chapter 6, I have analysed the role of grain boundary diffusion in fission gas release by two methods; first by assessing the distance a fission product can migrate in a grain boundary containing traps of variable efficiency; second by examining experimental data on Xe release from trace-irradiated $UO_2$.

The **third part** of the dissertation reports on the development of an improved model for fission gas release, and consists of three chapters. Chapter 7 describes the mathematical concept, which is based on that of Kogai but includes the necessary improvements brought

up in the analysis of the existing models (cf. § 3.4). Given the importance of the saturation process at the grain boundaries, I focus my modelling efforts on the intergranular module.
In chapter 8, I discuss the programme implementation together with the choice of the numerical parameters in the model. The determination of the numerical parameters relies on the Taguchi approach, which provides a limited number of tests with a judicious combination of all parameters under consideration. The key issue is the reduction of the calculation time while assuring sufficient precision. Most of my efforts for the implementation are devoted to the intragranular module, since it is invoked a large number of times and the majority of the fission gas remains in the grains under normal operating conditions.
The application of the fission gas release model is the subject of chapter 9. Since the model contains a large number of physical parameters and constants, I start with a sensitivity study. Subsequently, I compare the model with well qualified experimental data from the open literature, as well as with the predictions from others.

In the fourth and **last part** of the thesis, I summarise the main achievements and draw the conclusions of my investigation. In addition, I enumerate a number of recommendations for further research, some of which have already been launched.

# Part II

# Contributions to the description of the grain boundary behaviour of fission products

The overview of mechanisms involved in the fission gas release process in LWR fuel revealed a number of issues that require further research (cf. § 2.13). In particular, there is a need to address issues related to the intergranular behaviour of fission gas atoms.

Metallic as well as volatile and gaseous fission product precipitates have been observed in grain boundaries above certain temperatures and burnup values. In a first step (chapter 5), I have therefore looked at the intergranular precipitation process of fission products. In a second step (chapter 6), I have evaluated the consequences of the precipitation process on the contribution of grain boundary diffusion to the venting of inert gas atoms from the fuel pellets.

# Chapter 5

# Modelling the precipitation of fission products at grain boundaries

Contents

## 5.1 Introduction

In general, the precipitation at grain boundaries influences the pellet-cladding mechanical interaction through swelling of the fuel, the amount of volatile fission products vented during a burst release at high burnup, and it can inhibit the migration of fission products along the grain faces. Accordingly, the correct prediction of intergranular precipitation constitutes an important aspect of a fuel behaviour code.

Trapping or precipitation of fission products can occur at different types of traps such as structural defects, gas filled bubbles and pores, and metallic precipitates. In addition, volatile fission products such as Cs and I can be immobilised by means of a chemical interaction with the fuel (e.g. uranates) or with other fission products (e.g. CsI). As a result, the precipitation or trapping of fission products is dependent on the temperature and burnup [99–104], on the species under consideration [52, 93, 103, 105], on stoichiometry deviations and additives [45, 106], as well as on the "geometrical" parameters such as the number density and the size of the trapping centers. The influence of these parameters on the precipitation rate is generally embodied in a rate coefficient ($k$), since the reactions of point defects with traps are usually described in terms of phenomenological rate equations of chemical kinetics. At present, several diffusion-controlled reaction rate coefficients are in use, derived basically from the Smoluchowsky theory of coagulation [56, 181, 228]. In these models, the traps are considered to be isolated, that is they are not affected by the presence of each other. The mean field approach [229–231] considers the traps to be isolated particles as well, though in addition it accounts for a source term under continuous irradiation conditions. For higher trap concentrations, the diffusion field surrounding a trap will become disturbed by those of neighbouring traps. In order to account for competition between neighbouring traps, Ham [232, 233] proposed the cell-model without source term and Wood [234] used the modified effective medium approach in two dimensions developed earlier by Brailsford et al. [235, 236] in three dimensions. However, the models for the precipitation of volatile fission products, and those describing void formation by accumulation of vacancies, considered the traps to be perfect absorbers or black spheres. Accordingly, they do not enable us to account for the variable efficiency of the traps at trapping fission products impinging on their surface ($k_{in}^{'}$) which can result from the variation of the temperature, the stoichiometry, the composition etc. as indicated above.

The objective of the present chapter is twofold. First, I develop a model for intergranular precipitation of fission products which accounts for the variable trap efficiency, in addition to the overlapping diffusion fields or competition between traps, and the source term under continuous irradiation conditions. The second objective consists in analysing the effect of these parameters on the precipitation rate in grain boundaries according to different theories. To this end, I have extended several models from the open literature in order to account for the variable efficiency of the traps at holding fission products impinging on their surface. I

start by introducing assumptions in order to simplify the mathematical problem at hand. In the following section I present several theories for the rate-theory representation of fission product precipitation in a grain boundary. Subsequently I compare the predictions of the models in steady-state or quasi steady-state conditions and assess the influence of the various parameters involved. Furthermore I will establish interrelationships among the models and discuss their limitations and range of validity.

## 5.2 Preliminary assumptions

In the present analysis I disregard the creation or nucleation of the traps. The presence of sinks implies that the precipitation is diffusion-controlled rather than governed by the possibility of an encounter of two or more fission products [68].

As indicated above, I consider traps in a more general sense. For instance, sinks could correspond to intergranular bubbles and metallic precipitates appearing after a short irradiation time [109–111], as well as defects, e.g. those created by fission fragments. The latter idea is in accordance with the experimental observations on intragranular bubble nucleation in the wake of fission products [237], and with the idea of Khoruzhii et al. [122] about a new retardation force on grain growth in trace irradiated $UO_2$ due to inclusions in grain boundaries generated when fission tracks intercept the grain face.

The grain boundary traps are assumed to be immobile [71, 135], in other words I consider the velocity of the traps to be negligible with respect to the velocity of the fission products. I further adopt a quasi-stationary approach for their growth, that is I presume their size to remain constant during a certain time step.

Each trap is assumed to be circular, corresponding, for example, to the intersection of a lenticular grain boundary bubble with the grain face. I further suppose that all the traps are equi-sized with radius $R_{tr}$ in the plane of the grain boundary, as was indicated for gas-filled bubbles in $UO_2$ by Tucker [111, 238, 239].

The fission products arrive at the grain boundary uniformly. A fraction, equal to the fraction of the grain boundary surface occupied by the traps ($\phi$), is directly captured by the traps. The other fraction is dissolved in the grain boundary layer and can be trapped when they impinge on a trap while migrating along the grain boundary. Long-range interaction potentials, appropriate to ionic reactants because of the charge effects, are indirectly accounted for in our investigation by considering a variable effective trapping radius [228, 230, 231].

Finally, I assume that grain boundary traps exist as separate entities, i.e. they do not interconnect, which implies that $\phi$ is limited to the order of 40% (e.g. [240]). Nevertheless, I have extended the calculations for cases were grain faces are almost entirely covered by traps in order to analyse the validity of some approaches.

## 5.3 The intrinsic reaction rate at the trap surface

The boundary condition for the fission product concentration at the intergranular trap surface ($C_{gbv}(R_{tr},t)$) is determined by the intrinsic rate coefficient $k_{in}$, that is the reaction rate when the migrating species and the traps are in contact. In the event of an infinite intrinsic reaction rate, the absorption of the fission product on collision with a trap occurs instantaneously. Under those circumstances the Smoluchowsky boundary condition (SBC) [229,241,242], sometimes referred to as the black-sphere approximation [228], applies:

$$C_{gbv}(R_{tr},t) = 0. \tag{5.1}$$

In the case of a finite intrinsic reaction rate one obtains the so-called radiation boundary condition (RBC), corresponding to a partial reflection of the particle flux from the reaction surface [228,229,241–243]

$$\oint_{trap} \vec{J} \cdot \vec{n}\, dS = 2\pi R_{tr} D_{gb} \left.\frac{\partial C_{gbv}(R,t)}{\partial R}\right|_{R_{tr}} = k_{in} C_{gbv}(R_{tr},t), \tag{5.2}$$

where $k_{in}$ is the intrinsic rate coefficient on the trap surface and $k_{in}^{'} = k_{in}/2\pi D_{gb}$ is defined as the dimensionless intrinsic rate coefficient on the trap surface. This boundary condition was introduced in the theoretical treatment of the kinetics of diffusion-limited reactions [243] and has been applied to fluorescence quenching [229] and Frenkel defect recombination in ionic solids [228], as well as to the void-point defect interactions in nuclear fuel [235,241,244]. The RBC enables us to assess the influence of the so-called saturation of the intrinsic capture rate on the global capture rate coefficient ($k$). Such a reduction of $k_{in}^{'}$ could result, for instance, from a lack of vacancies to accommodate the fission gases in a grain boundary bubble or from a temperature variation which in turn can affect the reaction rate of a chemically active fission product with the trap.

Most fission product release models account also for the fact that a fraction of the atoms precipitated or accumulated in the intergranular traps can be re-dissolved into the adjacent grains by interaction with a fission fragment, referred to as irradiation induced re-solution [67, 70, 245]. This phenomenon constitutes an essential element in the boundary condition for the transport of the fission products within the grains. However, the irradiation induced re-solution has no direct influence on the reaction rate between the grain boundary traps and the fission products migrating along the grain faces, that is on the boundary conditions of the trap surface. Consequently it will not be considered in the present study directly. However, the effect of the re-solution process is *indirectly* accounted for, since it affects the trap (bubble) size which is taken as a variable parameter in the following analysis.

## 5.4 Models for the precipitation rate coefficient

In general, reactions of point defects or fission products with traps are described in terms of chemical rate equations. For this purpose, a rate coefficient ($k$) is required for each fission product involved. In the following, I will derive a relationship for the capture rate coefficient or the trap strength as a function of the geometrical parameters of the trapping centra, the grain boundary diffusion coefficient of the fission products ($D_{gb}$) and the efficiency of the traps at trapping fission products impinging on their surface ($k_{in}^{'}$), according to different approaches.

### 5.4.1 The Smoluchowsky approach

For the description of diffusion-controlled reactions, many rate coefficients are derived basically from the Smoluchowsky theory of coagulation in which only one sink species is assumed with such a low concentration that the diffusion field surrounding a trap is not disturbed by the diffusion fields of neighbouring traps [56, 228, 229, 241, 242]. This approach is therefore equivalent to the isolated particle approximation mentioned by Ham [232,233] for precipitation of point defects on dislocations.

The Smoluchowsky formalism has been applied successfully to photochemistry [246] and diffusion-influenced fluorescence quenching [229], which is characterised by the kinetic scheme $A^* + B \rightarrow A + B$ where $A^*$is an excited state of $A$ and $B$ is a quencher acting like an indestructible trap. The model is exact when the diffusion coefficient of $A^*$ approaches zero and the $B$'s do not interact with each other [229]. Accordingly, this approach is expected to be poor for the problem of absorption of a diffusing particle by static traps, especially at high trap densities where overlapping diffusion fields become important.

Rather than using the concentration of fission products dissolved in the grain boundary, the correlation derived from the Smoluchowsky theory considers the distribution function of the fission products $U(R,t)$ [56, 228, 229, 241]. The distribution function is a solution of the Smoluchowsky equation:

$$\frac{\partial U(R,t)}{\partial t} = D_{gb} \triangle U(R,t). \tag{5.3}$$

The partial differential equation is subject to the uniform initial condition $U(R,0) = 1$, and to the SBC or RBC at the reaction surface, while the distribution function (concentration) should remain finite at large distances from the trap. The time dependent (global) rate coefficient is obtained by integrating the normal component of the flux over the surface of the trap [229,241]

$$k(t) = \oint_{trap} D_{gb} \nabla U dA. \tag{5.4}$$

Following this procedure, I obtain the time dependent rate coefficient for intergranular trap-

ping (cf. Appendix B.1):

$$k\left(t\right)=\frac{8\left(k_{in}^{'}\right)^{2}D_{gb}}{\pi}\int_{0}^{\infty}\frac{e^{-D_{gb}\lambda^{2}t}}{F\left(\lambda,k_{in}^{'}\right)}\frac{d\lambda}{\lambda}, \tag{5.5}$$

where

$$F\left(\lambda,k_{in}^{'}\right)=\left[\lambda R_{tr}J_{1}\left(\lambda R_{tr}\right)+k_{in}^{'}J_{0}\left(\lambda R_{tr}\right)\right]^{2}+\left[\lambda R_{tr}Y_{1}\left(\lambda R_{tr}\right)+k_{in}^{'}Y_{0}\left(\lambda R_{tr}\right)\right]^{2}. \tag{5.6}$$

When the boundary condition at $R_{tr}$ reduces to Eq. (5.1), this simplifies to the expression obtained by Szabo [229]:

$$k\left(t\right)=\frac{8D_{gb}}{\pi}\int_{0}^{\infty}\frac{e^{-D_{gb}\lambda^{2}t}}{F\left(\lambda\right)}\frac{d\lambda}{\lambda}, \tag{5.7}$$

where

$$F\left(\lambda\right)=J_{0}^{2}\left(\lambda R_{tr}\right)+Y_{0}^{2}\left(\lambda R_{tr}\right). \tag{5.8}$$

### 5.4.2 The mean field approach

Alike the previous model, the mean field approach (MFA) corresponds to the isolated particle approximation subject to the condition that the concentration reaches a constant bulk value ($C_{bulk}$) at large distances from the trap [229–231]. In the mean field approximation, one assumes that the deviation from the bulk value, $\delta C\left(R\right)=C\left(R\right)-C_{bulk}$, satisfies

$$D_{gb}\triangle\delta C\left(R\right)=k_{ss}C_{tr}\delta C\left(R\right), \tag{5.9}$$

where $C_{tr}$ represents the number of intergranular traps per unit of grain boundary surface and $k_{ss}=\lim_{t\rightarrow\infty}k\left(t\right)$ is the steady-state rate coefficient. This equation is solved subject to either Eq. (5.1) or Eq. (5.2). The steady-state rate coefficient is then equated to the flux at contact, divided by $C_{bulk}$ and multiplied by the trap density $C_{tr}$. Since $C\left(R\right)$ is a function of $k_{ss}$, this procedure leads to an implicit equation for $k_{ss}^{'}=k_{ss}/2\pi D_{gb}$ which is characteristic for the mean field approximation (cf. Appendix B.2)

$$k_{ss}^{\prime}=\frac{k_{in}^{'}\sqrt{2k_{ss}^{'}\phi}K_{1}\left(\sqrt{2k_{ss}^{'}\phi}\right)}{\sqrt{2k_{ss}^{'}\phi}K_{1}\left(\sqrt{2k_{ss}^{'}\phi}\right)+k_{in}^{'}K_{0}\left(\sqrt{2k_{ss}^{'}\phi}\right)}, \tag{5.10}$$

where $\phi=C_{tr}\pi R_{tr}^{2}$ represents the fraction of the grain boundary covered by the traps. Taking the limit for $k_{in}^{'}\rightarrow\infty$, corresponding to perfect trap conditions, I obtain the same result as found previously by Szabo [229]. Taking the limit for $\phi\rightarrow0$ and making use of the modified

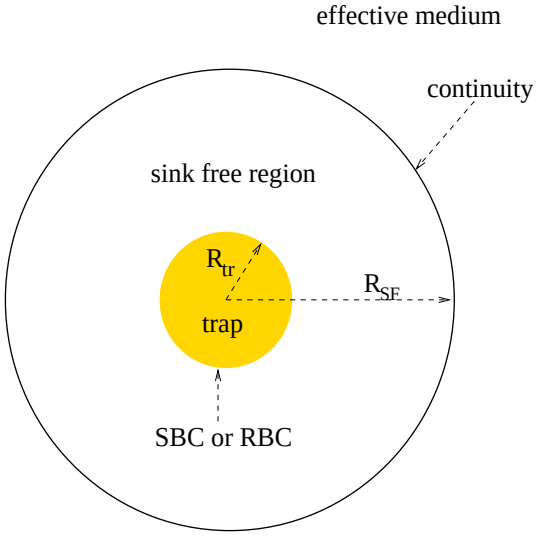


Figure 5.1: Schematic representation of the effective medium model

Bessel function's properties [247] I obtain

$$\frac{k_{ss}}{2\pi D_{gb}} \triangleq k_{ss}^{'} = \frac{k_{in}^{'}}{1 - k_{in}^{'}\left(\gamma + \ln\sqrt{\frac{k^{'}\phi}{2}}\right)}. \tag{5.11}$$

The mean field approach can be shown to be equivalent with the embedding procedure of Brailsford et al. [235, 244] which is derived from the rate theory formulation for point defect sink strengths and assumes a steady-state condition as well. In this model, the discrete random array of traps is approximated by an equivalent homogeneous medium. The latter must be such that if we excavate from it a spherical surface of radius $R_{SF}$ and replace it by an equal surface comprised of a spherical shell of a trap free zone surrounding just one inclusion, then the macroscopic properties of the composite thus formed must be the same as those of the medium itself. This is schematically represented in Fig. 5.1. The trap strength is obtained by solving the following coupled system of differential equations

$$\begin{cases} D\triangle C + S = 0 & R_{tr} \leq R \leq R_{SF} \\ D\triangle C + S + S^{e} - k_{ss}CC_{tr} = 0 & R \geq R_{SF} \end{cases} \tag{5.12}$$

subject to the boundary condition (5.1) or (5.2) on the trap surface, and where $S^{e}$ represents the point defect emission rate from all traps. They derive the net flux of point defects to the central trap and this must equal the net loss rate per sink in the medium. When the trap is directly embedded in the effective medium, in other words, when omitting the trap free region surrounding the trap ($R_{SF} = R_{tr}$), the equation governing the fission product concentration

in the homogeneous medium becomes equivalent to Eq.(5.9) since we have

$$\lim_{R\to\infty} C(R) = C_{bulk} = \frac{S + S^e}{k_{ss} C_{tr}} \tag{5.13}$$

at large distances from the trap surface.

The embedding procedure is only strictly appropriate when the traps are randomly distributed, although it has been judiciously modified to encompass even regular arrays of traps in a perfect lattice [236]. Wood and co-workers [220, 234] have applied this modified effective medium (MEM) approximation to grain boundary bubble swelling. Their model is closely related to the treatment of Speight et al. [218] to void growth on grain boundaries and has been verified by Yang et al. [222] by means of small angle neutron scattering.

Unlike the model derived from the Smoluchowsky theory indicated above, the mean field approach accounts for a source term under continuous irradiation conditions. Nevertheless, the steady-state rate coefficient obtained with the effective medium procedure can be shown to be equivalent to the quasi-steady-state approximation obtained with modified Smoluchowsky equations [56] in spherical geometry, provided the same boundary conditions are applied at the trap surface. In view of the equivalence of the MFA with the Smoluchowsky approach [229] and the effective medium approximation mentioned above, I will only present the MFA results. In addition, the rate coefficient derived from the MFA can be expressed as a function of the dimensionless quantities $\phi$ and $k'_{in}$.

### 5.4.3 The cell model without source term

The cell model is based on the work of Ham [232]. I assume the presence of a regular array of traps with a number density $C_{tr}$, in accordance with the computations of Tucker for gas filled bubbles [111, 238, 239] who indicated that a random array of freshly nucleated bubbles will begin to spread out into a more uniform distribution as they grow. Fixman [248] and Wood [234] have shown that this entails a larger global trapping rate in comparison with an irregular distribution of the traps. Given the symmetry of the trap distribution on the grain face, I assume that the same property holds for the concentration profile. A unit cell, or capture surface, surrounding each sphere is then defined as the portion of the surface that can be associated with each circular trap. The entire surface is divided into $C_{tr}$ identical polyhedra or cells each containing one trap at its centre in order to reproduce (on average basis) the system of surface plus traps (cf. Fig. 3.2 p. 43). For ease of computation it is convenient to approximate each polyhedron by a circle with a radius chosen to satisfy the requirement that the $C_{tr}$ cells occupy the entire surface. Thus each trap or bubble can be considered to be isolated (Wigner-Seitz approach [249]) in a circular zone of radius $R_s$ defined by

$$C_{tr}\pi R_s^2 = 1 \tag{5.14}$$

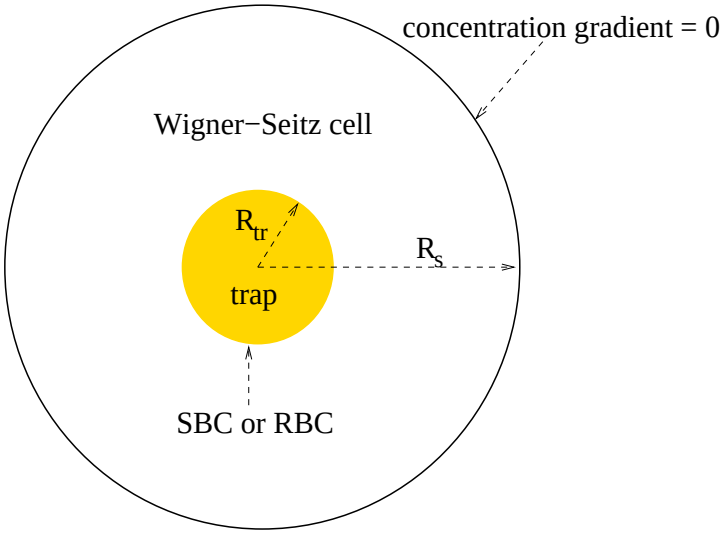


Figure 5.2: Schematic representation of the cell model

(cf. Fig. 5.2), or an equivalent square cell with the same size $s^2 = \pi R_s^2$ (cf. Fig. 3.2). As a result of the symmetry of the concentration profile, the normal component of its gradient vanishes on this surface, or equivalently, an equal number of fission products crosses the cell border in each direction.

I further assume that the concentration satisfies the time-dependent diffusion equation

$$\frac{\partial C_{gbv}(R,t)}{\partial t} = D_{gb} \triangle C_{gbv}(R,t) \tag{5.15}$$

at all points of the grain face ($R_{tr} \leq R \leq R_s$) and I consider a uniform initial distribution of the fission products ($C_{gbv}(R, t=0) = \theta$). These circumstances correspond to a post-irradiation annealing situation, where the initial state could result from a very low temperature irradiation such as to immobilise the fission products. The reaction is subsequently resumed at temperatures high enough to allow intergranular diffusion to be operative but low enough so that the fission products in the adjacent grains may be considered to be immobile. This is plausible in the light of the general accepted idea that the activation energy for intragranular diffusion is higher in comparison with the activation energy for intergranular diffusion [83].

The solution to the diffusion equation governing the concentration profile in each cell in case of radiation boundary conditions can be expressed as follows (cf. Appendix B.3):

$$C_{gbv}(R,t) = -\pi k_{in}^{'} \theta \sum_{n=1}^{\infty} \left[ \frac{C\left(\lambda_n, k_{in}^{'}, R\right)}{F\left(\lambda_n, k_{in}^{'}\right)} \right] e^{-D_{gb}\lambda_n^2 t}, \tag{5.16}$$

where

$$C\left(\lambda_n, k_{in}^{'}, R\right) = J_0\left(\lambda_n R\right)\left[\lambda_n R_{tr} Y_1\left(\lambda_n R_{tr}\right) + k_{in}^{'} Y_0\left(\lambda_n R_{tr}\right)\right] - Y_0\left(\lambda_n R\right)\left[\lambda_n R_{tr} J_1\left(\lambda_n R_{tr}\right) + k_{in}^{'} J_0\left(\lambda_n R_{tr}\right)\right], \tag{5.17}$$

$$F\left(\lambda_n, k_{in}^{'}\right) = \left[\frac{\lambda_n R_{tr} J_1\left(\lambda_n R_{tr}\right) + k_{in}^{'} J_0\left(\lambda_n R_{tr}\right)}{J_1\left(\lambda_n R_s\right)}\right]^2 - \left(\lambda_n^2 R_{tr}^2 + k_{in}^{'2}\right), \tag{5.18}$$

where $\lambda_n$ are the positive roots of a transcendental equation involving Bessel functions of the first and second kind:

$$\left[\lambda_n R_{tr} J_1\left(\lambda_n R_{tr}\right) + k_{in}^{'} J_0\left(\lambda_n R_{tr}\right)\right] Y_1\left(\lambda_n R_s\right) = \left[\lambda_n R_{tr} Y_1\left(\lambda_n R_{tr}\right) + k_{in}^{'} Y_0\left(\lambda_n R_{tr}\right)\right] J_1\left(\lambda_n R_s\right). \tag{5.19}$$

Taking the limit for $k_{in}^{'} \to \infty$, that is when the perfect trap boundary condition applies at $R_{tr}$, I obtain the same result as obtained by Ham [233].

Integrating the diffusion equation (5.15) from $R_{tr}$ to $R_s$ and dividing by the surface $\pi\left(R_s^2 - R_{tr}^2\right)$, I obtain a balance equation which defines the (global) rate coefficient $k\left(t\right)$

$$\frac{d\overline{C}_{gbv}}{dt} = -k\left(t\right) C_{tr} \overline{C}_{gbv,} \tag{5.20}$$

where

$$\overline{C}_{gbv} = \frac{2}{R_s^2 - R_{tr}^2} \int_{R_{tr}}^{R_s} C_{gb}\left(R, t\right) R dR \tag{5.21}$$

corresponds to the spatially averaged concentration of the diffusing fission products due to the reaction with the trap species characterised by a number density $C_{tr}$. Inserting (5.16) in (5.21) and taking the derivative with respect to time one obtains the time dependent rate coefficient

$$k(t) = \frac{D_{gb}}{C_{tr}} \frac{\sum_{n=1}^{\infty} \frac{e^{-D_{gb}\lambda_n^2 t}}{F\left(\lambda_n, k_{in}^{'}\right)}}{\sum_{n=1}^{\infty} \frac{e^{-D_{gb}\lambda_n^2 t}}{\lambda_n^2 F\left(\lambda_n, k_{in}^{'}\right)}}. \tag{5.22}$$

In the quasi steady-state, $k(t)$ reduces to a time-independent value ($k_{qs}$) which is determined by the smallest eigenvalue of (5.19), also referred to as the first harmonic or fundamental mode:

$$\lim_{t \to \infty} k\left(t\right) = k_{qs} = \frac{D_{gb}\lambda_0^2}{C_{tr}}. \tag{5.23}$$

### 5.4.4 The cell model with source term

The assumptions are similar to those of the previous model if it isn't for the continuous irradiation conditions. This will enable me to assess the effect of a source term on the correction factor to be applied to the rate coefficient, as suggested by Gösele in a three dimensional spherical geometry [241].

Under continuous irradiation conditions, the right-hand side of the diffusion equation (5.15) in the cell contains a source term, $S$, corresponding to the number of fission products arriving at the grain face per unit of surface and time ($\mu m^{-2} s^{-1}$). The initial concentration is taken to be zero ($C_{gbv}(R, t=0) = 0$). When the radiation boundary condition applies at the trap surface, the solution to this problem can be written in the form (cf. Appendix B.4):

$$C_{gbv}(R,t) = C_{\infty}(R) - \frac{S}{D_{gb}} \sum_{n=1}^{\infty} \left[ \Psi_n \left( \lambda_n, k_{in}^{'} \right) C \left( \lambda_n, k_{in}^{'}, R \right) \right] e^{-D_{gb} \lambda_n^2 t}, \tag{5.24}$$

where

$$C_{\infty}(R) = \frac{S}{4 D_{gb}} \left[ \left( R_{tr}^2 - R^2 \right) + R_s^2 \ln \left( \frac{R}{R_{tr}} \right)^2 + \frac{2}{k_{in}^{'}} \left( R_s^2 - R_{tr}^2 \right) \right] \tag{5.25}$$

represents the stationary concentration profile, $C(\lambda_n, k_{in}^{'}, R)$ is given by Eq. (5.17), $\lambda_n$ are the positive roots of Eq. (5.19), and

$$\Psi_n \left( \lambda_n, k_{in}^{'} \right) = \frac{1}{F \left( \lambda_n, k_{in}^{'} \right)} \left\{ \frac{R_s \left[ \lambda_n R_{tr} Y_1 (\lambda_n R_{tr}) + k_{in}^{'} Y_0 (\lambda_n R_{tr}) \right]}{\lambda_n Y_1 (\lambda_n R_s)} - R_s^2 - \frac{k_{in}^{'}}{\lambda_n^2} \right\}, \tag{5.26}$$

where $F \left( \lambda_n, k_{in}^{'} \right)$ is given by Eq. (5.18).

The time dependent rate coefficient can be inferred from the integrated diffusion equation in a similar way as before:

$$\frac{d \overline{C}_{gbv}}{dt} = -k(t) C_{tr} \overline{C}_{gbv} + S, \tag{5.27}$$

hence

$$k(t) = \frac{D_{gb}}{C_{tr}} \left[ \frac{\left( R_s^2 - R_{tr}^2 \right) + 4 k_{in}^{'} \sum_{n=1}^{\infty} \Psi_n \left( \lambda_n, k_{in}^{'} \right) e^{-D_{gb} \lambda_n^2 t}}{\frac{D_{gb}}{S} \left( R_s^2 - R_{tr}^2 \right) \overline{C}_{\infty} + 4 k_{in}^{'} \sum_{n=1}^{\infty} \frac{\Psi_n \left( \lambda_n, k_{in}^{'} \right)}{\lambda_n^2} e^{-D_{gb} \lambda_n^2 t}} \right], \tag{5.28}$$

where

$$\overline{C}_{\infty} = \frac{S}{8 D_{gb}} \left\{ \left[ \left( R_{tr}^2 - 3 R_s^2 \right) + \frac{2}{k_{in}^{'}} \left( R_s^2 - R_{tr}^2 \right) \right] + \frac{2 R_s^4}{\left( R_s^2 - R_{tr}^2 \right)} \ln \left( \frac{R_s}{R_{tr}} \right)^2 \right\} \tag{5.29}$$

corresponds to the average concentration in steady-state conditions. The steady-state rate coefficient, denoted by $k_{ss}$, is obtained from the long-time limit of the time-dependent rate

coefficient

$$\begin{aligned}\lim_{t\to\infty} k(t) = k_{ss} &= \frac{S}{C_{tr}\overline{C}_{\infty}} \\ &= \frac{8\pi D_{gb}(1-\phi)}{(1-\phi)\left[(\phi-3)+\frac{2}{k_{in}^{'}}(1-\phi)\right]-2\ln\phi}.\end{aligned} \tag{5.30}$$

Taking the limit of $k_{ss}$ for $k_{in}^{'} \to \infty$, corresponding to a Smoluchowsky boundary condition at $R_{tr}$, I obtain the result of the modified effective medium approach [234].

### 5.4.5 The model of Kogai

The formulation for grain boundary gas precipitation used by Kogai [181] in his fission gas release model is derived from the Smoluchowsky theory in quasi steady-state conditions in a spherical three dimensional geometry ($k_{qs}$). The corresponding sink strength in the case of a Smoluchowsky boundary condition on the bubble surface can be written as [228, 241]:

$$k_{qs} = 4\pi R_{tr} D_{gb.} \tag{5.31}$$

In order to obtain the correct dimensions ($\mu m^2/s$) for the global precipitation coefficient, this rate coefficient has been divided by the distance separating two traps (cf. Fig. 3.2), $s = \sqrt{\pi R_s^2}$. As a result one obtains the following expression for the trapping rate coefficient:

$$k_{qs} = 4\pi D_{gb}\frac{R_{tr}}{s} = 4\sqrt{\pi} D_{gb}\sqrt{\phi}. \tag{5.32}$$

## 5.5 Results and discussion

The comparison of the different models for the (global) capture rate coefficient or the sink strength is performed in terms of the dimensionless rate coefficient $k^{'} = k/2\pi D_{gb}$ in steady-state ($k^{'} = k_{ss}^{'}$) or quasi steady-state ($k^{'} = k_{qs}^{'}$) conditions. (The results are therefore independent of the grain boundary diffusion coefficient for fission products, which is not well characterised at present). In the event of a regular array of traps with Smoluchowsky boundary conditions, it can be shown that the second smallest root ($\lambda_1$) of equation (5.19) is always larger than $3\lambda_0$ when $\phi$ ranges between 1% and 99% (cf. Fig. 6.5). Consequently, it suffices to describe the system with a single term in the cell model, except during an initial transient of duration roughly $\tau_0 = 1/D_{gb}\lambda_0^2$. The amount of precipitate associated with the initial transient is only significant when the traps are not small or when the initial distribution is not uniform [232, 243]. Whenever the transient is important, the precipitation rate can still be calculated by using the complete analytical solution provided in sections 5.4.3 and 5.4.4 for a regular array of traps, or by neglecting the competition between adjacent traps. In the

latter case, the flux is evaluated as if each particle were isolated in an infinite medium. The precipitation rate will be correct for small values of time, when competition is unimportant, though it will be overestimated as the time increases. For large values of the time, when the isolated particle approximation for the precipitation rate exceeds the value given by the (quasi) steady-state solution, the latter forms an excellent approximation.

### 5.5.1 The effect of the size and concentration of traps

When the traps operate as perfect absorbers, the dimensionless rate coefficient under steady-state or quasi-steady-state conditions can be expressed as a function of a single parameter, namely the fraction of the grain boundary surface occupied by the traps ($\phi = C_{tr}\pi R_{tr}^2$). The sensitivity of $k^{'}$ to $\phi$, computed by means of the models described above, is depicted in Fig. 5.3. The sink surface fraction ranges from 1% to 99% which covers a wide range of experimental values (in practice $\phi$ will be limited to the order of 50%). The figure reveals the limited rate coefficient along with a limited variation of $k^{'}$ with $\phi$ according to the mean field approach in comparison with the cell models. This reflects the neglect of the overlapping diffusion fields or the competition between traps in the MFA as observed earlier [241] in three dimensions. Similar conclusions hold for the Smoluchowsky theory in the case of trapping of point defects by immobile traps, whereas Szabo [229] indicated that this theory constitutes an exact solution in the quenching problems where traps are mobile and do not interact with one another.

Fig. 5.3 also features the much lower capture rate coefficient resulting from the expression used in the model of Kogai in comparison with the other models, even for small values of $\phi$. The reason for the much lower values is two-fold. The first reason stems from the geometrical effect for the approximation used by Kogai is only valid in three dimensions with spherical traps whereas the other approximations were derived in a two-dimensional geometry. The rate for migrating fission products to be trapped is much larger in the latter case in view of the reduced number of degrees of freedom. Second, the model of Kogai is derived from the Smoluchowsky theory which is equivalent to the isolated particle approximation. As a result, the discrepancy increases as the fraction of the grain boundary surface occupied by the traps is raised. The cell models will tend to $\infty$ in the limit for $\phi \rightarrow$100% unlike the models based on the isolated particle approximation. On the other hand, the results of all the two-dimensional models should be identical for very small values of $\phi$, though this is not shown in the plot because of the limited range for $\phi$.

### 5.5.2 The source term effect

The influence of the continuous irradiation conditions can be inferred from Fig. 5.3, by comparing the results of the cell models with (CM2) and without source term (CM1). The effect is negligible in comparison with the effect of the overlapping diffusion fields, in accordance with

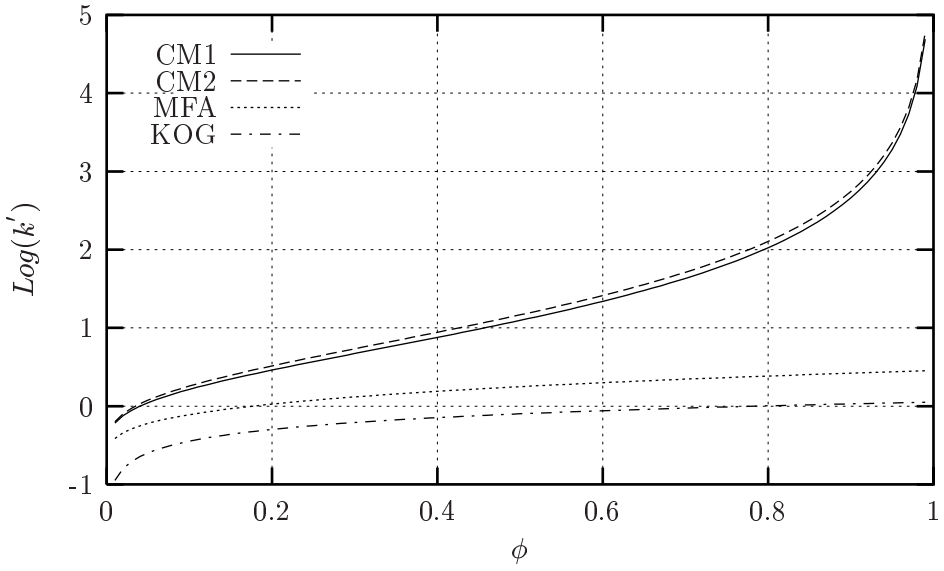


Figure 5.3: Dimensionless capture rate coefficient ($k^{'}$) in case of perfectly absorbing traps as a function of the fraction of the grain boundary surface occupied by the traps ($\phi$), according to the cell model without source term (CM1), the cell model with source term (CM2), the mean field approach (MFA), the model of Kogai (KOG)

observations in three dimensions [241]. One would expect a difference based on the following: in the case of annealing conditions, the point defects very close to the trap are captured during an initial transient, that is where not only the lowest eigenfunction in the series solution of the cell model (Eq. (5.16)) contributes to the precipitation rate. After some time, the precipitation rate will be reduced and only the first harmonic remains in accordance with Eq. (5.23). However, in the event of continuous irradiation, new point defects will be generated in the vicinity of the trap surface, entailing a faster reaction rate. Nevertheless, the difference between CM1 and CM2 is insignificant because both curves rely on almost the same diffusion problem in two dimensions. In view of this, and because the cell model including the source term is more representative than that without source term for in-pile conditions, only the results of the former will be presented in the following.

### 5.5.3 The effect of the intrinsic reaction rate coefficient

If a reaction barrier at the surface of the traps is taken into account, the dimensionless rate coefficient depends both on the intrinsic reaction rate at the trap surface ($k_{in}^{'}$) and on the trap surface fraction ($\phi$). According to the model of Kogai, $k^{'}$ is not dependent on $k_{in}^{'}$ hence his model has not been included in the comparison of the models under radiation boundary conditions. The dimensionless capture rate coefficient, computed by means of the other models, is depicted in Figs. 5.4 and 5.5 as a function of $\phi$, where the bubble surface fraction ranges

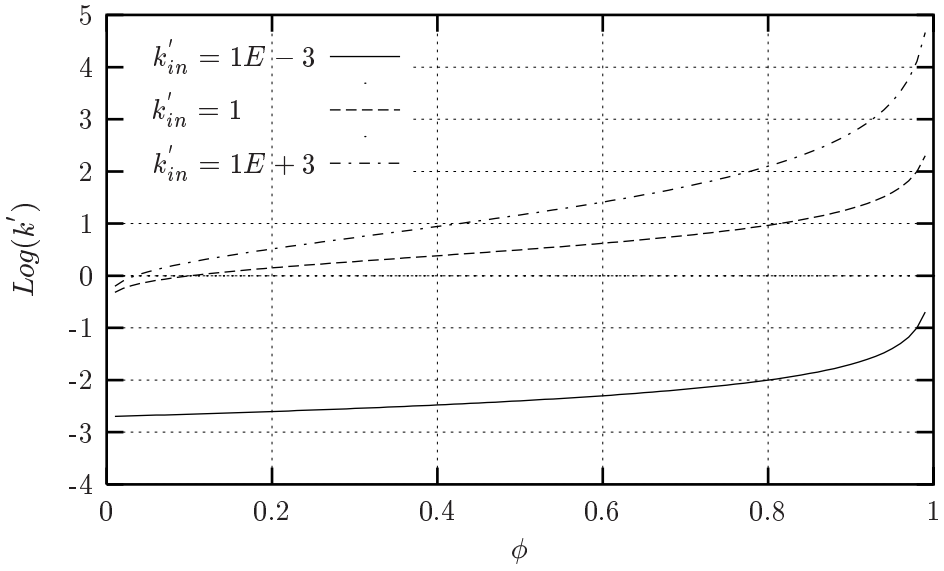


Figure 5.4: Dimensionless capture rate coefficient ($k'$) in case of radiation boundary conditions at the trap surface as a function of the fraction of the grain boundary surface occupied by the traps ($\phi$), according to the cell model with source term (CM2)

from 1% to 99%, for three different values of $k'_{in}$. The range of $k'_{in}$ from $10^{-3}$ to $10^{+3}$ suffices to assess the sensitivity of the dimensionless rate coefficient to this parameter. Indeed, for $k'_{in} = 10^{+3}$, the dimensionless rate coefficient in Figs. 5.4 and 5.5 almost converged to the corresponding limiting case of the Smoluchowsky boundary condition in Fig. 5.3. At decreasing values of the intrinsic rate coefficient, though with $k'_{in} \geq 1$, the rate coefficient becomes less sensitive to variations of $\phi$ according to all the models, especially at values of $\phi \geq 50\%$. The reason for this reduced sensitivity stems from the role played by intergranular traps, decreasing as the intrinsic rate coefficient decreases.
From Figs. 5.4 and 5.5 it also comes into view that the capture rate coefficient will be underpredicted by the mean field approach for large values of $\phi$ and for all values of $k'_{in}$, in accordance with the results under perfect trap conditions. This reflects the equivalence with the isolated particle approximation.

The sensitivity of $k'$ to $k'_{in}$ is depicted in Figs. 5.6 and 5.7 for three different values of $\phi$. It is obvious that a reduction of the intrinsic capture rate coefficient at the trap surfaces will entail a reduction of the global capture rate coefficient. However, from Figs. 5.6 and 5.7 there appears to be a critical value for the influence of $k'_{in}$ (namely $k'_{in} \approx 1$) especially for values of $\phi \leq 50\%$ which is of most practical interest. At values of $k'_{in} \leq 1$, the influence of $k'_{in}$ on the capture rate coefficient is more pronounced and the sensitivity of $k'$ to $\phi$ is independent of $k'_{in}$, entailing parallel curves in Figs. 5.4 and 5.5. Physically this corresponds to the regime where the precipitation of fission products is limited by the intrinsic reaction-rate between the

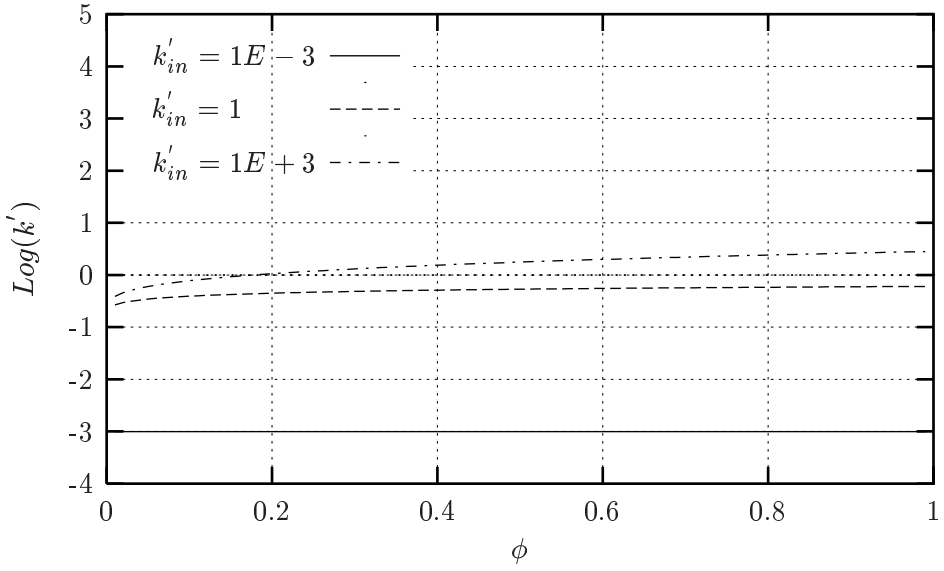


Figure 5.5: Dimensionless capture rate coefficient ($k'$) in case of radiation boundary conditions at the trap surface as a function of the fraction of the grain boundary surface occupied by the traps ($\phi$), according to the mean field approach (MFA)

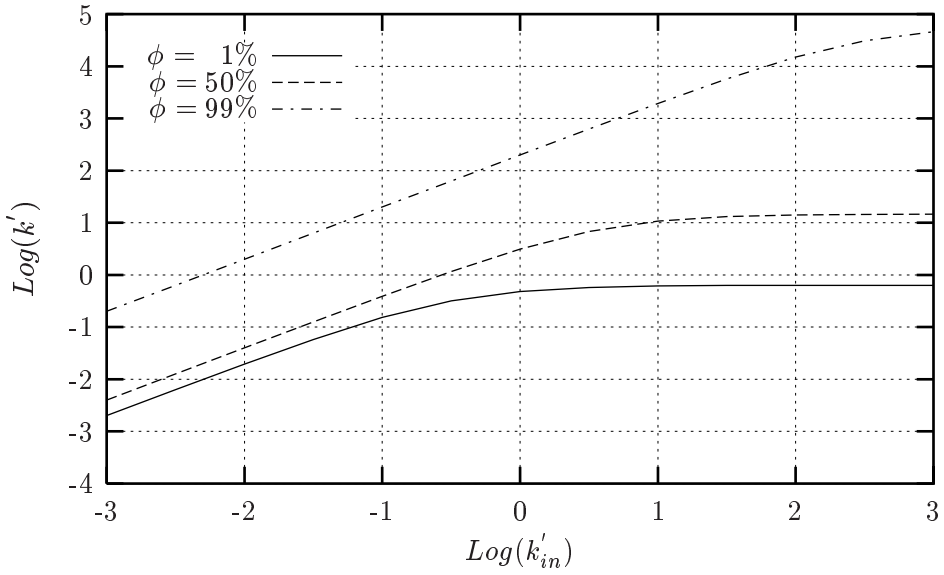


Figure 5.6: Dimensionless capture rate coefficient ($k'$) in case of radiation boundary conditions at the trap surface as a function of the dimensionless intrinsic rate coefficient at the trap surface ($k'_{in}$), according to the cell model with source term (CM2)

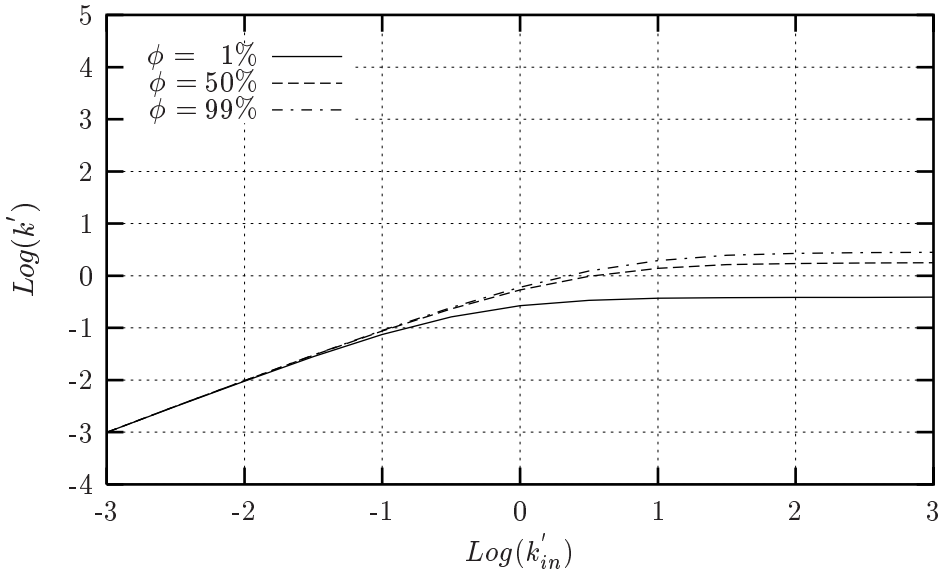


Figure 5.7: Dimensionless capture rate coefficient ($k^{'}$) in case of radiation boundary conditions at the trap surface as a function of the dimensionless intrinsic rate coefficient at the trap surface ($k^{'}_{in}$), according to the mean field approach (MFA)

fission product and the precipitate rather than diffusion controlled. This is also reflected in Figs. 5.6 and 5.7 for all the models, where $k^{'}$ becomes proportional to $k^{'}_{in}$. Such small values of $k^{'}_{in}$ could result for instance from a temperature variation in the case of a chemical active fission product, or from a lack of vacancies in grain boundary bubbles to accommodate fission gases [113, 146], or it could be related to thermal re-solution of volatile fission products from gas-filled bubbles [71, 250]. Nevertheless, the latter approach is rather controversial [18, 129] since it conflicts with the long-held assumption that volatile fission products, in particular inert gases, are essentially insoluble in $UO_2$.

For values of $k^{'}_{in} \geq 1$, the relative change of the rate coefficient is almost independent of the relative change of the intrinsic capture rate coefficient (cf. Figs. 5.4 to 5.7) except when $\phi \geq 50\%$. In present day models for fission gas release [1, 71, 181], the intrinsic reaction rate coefficient for intergranular bubbles is taken to be infinite, that is they consider Smoluchowsky boundary conditions. In practice, the intrinsic rate coefficient for different fission products and intergranular traps is unknown. However, it seems reasonable to assume that $k^{'}_{in} > 1$ for several fission products (e.g. noble gases, metallic fission products), given the negligible solubility and the observation of metallic precipitates associated with gas-filled bubbles at grain boundaries [109–111]. Accordingly, it seems well justified to apply the Smoluchowsky boundary conditions, for instance in the model of Matthews and Wood [220], under stationary conditions for inert gases. In addition, the relative insensitivity of $k^{'}$ to $k^{'}_{in}$ for $k^{'}_{in} \geq 1$ could explain the similar global precipitation rate at grain boundaries of several fission products.

For instance, Walker et al. [104] found that similar amounts of Xe and Cs were precipitated in the grain boundary gas bubbles of $UO_2$ fuel above 1573 K, although dissimilarities would be expected from the differences in charge, ionic radius and solubility.

## 5.6 Summary and conclusions

I have developed a model for precipitation of fission products in a grain boundary which embodies the variable efficiency of the traps at trapping fission products impinging on their surface ($k_{in}$), in addition to the overlapping diffusion fields between traps and the source term under continuous irradiation conditions [251]. The variable intrinsic reaction rate enables me to account for modifications of the local fuel chemistry or to distinguish between the behaviour of different migrating species.

The effect of the various parameters, especially $k_{in}^{'}$, on the intergranular precipitation rate has been assessed according to different approaches. Results in steady-state or quasi-steady-state conditions reveal that models derived from the Smoluchowsky theory of coagulation, the mean field approach and the effective medium approximation are only accurate when the trap concentration is very low since they neglect the competition between neighbouring traps. The formalism adopted by Kogai in a fission gas release model is based on the Smoluchowsky theory in a three dimensional spherical geometry and underpredicts the capture rate by an order of magnitude. In addition, it does not enable to account for variations of the intrinsic reaction rate. The cell model including a source term appears to provide an appropriate expression for the capture rate coefficient ($k$), for it embodies all the variable parameters indicated above and it can be applied to non-stationary conditions as well.

There appears to be a critical value for the influence of $k_{in}^{'}$ (namely $k_{in}^{'} \approx 1$) on $k^{'}$, especially for fractions of the grain boundary surface occupied by traps ($\phi$) below $\sim$50 %, which is of most practical interest. At values for $k_{in}^{'}$ in excess of 1, which is believed to be representative for inert gases, the influence of $k_{in}^{'}$ on the precipitation rate coefficient $k^{'}$ is reduced significantly. This is beneficial given the uncertainty pertaining to this parameter. In addition, it justifies the assumption of an infinite intrinsic reaction rate coefficient for intergranular bubbles in fission gas release models and it could explain the similar behaviour of different species for which $k_{in}^{'} > 1$. Nevertheless, experimental work and/or molecular dynamics calculations are required in order to acquire quantitative information about $k_{in}$.

# Chapter 6

# The role of grain boundary diffusion in fission gas release

**Contents**

## 6.1 Introduction

Grain boundary diffusion is the most commonly observed route for impurity migration in polycrystalline metals [46,83]. In nuclear fuels, the same process is believed to assist transport of oxygen [89], burnable poisons [90], and plutonium [91, 252]. In a similar way, Turnbull and co-workers [92–94] have considered grain boundary diffusion in their analysis of in-pile release of volatile fission products (Te, I) in trace-irradiated $UO_2$ fuels. Olander and co-workers [95, 96, 105] followed the same idea in their post-irradiation analysis of low burnup $UO_2$ samples, as did Akabori et al. [97] for Cs release in $ThO_2$. In both investigations, the grain boundary was considered to be a high-diffusivity pathway for the release of the fission products on the scale of the pellet.

The inert fission gases Xe and Kr present a more confused picture. Out-of-pile annealing experiments with $UO_2$ samples, irradiated until a burnup in the range of $10^{-8}\%$ - $10^{-2}\%$, indicated larger Xe release fractions in fine-grained specimens in comparison with the single-crystal samples [60]. In contrast, in-pile release experiments at 0.1% burnup showed that Xe was more mobile in single-crystal $UO_2$ than in polycrystalline material [144]. This observation was attributed to natural traps for fission gas atoms in the grain boundary; intergranular bubble formation was not reported. On the basis of similar in-pile tests, Turnbull and Friskney [93] excluded Xe from the group of volatile fission products whose release is aided by grain boundary diffusion. They observed no difference in the release-to-birth rate ratio between single-crystal and polycrystalline $UO_2$ specimens. Rather than acting as traps, Turnbull et al. considered this observation to mean that the grain boundaries in $UO_2$ offered the same mobility to fission gases as the lattice of the grains.

Although I know of no experimental evidence that demonstrates enhanced release due to diffusion of Xe in the grain boundaries of $UO_2$, numerous sources have claimed that the grain boundaries are high-diffusivity pathways, even in the absence of interlinked porosity. This belief is - in part at least - due to the pervasive and persistent influence of Booth's model [158,159], in which fission gas release is completely controlled by intragranular diffusion in an "equivalent sphere". The physical entity often associated with Booth's equivalent sphere is the grain. This assignment of the rate-controlling step to intragranular diffusion then requires that the grain boundaries offer no resistance to Xe transport to free surfaces. This picture is often justified by the common observation that fission gas release decreases as grain size increases. While this effect is clearly consistent with the Booth model, it is no proof of the model. For example, the same behavior would occur if intragranular diffusion were rapid and the release process were controlled entirely by diffusion in the grain boundaries (because larger grain size reduces the number of grain boundaries available for solute transport).

An example of the implicit assumption of rapid grain boundary transport can be found in Ref. [253], in which release from the grains is equated to release from the fuel. Another example is the VICTORIA code [254], which treats release from the grains as tantamount to

release to natural internal porosity (not the kind produced by interlinked gas bubbles on grain boundaries). Olander [95] modeled transport in polycrystalline $UO_2$ of solute species with known lattice/grain boundary segregation coefficients and subsequently [96] included grain growth and a distribution of grain sizes. The models were applied to all freely migrating solute atoms confined to grain boundaries. The error in these papers was to overlook the dissimilar behaviour of the different species, in particular, to consider fission gases to represent this class of solute. Guérin et al. [98] claim to have experimental evidence of long-range grain boundary diffusion of fission gas in the U-rich oxide component of MOX fuel. This assertion is based on the lower-than-expected gas content of the central portions of PWR rods, without visible precipitation of intergranular bubbles. Although plausible, this explanation is only a hypothesis, not a mechanistic demonstration. The justification given by Guérin et al. is based on the known higher cation grain boundary diffusion coefficient in mixed oxide compared to $UO_2$. However, this fact cannot be transferred to electrically neutral gas species for the same reason that Te, I, and Cs intergranular mobility is not reflected by Xe.

Most present day models for fission product release in high burnup $UO_2$ disregard grain boundary diffusion entirely [1,7,58,59,71,107,108]. They assume that fission gas atoms arriving at the grain boundaries precipitate into bubbles until interlinkage occurs, entailing the opening of the tunnel network along the grain edges and the venting of the bubbles. Their conjecture is mainly based on the observed incubation behaviour (cf. § 3.3.1), and on the presence of grain boundary bubbles in high burnup fuel [109–113] which seems to be inconsistent with rapid grain boundary diffusion.

In view of the preceding there appears to be a contradiction about the role of the grain boundary with respect to inert fission gas atoms: either it is considered to be a perfect sink where gas atoms are immobile and precipitate to form bubbles (in high burnup fuel), or the grain boundary serves as a high diffusivity pathway for the release of fission products (in trace-irradiated fuel). In both approaches the grain boundary was considered to be a homogeneous phase.

I proposed [255, 256] to reconcile both points of view by accounting for the inhomogeneous characteristics of the grain boundaries in ceramics. Alike Speight [57] for the diffusion with trapping and re-solution of fission products in the grains, I considered grain boundary diffusion along with trapping and irradiation induced re-solution at grain boundary traps. Consequently, grain boundary diffusion should be operative in trace-irradiated fuel while there would be a switch to growth and interlinkage of grain boundary bubbles in controlling intergranular fission gas migration under certain conditions. This idea, however, raises several questions, among which:

1. Is there experimental evidence for grain boundary diffusion to assist the release of inert gas atoms in trace-irradiated fuel, in a similar way as for the volatile fission products Te and I?

2. What are the conditions for the transition from release assisted by grain boundary diffusion to growth and interlinkage of intergranular bubbles in controlling fission gas release?

3. How can I explain the different behaviour of inert gas atoms relative to the other volatile fission products (e.g. Te, I) in grain boundaries of $UO_2$?

In order to answer the first question, Professor Olander and myself [257] have re-analysed data on Xe release in trace-irradiated $UO_2$ obtained by Mansouri and Olander [27,28]. In order to address the second issue, I have assessed the intergranular migration distance [256, 257], that is the distance a gas atom can migrate in a grain boundary containing a specific population of traps before being swallowed up by one of the traps.

The short answer to the third question is that Xe and Kr are neutral and inert, whereas the other volatile species (e.g. I, Te) are ionic [105, 258]. Agglomeration of Xe and Kr into bubbles is not only possible, it is energetically favoured. On the other hand, precipitation of ionic species is restricted (and probably hindered) by electrical neutrality requirements. However, the molecular dynamic calculations needed to quantitatively demonstrate this hypothesis for grain boundaries in ceramic fuels remain to be performed. Despite this lack of quantitative knowledge, I have introduced a variable intrinsic reaction rate coefficient between the intergranular traps and the migrating species (cf. § 5.3). This variable parameter enabled me to assess qualitatively the difference between the different species, thus providing a partial answer to the last question.

## 6.2 The mechanisms of fission gas release prior to bubble interlinkage

Gas release from trace-irradiated specimens and from low-burnup fuel is small but not zero. In typical PWR fuel, fractional Xe releases are ~0.1% at 10 MWd/kgU and rise rapidly at burnups in excess of ~20 MWd/kgU [98]. The accelerated release at high burnup (which also occurs during transients) is believed to be due to intergranular bubble formation and interlinkage. The low-burnup release results from recoil and knockout with a diffusional contribution from the hottest parts of the fuel. However, because of the low gas concentrations, trace-irradiated specimens do not exhibit interlinked porosity, so the usual high-burnup model is inapplicable. Nevertheless, grain boundaries of lightly-irradiated $UO_2$ could also contain traps. The detailed nature of these traps need not be specified; they may consist of segregated impurity clusters, dislocations walls, or structural non-uniformities on the crystal face of the grain.

Analysis of post-irradiation annealing experiments on trace-irradiated $UO_2$ specimens provides an excellent method of determining whether grain boundary diffusion is active in xenon release. Intergranular bubbles have not been reported in trace-irradiated specimens, and these

samples are at a uniform temperature during gas release. A consistent observation in these experiments is the higher apparent diffusivity of Te and I compared to Xe, often by as much as a factor of 100 [28, 93, 105]. These species-dependent differences have been interpreted as a consequence of more effective trapping of Xe in grain boundaries than of the other volatile fission products. These latter species are thereby free to utilize the grain boundaries as fast-diffusion pathways to free surfaces.

To test this notion, Olander and myself [257] have re-examined previously published data on fission-gas release from trace-irradiated, stoichiometric $UO_2$ [28] to ascertain whether they contain any evidence of grain-boundary-assisted release of fission gas. In these experiments, the specimens were disks cut from reactor fuel pellets to thicknesses of 0.9 to 1.5 mm and irradiated to a fractional burnup[a] of $10^{-8}$. This dose is well below the value at which radiation effects on the diffusion coefficient appear. Prior to irradiation and during the subsequent post-irradiation annealing, the specimens were maintained in a $H_2/Ar$ atmosphere that maintained the stoichiometry at exactly 2.00. Five data points were obtained at anneal temperatures ranging from 1400 °C to 1700 °C. Release fractions were obtained by measuring the 81-keV photopeak of $Xe^{133}$ for the released gas collected in liquid-nitrogen-cooled charcoal with a Ge-Li detector and comparing the intensity to that of the same peak in the original disk specimen.

The question is how to analyze these five data points. One approach is to utilize the theory of combined grain-boundary and lattice diffusion developed in Ref. [95] and modified to include trapping of Xe in the grain boundaries. The transport parameters to be fitted to the data in such an approach are the pre-exponential factors and activation energies of the lattice and grain-boundary diffusion coefficients. In addition, the trap concentration ($C_{tr}$) and their areal coverage ($\phi$), introduced in chapter 5 to characterize the intergranular traps, need to be fitted in the model. However, fitting five data points to a model with six parameters cannot produce believable results; the number of unknowns to be fitted to the data needs to be reduced. This can be accomplished by fixing the lattice diffusion coefficient from literature data and fitting the release data with only the two grain-boundary diffusivity parameters and a third parameter obtained by collapsing the two intergranular trap morphology parameters into a single quantity.

Unfortunately, the lattice diffusivity of Xe in $UO_2$ is not well established; Matzke's review [17], for example, presents several data sets covering a spread of a factor of 100 in $D$ at $1400°C$ (from $10^{-14}cm^2/s$ to $10^{-12}cm^2/s$). In addition, many fission gas release/swelling models utilize older lattice diffusivity data obtained by Davies and Long [259], which is even lower ($5 \times 10^{-15}cm^2/s$ at 1400 °C) than those in Matzke's review. By far the lowest value of $D$ was reported by Cornell [135]; at 1400 °C, his value is $3 \times 10^{-16}cm^2/s$. In order to narrow this vast range, the two extreme results are rejected and two intermediate cases are used. The

[a] fraction of initial metal atoms

first, representing "low" values, is the Davies and Long [259] equation:

$$D = 7.6 \times 10^{-6} \exp\left(-293/RT\right), \tag{6.1}$$

where $D$ is in $cm^2/s$, the activation energy in kJ/mole, and R = 8.315 J/mole-K. The "high" value is taken to be the composite based on three sets of data reported in Matzke's paper (called the "Xe low concentration" line in Fig. 8 of Ref. [17]):

$$D = 1.0 \times 10^{-4} \exp\left(-289/RT\right). \tag{6.2}$$

The two equations give $D$ values differing by slightly more than an order of magnitude. Separate analyses of the Xe release data are performed for each of the lattice diffusion formulas.

### 6.2.1 Release by direct lattice diffusion

Prior to embarking on data fitting using the grain-boundary diffusion model, a simpler alternative approach is tried. This approach is based on the following view of the process: even if the grain boundary diffusion coefficient ($D_{gb}$) were zero and the grain boundaries acted as perfect traps for fission gas, there would be some release of fission gas by direct lattice diffusion from the exposed grains at the surfaces of the specimens. For the purpose of this analysis, the following assumptions are made (cf. Fig. 6.1):

1. The surface is perfectly flat (roughness is neglected).
2. Diffusion occurs only in the $UO_2$ lattice in the direction ($y$) normal to the surface. The finite-cylinder geometry of the actual specimen is not treated.
3. The solid is infinite in the $y$ direction.
4. The initial concentration distribution ($c_0$) is uniform in $y$.

These restrictions lead to the familiar error-function concentration distribution:

$$c = c_0 erf\left(\frac{y}{2\sqrt{Dt}}\right). \tag{6.3}$$

The penetration distance of the concentration disturbance is $2\sqrt{Dt}$. For the experiments reported in Ref. [28], the penetration distances using $D$ from Eq.(6.1) range from 0.1 to 1.5 $\mu m$. For $D$ from Eq.(6.2), the corresponding penetration distances are about a factor of three greater. All of these penetration distances are smaller than the grain diameter in the specimens, which was 8 $\mu m$. They are also less than the range of fission fragments ($\mu_{ff}$) in $UO_2$, which is about $7\mu m$.

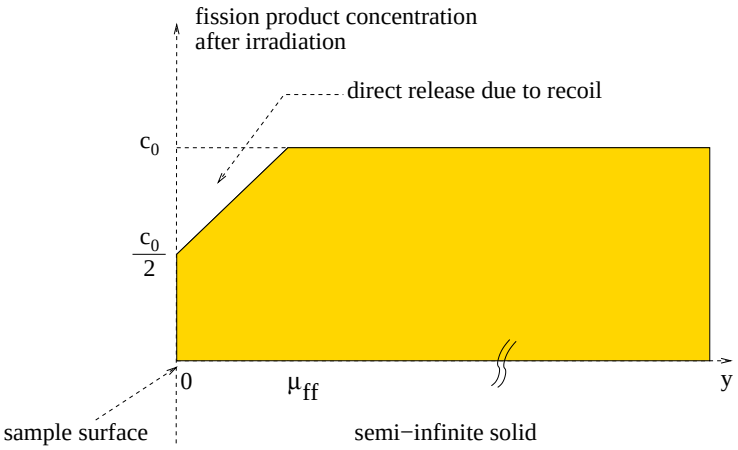


Figure 6.1: Schematic concentration profile in the samples after irradiation

| | | | | Low diffusivity | | High diffusivity | |
|---|---|---|---|---|---|---|---|
| T (°C) | t (h) | H (cm) | $f_{exp}$ (%) | $D$ (cm$^2$/s) | $f_{dir}/f_{exp}$ | $D$ (cm$^2$/s) | $f_{dir}/f_{exp}$ |
| 1400 | 5 | 0.076 | 0.16 | $5.4 \times 10^{-15}$ | 0.05 | $1.0 \times 10^{-13}$ | 0.20 |
| 1450 | 5 | 0.071 | 0.20 | $1.0 \times 10^{-14}$ | 0.05 | $1.8 \times 10^{-13}$ | 0.24 |
| 1500 | 5 | 0.053 | 0.81 | $1.8 \times 10^{-14}$ | 0.02 | $3.2 \times 10^{-13}$ | 0.11 |
| 1600 | 10 | 0.044 | 1.80 | $5.1 \times 10^{-14}$ | 0.03 | $9.0 \times 10^{-13}$ | 0.16 |
| 1700 | 10 | 0.072 | 4.00 | $1.3 \times 10^{-13}$ | 0.01 | $2.3 \times 10^{-12}$ | 0.08 |

Table 6.1: Comparison of experimental post-irradiation Xe release fractions [28] with simple volume diffusion theory.

Integrating Eq.(6.3) over the half-thickness $H$ of the disk and dividing by the initial charge $(c_0 H)$ yields the fractional release

$$f_{dir} = \frac{2}{\sqrt{\pi}} \sqrt{\frac{Dt}{H^2}}. \tag{6.4}$$

The short penetration distances calculated above invalidates the fourth restriction used to obtain Eqs.(6.3) and (6.4). Direct recoil escape from depths up to the fission fragment range $(\mu_{ff})$ changes the initial condition for the diffusion problem to [6] (cf. Fig. 6.1)

$$c = \begin{cases} \frac{c_0}{2}\left(1 + \frac{y}{\mu_{ff}}\right) & 0 \le y \le \mu_{ff} \\ c_0 & y > \mu_{ff} \end{cases} \tag{6.5}$$

Numerical solution of the diffusion equation using Eq. (6.5) as the initial condition gives fractional releases that are about a factor of two smaller than those predicted from Eq. (6.4). If direct lattice diffusion from surface grains is the dominant mechanism, the computed fractional releases, $f_{dir}$, should be the same as the measured fractional releases, $f_{exp}$. The first

four columns of Table 6.1 give the experimental conditions and release fractions of the post-irradiation anneals. The next two columns give, respectively, the diffusion coefficient from Eq.(6.1) and the ratio $f_{dir}/f_{exp}$. The last two columns give the analogous information based on the diffusion coefficient of Eq.(6.2).

In all cases, the values of $f_{dir}/f_{exp}$ are less than unity by factors ranging from 4 to 100. The first restriction listed earlier was related to the surface roughness and the corresponding surface-to-volume ratio. $UO_2$ is a sintered material with a $S/V$ value greater than the geometrical value. A larger surface over which $Xe^{133}$ was released would yield higher release fractions. However, this cannot explain all of the discrepancy. The second restriction cannot account for it either. Accordingly, it is concluded that some other process, in particular grain boundary diffusion, enhanced the Xe release process in the experiments reported in Ref. [28].

### 6.2.2 Release by lattice and grain boundary diffusion with intergranular trapping

In order to rationalize the experimental fractional releases in Table 6.1, a model involving grain boundary diffusion coupled with grain boundary trapping and lattice diffusion is developed. The grain boundaries provide pathways for escape to the free surface of Xe released from grains in the interior of the specimen. Migration is hindered by permanent capture of Xe by intergranular traps discussed in section 6.2. Grain boundary sweeping is not considered because no grain growth was observed in the experiments utilizing stoichiometric $UO_2$ [28].

The grains are assumed to be spheres of radius $R_{gr}$. During high-temperature annealing, Xe diffuses from the grain interior to the grain boundary. The grain boundaries are black sinks for Xe, which means that the Xe concentration in the solid immediately adjacent to the grain boundary is zero. In the short-time limit, the flux of Xe to the grain boundary from inside the grain is given by[b] [4]

$$J_g = \frac{Dc_0}{R_{gr}} \left( \frac{1}{\sqrt{\pi\tau}} - 1 \right), \tag{6.6}$$

where $c_0$ is the initial concentration of Xe in the grains and the dimensionless time is defined by

$$\tau \equiv \frac{Dt}{R_{gr}^2}. \tag{6.7}$$

The specimen is a disk with diameter $d_{disk} = 8.7$ mm, and surface-to-volume ratio $\frac{S}{V} = \frac{d_{disk}+4H}{Hd_{disk}}$ (which was approximated by the reciprocal of the half-thickness in § 6.2.1). All surfaces, however, are assumed to face solid of infinite depth, which is only valid when $\tau \ll 1$.

The polycrystalline medium is characterized geometrically by the total length of grain-

[b] Eq.(6.6) is valid for $\tau < 0.15$. This limit is applicable to most of the data analysed. For a few points were $\tau > 0.15$, the expression in parentheses in Eq.(6.6) is replaced by $2e^{-\pi^2\tau}$.

boundary trace exposed in a unit area of a random section through the solid, $\lambda$, and by the total surface area of the separated grains per unit volume of solid, $\sigma$ (the grain surface area in the intact solid is $\sigma/2$). For any grain shape, it can be shown that $\sigma/\lambda = 8/\pi$. For spherical grains, $\sigma = 3/R_{gr}$.

Transport of Xe in the grain boundary is governed by the grain boundary diffusivity $D_{gb}$. In addition, the grain boundaries contain a population of traps that permanently immobilize any Xe that reaches them, either by direct lattice diffusion from the grain or by diffusion in the boundary. As in § 5.2, the traps are assumed to be circular and to occupy a fraction of $\phi$ of the grain boundary area. The areal number density of the traps is $C_{tr}$.

The rate of removal of mobile Xe from the grain boundary by the traps can be given by the same formula that describes the sink effect of dislocations in a three-dimensional solid, since it constitutes a similar diffusion problem in cylindrical geometry. The corresponding formula reads [68]:

$$J_{trap} = \frac{2\pi}{\ln(1/\phi)} D_{gb} c_{gb} \quad \left[\frac{removed\,atoms}{s \cdot trap}\right], \tag{6.8}$$

where $c_{gb}$ is the local areal concentration of mobile Xe in the grain boundary. It does not include the Xe removed by the grain boundary traps. The traps are assumed to be black in the sense that the mobile Xe concentration immediately adjacent to the trap is zero.

Adding trapping to the method outlined in Ref. [95], the conservation equation for mobile Xe in the grain boundaries is given by:

$$\frac{\sigma}{2}\frac{\partial c_{gb}}{\partial t} = \lambda D_{gb}\frac{\partial^2 c_{gb}}{\partial y^2} + \sigma(1-\phi) J_g - \frac{\sigma}{2} C_{tr} J_{trap}, \tag{6.9}$$

where the distance $y$ is measured normal to the solid surface. In addition to Eq.(6.7), the following dimensionless quantities are defined:

$$X \equiv y/R_{gr} \tag{6.10}$$

$$U \equiv \frac{\pi}{8}\frac{D_{gb}}{D}\frac{c_{gb}}{R_{gr} c_0} \tag{6.11}$$

$$\kappa \equiv \frac{\pi}{4}\frac{D_{gb}}{D} \tag{6.12}$$

$$G \equiv \frac{8 C_{tr} R_{gr}^2}{\ln\left(1/\sqrt{\phi}\right)} \tag{6.13}$$

Since intergranular bubbles have not been observed in trace-irradiated samples, it is reasonable to assume that $\phi \ll 1$. Neglecting $\phi$ compared to unity in the grain source term, Eq.(6.9) becomes

$$\frac{1}{\kappa}\frac{\partial U}{\partial \tau} = \frac{\partial^2 U}{\partial X^2} + \left(\frac{1}{\sqrt{\pi\tau}} - 1\right) - G\,U. \tag{6.14}$$

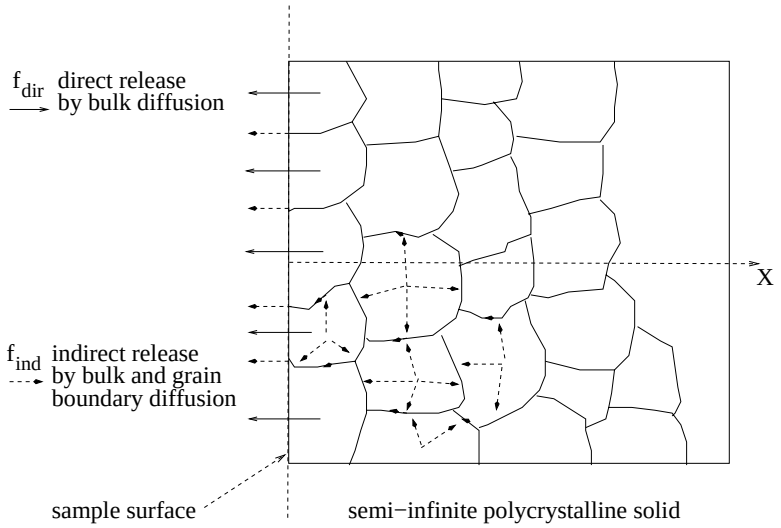


Figure 6.2: Schematic representation of the direct ($f_{dir}$) and indirect ($f_{ind}$) release mechanisms during the post-irradiation annealing experiments with trace-irradiated samples

The initial condition is

$$U = 0 \quad at \quad \tau = 0, \forall X, \tag{6.15}$$

which assumes that all Xe is in the grains prior to the high-temperature anneal. The boundary conditions are:

$$\begin{aligned} U &= 0 \quad at \quad X = 0 \\ \partial U/\partial X &= 0 \quad at \quad X \to \infty \end{aligned} \tag{6.16}$$

As in the direct diffusion analysis, the surface roughness is disregarded. In addition, the above formulation neglects effects such as direct release from the surface grains by lattice diffusion and the depletion of the surface region by recoil escape during irradiation (cf. Fig. 6.1). However, the action of grain boundary diffusion should allow release from greater depths than purely lattice diffusion from the surface grains. Indeed, fission gas atoms reaching a grain face in the middle of the sample may reach the free surface via the grain boundaries as illustrated in Fig. 6.2. Accordingly, the details at the surface are less critical to the analysis than in the direct lattice diffusion calculation.

Equations (6.14) - (6.16) are solved for $(\partial U/\partial X)_{X=0}$ and the fractional release ($f_{ind}$) calculated from this solution by integrating the flux leaving the grain boundaries at the surface over time. The total quantity of Xe released from the specimen of surface area S is

$$Xe\ released = \lambda D_{gb} S \int_0^\tau \left(\frac{\partial c_{gb}}{\partial y}\right)_{y=0} dt'. \tag{6.17}$$

The total Xe initially in the specimen is $Vc_0$, where $V$ is the specimen volume. Divid-

ing these two quantities and converting to dimensionless variables gives the fraction released according to the indirect route (lattice diffusion followed by grain boundary diffusion):

$$f_{ind} = 3\left(\frac{R_{gr}S}{V}\right)\int_0^{\tau}\left(\frac{\partial U}{\partial X}\right)_{X=0} d\tau'. \tag{6.18}$$

The following analytical solution for the surface gradient is developed in the Appendix C:

$$\left(\frac{\partial U}{\partial X}\right)_{X=0} = \sqrt{\kappa}\exp\left(-\frac{1}{2}G\kappa\tau\right) I_0\left(\frac{1}{2}G\kappa\tau\right) - \frac{erf\left(\sqrt{G\kappa\tau}\right)}{\sqrt{G}}, \tag{6.19}$$

where $I_0$ is the modified Bessel function of the first kind of order zero. This solution is restricted to $\tau < 0.15$ because of the short-time approximation for the Xe flux to the grain boundary from the grains as expressed by Eq. (6.6). For larger $\tau$ values, Eqs. (6.14) - (6.16) are solved numerically.

In the absence of trapping ($G = 0$), Eq. (6.19) is sufficiently simplified that the integral in Eq. (6.18) can be performed analytically. The resulting theoretical fractional release is

$$f_{ind} = 3\left(\frac{R_{gr}S}{V}\right)\sqrt{\kappa}\left(\tau - \frac{4}{3\sqrt{\pi}}\tau^{3/2}\right). \tag{6.20}$$

The interesting feature of this result is the absence of the $\sqrt{\tau}$-time dependence usually associated with diffusional processes (e.g. Eq. (6.4) for the direct release mechanism). This can be attributed to the series coupling of bulk and grain boundary diffusion.

The above indirect release model was fitted to the data given in the first four columns of Table 6.1. Separate data fitting was performed for the "low" and "high" lattice diffusivities of Eqs. (6.1) and (6.2). Two of the fitting parameters are the pre-exponential factor and the activation energy of the $\kappa$ parameter defined by Eq. (6.12) and expressed as

$$\kappa = \kappa_0 e^{T_\kappa/T}. \tag{6.21}$$

The form of this equation assumes that the activation energy of $D_{gb}$ is lower than that of $D$ [83]. The quantity $T_\kappa$ is the activation energy of the ratio $D_{gb}/D$ divided by the universal gas constant.

The third fitting parameter is the quantity $G$ defined by Eq. (6.13). This parameter was assumed to be the same at all temperatures and to remain constant during the time at temperature. That is, the microstructure of the intergranular traps was not permitted to anneal during the release process.

Experience in the fitting process showed that instead of $\kappa_0$, error minimization was much more sensitive to the value of $\kappa$ at a temperature in the middle of the experimental range

| $G$ | min. error | $\log \kappa\,(1773)$ | $T_\kappa$(K) |
|---|---|---|---|
| 0.00 | 0.23 | 3.80±0.01 | 28000±500 |
| 0.01 | 0.24 | 3.84±0.02 | 23000±1300 |
| 0.02 | 0.24 | 3.92±0.01 | 22000±700 |
| 0.10 | 0.36 | 4.14±0.04 | 500 - 30000 |

Table 6.2: Results of fitting Xe release data to the indirect model using the "low" lattice diffusivity formula (Eq.(6.1)).

(1773 K). Thus, the actual fitting parameters were $G$, $T_\kappa$, and

$$\log \kappa\,(1773) = \log \kappa_0 + \frac{T_\kappa}{(2.3)\,(1773)}. \tag{6.22}$$

Fitting of the data proceeded in the following fashion:

- Select a lattice diffusivity ("low" or "high").
- Fix the parameter $G$, starting at $G = 0$.
- Vary $\log \kappa\,(1773)$ and $T_\kappa$ until the error measure or objective function defined in Eq. (6.23) is a minimum.
- Increase the parameter $G$ and repeat error minimization.

$$error = \frac{1}{5}\sum_{1}^{5}\left|\frac{f_{ind} - f_{exp}}{f_{exp}}\right| \tag{6.23}$$

The above process is terminated when the minimum error starts to increase above the low-$G$ limiting value.

Table 6.2 shows the results of fitting the data to the indirect release model with the "low" lattice diffusion coefficient.

Equally satisfactory agreement of the model and the data (i.e. the same minimum error) was achieved for all values of the grain boundary trap parameter $G \leq 0.1$. The minimum error increases rapidly for larger $G$ values.

Similar results have been obtained by means of the general Levenberg-Marquardt method (implemented in the software PEST [260]), or when applying the absolute difference between theory and data as the objective function. Both approaches gave results with a better fit to the large release fraction experiments than obtained with the error based on the fractional difference as in Eq. (6.23), in contrast with the fit for the low temperature data points. Nevertheless, the results indicated that the experimental data do not support a two-step diffusional model that is accompanied by strong intergranular trapping of Xe. By way of comparison, Eq. (6.13) shows that the values for the least efficient trap microstructure in

| $G$ | min. error | $\log \kappa\,(1773)$ | $T_\kappa$ (K) |
|---|---|---|---|
| 0.00 | 0.26 | 1.42±0.03 | 2440±580 |
| 0.01 | 0.27 | 1.45±0.04 | 1350±340 |
| 0.02 | 0.27 | 1.43±0.03 | 1620±470 |
| 0.10 | 0.28 | 1.44±0.03 | 1770±430 |
| 0.20 | 0.28 | 1.58±0.05 | 1620±450 |
| 0.50 | 0.35 | 1.74±0.04 | 1730±450 |
| 1.50 | 0.43 | 2.02±0.13 | 800 - 15000 |
| 5.00 | 0.62 | 2.36±0.07 | 800 - 15000 |

Table 6.3: Results of fitting Xe release data to the indirect model using the "high" lattice diffusivity formula (Eq.(6.2)).

§ 6.3.4 (i.e. $C_{tr} = 0.1\ \mu m^{-2}$, $\phi = 0.01$) has a trapping parameter $G = 5.6$. The data from Ref. [28] are consistent with gas release by sequential lattice and grain boundary diffusion unimpeded by trapping at natural intergranular defects.

The last two columns in Table 6.2 give the grain boundary diffusivity parameters associated with the best fit of the data. As suggested by the small errors, the minimum error is well defined in the coordinate represented by $\log \kappa\,(1773)$; the average value of this parameter in the range $0 < G < 0.1$ is 3.85±0.01. This gives a reasonable reliable value of $D_{gb} = 1.6 \times 10^{-10}\mathrm{cm}^2/\mathrm{s}$ at 1773 K.

The activation energy of $\kappa$ is contained in the last column of Table 6.2. The uncertainty in $T_\kappa$ is even greater than implied by the errors associated with this parameter at a fixed $G$. The error measure of Eq.(6.23) can be thought of as a surface dependent on the two $\kappa$ fitting parameters. The minimum error on such a surface lies along a trough with the walls rising sharply in the $\log \kappa\,(1773)$ direction but running like a canyon floor in the $T_\kappa$ direction. For example, error measures just 0.02 greater than the minimum values shown in the table are obtained over a range $1000 < T_\kappa < 30000$. With this caveat, accepting the average value of 24000 K from the first three rows of Table 6.2 yields a grain boundary diffusivity of

$$D_{gb}^{(low\ D)} = 9 \times 10^{-8} \exp\left(-92/RT\right) \quad cm^2/s. \tag{6.24}$$

The accuracy of this equation is high at T = 1773 K but Eq.(6.24) is much less reliable at other temperatures.

If the "high" lattice diffusivity (Eq.(6.2)) is used in fitting the data to the indirect release model, Table 6.3 shows that a constant minimum error is achieved for all $G \leq 0.5$. In this range of $G$, the error measure is quite sensitive to the $\log \kappa\,(1773)$ parameter but quite insensitive to the activation energy parameter $T_\kappa$. The grain boundary diffusivity deduced from the value of $\log \kappa\,(1773) = 1.43$ at the minimum error is $D_{gb} = 1.1 \times 10^{-11}\mathrm{cm}^2/\mathrm{s}$ at 1773 K, which is a factor of 15 smaller than the corresponding value obtained using the "low" lattice diffusivity

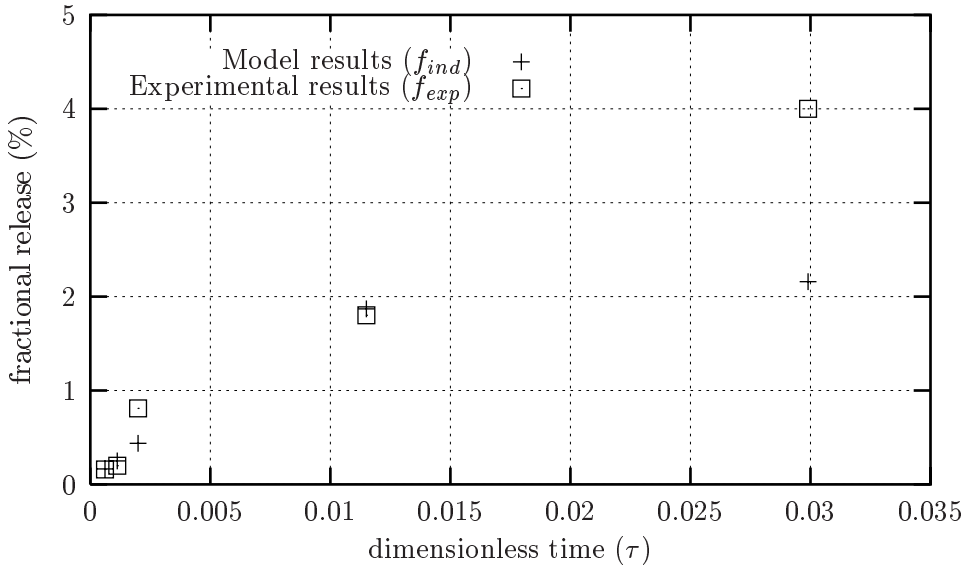


Figure 6.3: Comparison of indirect model results ($G = 0$, $\log \kappa\,(1773) = 3.80$, $T_\kappa = 27500$ K) with experimental data using Eq. (6.1) for $D$.

in the data analysis.

Taking the average of the entries in the last column of Table 6.3 ($T_\kappa \sim 1800$ K), the temperature dependence of the Xe grain boundary diffusivity is obtained as:

$$D_{gb}^{(high\ D)} = 1.3 \times 10^{-3} \exp\left(-272/RT\right) \quad cm^2/s \tag{6.25}$$

As in the "low" lattice diffusivity analysis, the temperature dependence implied by this result is much less reliable than the value of $D_{gb}$ at 1773 K. The significant difference between the $D_{gb}$ formulas deduced from the data is entirely due to the order-of-magnitude discrepancy in $D$ from Eqs. (6.1) and (6.2).

Figures 6.3 and 6.4 compare the Xe release data with the minimum-error indirect model predictions for the two lattice diffusivities employed in the fitting process. The theoretical points neglect intergranular trapping, although essentially the same results are obtained for any $G$ less than the values in Table 6.2 and Table 6.3 where the minimum error begins to rise. The quality of the agreement between theory and experiment (as gauged by Eq. (6.23)) is roughly the same for the "low" and "high" lattice diffusion coefficient formulas. For either $D$, the indirect model cannot reproduce the experiment release fractions at the longest dimensionless time ($\tau$). The predicted increase in $f_{ind}$ between the last two $\tau$ values is small because the difference in the thickness of the specimens counteracts the effect of temperature on the diffusion coefficient. I suspect that the last experimental points give too large a fractional release.

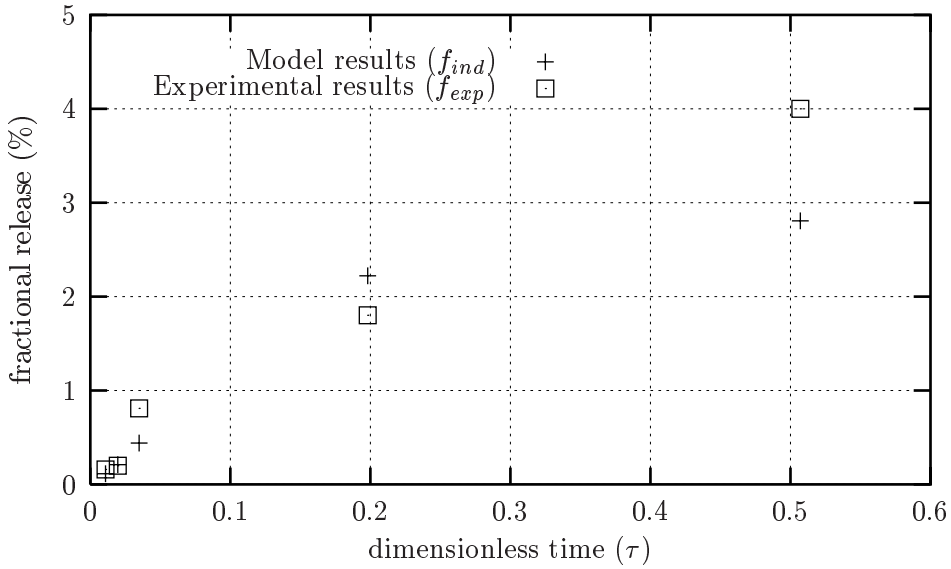


Figure 6.4: Comparison of indirect model results ($G = 0$, $\log \kappa\,(1773) = 1.41$, $T_\kappa = 1030$ K) with experimental data using Eq. (6.2) for $D$.

## 6.3 The intergranular migration distance

In the present analysis, I rely on the assumptions mentioned in section 5.2.

### 6.3.1 Approach

The second question listed at the end of § 6.1 deals with the conditions for the transition from release assisted by grain boundary diffusion to growth and interlinkage of intergranular bubbles in controlling fission gas release. In order to answer this question, I have compared the intergranular migration distance, $L$, to the distance separating the traps, $R_s$. The latter is related to the areal number density of intergranular traps, $C_{tr}$, by Eq.(5.14). $L$ is the crow-flight distance[c] from the point where the gas atom enters the grain boundary to the point where it is absorbed by an intergranular trap, and will be assessed by two methods in the following section. If $L/R_s$ is large, a migrating gas atom wanders past many intergranular traps before being swallowed up. In this case, the gas atom stands a good chance of being released to open porosity or cracks. On the other hand, if $L/R_s < 1$, there is a high probability that the gas atom will be trapped before reaching an escape surface.

Aside from the geometric features given above ($\phi$ and $C_{tr}$), the only relevant physical property of the trap is its capture efficiency for particular types of solutes migrating as single atoms in the boundary. This efficiency is reflected in the intrinsic rate coefficient (cf. $k_{in}^{'}$ defined

[c]The "crow-flight distance" is the shortest distance, that is along a straight line, from the point where the fission product enters the grain face to the point where it is ultimately absorbed by an intergranular trap.

in § 5.3), which provides a clue to the third question posed in section 6.1. A highly efficient trap ($k'_{in} \to \infty$) absorbs all solute reaching its periphery, and so reduces the concentration of the solute to zero at this location. This Smoluchowsky boundary condition is most commonly used in fission gas analysis in reactor fuel [1, 71, 181]. If the trap is less efficient in capturing arriving solute atoms, the concentration of the latter at the trap surface is greater than zero. This radiation boundary condition better reflects the behaviour of the other volatile fission products, as discussed below.

### 6.3.2 Regular array of traps

In this section, I consider circular traps to be arranged on a regular square array (cf. Fig. 3.2). The method applied for the computation of the intergranular migration distance in this array of traps is similar to that adopted for assessing the thermal diffusion length of neutrons in an absorbing medium [261]. Consider a point source at the origin of an infinite planar medium emitting a fission product per second. The atom will diffuse about in the grain face, moving in complicated paths until it is eventually absorbed. None can escape since the medium is infinite. The probability distribution function $p_t(R)$, that is the probability of finding the atom in a surface element $2\pi RdR$ at a distance $R$ from the origin after a time $t$, corresponds to the Green's function [262]

$$p_t(R) = \frac{e^{-\frac{R^2}{4D_{gb}t}}}{4\pi D_{gb}t}. \tag{6.26}$$

Accordingly, the mean square displacement can be written as

$$\overline{R^2} = \oint R^2 p_t(R)\, dS = 2\pi \int_0^\infty p_t(R)\, R^3 dR \tag{6.27}$$

Taking into account that [263]

$$\int_0^\infty t^{2n+1} e^{-at^2} dt = \frac{n!}{2a^{n+1}}, \tag{6.28}$$

the mean square displacement in a grain boundary free of traps may be written as

$$\overline{R^2} = 4D_{gb}t = L^2. \tag{6.29}$$

In the presence of traps, the actual diffusion length in the grain boundary will be reduced.

In order to calculate $L$ in a field of traps by means of Eq.(6.29), I need to assess the lifetime ($\tau$), that is the elapsed time between arrival of an atom from the grain and its capture by a grain boundary trap. This corresponds to the thermal diffusion time of neutrons [261]. Given the symmetry of the trap array, I assess the lifetime by solving the transient diffusion problem in the annular unit cell $R_{tr} \leq R \leq R_s$ (cf. Fig. 5.2). The concentration profile of the fission

products in the unit cell with a partially reflective boundary condition on the trap surface can be expressed as follows (cf. Appendix B.4):

$$C_{gbv}(R,t) = C_{\infty}(R) - \sum_{n=0}^{\infty} \Omega_n(R)\, e^{-\frac{t}{\tau_n}}, \tag{6.30}$$

where $C_{\infty}(R)$ represents the stationary concentration profile, and the time constants $\tau_n$ are given by

$$\tau_n = \frac{1}{D_{gb}\lambda_n^2}, \tag{6.31}$$

where $\lambda_n$ are the positive roots of Eq. (5.19). The time constants $\tau_n$ are identical to those obtained in the expression for the concentration profile of the cell model without a source term and non-zero initial concentration (cf. § 5.4.3). The longest time constant ($\tau_0$) can thus be interpreted as the characteristic time after which the concentration decreased by a factor $e$ in the event of the cell model without source term. Therefore, the lifetime of a fission product in the grain boundary ($\tau$) is approximated by the largest time constant $\tau_0$ defined in (6.31). This is in accordance with the approach of Ham [233], who analysed stress-assisted precipitation of point defects on dislocation lines. The resulting expression for the intergranular diffusion length reads:

$$L \simeq \sqrt{4 D_{gb}\tau_0} = \frac{2}{\lambda_0}. \tag{6.32}$$

In the following, I will also make use of a dimensionless intergranular diffusion length, $l = L/R_s$, which provides an estimation of half the number of unit cells a fission product can migrate in the grain boundary before being absorbed by a trap.

In order to verify the range of validity of my approximation, I have computed the second smallest root ($\lambda_1$) of Eq.(5.19) under SBC, in addition to $\lambda_0$. The ratio $\Lambda = \lambda_1/\lambda_0$ is shown in Fig. 6.5 and confirms that our approximation $\tau \simeq \tau_0$ is most appropriate for small values of $\phi$. According to the same plot, $\Lambda$ is always larger than 3 for $1\ \% \leq \phi \leq 99\ \%$, hence the maximum contribution of $\tau_1$ to the total time span $\tau$ is at maximum 10 % in view of the definition of $\tau_n$ in Eq. (6.31).

### 6.3.3 Random array of traps

Professor Olander [264] proposed a method to alleviate the main non-conservative assumption in the previous section by considering identical circular traps randomly placed on the grain boundary. The grain face is represented by a two dimensional plane with a square lattice of sites on which atoms jump in a random walk. The distance between sites, or the jump distance, is $a_0$.

From random walk theory, the straight-line distance travelled by a particle in this number of

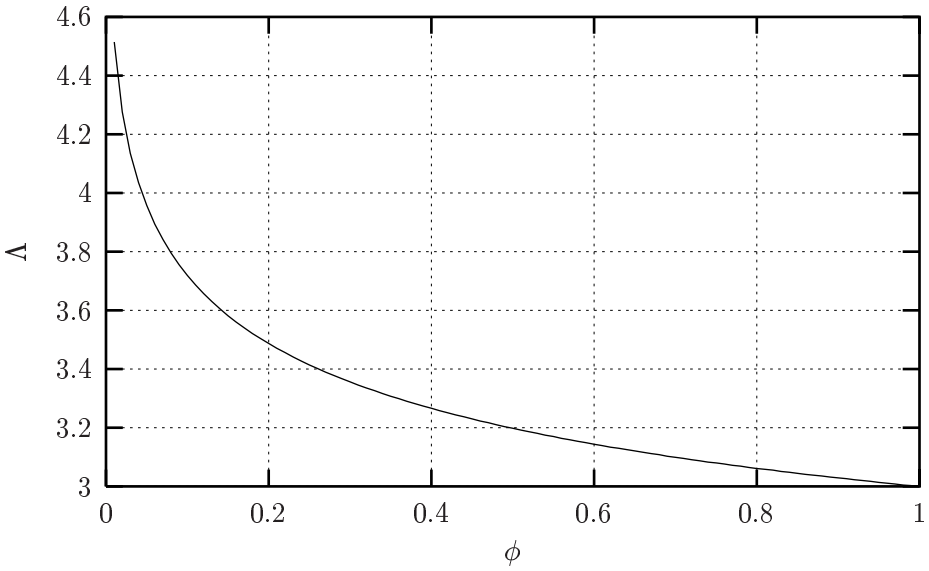


Figure 6.5: Ratio of the first two eigenvalues of the diffusion equation in the cell-model ($\Lambda = \lambda_1/\lambda_0$) as a function of the bubble surface fraction ($\phi$) under Smoluchowsky boundary conditions

jumps is [46]:

$$\overline{L^2} = \overline{j} a_0^2 \tag{6.33}$$

where $\overline{j}$ represents the average number of jumps that an atom makes before absorption by a trap occurs, which is assessed by means of jump probability methods (cf. Appendix D). Inserting the expression for $\overline{j}$ in Eq. (6.33), and dividing by $R_s$ of Eq. (5.14) yields the dimensionless migration distance $l$:

$$l = \sqrt{\frac{\left\{k'_{in} ln\phi \left[1 - \phi\left(1 - 2\frac{a_0}{R_{tr}}\right)\right] - 2\left(1-\phi\right)\right\}\left(k'_{in} ln\phi - 2\right)}{\left(k'_{in} ln\phi\right)^2}} \cdot \sqrt{\left[1 - \phi\left(1 - 2\frac{a_0}{R_{tr}}\right)\right]\frac{(1-\phi)}{4\phi}} \tag{6.34}$$

The equation for $l$ reduces to

$$l = \left[1 - \phi\left(1 - 2\frac{a_0}{R_{tr}}\right)\right]\sqrt{\frac{(1-\phi)}{4\phi}} \tag{6.35}$$

when $k'_{in} \to \infty$, that is, under the Smoluchowsky boundary condition. Compared to the analogous results for the diffusion analysis in § 6.3.2, Eqs. (6.34) and (6.35) contain the additional parameter $a_0/R_{tr}$. However, as will be shown later, this quantity is much smaller

than unity and hence may be neglected.

### 6.3.4 Results and discussion

#### 6.3.4.1 The migration distance in the case of perfectly absorbing traps

From expressions (5.19), (6.32) and (6.35) it follows that for perfectly absorbing grain boundary traps, that is when $k'_{in} \rightarrow \infty$ , the intergranular migration length for fission products is a function only of the trap concentration $C_{tr}$ (which fixes $R_s$ by Eq. (5.14)) and their surface fraction ($\phi$):

$$L = \frac{l(\phi)}{\sqrt{\pi C_{tr}}} \tag{6.36}$$

In addition, $L$ is independent of the intergranular diffusion coefficient. (This feature is beneficial, given the uncertainty in this property). The dimensionless diffusion length ($l$), on the other hand, can be expressed as a function of a single parameter, namely the fraction of the grain boundary surface occupied by the traps ($\phi$). According to Eq. (6.35), the relative distance travelled by an atom in a random array of perfect traps is dependent on $\phi$, and on the ratio of the atomic lattice parameter of the grain boundary to the trap radius ($a_0/R_{tr}$). However, the influence of $a_0/R_{tr}$ on $l$ can be neglected when $a_0$ ranges between 0.06 $nm$ and 6 $nm$, $C_{tr}$ ranges between 0.1 $\mu m^{-2}$ and 10 $\mu m^{-2}$, while $\phi$ ranges between 1 % and 99 %.

The variation of $l$ with $\phi$ is depicted in Fig. 6.6 ; I have plotted the relative distance travelled by an atom in a random array for a lattice parameter on the grain boundary of $a_0 = 0.6\,nm$, which is somewhat less than twice the lattice constant in crystalline $UO_2$, and a trap density of $C_{tr} = 0.1\,\mu m^{-2}$. The trap surface fraction ranges from 1 % to 99 % which covers a wide range of experimental values (in practice $\phi$ will be limited to the order of 50 %).

Fig. 6.6 reveals that in a regular array of traps, the fission products can migrate at maximum a single cell diameter once the grain boundary surface is covered by 1% of perfectly absorbing sinks. However, the fact that $L$ is limited to the cell diameter when the traps are regularly distributed is not inherent to the cell model. The zero particle flux at the cell surface is equivalent to the assumption that the walls of the cell surrounding each trap are impenetrable, but these boundary conditions arise only from the assumed symmetry of the concentration profile $C_{gb}(R)$ and not from a real impenetrability. This is confirmed by the results with partially reflective boundary conditions on the trap surfaces (cf. § 6.3.4.2).

The intergranular migration distance of a fission product ($L$) can be inferred from Fig. 6.6 and Eq. (6.36). The trap density ranges between 10 $\mu m^{-2}$ and 0.1 $\mu m^{-2}$, corresponding to bubble densities observed on fractographs of $UO_2$ [147, 184, 265]. When there is only 0.1 perfect trap/$\mu m^2$ and the fraction of the grain face covered by traps is 1 %, the maximum distance a solute atom can diffuse in the grain boundary with a regular array of sinks is in the order of $\sim 3.2\,\mu m$. For higher values of either $C_{tr}$ or $\phi$, the intergranular diffusion distance will drop below 1 $\mu m$. As indicated in § 6.3.2, $L$ represents an overestimation due to the

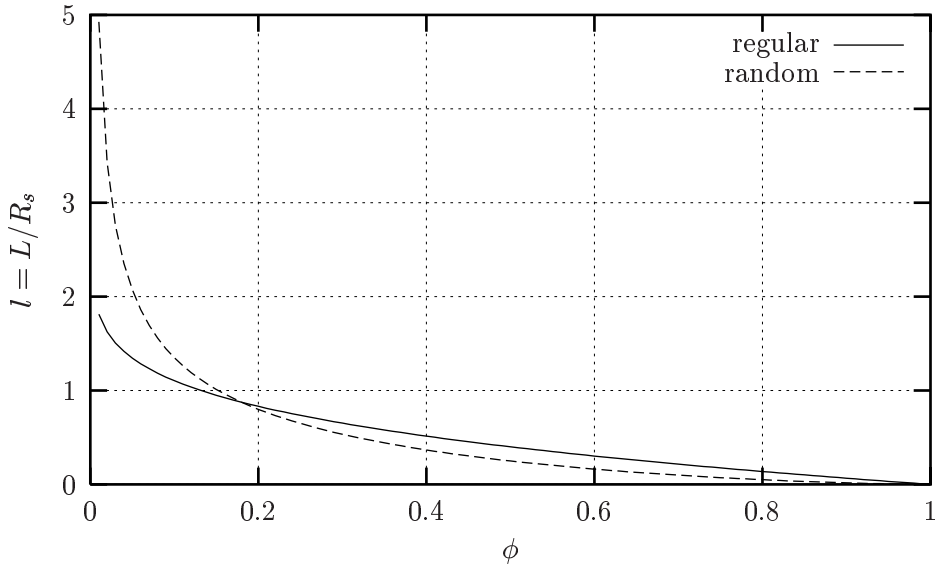


Figure 6.6: Dimensionless intergranular diffusion length ($l$) in a regular and in a random distribution of sinks as a function of the bubble surface fraction ($\phi$) under Smoluchowsky boundary conditions

application of the expression for the diffusion length in an infinite planar medium *without* traps to the grain boundary *with* traps. The overestimation is even more pronounced by the fact that I have considered a constant trap radius in the course of precipitation, whereas e.g. bubble growth is expected to reduce the lifetime of the migrating atoms.

When the grain boundary is covered by 1 % of perfect traps distributed randomly, the maximum distance a fission product can migrate is about 8.8 $\mu m$. However, even if $L$ is as large as the grain size, there is no open porosity surrounding each grain when the fraction of the grain face covered by traps amounts to 1 %. As a result, the majority of the gas atoms diffusing in the grain boundary will not reach the open porosity and be released under these circumstances. They are more likely to be trapped by one of the traps to which they are originally closest. Therefore, I conclude that the contribution of the grain boundary diffusion to the overall release process of fission gas atoms on the pellet scale is strongly inhibited for values of $C_{tr}$ and $\phi$ observed for gas bubbles in fractography of irradiated fuel.

#### 6.3.4.2 The migration distance in the case of inefficient traps

In the event of partially reflecting or radiation boundary conditions at regularly arranged traps, the intergranular migration distance is a function of three parameters: $L\left(C_{tr}, \phi, k_{in}^{'}\right)$. The sensitivity of $l$ to $k_{in}^{'}$ is depicted in Figs. 6.7 and 6.8 for three different values of $\phi$. The range of $k_{in}^{'}$ from $10^{-3}$ to $10^{+3}$ suffices to assess the sensitivity of the migration distance to this parameter. Indeed, for $k_{in}^{'} = 10^{+3}$, the relative migration distance almost converged to

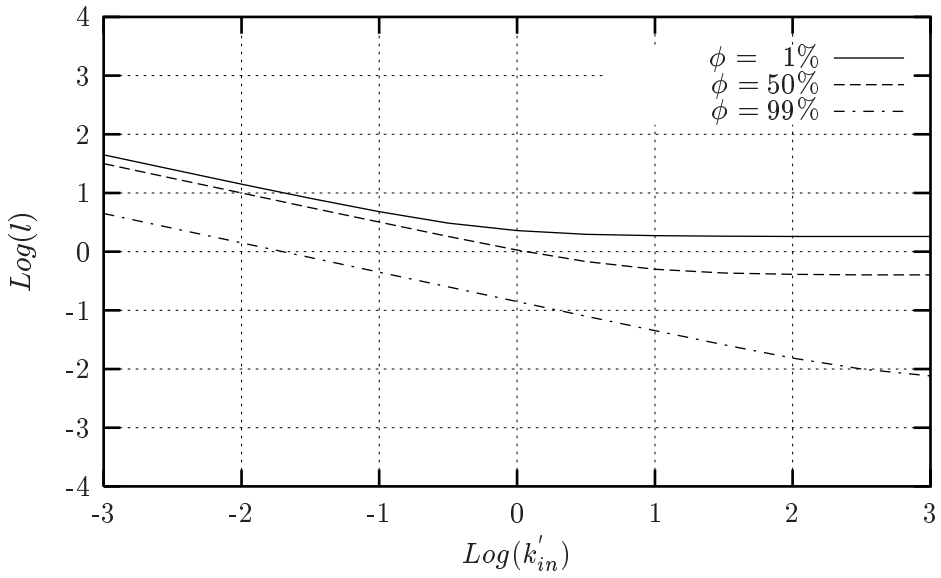


Figure 6.7: Dimensionless intergranular diffusion length ($l$) in a regular array of sinks as a function of the dimensionless intrinsic reaction rate constant ($k'_{in}$) for three different values of the grain boundary bubble surface fraction ($\phi$)

the limiting case of the Smoluchowsky boundary condition ($k'_{in} \to \infty$) in Fig. 6.6.

In general, the greater the capture efficiency of the trap, the shorter the distance that a solute atom can move before being removed by trapping and the greater is the impediment to release. However, from Figs. 6.7 and 6.8, there appears to be a critical value for the influence of $k'_{in}$ (namely $k'_{in} \simeq 1$), especially for values of $\phi \leq 50\%$ which is of most practical interest. When $k'_{in} \leq 1$, the influence of $k'_{in}$ on the diffusion length is more pronounced. For $k'_{in} > 1$, the relative change of the intergranular migration distance is not very dependent on the relative change of the trap efficiency, except when $\phi \geq 50$ % which is rarely encountered in practice. In the case of a regular array of traps, this feature is not surprising; it simply reflects the influence of $k'_{in}$ on the global precipitation rate coefficient ($k$) according to the cell model (cf. § 5.5.3). This is because the calculation of the migration distance in the square array of traps in § 6.3.2 relies on the same diffusion problem. Nevertheless, the random-walk model confirms the insensitivity of $l$ to $k'_{in}$ when $k'_{in} > 1$ in the case of a random array of traps.

The results shown in Figs. 6.7 and 6.8 only provide information about the relative or dimensionless intergranular migration length. The average crow-flight distance a fission product actually diffuses in the grain boundary before being captured can be inferred from these figures in combination with Eq. (6.36). For example, the maximum distance a fission product can migrate in the grain boundary covered by 1 % of perfect traps distributed randomly was about 8.8 $\mu m$. When the intrinsic rate coefficient is reduced to $k'_{in} = 1$ (corresponding to $p_a = 0.7$ since $\phi = 1$ %), this distance increases to 12.6 $\mu m$ which is again in the same order

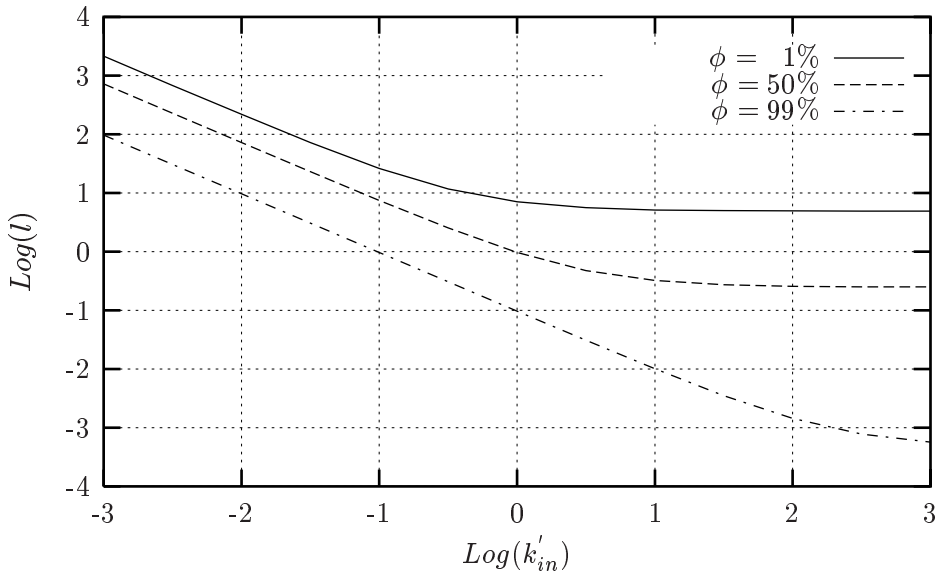


Figure 6.8: Dimensionless intergranular diffusion length ($l$) in a random array of sinks as a function of the dimensionless intrinsic reaction rate constant ($k'_{in}$) for three different values of the grain boundary bubble surface fraction ($\phi$)

of magnitude as the grain size. In the case of a regular distribution of bubbles with $\phi = 1$ % and $C_{tr} = 0.1\,\mu m^{-2}$, $L$ increases from 3.2 $\mu m$ under Smoluchowsky boundary conditions to 4.1 $\mu m$ when $k'_{in} = 1$.

The two calculation methods, applied respectively in a regular and in a random array of traps, are in good agreement at large trap fractional coverages but deviate by more than a factor of two at the combination of low trap density and small fractional coverage (cf. Fig. 6.6). This difference is qualitatively in line with the result of Fixman [248], who analysed stress-assisted precipitation on dislocations and found, like Wood [234] for grain boundary cavities, that a random array of traps entails a smaller global trapping rate in comparison with a regular distribution of the traps. Despite this difference, all the results indicate that a fission product will on average wander past many traps in the grain boundary when $k'_{in}$ is smaller than 1 and provided that $\phi$ remains lower than 50 %. In all other cases of the parameter space used in my analysis, the solute atom will be trapped by one of the sinks to which it is originally closest, that is the intergranular migration distance is at most a few times the size of the unit cell associated to each trap.

#### 6.3.4.3 Practical implications

The trapping efficiency of intergranular bubbles is implicitly taken to be infinite in most fission gas release models [1, 71, 181], although there are no experimental data, nor molecular dynamics calculations available to determine the intrinsic rate coefficient between the fission

products and these traps. Therefore, and in order to distinguish between the behaviour of different migrating species, I have introduced the variable trapping efficiency.

In view of the small solubility of fission gas atoms in $UO_2$, it seems (more) reasonable to assume that generally $k_{in}^{'} > 1$. Consequently, Figs. 6.7 and 6.8 indicate that the intergranular diffusion length is not strongly affected by $k_{in}^{'}$ since $\phi \leq 50$ % in most common circumstances. This provides a justification for the application of Smoluchowsky boundary conditions for intergranular bubbles in fission gas release models. Furthermore, the calculations show that for areal number densities and fractional coverages by intergranular bubbles observed in fuel irradiated to burnups exceeding $\sim$ 20 MWd/kgU, fission gas atoms are trapped after a migration distance equal to the size of a grain or less. Under these conditions, long-range grain boundary diffusion to free surfaces cannot contribute to the release of fission gas atoms. Instead, it will contribute on a local scale to grain-face bubble nucleation and growth. Kogai adopted such an intermediate approach [181]. In view of the absence of any measurement of $D_{gb}$ of Xe in $UO_2$, however, Kogai had to resort to using the value for $U^{4+}$.

The variable trap efficiency also provides a qualitative explanation for the observed difference between the release of Xe atoms and the volatiles Te and I in the post-irradiation annealings of trace-irradiated $UO_2$ specimens [28, 93, 105]. A consistent observation in these experiments is the higher apparent diffusivity of Te and I, often by as much as a factor of 100. This species-dependent property has been interpreted as a consequence of more effective trapping of Xe in grain boundaries than of the other volatile fission products. The reduced trap efficiency can be attributed to the different size and charge of the migrating atoms [258, 266]. Our calculations enable to account for such a reduced trapping efficiency by means of two parameters, namely the intrinsic trapping rate coefficient ($k_{in}^{'}$) as well as the effective surface fraction of the traps ($\phi_{eff} = \pi R_{eff}^2 C_{tr}$). The latter is based on the effective reaction radius for the trapping centra ($R_{eff}$) in the case of charged particles, reflecting the Coulomb interaction [228, 230, 231]:

$$R_{eff} = \frac{\pm L_{on}}{\exp\left(\frac{\pm L_{on}}{R_{tr}}\right) - 1}, \tag{6.37}$$

where $L_{on}$ symbolises the so-called Onsager radius at which the Coulomb interaction energy equals the thermal energy $k_B T$. The positive or negative sign in front of $L_{on}$ corresponds to repulsion or attraction respectively.

For volatile fission products such as Te and I, one would thus expect a low intrinsic trapping rate coefficient ($k_{in}^{'} < 1$) in view of their higher release rates. However, Te and I are chemically active and their charge depends on the stoichiometry [105,258]. This will render the assessment of $k_{in}^{'}$ more problematic.

Having determined conditions for the transition from grain boundary diffusion to growth and interlinkage of bubbles, it seems natural to assess the equivalent burnup. From the post-irradiation analysis for the volatile fission product Cs in $ThO_2$ [97], and from the in-pile results

of Turnbull et al. [93, 94] in $UO_2$, the equivalent burnup appears to be extremely small.

The calculation of the equivalent burnup, however, involves a number of poorly characterised parameters. For example, with a trap surface coverage of 1%, one needs to determine the trap number density, $C_{tr}$, in order to know the trap radius, $R_{tr}$, and their volume. According to experimental data for intergranular bubbles [147, 184, 265], $C_{tr}$ ranges between 0.1 $\mu m^{-2}$ and 10 $\mu m^{-2}$. The smaller values resulted from interlinkage of bubbles, whereas the higher values can be associated with situations where interlinkage is negligible [184]. It should be emphasised that the experimental data were obtained by means of scanning electron microscopy, hence the minimum detectable bubble radius was in the order of 0.1 $\mu m$. Smaller, undetected bubbles could yield higher values of $C_{tr}$. In addition, traps should be defined in a more general sense, that is not only gas filled bubbles but also defects, e.g. those created by fission fragments. This is in accordance with the experimental observations on intragranular bubble nucleation in the wake of fission fragments [65, 66, 237], and with the idea of Khoruzhii et al. [122] about a new retardation force on grain growth in trace-irradiated $UO_2$ due to inclusions in grain boundaries generated when fission tracks intercept the grain face.

In view of the uncertainty both on the type and density of traps in trace-irradiated fuel, and because of the lack of experimental data on intergranular bubble radii below 0.1$\mu m$, it is of primary importance to analyse grain boundary bubble nucleation, e.g. by means of transmission electron microscopy. In addition to $C_{tr}$, there is an uncertainty both on the temperature and on the hydrostatic pressure around the bubble [59, 184, 219]. The equivalent burnup will also depend on the irradiation history. Finally, it should be emphasised that in mixed oxide fuels with a non-homogeneous distribution of the fission density [98] it is even more difficult to determine the equivalent burnup.

## 6.4 Summary and conclusions

I have addressed three questions with respect to the role of the grain boundaries in the fission product release process in polycrystalline $UO_2$ that were posed at the end of section 6.1.

The post-irradiation annealing experiments utilizing trace-irradiated $UO_2$ provide an excellent method to ascertain whether grain boundary diffusion assists xenon release. The specimens do not exhibit intergranular porosity because the gas concentration is too low to nucleate bubbles. However, natural microstructural defects or impurities in the grain boundaries of fresh $UO_2$ may play the same trapping role as do bubbles in irradiated fuel. To investigate this possibility, recent data on Xe release from stoichiometric trace-irradiated $UO_2$ disks were analyzed by two models. The first approach, called the direct release model, neglects intergranular transport and ascribes gas release solely to lattice diffusion from solid at the surface of the specimens. The predicted release fractions were far smaller than the observations, suggesting the need for a mechanism that allows transport from deeper within the specimens.

The second, indirect model posits release from the grains by lattice diffusion followed by transport to the free surface by intergranular diffusion. This model had previously been successfully applied to Te and I release, but its applicability to the rare gases has been generally rejected (at least for power-reactor fuel). The indirect release model was modified to account for intergranular trapping of Xe, since this process was believed to be the principal reason why the rare gases are retained in irradiated fuel for substantial burnups.

Comparison of the indirect model with the Xe release data involved adjustment of three parameters: two for $D_{gb}$ and a third parameter representing the intergranular traps. The best agreement between theory and experiment was achieved for little or no trapping, or at least for $G$ values an order of magnitude smaller than those representing bubble populations observed by fractography of irradiated fuel. Our analysis thus supports the assistance of grain boundary diffusion to fission gas release release from trace-irradiated $UO_2$.

The fitting procedure fairly accurately fixed $D_{gb}$ at 1500 °C, but was unable to determine a reliable activation energy for this property. The grain boundary diffusion coefficients deduced from application of the indirect model to this small set of data are no more accurate than the lattice diffusivities of Xe in $UO_2$ needed in the calculation. The uncertainty in this property is at least one order of magnitude.

The second question concerned the conditions for the transition from release assisted by grain boundary diffusion to growth and interlinkage of the intergranular bubbles in controlling fission gas release. In order to address this issue, I have assessed the mean migration distance of a fission gas atom in a grain boundary decorated with a population of circular traps. The analysis encompassed the influence of the trap number density and their fractional coverage in both a regular and a random array of sinks. In addition, I have evaluated the influence of their efficiency at trapping gas atoms impinging on their surface.

My approach of the grain boundary reconciles the two contradictory roles of the grain faces in fission gas release. In addition, the results provide quantitative conditions for the switch. Both the intergranular diffusion coefficient ($D_{gb}$) and the dimensionless intrinsic capture rate on the surface of the bubbles ($k'_{in}$) are not well characterised at present. Yet, the results are independent of $D_{gb}$, whereas the influence of $k'_{in}$ on the intergranular diffusion length is strongly limited under most common circumstances. It is thus fair to conclude from the computations, that for values of the geometric parameters that roughly encompass the intergranular bubble populations observed in irradiated fuel, a fission gas atom will be trapped after a migration distance in the grain boundary equal to the size of a grain or less. This result simply provides a theoretical justification for the universal rejection of grain boundary transport as a release mechanism for fission gas in irradiated $UO_2$.

Finally, the calculations also offer a qualitative explanation for the dissimilar release rates observed in trace-irradiated $UO_2$ for Te and I in comparison with Xe. More precisely, the reduced trap efficiency for the ionic species is well reflected in the variable intrinsic reaction

rate ($k_{in}^{'}$), as well as the (effective) trap surface fraction ($\phi_{eff}$). Nevertheless, experiments or molecular dynamic calculations are needed to pin down the quantitative data.

# Part III

# An improved model for fission gas release

Fission gas release modelling in nuclear fuels has received much interest for several decades. Despite all the efforts, there is still room for improvement. Two of the most important issues that models should be able to cope with from an industrial point of view, are the incubation behaviour (cf. § 3.3.1) and the burst phenomenon during power variations (cf. § 3.3.3), especially at high burnup. This requires a proper description of the release kinetics, both in the grains and along the grain boundaries. To this end, the recent model of Kogai [181] provides the most appropriate basis (cf. § 3.4). Nevertheless, some limitations of this model have been highlighted and will be tackled in this part.

Following the description of my own model development in chapter 7, I will compare it with the fission gas release models from the open literature. In chapter 8, I discuss its numerical implementation, more precisely the choice of the routines required to solve the problems at hand as well as the corresponding numerical parameters. Chapter 9 deals with the validation procedure of the model. In view of the interrelationship with other phenomena, it was necessary to couple the gas release model with a general fuel performance code. To this end, I have used the FTEMP2 code [267] of the OECD Halden Reactor Project as well as the COMETHE-IV code [173] from BELGONUCLEAIRE to provide on input the radial distribution of the temperature, the power, and the burnup in the pellets.

# Chapter 7

# Model description

## Contents

The model treats the release process of the fission gas atoms in $UO_2$ fuel in two consecutive phases. These two phases are treated in distinct, but coupled, modules. The first module deals with the transport of the fission gas atoms on a microscopic scale, that is in the grains where they are supposed to be generated uniformly. The second module considers the transport of the fission gas atoms on a macroscopic scale, that is along the grain boundaries to the free volume in the fuel rod.

## 7.1 Intragranular module

The intragranular module of a fission gas release model in LWR fuel is crucial in many respects. First of all, the storage capacity of the grains is much more important compared to that offered by the grain boundaries, and the main fraction of the fission products remains in the grains under normal operating conditions. Second, the flux of gas atoms reaching the grain boundaries constitutes the source term for the intergranular module, which governs the onset of release. Last but not least, the intragranular diffusion process becomes rate-determining as soon as a tunnel network is established along the grain boundaries through which gas atoms may be vented.

When this PhD-work was launched at the end of 1994, there was a general consensus regarding the behaviour of fission gas atoms in the grains [268]:

> The gas atoms are created by fission in the fuel matrix. They then diffuse in the grains. Two different phenomena are involved: the thermal diffusion and the irradiation induced diffusion. Small intragranular bubbles with a diameter of 1 to 2 nm are observed in irradiated fuel. They are created in the wake of the fission spikes and then grow by diffusion. They are continuously destroyed by fission spikes (irradiation enhanced resolution). There is no bubble migration except at very high temperature.
>
> The bubbles are out of equilibrium (quasi-crystallites). The intragranular bubbles act as sinks for the gas atoms. They contribute to decrease the amount of gas available for release. This can be simulated by a reduction of an effective gas atom diffusion coefficient.

Despite this general agreement, there were different reasons to develop a new intragranular module. First of all, there was no model available in the open literature that could account simultaneously for the main mechanisms governing the release process (i.e. atomic diffusion, precipitation and re-solution), the coupling between the intra- and intergranular module, and the grain size distribution. Secondly, none of the concepts coupled the intra- and intergranular modules properly (cf. § 3.2.2.2). Finally, some models [96, 169] accounted for the grain size distribution (cf. § 3.2.3) but the coupling between the intra- and intergranular modules was incomplete.

### 7.1.1 Description of the grains

The grains in the $UO_2$ pellets are represented by a collection of spheres, and so the intragranular migration of fission gas may be treated in one dimension. This implicitly implies that the grain boundary concentration is identical at each face of a grain.

In polycrystalline materials, the grains are characterised by a size distribution function $P(R_{gr})$, where $P(R_{gr})\,dR_{gr}$ is the fraction of grains with radii between $R_{gr}$ and $R_{gr} + dR_{gr}$. Olander and co-workers [30, 96] implemented the size distribution proposed by Hillert [118] in their model for fission gas release. They revealed the necessity to do so in order to avoid the overprediction of the released fraction of fission gas atoms [30, 96]. For this reason, I have employed the same approach.

Hillert derived the grain size distribution function in the framework of his normal grain growth theory. The major feature of the size distribution he obtained is that it is time-invariant when expressed in terms of the size variable

$$u = \frac{R_{gr}}{R_c}\,, \tag{7.1}$$

where $R_c$ is the so-called critical grain radius, i.e. a threshold value above which grains will grow and below which they will disappear during normal grain growth. The critical radius is related to the mean grain radius ($\overline{R_{gr}}$) by $R_c = 9\overline{R_{gr}}/8$.

The distribution function in terms of $u$ is related to that in terms of $R_{gr}$ by:

$$P(u)\,du = P(R_{gr})\,dR_{gr}\,, \tag{7.2}$$

or

$$P(R_{gr}) = \frac{P(u)}{R_c}\,. \tag{7.3}$$

The Hillert distribution for three-dimensional grains is

$$P(u) = 24e^3 \cdot \frac{u}{(2-u)^5} \cdot \exp\left(-\frac{6}{2-u}\right)\,, \tag{7.4}$$

which is depicted in Fig. 7.1. This distribution function is properly normalised to unity:

$$\int_0^2 P(u)\,du = 1\,. \tag{7.5}$$

It should be noted that in normal grain growth, no grains larger than twice the critical size $R_c$ exist [118].

Despite the fact that I disregard grain growth in my FGR model, the time-invariant grain size distribution in Eq.(7.4) remains applicable. Taking into account this (discretised) size distribution of the grains, I have classified the collection of spherical grains according to three

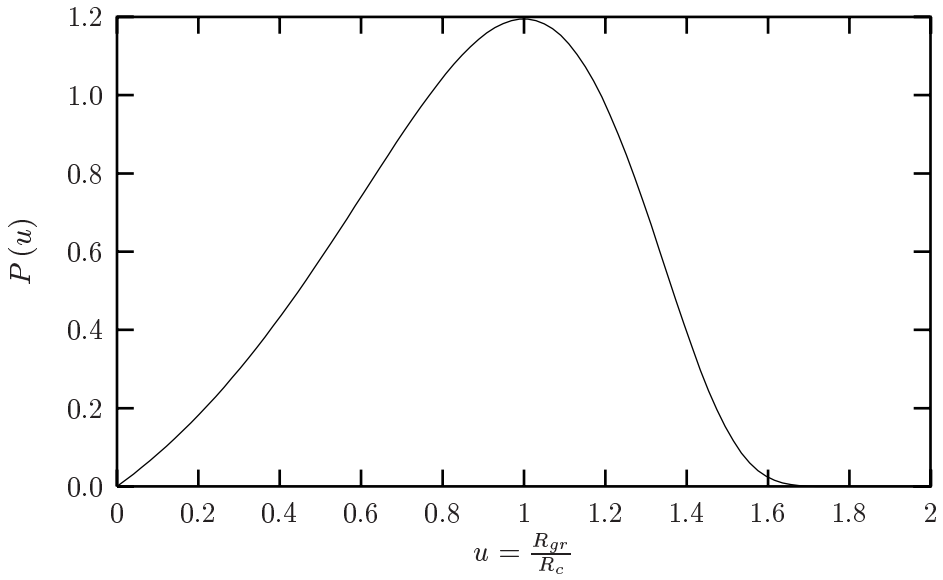


Figure 7.1: The grain size distribution function derived by Hillert [118] in three dimensions

indices:

$k$ corresponding to the grain size;

$l$ corresponding to the composition of the grain, which enables to extrapolate the model to mixed oxide fuels (e.g with $UO_2$ and $PuO_2$ grains);

$m$ corresponding to the macroscopic annulus of the pellet in which the class of grain is embedded (cf. intergranular module in § 7.2)

The intragranular diffusion equation (described below) is solved in each class or type of spherical grain, rather than in all the grains of a pellet. The indices, however, will be omitted in most of the equations for the sake of clarity.

### 7.1.2 The intragranular diffusion equation

The migration of the gas atoms in the fuel matrix during irradiation in a LWR occurs mainly by atomic diffusion during irradiation at temperatures below $\sim$1600 °C. A fraction precipitates into small intragranular bubbles and reduces the amount available for release. The intragranular module is therefore based on a one-dimensional diffusion equation in spherical coordinates:

$$\frac{\partial C_v(r,t)}{\partial t} = D_{eff} \triangle C_v(r,t) + S_v(r,t) - \lambda C_v(r,t) \ , \tag{7.6}$$

where $C_v$ represents the bulk concentration, $D_{eff}$ is the effective bulk diffusion coefficient in the $UO_2$ matrix (cf. Eq.(2.11) in § 2.4), $S_v$ represents the source term, and $\lambda$ is the radioactive

decay constant of the species under consideration.

The partial differential equation is complete with a zero initial condition ($C_v(r,0) = 0$) and with two boundary conditions:

$$\left.\frac{\partial C_v}{\partial r}\right|_{r=0} = 0\,, \tag{7.7}$$

$$\left.\frac{\partial C_v}{\partial r}\right|_{r=R_{gr}} = \frac{C_{gbv} - C_v(R_{gr},t)}{\delta_s}\,, \tag{7.8}$$

where $C_{gbv}$ denotes the concentration of gas atoms dissolved in the grain boundary, which is provided by the intergranular module (cf. § 7.2), and $\delta_s$ stands for the width of an imaginary supplementary layer. The Neumann-type condition in Eq.(7.8) is a mathematical trick that I have introduced in order to reduce the gradient at the grain face. This is especially needed in the outer part of the fuel pellets, where substantial gradients may develop near the grain faces. The value of $\delta_s$, however, is so small (0.3 nm) that its effect on the mass balance is negligible (cf. § 8.4.2.3). Note that the boundary condition at the grain face may vary linearly with time according to the numerical routine applied for the solution of the intragranular diffusion equation (cf. § 8.4). The central boundary condition in Eq.(7.7) reflects the symmetry of the intragranular concentration profile. This results from the uniform grain face concentration that I assume to prevail within each macroscopic annulus of the pellet (cf. § 7.2).

### 7.1.3 The volume diffusion coefficient

The single gas atom diffusion coefficient is rather poorly characterised. The most commonly applied expression was originally proposed by Turnbull and co-workers [49]. Yet, the actual measured values of $D$ may differ from the Turnbull line by a factor of five up or down, at any temperature [1]. This is reflected in the various expressions for the diffusion coefficient applied in the FGR models reported in the open literature.

In the expression for the effective diffusion coefficient ($D_{eff} = D \cdot b/(b+g)$), I started with the composite formulation for $D$ used by Kogai [181]:

$$D = D_a + D_b + D_c \quad [m^2/s] \tag{7.9}$$

where

$$D_a = D_a^\circ \exp(-70000/RT) \tag{7.10}$$

$$D_a^\circ = \begin{cases} 7.6\times10^{-10} + 6.84\times10^{-9}\,\frac{bu}{40} & bu \le 40\,GWd/t \\ 7.6\times10^{-10} + 6.84\times10^{-9} & bu > 40\,GWd/t \end{cases} \tag{7.11}$$

denotes the intrinsic diffusion coefficient which dominates at high temperatures (T $\geq$ 1400 °C). The second contribution dominates when 1000 °C $\leq T \leq$ 1400 °C and describes diffusion via

thermal and irradiation induced cation vacancies:

$$D_b = s_v^2 \cdot j_v \cdot V \tag{7.12}$$

where

$$s_v = \Omega^{1/3} = 3.4454 \times 10^{-10}\ [m] \tag{7.13}$$

$$j_v = 10^{13} \exp\left(-55200/RT\right)\ [s^{-1}] \tag{7.14}$$

$$V = \frac{\left(\alpha_s s_v^2 + Z V_0\right)}{2Z}\left[\sqrt{1 + \frac{4K'Z}{j_v\left(\alpha_s s_v^2 + Z V_0\right)^2}} - 1\right] \tag{7.15}$$

$$V_0 = \exp\left(-55200/RT\right) \tag{7.16}$$

and where $\alpha_s = 10^{15}$ m$^{-2}$, $Z = 100$, $R = 1.987$ cal/(mol·K), and $K^{'} = 2 \times 10^{-4}$ s$^{-1}$. The last contribution to the bulk diffusion coefficient corresponds to the athermal term:

$$D_c = 2 \times 10^{-22} \cdot \dot{F}\,, \tag{7.17}$$

where the fission rate density ($\dot{F}$) is expressed in $\mu m^{-3} s^{-1}$, and dominates at low temperatures (T $<$ 1000 °C).

This composite formulation for $D$ was originally proposed by Turnbull, although he did not include the burnup effect. Kogai added a continuously increasing term with burnup in the pre-exponential factor of the first "intrinsic" diffusion term in Eq.(7.11) to fit the data.

In line with the conclusions of Turnbull et al. [49], I have modified the equation of $D$ for stable gas release to take account of intragranular bubbles. More precisely, I have applied the trapping ($g$) and re-solution ($b$) parameters proposed by White and Tucker [1], and later implemented by various authors (e.g. [58, 189]):

$$g = 4\pi \overline{r_{bl}} D n_{bl} \tag{7.18}$$

$$b = 3.03 \dot{F} \pi \mu_{ff} \left(\overline{r_{bl}} + \delta_0\right)^2 \tag{7.19}$$

where

$$n_{bl} = \frac{1.52\alpha}{\pi \mu_{ff} \left(\overline{r_{bl}} + \delta_0\right)^2} \tag{7.20}$$

represents the intragranular bubble density [m$^{-3}$], and

$$\overline{r_{bl}} = 5 \times 10^{-10}\left[1 + 106 \exp\left(-8702.7/T\right)\right] \tag{7.21}$$

is the mean bubble radius [m]. Furthermore, following the preliminary results of the FGR

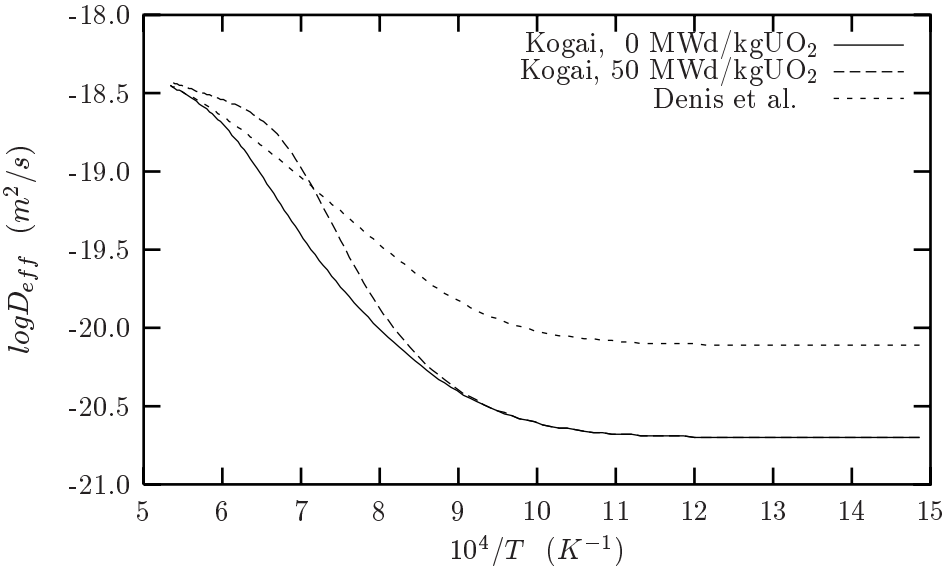


Figure 7.2: The effective volume diffusion coefficient of inert gas atoms in $UO_2$ between 400 $^\circ C$ and 1600 $^\circ C$ at a fission rate density of $10^{19}$ $m^{-3}s^{-1}$ according to Kogai [181] and Denis et al. [58]. The diffusion coefficient according to Kogai is provided for two burnup values.

model (cf. § 9.3), I have applied the composite expression for $D$ proposed by Denis et al. [58]:

$$D = D_a + 4D_b + 4D_c\,, \tag{7.22}$$

where the burnup effect is omitted in $D_a$. The athermal diffusion coefficient is still within the band of reliable data presented by Matzke [16], and corresponds to the value proposed by Turnbull et al. [9] (cf. Eq.(2.4) in § 2.3). The resulting Arrhenius plots of the effective volume diffusion coefficients according to Kogai [181] and Denis et al. [58] are compared in Fig. 7.2.

### 7.1.4 The intragranular source term

The source term of the intragranular diffusion equation contains two contributions:

$$S_v\,(r,t) = S_{fis} + S_{res}\,(r,t)\ . \tag{7.23}$$

The first part stems from the fission process, which is assumed to produce fission products homogeneously in the grains at a constant rate during each time step. The overall yield $y$ of a given nuclide includes the contribution due to beta decay of the precursors in the mass chain as well as the independent yield of the nuclide. Thus, the uniform stable gas generation rate is

$$S_{fis} = y \cdot \mu \cdot \dot{F} \quad \left[\frac{\mu m^3_{gas}}{\mu m^3_{ox} \cdot s}\right], \tag{7.24}$$

where $y = 0.29$ [269] and the factor $\mu = 22.4 \times 10^{-8}\, \mu m^3_{gas}/6.023$ atoms converts the units of the concentration from a number of atoms to a volume of gas at standard pressure and temperature.

Irradiation induced re-solution of gas atoms accumulated in the grain boundaries provides the second contribution to the intragranular source term. Unlike the first uniform contribution, the re-solution process only operates in a thin zone near the grain face, hence a numerical solution of Eq.(7.6) is required. In seeking such a solution, it is possible either to assume that all atoms undergoing re-solution are deposited at a characteristic depth $\delta_R$ from the grain boundary [4] (cf. Fig. 3.1 p.41), or that they are precipitated uniformly throughout a layer of thickness $2\delta_R$ [188]. More recently, Denis et al. [58] proposed a general distribution function between $R_{gr}$ and $R_{gr} - 2\delta_R$ with a maximum at $r = R_{gr} - \delta_R$, although they did not specify the distribution function. Furthermore, given the uncertainty pertaining to $\delta_R$, I have implemented the smeared model of Dowling and co-workers [188].

In order to compute $S_{res}$ according to the smeared model, it is necessary to determine the number of gas atoms leaving the grain boundary per unit of time and the volume of the layer in which the atoms are redistributed. If the rate at which gas atoms are knocked from the grain boundary into the two adjacent grains is $\Gamma_r$, then there are

$$\Gamma_r \frac{4\pi R_{gr}^2}{2} \frac{\left(\hat{C}_{gbv} + \hat{C}_{gbb}\right)}{S_{gb}} \tag{7.25}$$

atoms entering each grain with radius $R_{gr}$ per unit of time, where $\hat{C}_{gbv}$ and $\hat{C}_{gbb}$ correspond to the concentration of gas atoms dissolved in the grain face and accumulated in grain boundary bubbles respectively, and $S_{gb}$ denotes the specific surface of the grain boundaries. (The quantities related to the intergranular module are defined in more detail in the following section). The atoms undergoing re-solution are redistributed in a layer with thickness $2\delta_R$, hence

$$S_{res}\,(r,t) = \begin{cases} \frac{\Gamma_r R_{gr}^2 \left(\hat{C}_{gbv}(t) + \hat{C}_{gbb}(t)\right)}{4 S_{gb} \delta_R \left(R_{gr}^2 - 2 R_{gr} \delta_R + \frac{4}{3}\delta_R^2\right)} & R_{gr} - 2\delta_R \leq r \leq R_{gr} \\ 0 & 0 \leq r < R_{gr} - 2\delta_R \end{cases} \tag{7.26}$$

## 7.2 Intergranular module

A proper description of the grain boundary behaviour of the fission gas atoms in LWR fuel is a prerequisite for any fission gas release model. For example, the grain boundary bubble growth and the ensuing interconnection determine the conditions for the so-called grain boundary saturation, which in turn triggers the onset for (thermal) gas release. Accurate modelling of the corresponding kinetics is thus crucial for the simulation of the incubation behaviour, as well as the burst release phenomenon (cf. § 3.3.1 and § 3.3.3). Therefore, and in view of the open questions and difficulties discussed in Part I, most of the attention has been devoted to

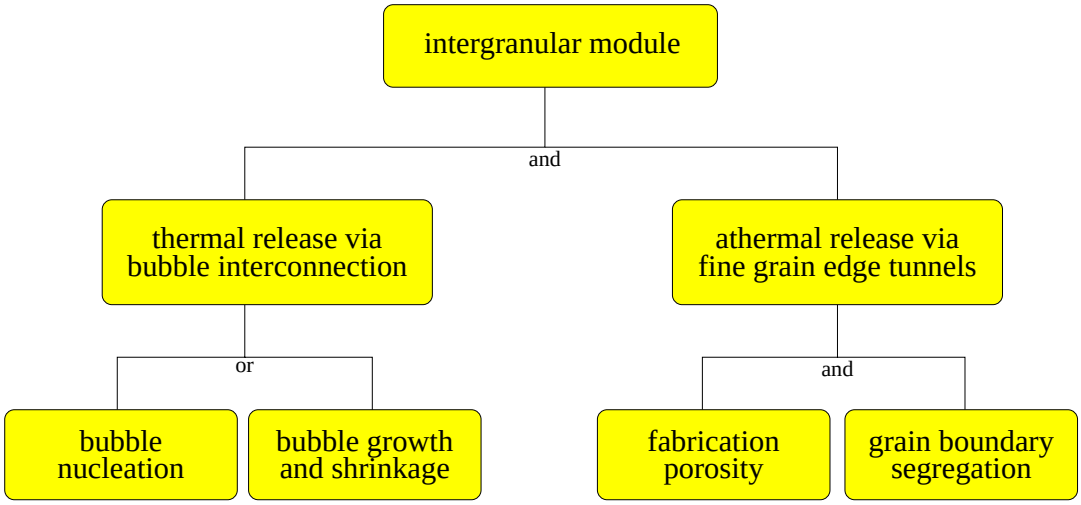


Figure 7.3: Global structure of the intergranular module in the fission gas release model

the intergranular module of the fission gas release model.

The temperature is a key parameter for the fission gas release process. It determines whether the fuel operates in an athermal ($\leq 1100$ °C) or in a thermal domain [102]. In accordance with this, I have subdivided the mechanisms involved in the intergranular module in two classes (cf. Fig 7.3). The corresponding models have been developed and implemented in two steps.

### 7.2.1 The grain boundary mechanisms in the thermal domain

In the thermal domain ($\geq 1100$ °C), lenticular gas bubbles develop at the grain boundaries at a certain burnup level. The fission gas atoms are therefore considered to co-exist in two phases at the grain boundaries. One fraction is dissolved in the grain face ($C_{gbv}$), whereas the other part is accumulated in bubbles ($C_{gbb}$). The ratio $C_{gbv}/C_{gbb}$ may vary by several orders of magnitude: e.g. from around 500 at 700 °C down to $10^{-6}$ at 1500 °C. This strong temperature dependency mainly reflects the diffusion controlled precipitation in the grain boundaries.

The grain boundary concentrations $C_{gbv}$ and $C_{gbb}$, expressed per unit of volume of the grain boundary, are converted to the quantities $\hat{C}_{gbv}$ and $\hat{C}_{gbb}$ respectively, in order to express them per unit volume of the macroscopic solid:

$$\hat{C}_{gbv} = C_{gbv}\delta_{gb}S_{gb} \tag{7.27}$$

$$\hat{C}_{gbb} = C_{gbb}\delta_{gb}S_{gb} \tag{7.28}$$

The conversion of units relies on two quantities. The first parameter is the grain boundary thickness, $\delta_{gb}$, which is in the order of 0.5 nm [83]. The second parameter is the specific surface

of the grain boundaries in the polycrystalline material, denoted by $S_{gb}$. Since I consider the oxide to be made up of a distribution of spherical grains, the specific grain boundary surface is calculated in each macroscopic ring of the pellet with index $m$ by means of

$$S_{gb}(m) = \sum_{k,l} \frac{N_{klm} \left(\frac{4\pi}{2} R_{klm}^2\right)}{V_m}, \tag{7.29}$$

where I have accounted for the fact that the grain boundary is shared by two adjacent grains. $R_{klm}$ and $N_{klm}$ denote the average radius and the number of grains of class $(k, l, m)$, respectively. $N_{klm}$ may be inferred from the volume fraction of the grains of the corresponding type $(f_{klm})$, and the volume of the macroscopic annulus with index $m$ $(V_m)$:

$$f_{klm} V_m = N_{klm} \left(\frac{4\pi}{3} R_{klm}^3\right). \tag{7.30}$$

The expression for the specific grain boundary surface therefore becomes:

$$S_{gb}(m) = \frac{3}{2} \sum_{k,l} \frac{f_{klm}}{R_{klm}}. \tag{7.31}$$

In the following, I describe the set of equations governing the two quantities $\hat{C}_{gbv}$ and $\hat{C}_{gbb}$ in the $UO_2$ pellets.

#### 7.2.1.1 General form of the intergranular equations

In the first version of the intergranular module, I have considered grain boundary diffusion impeded by bubbles [255]. To this end, I have converted the flux of gas atoms along the grain boundaries into an equivalent flux across a unit area of the pellet, in line with the model of Levine et al. [270] for self-diffusion in polycrystals. My approach extended the idea of Speight [57] for the gas behaviour in the spherical grains and resulted in a coupled system of partial differential equations. It was mainly intended to assess the conditions for the transition, from FGR assisted by grain boundary diffusion, to release controlled by bubble interlinkage.

In addition to the mathematical complexity, the first version of the intergranular module suffered from two conceptual limitations. First of all, it did not take into account the radial, circumferential and axial cracks in the pellet (cf. Fig. 7.4). Such cracks appear after the first start-up of the reactor and provide a shortcut to the diffusion process along the grain boundaries on the scale of the pellet. In spite of this limitation, Kourti et al [87] have considered grain boundary diffusion of cation vacancies from the pellet periphery to the pellet center in their model for intergranular fuel swelling.

Second, the assessment of the intergranular migration distance of fission gas atoms leads to the conclusion that long-range grain boundary diffusion to free surfaces cannot contribute to

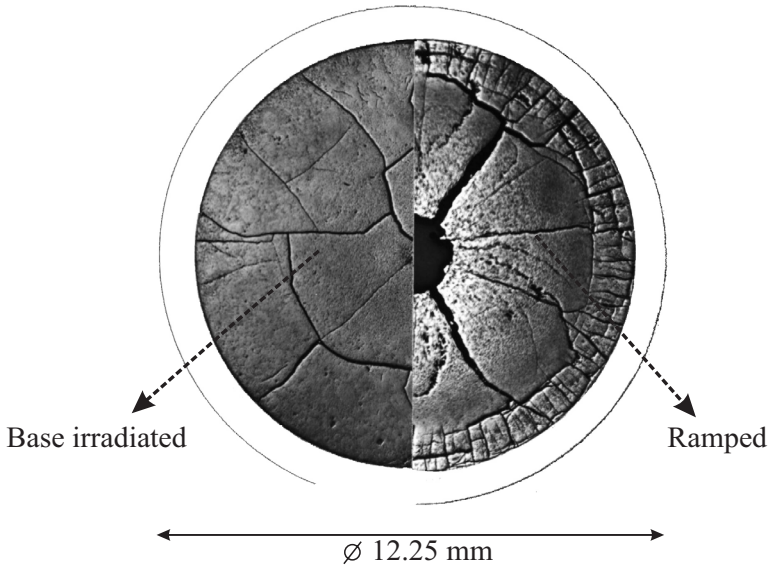


Figure 7.4: Diametrical cross section of a $UO_2$ fuel rod after base irradiation (left) and after a power ramp (right), featuring radial and circumferential cracks.

their release (cf. § 6.4). Instead, it contributes on a local scale to grain-face bubble nucleation and growth. This was supported by my simulation of the release observed in an instrumented fuel assembly (IFA-519) of the Halden boiling water reactor [227, 255]. I could not predict the onset of release properly because the calculated release due to grain boundary diffusion was too large during the initial irradiation at 15 kW/m.

Given the state of affairs described above, I developed a simplified version of the intergranular module. In this model, it is assumed that thermal release mainly takes place via a three-dimensional tunnel network of interconnected grain boundary bubbles. Before this occurs, there will be no (radial) transfer of gas atoms along the grain boundaries on the pellet scale. I have therefore subdivided the cylindrical pellet into independent annuli (cf. Fig. 7.5). In each annulus, I compute the release of the mean grain boundary bubble to the free volume in the rod via a tube representing the escape tunnels (cf. Fig. 3.3 p. 44), in accordance with Kogai et al. [186]. The decoupled annuli should be isothermal since the tunnel formation is mainly temperature dependent.

An important consequence of the decoupling for the intergranular module was that I no longer had to solve a diffusion problem in a cylindrical geometry; I obtained a system of ordinary differential equations (ODE) in each macroscopic ring. One of the equations of the set of ODE describes the evolution of the average bubble size in the macroscopic ring. I have applied a conventional separation of nucleation and growth for the grain boundary bubbles, leading to two different systems of ODE.

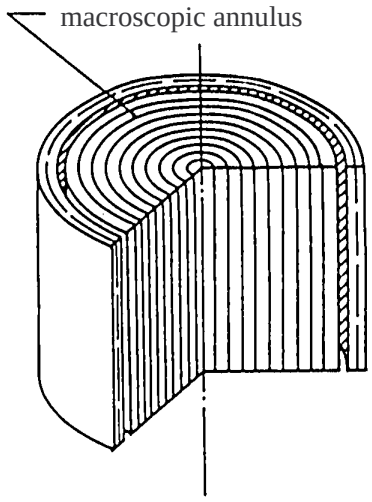


Figure 7.5: Schematic representation of the decoupled (isothermal) annuli of the pellet, as applied in the macroscopic (intergranular) module of the FGR model.

**Intergranular model for the grain boundary bubble nucleation phase** An experimental investigation of the intergranular bubble nucleation would require an analysis by means of transmission electron microscopy. To my knowledge, such studies have been performed in metals, but not yet in irradiated $UO_2$.

The theoretical analysis of the nucleation and growth of gas-filled cavities on grain boundaries of irradiated materials should be tackled by means of the Fokker-Planck theory in order to account for the statistical fluctuations in the clustering process [271, 272]. Such an approach, however, can not be implemented in a straightforward manner in a model for fission gas release.

Conventionally, the nucleation and growth stages are therefore separated in order to simplify the mathematics [273, 274]. Furthermore, the classical nucleation theory enables to obtain terminal cavity densities in nuclear fuels [271]. According to scanning electron microscopy measurements grain face bubbles are nucleated at a number density on the order of 1 bubble/$\mu m^2$, and subsequent changes in the grain face porosity are due to bubble growth rather than the nucleation of additional bubbles [184]. Kogai [181] implemented this sequence of events in his model for fission gas release.

I have adopted the simplified approach of Kogai as well, since one of the objectives of my fission gas release model is to describe the grain boundary saturation process, rather than the nucleation phase. Nevertheless, his intergranular module contains an inherent numerical problem in fresh fuel. Kogai avoided the description of the nucleation phase and considered the bubble growth according to Eq.(3.7). As a result, he had to define an initial bubble radius

containing a certain amount of gas, otherwise the bubble would shrink and disappear under the influence of the surface tension and any other externally applied force.

In accordance with Kogai, I presumed that bubbles are nucleated at defects in the grain boundary characterised by a radius ($R^0_{bl}$) and a fixed number density ($C^0_{bl}$). This implicitly implies that homogeneous nucleation is disregarded. However, rather than introducing an arbitrary amount of gas in freshly nucleated bubbles, I assumed that a fraction of the gas atoms reaching the grain boundary is captured by these nucleation sites, thereby creating a vacancy-gas-atom *cluster*. When the amount of gas atoms accumulated in a cluster reaches a critical value ($N^{cr}_{bl}$) it becomes a so-called *bubble*. (The conditions for the switch from the nucleation phase to the bubble growth phase are treated in more detail in § 7.2.1.3).

During the nucleation phase of the intergranular bubbles, the radius of the gas-vacancy cluster is supposed to remain constant until the critical amount of gas atoms is build up. Until then, the concentrations of the gas atoms dissolved in the grain boundary ($\hat{C}_{gbv}$) and those accumulated in the gas-vacancy clusters ($\hat{C}_{gbb}$) are governed by the following coupled set of ODE:

$$\frac{d\hat{C}_{gbv}}{dt} = (1-\phi_{bl})J_1 - J_2 - J_3^v - \lambda\hat{C}_{gbv} \tag{7.32}$$

$$\frac{d\hat{C}_{gbb}}{dt} = \phi_{bl}J_1 + J_2 - J_3^b - \lambda\hat{C}_{gbb} \tag{7.33}$$

where $J_1$ stands for the average out-coming flux from the grains, $J_2$ denotes the flux due to diffusion controlled precipitation in the grain boundary, and $J_3$ symbolises the fission induced re-solution flux. The expression for each flux term will be derived in § 7.2.1.2 starting on page 127. As shown in Appendix E, the coupled system of ODE can be re-written in a simplified form and may be integrated analytically over each time interval during which all coefficients are constant.

**Intergranular model for the grain boundary bubble growth and interlinkage phase**
Once the critical number of gas atoms in the clusters has been exceeded during the so-called nucleation period, the (lenticular) bubble can grow by means of a vacancy flow along the grain boundary. The balance between the bubble internal pressure ($P_{bl} \geq 0$), the hydrostatic pressure ($P_h \leq 0$) and the surface tension constitutes the driving force for the growth or shrinkage of the bubbles [216].

The expression for the expansion of the lenticular bubbles is based on the model for void growth on grain boundaries presented by Speight and Beere [218]. Yang et al. [222] verified this model by means of small angle neutron scattering. Matthews et al. [220] and Hayns et al. [221] have extended the idea of Speight et al. by considering gas filled bubbles rather than voids. To include the presence of gas within the cavity, they simply included the gas pressure

into the chemical potential of the cavity:

$$\frac{dV_{bl}}{dt} = \frac{2\pi\Omega D^v_{gb}\delta_{gb}}{k_B T}\left(P_{bl} + P_h - \frac{2\gamma\sin\theta}{R_{bl}}\right)\frac{4}{(1-\phi_{bl})(\phi_{bl}-3) - 2\ln\phi_{bl}}\,, \tag{7.34}$$

where $\phi_{bl} = \pi R^2_{bl} C_{bl}$, and the radius of the lenticular bubbles in the grain face is related to their radius of curvature by $R_{bl} = \rho_{bl}\sin\theta$, where $\theta = \arccos(\gamma_{gb}/2\gamma) = 50^\circ$ (cf. Fig. 2.4). However, since the volume of a lenticular bubble is given by [194]:

$$V_{bl} = \frac{4\pi}{3}\rho^3_{bl} f(\theta)\,, \tag{7.35}$$

where $f(\theta) = 1 - \frac{3}{2}\cos\theta + \frac{1}{2}\cos^3\theta$, the bubble growth law can be expressed as function of the radius of curvature of the grain boundary bubbles ($\rho_{bl}$):

$$\frac{d\rho_{bl}}{dt} = \frac{\Omega\delta_{gb}}{4f(\theta)\,k_B}\frac{D^v_{gb}}{T\rho^2_{bl}}\left(P_{bl} + P_h - \frac{2\gamma}{\rho_{bl}}\right)k(\phi_{bl}) \tag{7.36}$$

where

$$k(\phi) = \frac{8(1-\phi)}{(\phi-1)(3-\phi) - 2\ln\phi}\,. \tag{7.37}$$

Matthews et al. [220] have compared their results on swelling in nuclear fuel successfully with the experimental data of Zimmerman [215]. Kashibe and Une [223,224], as well as White [225] have confirmed these findings more recently.

The growth (and shrinkage) of bubbles entails two important modifications to the intergranular module; Eqs.(7.32) and (7.33) are supplemented with an equation describing the evolution of the bubble size and several supplementary flux terms are introduced. The set of ODE governing the intergranular module becomes:

$$\frac{d\rho_{bl}}{dt} = \frac{\Omega\delta_{gb}}{4f(\theta)k_B}\frac{D^v_{gb}}{T\rho^2_{bl}}\left(P_{bl} + P_h - \frac{2\gamma}{\rho_{bl}}\right)k(\phi_{bl}) \tag{7.38}$$

$$\frac{d\hat{C}_{gbv}}{dt} = (1-\phi_{bl})J_1 - J_2 - J^v_3 - J_4 - \lambda\hat{C}_{gbv} \tag{7.39}$$

$$\frac{d\hat{C}_{gbb}}{dt} = \phi_{bl}J_1 + J_2 - J^b_3 + J_4 - J_5 - \lambda\hat{C}_{gbb} \tag{7.40}$$

where $J_1$, $J_2$ and $J_3$ correspond to the same fluxes as in Eqs.(7.32) and (7.33), $J_4$ represents the flux due to grain boundary bubble sweeeping, and $J_5$ denotes the gas flow through the interconnected tunnel network of grain boundary bubbles. The expressions for the various fluxes will be derived in the following section.

When bubble interlinkage starts off in the course of irradiation, that is when

$$R_{bl} = R^*_{bl} = \frac{1}{2\sqrt{C^0_{bl}}}\,, \tag{7.41}$$

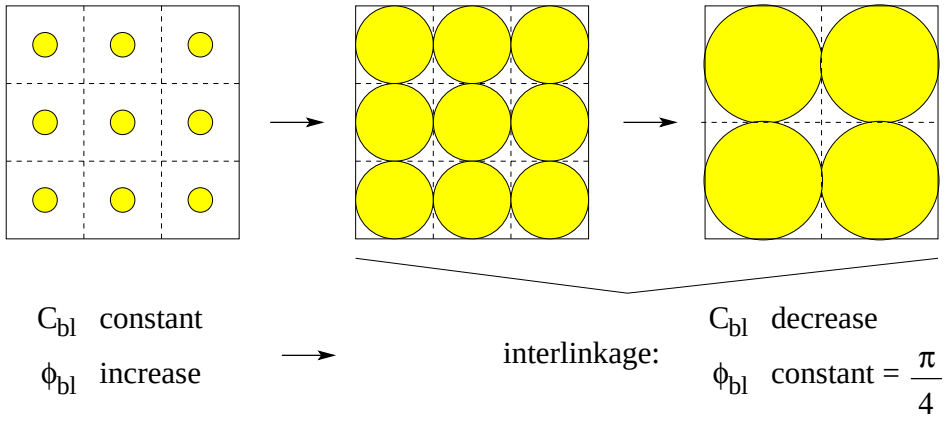


Figure 7.6: Schematic diagram to illustrate the change of the number density ($C_{bl}$) and the surface fraction ($\phi_{bl}$) of the intergranular bubbles during the growth and interlinkage phase, after Kogai [181].

the bubble surface fraction becomes constant while the bubble number density decreases, as illustrated in Fig. 7.6. In contrast, the bubble number density remains constant and the bubble coverage increases with $R_{bl}$ before interlinkage.

In order to derive a set of ODE that apply both before and after interlinkage of the bubbles, I have therefore expressed the different flux terms in the following section as a function of $\hat{C}_{gbv}$, $\hat{C}_{gbb}$, $\rho_{bl}$ and $\phi_{bl}$, where

$$\phi_{bl} = \begin{cases} \pi R_{bl}^2 C_{bl}^0 & R_{bl} < R_{bl}^* \\ \frac{\pi}{4} & R_{bl} \geq R_{bl}^* \end{cases} \tag{7.42}$$

and

$$C_{bl} = \frac{\phi_{bl}}{\pi R_{bl}^2} \,. \tag{7.43}$$

#### 7.2.1.2 Development of the different terms in the intergranular equations

**The intergranular source term** $J_1$ represents the average out-coming flux of a distribution of grains and is coupled to the intragranular module of the fission gas release model. Since the pellet has been subdivided in independent macroscopic annuli (with indices $m = 1, 2, \ldots NRJ$), I compute the source term in each of them separately. The flux of gas atoms entering the grain boundary in each macroscopic ring with index $m$ is given by:

$$J_{1,m} = \sum_{k,l} \frac{N_{klm}}{V_m} 2 \left[ -\frac{4\pi R_{klm}^2}{2} D_{klm} \left. \frac{\partial (C_{klm})}{\partial r} \right|_{r=R_{klm}} \right] , \tag{7.44}$$

where the bracketed term represents the out-coming flux of gas atoms from a grain with indices $(k, l, m)$, multiplied by the grain boundary area, which is shared by two adjacent grains. $D_{klm}$ indicates the volume diffusion coefficient in the grain of type $(k, l, m)$. The factor two in front of the brackets in the right hand side of Eq.(7.44) accounts for the fact that fission gas atoms

flow to or from both sides of a grain boundary.

The expression of $J_{1,m}$ can be re-written by means of the approximation in the microscopic module for the concentration gradient near the surface of the grain (cf. Eq.(7.8)):

$$\left.\frac{\partial C_{klm}}{\partial r}\right|_{r=R_{klm}} = \frac{C_{gbv} - C_{klm}(R_{klm},t)}{\delta_s} \tag{7.45}$$

$$= \frac{1}{\delta_s}\left[\frac{\hat{C}_{gbv}}{\delta_{gb}S_{gb}} - C_{klm}(R_{klm},t)\right] . \tag{7.46}$$

Consequently, the formula for $J_{1,m}$ becomes

$$J_{1,m}(t) = A_m(t) - B_m\hat{C}_{gbv}(t) , \tag{7.47}$$

where

$$A_m(t) = \frac{3}{\delta_s}\sum_{k,l}\frac{f_{klm}}{R_{klm}}D_{klm}C_{klm}(R_{klm},t) , \tag{7.48}$$

$$B_m = \frac{3}{\delta_{gb}S_{gb}\delta_s}\sum_{k,l}\frac{f_{klm}}{R_{klm}}D_{klm} . \tag{7.49}$$

**Diffusion controlled precipitation in the grain boundary** The flux $J_2$ represents the flow of gas atoms dissolved in the grain boundary to the intergranular bubbles by diffusive capture. The flux is derived from the cell model with source term in § 5.4.4, more precisely by inserting Eq.(5.30) in the first term on the right-hand side of Eq.(5.27):

$$J_2 = \left[\frac{8D_{gb}\phi_{bl}(1-\phi_{bl})}{(1-\phi_{bl})(\phi_{bl}-3) - 2\ln\phi_{bl}}\right]\frac{\hat{C}_{gbv}}{R_{bl}^2} , \tag{7.50}$$

where I have applied a Smoluchowsky boundary condition on the bubble surface. The grain boundary diffusion coefficient is given by:

$$D_{gb} = 6.9\times10^{-4}\exp(-322/RT) \quad [m^2/s] , \tag{7.51}$$

where the activation energy is expressed in kJ/mole. Eq.(7.51) is based on the expression for the grain boundary diffusion coefficient of U-vacancies in $UO_2$, originally proposed by Reynolds and Burton [86]. Following Kogai [181], I use this equation for gas atoms and U-vacancies alike.

**Fission induced re-solution at grain boundaries** The fission fragments can re-dissolve a fraction of the gas atoms accumulated in the grain boundary into the adjacent grains. The rate at which this occurs is determined by the re-solution rate coefficient $\Gamma_r$ ($s^{-1}$), which in turn is linearly dependent on the fission rate density ($\dot{F}$). The resulting flux of gas atoms

leaving the grain boundary bubbles can be written as:

$$\begin{aligned} J_3 &= J_3^v + J_3^b \\ &= \Gamma_r \left( \hat{C}_{gbv} + \hat{C}_{gbb} \right) \end{aligned} \tag{7.52}$$

where

$$\Gamma_r = \Gamma_r^* \frac{\dot{F}}{\dot{F}_{ref}}, \tag{7.53}$$

and the reference fission rate density ($\dot{F}_{ref}$) is taken at a linear heat generation rate of 20kW/m.

**Grain boundary bubble sweeping** In deriving the expression for the capture rate constant for the flux of gas atoms precipitating in intergranular bubbles, I have neglected bubble growth (cf. § 5.2). In order to account for the expansion of the grain boundary bubbles, I introduced a supplementary flux term ($J_4$) of fission gas atoms dissolved in the grain boundary to the intergranular cavities by bubble sweeping.

$J_4$ can be assessed from the volume of the grain boundary swept by the growing bubbles per unit of time:

$$2\pi R_{bl} \frac{\partial R_{bl}}{\partial t} C_{bl} A_{gb} \delta_{gb} \tag{7.54}$$

where $A_{gb}$ represents the grain boundary surface. The rate at which fission gas atoms are swept by the growing bubbles is then obtained by multiplying the swept grain boundary volume by the concentration of gas atoms dissolved in the grain boundary:

$$2\pi R_{bl} \frac{\partial R_{bl}}{\partial t} C_{bl} A_{gb} \delta_{gb} C_{gbv} \tag{7.55}$$

The flux $J_4$ in turn requires the volume of swept gas atoms to be expressed per unit of volume of the oxide, hence I replace $A_{gb}$ by $S_{gb}$:

$$\begin{aligned} J_4 &= 2\pi R_{bl} \frac{\partial R_{bl}}{\partial t} C_{bl} S_{gb} \delta_{gb} C_{gbv} \\ &= 2\pi R_{bl} \frac{\partial R_{bl}}{\partial t} C_{bl} \hat{C}_{gbv} \end{aligned} \tag{7.56}$$

This term has been omitted by Kogai [181] but should only be accounted for when the bubbles are growing, not when they shrink, e.g. due to the venting of the interlinked tunnel network by gas phase diffusion (cf. $J_5$). The expression for $J_4$ therefore becomes:

$$J_4 = \begin{cases} 2\frac{\phi}{\rho_{bl}} \frac{\partial \rho_{bl}}{\partial t} \hat{C}_{gbv} & \frac{\partial \rho_{bl}}{\partial t} > 0 \\ 0 & \frac{\partial \rho_{bl}}{\partial t} \leq 0 \end{cases} \tag{7.57}$$

where $\phi_{bl} = \pi R_{bl}^2 C_{bl}$ and $R_{bl} = \rho_{bl} \sin\theta$ is the bubble radius in the grain face.

**Gas flow through the interconnected tunnel network** As the grain boundary bubbles grow, those which are close enough to the grain edges may vent their content to the free volume of the rod. This gaseous flow through the tunnel network is incorporated in $J_5$. In line with Kogai et al. [181, 186], the expression for $J_5$ is derived from the equation of Poiseuille in a thin cylindrical tube, connecting the average bubble with the free volume as illustrated in Fig. 3.3 on p. 44.

The equation of Poiseuille [177, 185] provides a relationship between the viscosity of a gas ($\eta$), the time ($t$) needed for a certain volume ($V$) of gas to be evacuated via the tube of length $L$ and radius $a$ when the pressure at one side is $P_1$ and at the other side is $P_2$:

$$\frac{V}{t} = \frac{\pi a^4 (P_1 - P_2)}{8\eta L}. \tag{7.58}$$

This expression is equivalent with the equation of Darcy in a porous medium [177, 178, 180]. Both are valid for the viscous flow of an incompressible fluid or gas under stationary conditions [185], and assume that the fluid is inert with respect to the porous medium [177]. When the gas pressure decreases, such that the mean free path of gas molecules ($\lambda_{gas}$) becomes an appreciable fraction of the dimensions of the pore or capillary tube radius, then the velocity of the gas atoms will exceed that computed from Eq.(7.58). When the pressure decreases even more, such that $\lambda_{gas} \gg a$, then we have a free molecular flow or Knudsen flow [177]. In this case, each gas species of a gas mixture undergoes diffusion according to the gradient of its partial pressure, even when the total pressure gradient is zero across the tube.

In real situations, the average pore dimensions and the pressures are such that the application of the continuous medium approximation can be justified [180]. Kogai and coworkers [181, 186] applied the same approximation. It is important to note, however, that at some stages of the development of the porous fuel structure, the channels can be rather thin [102]. In this case, the gas flow is more of Knudsen type. Accordingly, there is a transition from molecular gas flow to the flow of a viscous fluid between the inlet and outlet of the channels, which is very difficult to model [180]. In addition, there are several parameters that remain poorly characterised (e.g. $L$, $P_h$, etc.) and there is an unknown tortuousity factor. In view of this, I have applied the simplified equation of Poiseuille, in line with Ivanov [180] and Kogai et al [181, 186].

In the case of gas release in $UO_2$ through the tunnel network, I assume that $P_1 = P_{bl} \gg P_2$ in Eq.(7.58). The gas flow rate from the average grain boundary bubble in each macroscopic ring to the plenum via the hypothetical thin tube can therefore be written as:

$$\frac{V}{t} = \frac{V_t P_{bl}}{\eta}, \tag{7.59}$$

where $V_t = \pi a^4 / 8L$.

The volume of gas leaving the bubble per unit of time can be converted to a corresponding

number of gas atoms by means of the van der Waals equation of state[a]:

$$P_{bl}\,(V_{bl} - N_{bl}\omega) = N_{bl}\,k_B T\,, \tag{7.60}$$

where

$$V_{bl} = N_v \Omega\,, \tag{7.61}$$

$N_v$ and $N_{bl}$ are the number of vacancies and gas atoms in the bubble respectively, $\Omega$ represents the U-vacancy volume in the $UO_2$-matrix, $k_B$ is the Boltzmann constant, and $\omega$ stands for the van der Waals constant for Xe ($= 8.5\times10^{-29}$ m$^3$per atom). The rate of fission gas atoms leaving the average bubble via the hypothetic fine tube thus becomes:

$$\begin{aligned} \frac{N_{bl}}{t} &= \frac{V_{bl}}{t} \cdot \frac{P_{bl}}{k_B T + P_{bl}\omega} \\ &= \frac{V_t}{\eta} \cdot \frac{P_{bl}^2}{k_B T + P_{bl}\omega}\,. \end{aligned} \tag{7.62}$$

In turn, the flux $J_5$, corresponding to the total volume of gas atoms ($\mu m^3_{gas}$) leaving all the intergranular bubbles per unit of time and per unit of volume of oxide ($\mu m^3_{ox}$) may be inferred from $N_{bl}/t$ by means of:

$$\begin{aligned} J_5 &= \frac{N_{bl}}{t}\mu C_{bl} S_{gb} \\ &= \frac{V_t}{\eta} \cdot \frac{P_{bl}^2 \mu C_{bl} S_{gb}}{k_B T + P_{bl}\omega}\,. \end{aligned} \tag{7.63}$$

The "volume" of the tube ($V_t$) determines the conductance of the gas in the capillary tube that represents the escape tunnels for release along the grain boundaries. The gaseous flow is assumed to increase by the shortening of the tube and/or thickening of the tube. Therefore, and because "the initiation of fission gas release often resembles this type of curve", Kogai [181] expressed $V_t$ as a product of two sigmoidal curves:

$$V_t = V_t^0 f(\phi_{bl}) g(\sigma_{eff})\,, \tag{7.64}$$

where

$$f(\phi_{bl}) = 1 - \exp\left[-\left(\frac{\phi_{bl}}{\phi^*}\right)^{10}\right]\,, \tag{7.65}$$

[a] In line with Kourti et al. [87] and Veshchunov [74], only the van der Waals correction to the total volume due to the unavailable volume of the gas atoms is considered. Cost et al. [275] discussed the different correction factors to be considered in the calculation of the number of gas atoms per bubble of inert gas in a solid. Kogai [181] applied the ideal gas law.

$$g(\sigma_{eff}) \quad = \quad 1 - \exp\left[ - \left( \frac{\sigma_{eff}}{\sigma_{ref}} \right)^{10} \right] , \tag{7.66}$$

$V_t^0 = 10^{-12} \mu m^3$ is the maximum "volume" of the tube or the normalisation factor of $V_t$, $\phi^* = \pi/4$ is the theoretical surface fraction of the grain boundary bubbles at which they should all interconnect (cf. Fig. 7.6), $\sigma_{ref} = 10$ MPa, and the "effective" tensile stress acting on the grain boundary $\sigma_{eff}$ is defined as the sum of the hydrostatic pressure imposed on the bubble (compressive) and the bubble pressure (tensile):

$$\begin{aligned} \sigma_{eff} &= \frac{P_h \pi R_s^2 + \pi R_{bl}^2 P_{bl}}{\pi R_s^2 - \pi R_{bl}^2} \\ &= \frac{P_h + \phi_{bl} P_{bl}}{1 - \phi_{bl}} \end{aligned} \tag{7.67}$$

The two monotonically increasing functions $f(\phi_{bl})$ and $g(\sigma_{eff})$ reflect, respectively, the influence of the bubble surface fraction and the effective tensile stress on the conductivity of the tube. As such, they will affect the kinetics of the fission gas release process. However, the effect of $P_h$ is accounted for twice in the fission gas release model of Kogai: once in the bubble growth law (Eq.(7.38)), and a second time in the tube conductivity (Eq.(7.66)), which is redundant. Moreover, according to Eq.(7.66) the release will also be enhanced in the case of a compressive (negative) effective stress, which is unacceptable. In view of this discrepancy, and because of the redundancy, I have eliminated the sigmoidal function $g(\sigma_{eff})$ from the expression for the tube conductivity in the course of the validation procedure of my fission gas release model.

Finally, inserting the expression for $V_t$ in Eq.(7.63) the expression for $J_5$ becomes

$$J_5 = \Psi \frac{\phi_{bl} f\left(\phi_{bl}\right) S_{gb} P_{bl}^2}{\sqrt{T} \rho_{bl}^2 \left(k_B T + P_{bl} \omega\right)} , \tag{7.68}$$

where

$$\Psi = \frac{V_t^0 \mu}{26.693 \times 10^{-19} \sqrt{M} \pi \sin^2 \theta} , \tag{7.69}$$

where I have introduced the expression for the absolute gas viscosity expressed in (sN/$\mu m^2$):

$$\eta \cong 26.693 \cdot 10^{-6} \frac{\sqrt{MT}}{\zeta^2} , \tag{7.70}$$

where $M$ represents the molecular weight of the gas atoms (131.3 for Xe), and $\zeta$ symbolises the hard sphere or collision diameter[b] of the gas (4.055 Å for Xe).

[b] In general, the attractive and repulsive interaction potential between molecules (e.g. the spherically symmetric Leonard-Jones potential) entails a collision integral in the nominator of the expression for the gas viscosity [276, 277]. However, we have taken the collision integral equal to 1, that is we neglect the intermolecular forces until actual collision occurs, in other words a molecule is approximated by a billiard ball.

#### 7.2.1.3 Conditions for the switch between the models for the nucleation and the growth phase

There are two types of switches between the "nucleation" and "growth" phase of the grain boundary bubbles that guarantee the reversibility of the intergranular module.

**Switch from the nucleation phase to the growth phase** The first type of transition occurs when the amount of gas atoms accumulated in the so-called gas-vacancy clusters reaches a critical value, denoted by $N_{bl}^{cr}$. The definition of $N_{bl}^{cr}$ is based on the corresponding critical bubble pressure ($P_{bl}^{cr}$). The bubble pressure is determined by means of the van der Waals equation of state (cf. Eq(7.60)). The critical number of gas atoms is defined such that the hydrostatic pressure ($P_h \leq 0$) and the surface tension forces ($\gamma$) are equilibrated by the bubble pressure:

$$P_{bl}^{cr} = -\left(P_h - \frac{2\gamma}{\rho_{bl}^0}\right), \tag{7.71}$$

where the tensile stresses are positive according to the classical convention, and $R_{bl}^0 = \rho_{bl}^0 \sin\theta$. Eliminating $P_{bl}$ from Eqs. (7.71) and (7.60) yields the critical number of gas atoms in a gas-vacancy cluster above which bubbles may grow:

$$N_{bl}^{cr} = -\left(P_h - \frac{2\gamma}{\rho_{bl}^0}\right) \frac{V_{bl}}{\left[k_B T - \omega\left(P_h - \frac{2\gamma}{\rho_{bl}^0}\right)\right]}. \tag{7.72}$$

This quantity is related to the concentration of gas accumulated in all the grain boundary bubbles of the macroscopic annulus ($\hat{C}_{gbb}^{cr}$), expressed in volume of gas at normal temperature and pressure per unit volume of the oxide, by the following relationship:

$$\hat{C}_{gbb}^{cr} = N_{bl}^{cr} \cdot C_{bl} \cdot S_{gb} \cdot \mu\,. \tag{7.73}$$

The expression for the gas concentration in the gas-vacancy clusters at which grain boundary bubbles start to grow may thus be written as follows:

$$\hat{C}_{gbb}^{cr} = -\left(P_h \rho_{bl}^0 - 2\gamma\right) \frac{\phi_{bl} S_{gb}}{\left[k_B T - \omega\left(P_h - \frac{2\gamma}{\rho_{bl}^0}\right)\right]} \frac{4 f(\theta)\mu}{3\sin^2\theta}, \tag{7.74}$$

where I have accounted for the lenticular shape of the grain boundary bubbles.

**Switch from the growth (shrink) phase to the nucleation phase** During the bubble growth phase of the intergranular module, I solve the set of ODE made up of Eqs.(7.38)-(7.40) along with an algebraic constraint, which corresponds to the condition for the transition. In particular, when the radius of the bubbles, calculated by means of Eq.(7.38), reaches a certain

lower limit, I assume that the nucleation phase starts over again. This can happen when the grain boundary bubbles shrink due to release via the tunnel network ($J_5$), fission induced re-solution or radioactive decay. The lower limit for the grain boundary bubble radius of curvature is set to $\rho_{bl}^{cr} = \rho_{bl}^{0}$ .

### 7.2.2 The grain boundary mechanisms in the athermal domain

The open surface of the fuel pellets provides an easy escape route for the gas atoms. In the previous sections, I described how at high temperatures ($\geq 1100$ °C) release mainly occurs via an open tunnel network along grain boundaries resulting from the precipitation, growth and interconnection of gas filled bubbles. At low temperatures such grain boundary bubbles are absent, hence athermal release takes place at the open surface resulting e.g. from the fabrication process [13, 14, 152]. In addition, Dehaudt and co-workers [102] pointed to the appearance of fine channels along the grain edges above certain burnup values, even when lenticular grain face bubbles are absent. A certain fraction of the grain boundary surface may thus be in contact with the open void at low temperatures, although gas filled grain boundary bubbles are not yet established. This portion of the grain boundary will be referred to as the *athermal* open porosity fraction, since it mainly affects fission gas release at low temperatures.

Several fuel performance codes for LWR fuel account for the initial porosity distribution in their fission gas release models empirically [152, 172, 173, 210]. Tayal et al. [155] introduced an empirical relationship for the fraction of the grain boundary bordering on the grain edge tunnels - assumed to be connected to the open void - as a function of burnup in CANDU fuel. The subject of the present section is to describe how I have accounted for this athermal open porosity fraction in my model for fission gas release in LWR fuel.

#### 7.2.2.1 General form of the intergranular equations

In a second step of the development of the intergranular module, I have considered two independent types of cavities at the grain boundaries. On one hand, there are the gas filled bubbles resulting from fission gas precipitation as described previously. They cover a fraction ($\phi_{bl}$) of the grain boundary surface. On the other hand, there is the athermal open porosity fraction resulting from the fabrication process and the grain edge tunnel formation. This open porosity covers another areal fraction ($\phi_a$) of the grain face.

As illustrated in Fig. 2.5 on p. 35, a part of the gas atoms arriving at the grain boundary by volume diffusion are released directly when impinging on this athermal open porosity ($\phi_a J_1$). Another fraction is accommodated in the gas filled bubbles ($\phi_{bl} J_1$), and the remainder is dissolved in the grain boundary $[(1 - \phi_{bl} - \phi_a)\, J_1]$. The athermal open porosity fraction thus affects the set of ODE governing the intergranular module, both in the nucleation phase:

$$\frac{d\hat{C}_{gbv}}{dt} = (1 - \phi_{bl} - \phi_a) J_1 - J_2 - J_3^v - \lambda \hat{C}_{gbv} \,, \tag{7.75}$$

$$\frac{d\hat{C}_{gbb}}{dt} = \phi_{bl} J_1 + J_2 - J_3^b - \lambda \hat{C}_{gbb} \,, \tag{7.76}$$

as well as in the growth phase:

$$\frac{d\rho_{bl}}{dt} = \frac{\Omega \delta_{gb}}{4 f(\theta) k_B} \frac{D_{gb}^v}{T \rho_{bl}^2} \left( P_{bl} + P_h - \frac{2\gamma}{\rho_{bl}} \right) k\left(\phi_{bl}\right) \,, \tag{7.77}$$

$$\frac{d\hat{C}_{gbv}}{dt} = (1 - \phi_{bl} - \phi_a) J_1 - J_2 - J_3^v - J_4 - \lambda \hat{C}_{gbv} \,, \tag{7.78}$$

$$\frac{d\hat{C}_{gbb}}{dt} = \phi_{bl} J_1 + J_2 - J_3^b + J_4 - J_5 - \lambda \hat{C}_{gbb} \,. \tag{7.79}$$

Rather than introducing another type of cavity at the grain boundary, I could have assessed an initial radius of the gas filled bubbles ($R_{bl}\left(t = 0\right)$) as a function of the initial open porosity fraction. However, in this case there would only have been release when the temperature was high enough for gas atoms to form interconnected grain boundary bubbles, because only then are they assumed to be in contact with the open volume in the rod. The introduction of $\phi_a$ enables gas atoms to be released, irrespective of the fact that gas filled bubbles are created along grain boundaries (cf. Fig. 2.5). As a result, gas atoms can be released during a very low temperature irradiation with low-density fuel, that is with a large initial open porosity fraction [13, 14].

#### 7.2.2.2 Evolution of the athermal open porosity

Having explained how I account for the athermal open porosity fraction in the intergranular module, I have to describe how I compute $\phi_a$.

The athermal open porosity fraction has two contributions:

$$\phi_a = \phi_{af} + \phi_{at} \,, \tag{7.80}$$

where $\phi_{af}$ corresponds to the open porosity fraction of the fabrication process, whereas $\phi_{at}$ reflects the establishment of fine grain edge tunnels due to the grain boundary segregation effects at temperatures between $\sim$ 600 °C and $\sim$ 1000 °C [102]. The athermal open porosity fraction therefore needs to be calculated as a function of the fabrication as well as the irradiation parameters.

**Athermal open porosity in fresh fuel** The fabrication process determines the open porosity in fresh fuel pellets. In particular, this porosity is closely related to the density of the pellets, as illustrated in Fig. 7.7.

The initil open porosity is mainly situated at the pellet periphery. Nevertheless, I assumed it to be uniformly distributed in the pellet since the latter will crack after the first start-up, entailing the opening of a fraction of the initially closed porosity in the pellet [279]. Moreover,

the open pores can be associated with flake-like pores, observed in plane microstructures by means of a scanning electron microsope, which extend longer into the interior of the pellet [278].

In order to infer an order of magnitude for the portion of the grain boundary surface occupied by the initial open porosity ($\phi^0_{af}$) from the corresponding volume fraction, $(\Delta V/V)^0_{open}$, I refer to a model for the open porosity in the sintering process of crystalline solids [280, 281]. According to this approach, the individual grains are assumed to possess a uniform average size and shape. The grain is represented by a polyhedron tetrakaidecahedron (cf. Fig. 3.1 on p. 41) because it has the smallest interfacial area in a polycrystalline compact for a given grain size. The features of the open pore phase structure are such that the pores may be approximated by a continuous cylinder along the three-grain edges of the polyhedrons. The aerial fraction of the grain boundary occupied by the tunnel network can therefore be written in terms of the corresponding volume:

$$\phi^0_{af} = 1.054\sqrt{\left(\frac{\Delta V}{V}\right)^0_{open}} - 0.6190\left(\frac{\Delta V}{V}\right)^0_{open}, \tag{7.81}$$

where I have accounted for the fact that three adjacent grains share each grain edge tunnel.

The representation of initial open porosity by fine grain edge tunnels has the advantage of providing an identical model for the athermal open porosity due to the fabrication process and that due to grain boundary segregation effects (cf. Eq.(7.80)).

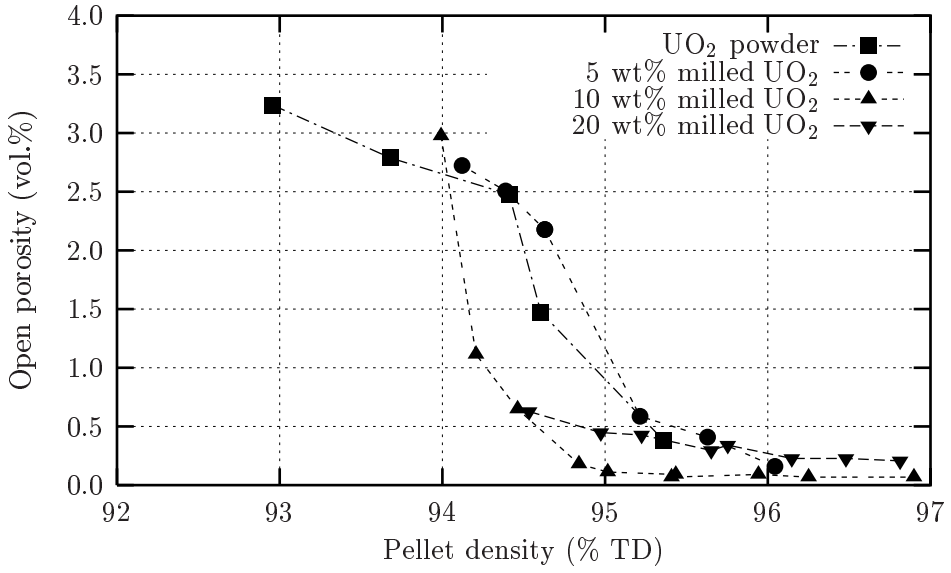


Figure 7.7: Volume fraction of open porosity, $(\frac{\Delta V}{V})^o_{open}$, as a function of the fabricated pellet density according to Song et al. [278].

**The influence of densification** The contribution of as fabricated open porosity is expected to be less important with increasing burnup because in-pile densification reduces the total porosity and therefore also the open porosity [152]. Accordingly, I assumed that the fraction of original porosity which has annealed out in the course of irradiation equals the fraction of initial open porosity fraction which has annealed out ($f_{dens}$).

The experimental investigation of Freshley et al. [226] revealed the different factors affecting densification: the temperature, the burnup, the fission rate as well as a combination of the initial density, the pore size distribution and the grain size. The ideal situation is thus to have a fundamental model for densification covering a wide range of fuel operating conditions and fuel characteristics. Assman et al. [282] and Suk et al. [283] proposed four densification zones with different mechanisms for each. However, values for the parameters involved are not always well known. Therefore many code developers have implemented empirical expressions for the fraction of the original porosity which has annealed out as a function of the local burnup, the absolute local temperature and the grain radius [152, 284, 285].

I have applied a modified version of the empirical relationship suggested by Jackson et al. [285] for LWR fuel:

$$f_{dens}\left(T, bu, R_{gr}\right) = \alpha \cdot \left[1 - \beta \exp\left(-a_1 bu\right) - \left(1-\beta\right) \exp\left(-a_2 bu\right)\right] , \tag{7.82}$$

where $a_2 = 1.5 \times 10^{-3}$ $(\mathrm{MWd/kgUO_2})^{-1}$, $a_1 = 100\, a_2$, $\alpha = 2 \exp\left[\left(T - 773\right)/300\right] / R_{gr}$ $(\mu m)^{-1}$, and $\beta = 5.12 \exp\left(-5100/T\right)/\alpha$. The modification was necessary in order to increase the annealing out of porosity at high temperatures. The resulting densification is depicted as a function of burnup in Fig. 7.8 for a grain radius of 8 $\mu m$ and for different temperature levels.

Finally, it should be underlined that the densification process of fabrication porosity is irreversible. Therefore, I have implemented $f_{dens}$ as a monotonically increasing function of burnup:

$$f_{dens}(bu_i) = max[f_{dens}(bu_{i-1}), f_{dens}(bu_i)] , \tag{7.83}$$

where the index $i$ corresponds to consecutive time intervals during which the temperature remains constant and $f_{dens}$ is calculated according to Eq.(7.82).

**Athermal open porosity in high burnup fuel** For the time being, I am not aware of systematic measurements regarding athermal open porosity due to the grain edge tunnel development as a function of burnup in LWR fuel. There are only experimental indications that, above $\sim$ 600 °C for burnup values in excess of 22 MWd/kgU and up to $\sim$ 1250 °C for burnup values in excess of 10 MWd/kgU, fine grain edge channels with a diameter less than a few tenths of a $\mu m$ can be observed in LWR fuel [102]. More recently, Lippens et al. [207] indicated similar observations in the cold zone of a pellet ($0.5 \leq R/R_{pellet} \leq 0.8$).

Hering [152] described the burnup dependence of fission gas release due to tunnel forma-

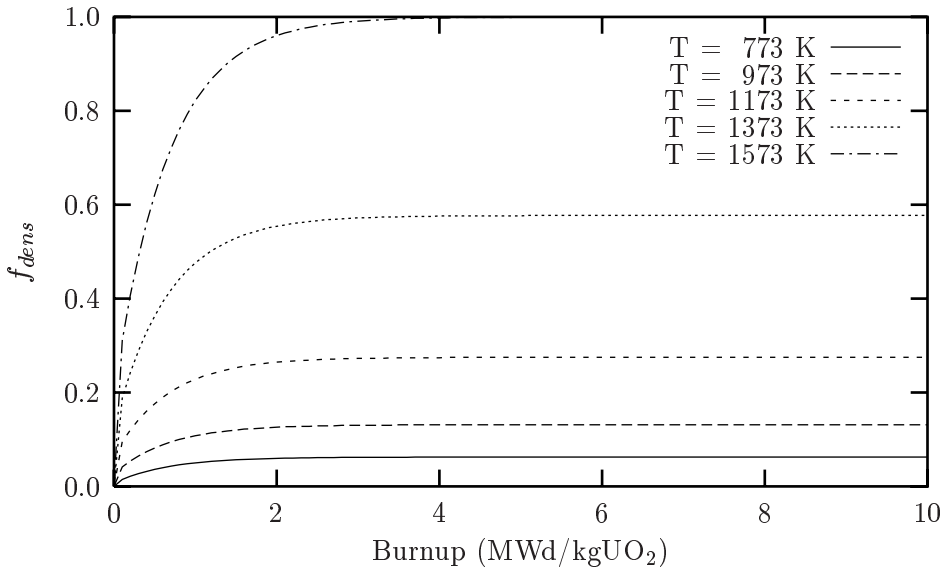


Figure 7.8: The fraction of initial open porosity fraction which has annealed out as a function of the burnup for a grain radius of 8 $\mu$m and different temperature levels, according to Eq.(7.82).

tion at grain edges empirically as a function of burnup for various temperatures. Tayal and co-workers [155] also suggested an empirical increase of the open porosity with the burnup in CANDU fuel. Dehaudt and co-workers [102] attributed the development of fine grain edge channels to segregated atoms in the grain boundaries. In line with their assumption, I consider a linear increase of $\phi_{at}$ with the concentration of fission products dissolved in the grain boundary ($\hat{C}_{gbv}$):

$$\phi_a\left(T, bu, R_{gr}\right) = \phi_{af} + \phi_{at} = \begin{cases} \phi^0_{af}\left[1 - f_{dens}\left(T, bu, R_{gr}\right)\right] + \alpha \cdot \hat{C}_{gbv} & T \geq 600\,^\circ C \\ \phi^0_{af}\left[1 - f_{dens}\left(T, bu, R_{gr}\right)\right] & T < 600\,^\circ C \end{cases} . \quad (7.84)$$

I account for the fact that grain edge tunnel development has not been observed below $\sim 600\,^\circ$C [102], whereas densification has been observed even at temperatures as low as 400 $^\circ$C [226].

## 7.3 Discussion of the fission gas release model

### 7.3.1 Comparison with other models

When introducing a new model one should emphasise its distinct features in comparison with existing models. I have already summarised and discussed the models for fission gas release from the open literature in chapter 3 . At present, I can complete this discussion by comparing them with my own approach. Nevertheless, I have restricted the present comparison to those models that consider the kinetics of the intergranular behaviour.

A conventional comparison of models is made (e.g. in the framework of a benchmark or a round-robin exercise) in terms of their performance. However, regardless of its own shortcomings, the outcome of a fission gas release model strongly depends on the performance of the other modules of the code in which it is being incorporated [13]. As a result, it is difficult to draw definite conclusions from such an exercise. Accordingly, I will mainly discuss the features of the different models for fission gas release.

Several theories [92–96, 105] only considered grain boundary diffusion to the open surface, and disregarded the intergranular bubble formation in their intergranular module. These models were therefore only applied to very low burnup fuel (cf. § 6.1), since they are not applicable to burnup levels achieved in commercial LWR fuel rods [257].

Another important group of models (e.g. [58, 107]) relies on the original work of White and Tucker [1]. The main differences of my model with respect to the latter are:

- I allow for a two-directional coupling of the kinetics of intra- and intergranular gas behaviour, both before and after the onset of release, instead of applying a correction factor to the Booth flux (cf. § 3.2.2.2).

- Gas atoms are considered to co-exist in two phases at the grain boundaries (cf. § 7.2.1), rather than simply being precipitated in bubbles. Grain boundary diffusion has been incorporated on a local scale in order to contribute to intergranular bubble growth (cf. § 6.3.4.3).

- Rather than using a fixed radius for grain boundary bubbles ($\sim 0.5\ \mu m$) with an increasing number density, I consider an increasing radius and a constant number density before the onset of thermal release, and a reduction of the number density accompanied by bubble growth once their interconnection begins (cf. Fig. 7.6 p. 127).

- I account for the effect of the hydrostatic pressure on the kinetics of fission gas release, in accordance with several experimental observations [109, 113, 186, 211, 215, 224] (cf. § 3.3.4).

- The open porosity resulting from the fabrication process is represented by means of a mechanistic model, based on the sintering process of polycrystalline solids (cf. § 7.2.2.2), instead of computing the equivalent Booth sphere radius with an empirical relationship (cf. § 3.3.5).

It should be underlined that in his most recent model for fission gas release, White [225] considers many of these modifications as well.

The last group of models introduced an equation based on Darcy's law, describing explicitly the gaseous flow through the porous medium. Hoffman et al. [176], O'Caroll et al. [179] and Ivanov [180] considered the non-stationary gas transport through the porous pellet only in

the radial direction. Furthermore, while the gas transport equation contained the source term associated with the flux of atoms leaving the grains, their model disregarded entirely the coupling with the intragranular module in the opposite direction. Lastly, they did not touch on the bubble growth or shrinkage. Consequently, their concepts are inadequate to describe the onset of release.

In view of these considerations the formalism of Kogai [181] appeared to be the best starting point for the development of my model (cf. § 3.4). Nevertheless, I had to introduce several innovations and apply a few corrections:

- Trapping and irradiation induced re-solution processes associated with intragranular bubbles have been incorporated explicitly in the effective bulk diffusion coefficient (cf. Eqs.(7.18) and (7.19)).
- The coupling between the intra- and intergranular modules is completed by the introduction of fission-induced re-solution at the grain faces (cf. Eq.(7.26)), and by using the time-varying grain boundary concentration in the boundary condition for the intragranular module (cf. Eq.(7.8)).
- The bubble sweeping effect during intergranular bubble growth has been implemented as an additional mechanism for precipitation of fission gas atoms in the grain boundary (cf. Eq.(7.57)).
- The formalism for intergranular precipitation is based on a cell model with a source term in two dimensions (cf. § 5.4.4), rather than on an isolated particle approximation in three dimensions (cf. § 5.4.5) according to which the capture rate was underpredicted by an order of magnitude [251].
- Unlike Kogai, I treat the intergranular cavities consistently as lenticular bubbles in all the expressions (e.g. in the bubble growth law, the volume calculation, etc. ) and I apply the van der Waals equation of state instead of the ideal gas law (cf. § 7.2.1.2 and § 7.2.1.3).
- The influence of the hydrostatic stress on the tube conductivity in the intergranular module (cf. Eq.(7.64)) has been eliminated since it was redundant and physically unacceptable (even compressive stresses were considered to foster bubble interconnection).
- I have introduced an athermal release mechanism that can reproduce the observations at high burnup and low temperature, where grain boundary bubble interconnection is not established (cf. § 7.2.2). Furthermore, it allows to account for another important fabrication parameter, namely the open porosity fraction (cf. § 3.3.5), while it enables to eliminate the burnup dependency of the bulk diffusion coefficient in the model of Kogai (cf. Eq.(7.11)).

Finally, unlike in the model of Kogai and White, I considered the grain size distribution in order to avoid overprediction of the released fraction [30, 96] (cf. § 3.2.3).

### 7.3.2 Limitations of the model

#### 7.3.2.1 Transient release

The validity domain of the present model is limited to normal steady state operating conditions in a PWR. Abrupt temperature or power variations may provoke macro- and micro-cracking in the pellets [14, 149–151]. I have not incorporated the influence of cracking along grain boundaries in the evolution of $\phi_a$. Cracking does not give rise to a gradual increase of the athermal open porosity as described in Eq.(7.84). Instead, it entails the sudden opening of a fraction of the grain boundaries with the instantaneous venting of the corresponding portion of accumulated gas atoms. Ideally, including this effect in a FGR model would require the precise knowledge of the local conditions (e.g. stress, temperature, etc.). Given the uncertainties pertaining to some of those parameters, most authors accounted for the cracking phenomenon in an empirical manner [13, 153–155].

Very recently, *Lösönen* [137] pointed out that the use of a conventional effective diffusion coefficient in the grains according to Speight [57] might lead to an underprediction of the release under transient conditions when pronounced bubble coarsening takes place. Nevertheless, the lack of an effective numerical method to solve the resulting set of non-linear differential equations hinders its implementation in a mechanistic model for fission gas release.

Last but not least, when the local temperature levels attained in the pellet during a severe transient are sufficient to cause restructuring ($\sim$ 1600 °C), there is a need to account for grain boundary sweeping in the release process (cf. § 2.9 and § 3.2.3). Unlike the models of Kogai and White, my model disregards this mechanism. For that reason, it would underpredict the release fraction under such circumstances, irrespective of the shortcomings mentioned above.

#### 7.3.2.2 Ultra high burnup release

Three experimental data points have recently been indicated [192] below the empirical Halden curve (cf. Eq.(3.5)) at burnup levels between 50 and 60 MWd/kg$UO_2$. Several codes have introduced a burnup dependent diffusion coefficient [171, 173], or they considered an empirical dependence of the athermal released fraction on the burnup [172, 210] in order to explain the decrease of the release threshold at high burnup values. Turnbull [192] has also considered the re-solution probability at the grain boundary bubbles to decrease with burnup.

My formalism for athermal release through the fine grain edge tunnels provides an alternative explanation. It is in line with the observations indicated recently by Lippens et al. [207] in the cold zone ($0.5 \leq R/R_{pellet} \leq 0.8$), i.e. where the temperature exceeds $\sim$ 500 °C but remains below $\sim$ 1000 °C. In this region, athermal diffusion dominates and is sufficient to

transport gas to the grain boundaries such that fine grain edge porosity develops after a given burnup, although grain face bubbles are not reported [102, 207].

The condition applied in Eq.(7.84), however, implicitly implies that my fission gas release model does not treat the so-called rim structure in $UO_2$ pellets at very high burnup [201–204]. Accurate modelling of the release processes in this region would require the precise description of the athermal restructuring in the bulk of the material with the concomitant formation of large intragranular pores [204, 237, 286]. Nevertheless, the release from the rim region appears to be limited and is only relevant at ultra high burnup ($\geq$70 GWd/tM) [207, 208].

## 7.4 Summary and conclusions

I have developed a new mechanistic model for the release of fission gas to the free volume in LWR fuel rods. The concept embodies the underlying basic mechanisms operative under steady state conditions, couples the kinetics of the intra- and intergranular behaviour of the gas atoms *in both directions* (cf. Fig. 2.5), and includes important fabrication parameters such as the grain size distribution as well as the open porosity fraction. As a result, it provides an excellent tool to assess the contribution of each mechanism, as well as the influence of each parameter individually (cf. Chapter 9).

The model is developed in two separate, but coupled, modules. The first module treats the behaviour of the fission gas atoms on a microscopic scale, i.e. in spherical grains with a distribution of grain sizes. This module considers single atom diffusion, trapping and fission induced re-solution of gas atoms associated with intragranular bubbles, and re-solution from the grain boundary into a few layers adjacent to the grain face. It determines the source term of the second module.

The second module considers the transport of the fission gas atoms along the grain boundaries to the free volume in the fuel rod. Five mechanisms are incorporated: diffusion controlled precipitation of gas atoms into bubbles, grain boundary bubble sweeping, re-solution of gas atoms into the adjacent grains, gas flow through open porosity when grain boundary bubbles are interconnected, and segregation of gas atoms in the grain faces leading to the formation of fine grain edge tunnels when the temperature remains below $\sim$ 1100 °C.

According to the present model, the release of fission gas is determined by two different components: an athermal and a thermal release component. The former is determined by the athermal open porosity fraction, which in turn has two different contributions. First of all it depends on the initial open porosity fraction resulting from the fabrication process, which is modified by in-pile densification. Secondly, it is assumed to increase due to grain edge tunnel formation.

The thermal release component is controlled by the formation of an interconnected tunnel network of grain boundary bubbles. These channels are established as soon as the temperature

and the burnup are high enough so that a sufficient amount of gas atoms have precipitated into the intergranular cavities. The growth of these bubbles takes into account the effect of the hydrostatic stress on the grain boundary bubble size. Therefore, the present model is able to handle burst release due to the lowering of the pellet clad mechanical interaction and/or the thermal stress distribution during power reductions.

The athermal open porosity fraction enables release at low temperatures where fission gas filled bubbles at grain boundaries, resulting from diffusion controlled precipitation, are not yet developed. Consequently, it provides an alternative explanation for the decrease of the release threshold at high burnup, rather than introducing an increase of the bulk diffusion coefficient, or a reduction of the re-solution rate at the grain boundaries.

# Chapter 8

# Model implementation

## Contents

The fission gas release model that was presented in the previous chapter has been implemented in a programme of approximately 30 subroutines. This chapter discusses the structure, solution scheme, and the major subroutines involved in the solution scheme of the programme.

The most important issue for the programme implementation is the reduction of the calculation time, while assuring sufficient precision. The running time should be limited because of the large number of fuel performance calculations required in code validation and licensing procedures. The precision on the concentration profiles, in the order of 0.1 %, is imposed by the experimental values of fission gas release under normal operating conditions, generally in the order of a few percent. In this context, I will justify the choice of both the numerical routines and the corresponding parameters of the major modules of the programme. In addition, I will highlight the special features that were necessary to guarantee the programme convergence, and assess their influence on the precision of the outcome.

## 8.1 Global solution scheme

The model for fission gas release presented in the previous chapter has been implemented by means of the flowchart illustrated in Fig. 8.1 . The modular structure of the programme ensured a flexible implementation and facilitated the step-wise developments.

The flowchart begins with the case setup, following through the different loops, and ending with output. Each of the key modules will now be discussed, following the chronological structure of the flowchart.

## 8.2 Programme initialisation

The first portion of the flowchart has to do with case setup and initialisation, which is handled in the subroutine PROGRAMINIT. This includes reading input data and initialising the fixed physical variables such as the pellet dimensions, the mean grain size, ... along with the fixed numerical parameters such as the convergence criterion for the grain boundary concentrations (cf. § 8.4.2, § 8.5 and § 8.6).

In the second step of the programme initialisation, a subroutine (GENMESH) is called in order to generate the macro- and microscopic mesh points, and in order to compute the corresponding volumes. Before generating the grid points in the collection of spherical grains, however, I needed to define the discrete grain size distribution based on Eq. (7.4), which is carried out in a distinct subroutine (GRAINSDISTR).

The grain size distribution is divided in $NRK$ groups. Each group with index $k$ ($k = 1 \ldots NRK$) is characterised by a minimum and a maximum radius, $R_{gr}^{k,min}$ and $R_{gr}^{k,max}$ respectively. They are chosen at regular intervals between between 0 and $2R_c$ (cf. § 7.1.1):

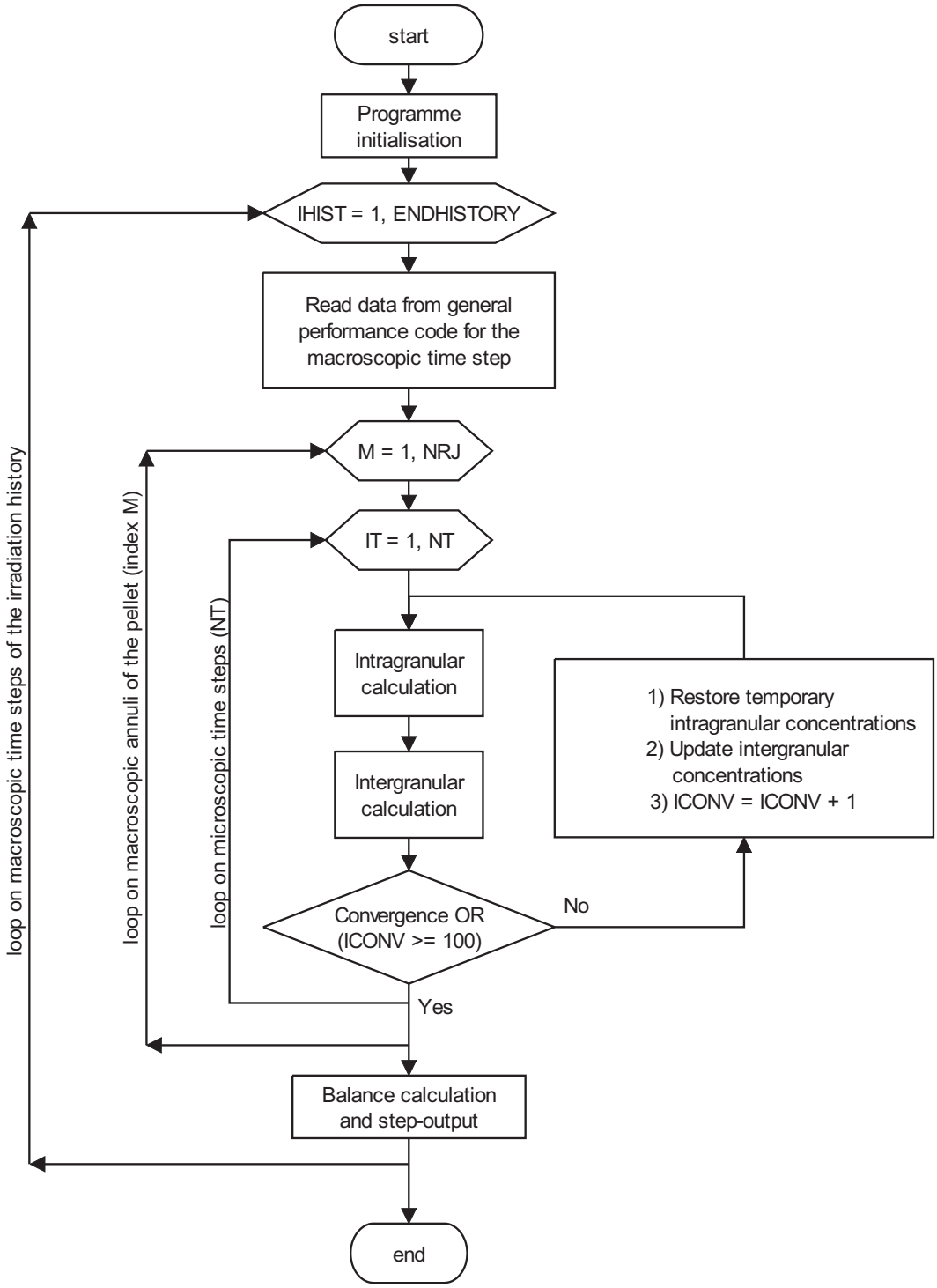


Figure 8.1: Simplified flowchart of the programme for the fission gas release calculation.

| type of mesh | formula | index |
|---|---|---|
| equidistant | $x_i = x_{i-1} + \frac{b-a}{NR}$ | 0 |
| equivolume | $x_i = \sqrt[3]{x_{i-1}^3 + \frac{(b-a)^3}{NR}}$ | 1 |
| dichotomic (1/2) | $x_i = \frac{1}{2}\left[x_{i-1} + (b-a)\right]$ | 2 |
| dichotomic (2/3) | $x_i = \frac{2}{3}\left[x_{i-1} + (b-a)\right]$ | 3 |

Table 8.1: Four different mesh types for the micro- and macroscopic geometries.

$R_{gr}^{k,max} - R_{gr}^{k,min} = 2R_c/NRK$. The average radius of the grains in group $k$ is given by:

$$\overline{R_{gr}^k} = \frac{\int_{R_{gr}^{k,min}}^{R_{gr}^{k,max}} R_{gr} P\left(R_{gr}\right) dR_{gr}}{\int_{R_{gr}^{k,min}}^{R_{gr}^{k,max}} P\left(R_{gr}\right) dR_{gr}} \quad \forall\, l, m \tag{8.1}$$

where $P\left(R_{gr}\right)$ is derived from the Hillert distribution function presented in Eq.(7.4). The volume fraction of the grains in group $k$ is computed by means of

$$f_{klm} = \frac{\int_{R_{gr}^{k,min}}^{R_{gr}^{k,max}} R_{gr}^3 P\left(R_{gr}\right) dR_{gr}}{\int_0^{2R_c} R_{gr}^3 P\left(R_{gr}\right) dR_{gr}} \quad \forall\, l, m\,. \tag{8.2}$$

The computation of the grain size distribution is needed for each index $l = 1, 2$, corresponding to the composition of the grain, as well as for each index $m = 1 \cdots NRJ$, corresponding to the macroscopic rings. However, in the present state of the model, I have only considered a single composition ($UO_2$), hence $f_{k2m} = 0 \quad \forall\, k, m$. The extension of the model to MOX fuel would require, among others, to account for the presence of Pu-rich agglomerates [91] wherein a high fractional release may occur that is accompanied by the formation of large pores [98, 287]. The structure in these agglomerates is sometimes even very similar to the rim structure observed in high burnup $UO_2$ fuel [98] (cf. § 7.3.2.2). For the time being several simple FGR models have been proposed for MOX fuel rods [154, 173]. Proper mechanistic modelling of FGR in MOX fuel requires additional research.

The next step in the subroutine GENMESH is to determine the micro- and macroscopic grid points and to compute the corresponding volumes. Four different mesh types have been implemented and are indicated in Table 8.1. For the macroscopic grid, I have chosen an equivolume type of grid (cf. § 8.5) with $a = R_{hole} = R_1 < \cdots < R_m < \cdots R_{NRJ+1} = R_{pellet} = b$, whereas in the grains, I have adopted a dichotomic (1/2) type of mesh with $a = 0 = r_1 \cdots < r_i < \cdots < r_{NRV+1} = b$ (cf. § 8.4.2).

The final step in the subroutine for the mesh generation is related to the implementation of the intragranular source term due to re-solution (cf. Eq.(7.26)). In order to model accurately the steep concentration gradients in the vicinity of the grain boundary, it was necessary that mesh points be bunched close together in that region (cf. § 8.4.2). To this end, the dichotomic

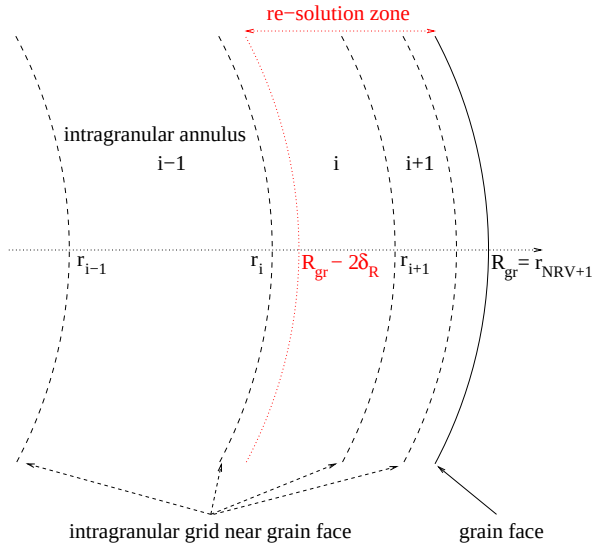


Figure 8.2: Schematic representation of the re-solution zone and the grid near the grain face

mesh type provided the most appropriate solution. However, the resulting mesh size at the grain face ($\sim$ 15 nm) is typically smaller than $2\delta_R$ ($\sim$ 40 nm). Therefore, the re-solution process at the grain boundary will deposit gas atoms in more than one layer, more precisely in those with an index $i$ ($1 \leq i \leq NRV$) between $NRL$ and $NRV$ (cf. Fig 8.2). I determined $NRL$ in two steps. First, I found out the intragranular annulus $i$ for which

$$r_i \leq R_{gr} - 2\delta_R \leq r_{i+1}\,. \tag{8.3}$$

In a second step, I verified whether the volume between $r_{i+1}$ and $(R_{gr} - 2\delta_R)$ is smaller or equal to the volume between $(R_{gr} - 2\delta_R)$ and $r_i$. If such is the case, then $NRL$ is set equal to $i+1$, otherwise $NRL$ is set equal to $i$:

$$NRL = \begin{cases} i+1 & (R_{gr} - 2\delta_R)^3 \geq \frac{r_i^3 + r_{i+1}^3}{2} \\ i & (R_{gr} - 2\delta_R)^3 < \frac{r_i^3 + r_{i+1}^3}{2} \end{cases} \tag{8.4}$$

After the computation of the different grain radii ($R_{klm} = \overline{R_{gr}^k}$) and the corresponding volume fractions ($f_{klm}$) by the subroutine GENMESH, it is possible to calculate the specific surface of the grain boundaries in each macroscopic annulus of the pellet according to Eq.(7.29) in the subroutine PROGRAMINIT.

Following the subroutine PROGRAMINIT, another subroutine (INITLSODAR) is invoked in order to allocate values to the fixed numerical parameters of the subroutine for the intergranular module described in section 8.6.

The programme initialisation is ended by the subroutine INIT1STEP, wherein the initial concentration profiles are allocated. There are two possibilities: either the fission gas release

calculation starts in fresh fuel, in which case the concentrations are zero; either the re-start option is being used, in which case the concentration profiles of a previous calculation are used.

## 8.3 Coupling with a general fuel performance code

Proper testing of a fission gas release model requires its coupling with a general fuel performance code - or simply *the code* - in view of the interrelationship with other phenomena. However, given the large calculation time consumed by a mechanistic model for FGR, the coupling is generally one-way. More precisely, the code provides the radial distribution of the temperature, the fission rate density, the burnup, and the time-step length on input for the stand-alone version of the fission gas release model. There is no feed-back from the stand-alone FGR model to the code.

The coupling of the FGR model with the fuel performance code is required at the beginning of each macroscopic time-step ($\Delta t_{macr}$). These time-steps correspond to periods in the irradiation history of the fuel rod during which the temperature as well as the fission rate density are deemed constant.

I have implemented the coupling with a general fuel performance code in two stages. In a first phase, I employed the temperature distribution generated by the FTEMP2 code of the OECD Halden Reactor Project [288]. This programme is very easy to use and assesses the radial temperature distribution in a LWR fuel rod, taking into account the porosity fraction, the enrichment, the neutron spectrum, etc. [267]. Nevertheless, the discretisation of the radial distribution is different in the FTEMP2 code from that in the FGR model. For this reason, and in line with Nakamura et al. [211], I have assumed a parabolic temperature distribution in the pellet:

$$T(R) = T_s + (T_c - T_s)\left[1 - \left(\frac{R}{R_{pellet}}\right)^2\right], \tag{8.5}$$

where the central and surface temperature, $T_c$ and $T_s$ respectively, were provided by FTEMP2.

A further simplification in the first stage of the model implementation came from the normalised fission rate distribution in the pellets ($\dot{f}$) [289], which was taken to be independent of burnup:

$$\dot{f}(x) = \frac{\dot{F}(x)}{\dot{F}_{avg}} = \frac{\phi(x)}{\int_0^1 \phi(y)\, y dy}, \tag{8.6}$$

where

$$\phi(x) = 1 + 0.4x^4, \tag{8.7}$$

$x = R/R_{pellet}$, and $\dot{F}_{avg}$ corresponds to the pellet averaged fission rate density. Equation (8.6) bore consequences on the radial distribution of the source term for fission products and the local burnup accumulation as well, since both are proportional to $\dot{f}$.

The last simplification in the first phase was related to the hydrostatic stress distribution. In line with Kogai, who inferred the hydrostatic pressure from the local clad deformation [181], I have introduced a constant and uniform value across the pellet in each case.

In a second stage of the coupling with a general fuel performance code, I have used the COMETHE code [173] from BELGONUCLEAIRE to provide on input the radial distribution of the temperature, the power and the burnup in the pellets, as well as the pellet-clad contact pressure [290]. As such, I was able to avoid the simplifications for the temperature and the power distributions introduced in the first stage. In addition, the pellet-clad contact pressure was used as a (rough) estimation for the hydrostatic stress distribution in the pellet. A more representative approximation of the local hydrostatic pressure requires the precise knowledge of the radial temperature distribution, irradiation and thermally induced creep, gaseous and solid fission product swelling, etc. . An attempt to obtain a better assessment of the hydrostatic stress distribution was presented by Nakamura et al. [211]. Yet, an accurate calculation is still not available [219].

Finally, the coupling of the fission gas release model with the COMETHE code requires the development of an interface, the subroutine COMETHE_INPUT. This routine not only handles disparities in the order of the arrays, it mainly serves the purpose of adapting the units of the fission rate, temperature, burnup and hydrostatic stress distributions.

## 8.4 Implementation of the intragranular module

The implementation of the intragranular module warrants special attention, both for the precision and the running time. The former requirement is due to the fact that the majority of fission gas atoms remain within the grains under normal operating conditions. Since the fraction of released gas atoms is generally in the order of a few percent, it is desirable to obtain a precision on the balance calculation of fission gas atoms in each grain in the order of 0.1%. The second requirement stems from the large number of times the subroutine is invoked by the main program. This, in turn, is due to the loops on the different classes of grains $(k, l)$ in each macroscopic ring $m$, as well as to the convergence loop on the grain boundary concentrations ($ICONV$). The two requirements are conflicting in the sense that, increasing the number of meshes and reducing the time-step length might be beneficial for the precision, but not for the calculation time.

Keeping in mind the constraints of precision and running time, it was necessary to address two important (generic) questions:

1. Which numerical technique/routine should I apply to solve the mathematical problem at hand?

2. How can I determine the value of the numerical parameters used by this routine in order to comply with the constraints?

These questions form the subject of the two following sections.

### 8.4.1 Determination of the numerical routine

The mathematical problem for the intragranular module described in § 7.1 is non-linear. This arises mainly from the boundary condition and the re-solution effect near the grain face. The non-linearity makes the use of a numerical method inevitable; analytical solutions can only be obtained under certain simplifying conditions [291].

The routine selected for the implementation of the intragranular module (PARDI) has been developed at BELGONUCLEAIRE and provides an approximate solution for the one-dimensional Sturm-Liouville equation in different geometries [292]. It rests on the restricted variational principle of Lebon-Lambermont [293], which is combined with Kantorovitch's separation of variables in order to reduce the partial differential equation to a set of ordinary differential equations. Euler's implicit partial integration method is then applied to this set of ODE. For a more detailed description of the numerical technique, I refer the interested reader to previous applications of the subroutine to problems of heat transfer [294, 295] and Pu-homogenisation in MOX fuel [91].

Verbeek [296] and van Vliet [297] enumerated the main advantages and draw-backs of the different numerical techniques on hand for the diffusion equation in one dimension. The main advantages of variational techniques are their short computational times, their simplicity and the fact that the solutions are given in analytic forms. Moreover, a judicious choice of parabolic trial functions of the radial variable in the separation of variables allowed to obtain the local concentrations, together with the average values in each finite element. This simplified the balance calculation after each time step, more precisely the volume integration of the concentration profile in each grain (cf. § 8.7). Finally, the implicit Euler technique for the time-integration required minimal computer memory - since it is a one-step method - while it assures unconditional stability for every time-step length. For these reasons, I have also employed the PARDI routine to solve the diffusion equation in each class of grains.

### 8.4.2 Determination of the numerical parameters

The numerical parameters required on input of the subroutine PARDI amount to five: the type of mesh ($MESHCV$), determined by the index in Table 8.1; the number of rings in every grain ($NRV$); the number of microscopic time steps ($NT$); the microscopic time-step length ($DT$); and the size of the imaginary supplementary layer near the grain face ($\delta_s$). It should be underlined that the last parameter affects the intergranular module as well (via the intergranular source term, see for instance Eq.(7.48)). Furthermore, $NT$ or $DT$ should be optimised, since they are related by $\Delta t_{macr} = NT \times DT$.

Testing the influence of these parameters on the precision of the subroutine PARDI has already been undertaken previously [91]. Nevertheless, the former analysis was limited for

various reasons:

- Only the precision has been taken into consideration while the calculation time has been disregarded.
- The precision ($P$) was assessed by comparing the analytic solution ($C_{ex}$) with the numerical result ($C_{num}$) in each mesh point and using the Euler norm of the corresponding vectors:

$$P = \log \left[ \frac{\sqrt{\sum_{i=1}^{NRV} \left(C_{ex}^{i} - C_{num}^{i}\right)^2}}{\sqrt{\sum_{i=1}^{NRV} \left(C_{ex}^{i}\right)^2}} \right] . \tag{8.8}$$

  This is a measure of the number of exact figures in the numerical result. Yet, it is less correlated to the precision on the fraction of FGR in comparison with the precision defined by Eq.(8.9) below.
- The influence of the imaginary supplementary layer width ($\delta_s$) on the balance of the fission gas atoms has not been investigated.
- The test design was based on the one-factor-at-the-time approach, which is both very slow and can lead to misleading results when important interactions exist between several parameters.

A properly chosen set of tests should therefore be carried out in order to optimise $NRV$, $NT$ (or $DT$), $MESHCV$, and $\delta_s$. Their optimisation involved several steps, which will be outlined in the following sections. For the sake of brevity, however, I will merely describe the methodology and summarise the results. The reader is referred to an internal report of 168 pages [291] for a comprehensive description of the optimisation procedure.

#### 8.4.2.1 Phase 1

**Criteria for the optimisation** Two responses were used as criteria for the optimisation of the parameters. The first criterion is the running time of PARDI, more precisely the central processing unit (CPU) time. The second criterion is the precision of PARDI after a certain period of time:

$$P = \log \left\| \frac{Q_{num} - Q_{ex}}{Q_{ex}} \right\| , \tag{8.9}$$

where $Q_{num}$ and $Q_{ex}$ are the balance of fission products in a single spherical grain obtained by means of PARDI and an analytic solution, respectively.

Two analytical solutions, describing the concentration profile in a single spherical grain with both constant and uniform parameters (source term and diffusion coefficient), have been developed [291]. One solution dealt with the stable isotopes whereas the second solution concerned the radioactive fission products. The initial condition and the boundary conditions were similar in both cases :

- a zero concentration gradient in the centre of the grain in view of the symmetry;
- a zero concentration at the grain boundary, which corresponds to the most severe condition from the numerical point of view (because of the large concentration gradient);
- a uniform initial concentration ($\theta_v$) in the grain.

Integrating the concentration profiles over the volume of the grain yielded the expression for $Q_{ex}$ as a function of time [291]:

$$\begin{aligned} Q_{ex}(t) &= \frac{S_v}{D_v}\left\{\frac{4\pi}{45}R_{gr}^5 - \frac{8R_{gr}^5}{\pi^3}\left[\sum_{n=1}^{\infty}\frac{1}{n^4}\exp\left(-\frac{n^2\pi^2 D_v}{R_{gr}^2}t\right)\right]\right\} \\ &\quad + \frac{8R_{gr}^3\theta_v}{\pi}\left[\sum_{n=1}^{\infty}\frac{1}{n^2}\exp\left(-\frac{n^2\pi^2 D_v}{R_{gr}^2}t\right)\right], \end{aligned} \tag{8.10}$$

for stable fission gas atoms, and

$$\begin{aligned} Q_{ex}(t) &= S_v\frac{8R_{gr}^3}{\pi}\left[\sum_{n=1}^{\infty}\frac{1}{n^2}\frac{1}{\left(\frac{n^2\pi^2 D_v}{R_{gr}^2}+\lambda\right)} - e^{-\lambda t}\sum_{n=1}^{\infty}\frac{1}{n^2}\frac{\exp\left(-\frac{n^2\pi^2 D_v}{R_{gr}^2}t\right)}{\left(\frac{n^2\pi^2 D_v}{R_{gr}^2}+\lambda\right)}\right] \\ &\quad + \theta_v e^{-\lambda t}\frac{8R_{gr}^3}{\pi}\left[\sum_{n=1}^{\infty}\frac{1}{n^2}\exp\left(-\frac{n^2\pi^2 D_v}{R_{gr}^2}t\right)\right] \end{aligned} \tag{8.11}$$

for radioactive fission gas atoms. The non-uniform contribution to the intragranular source term is disregarded:

$$S_v = S_{fis} = y\cdot\mu\cdot\dot{F}\,. \tag{8.12}$$

The precision of PARDI defined by Eq.(8.9) is more suitable in comparison with the precision according to Eq.(8.8). Indeed, the relative error on $Q_{ex}$ is more closely related to the relative error on the released fraction of gas atoms, in comparison with the Euler norm of the relative error on the concentration in each mesh point.

**Parameters under consideration** There were only three numerical parameters that could be taken into account: $NRV$, $DT$, and $MESHCV$. The effect of the supplementary layer width ($\delta_s$) could not be assessed because it is impossible to obtain an analytical solution including this parameter. Furthermore, $\delta_s$ affects the intergranular module as well. Therefore, the optimisation of $\delta_s$ should consider its influence on the (global) FGR calculation, instead of its effect on $Q_{ex}$ alone.

In addition to the numerical parameters, there were four physical parameters under consideration: the number of Fourier ($\beta = \frac{D_v\cdot NT\cdot DT}{R_{gr}^2}$), where I have used $R_{gr} = 8\mu m$; the fission rate density or source term ($S_v$); the decay constant of radioactive species ($\lambda$); and the initial concentration ($\theta_v$).

| Case | $\beta$ | $\dot{F}$ | $\lambda$ | $\theta_v$ | $NRV$ | $DT$ | $MESHCV$ |
|---|---|---|---|---|---|---|---|
| 1 | − | − | − | − | − | − | − |
| 2 | − | − | − | + | + | + | + |
| 3 | − | + | + | − | − | + | + |
| 4 | − | + | + | + | + | − | − |
| 5 | + | − | + | − | + | − | + |
| 6 | + | − | + | + | − | + | − |
| 7 | + | + | − | − | + | + | − |
| 8 | + | + | − | + | − | − | + |

Table 8.2: Test matrix corresponding to the $L_8\left(2^7\right)$ Taguchi procedure, which served as the basis for the experimental design in first phase of the intragranular parameter optimisation. The + and − sign correspond to the maximum and minimum value of the parameter, respectively.

It should be pointed out that I made use of the number of Fourier ($\beta$) in the first phase, unlike in the second phase where I employed the relative diffusion coefficient ($D_v^{'} = D_v/R_{gr}^2$). This is one of the modifications made in the course of the iterations between the several phases of the precision tests. This change, however, did not affect the conclusions of the first phase [291].

**Test matrix** In order to assess the influence of the 7 parameters on the intragranular module, I have assigned an upper and lower limit to each parameter. There was only one exception, namely $MESHCV$, for which there are four different values (cf. Table 8.1). Assessing the influence of the 7 parameters mentioned above by means of a full factorial design, would thus require $4 \times 2^6 = 256$ tests.

In order to reduce the number of tests and to determine the most important parameters, I applied a fractional factorial method, in particular the Taguchi approach [298–300]. This method basically consists of choosing a limited number of representative tests in a systematic manner. The test matrix for the first phase of the intragranular parameter optimisation according to the $L_8\left(2^7\right)$ Taguchi procedure is indicated in Table 8.2, where the + and − sign correspond to the maximum and minimum value of the parameter, respectively.

The most interesting feature of the test matrix is the orthogonality, i.e. the equal number of + and − signs in each column. This assures an equilibrated analysis since it is the only fair way to allow averaging out the effect of all remaining parameters when estimating one particular parameter effect. Indeed, the magnitude of the effect of each parameter is assessed by means of an analysis of means, using several response tables (i.e. a table for the precision and the calculation time). Since the parameters have 2 levels, the magnitude of the effect of each parameter is computed as the difference between the average response for both levels.

The upper and lower limit values for the parameters are tabulated in Table 8.3. The range of the physical parameters is representative of normal and off-normal irradiation conditions

| Parameter | unit | min (−) | max (+) |
|---|---|---|---|
| $\beta$ | - | $10^{-10}$ | 1 |
| $\dot{F}$ | $\#/\mu m^3_{ox}/s$ | 1 | 20 |
| $\lambda$ | $s^{-1}$ | $10^{-9}$ | 1 |
| $\theta_v$ | $\mu m^3_{gas}/\mu m^3_{ox}$ | 0 | 20 |
| $NRV$ | - | $2^2$ | $2^4$ |
| $DT$ | s | $6.2 \times 10^2$ | $6.4 \times 10^4$ |
| $MESHCV$ | - | 0 or 1 | 2 or 3 |

Table 8.3: Range of the parameters for the first phase of the intragranular parameter optimisation

in nuclear fuel [291], and is extremely high in comparison with the variation of the numerical parameters. The maximum value of $NRV = 16$ is limited by the dichotomic test, since the outer layer has a width on the order of $\frac{8\,\mu m}{2^{NRV-1}} = 0.24$ nm, which is less than the lattice constant of $UO_2$ (= 0.547 nm). The outer layer width is also determined by the grain radius. The latter has been fixed to 8 $\mu m$, which is a representative average value for LWR fuel.

The parameter $MESHCV$ may have 4 different values: 0/1/2/3. However, unlike indicated in Table 8.1, the indices correspond respectively to the equivolume / equidistant / dichotomic / sinusoidal type of mesh during the optimisation of the intragranular module. The latter type of mesh is defined by:

$$r_i = r_1 + (R_{gr} - r_1) \cdot \sin\left[\frac{(i-1)\,\pi}{2NRV}\right] . \tag{8.13}$$

In order to follow the $L_8\left(2^7\right)$ Taguchi procedure indicated in Table 8.2, the parameters may only have two different values (min. or max.). In order to cope with the four values of $MESHCV$, I have therefore reproduced the same table, though with different values for the parameter $MESHCV$. More precisely, I have used 0 and 2 for the minimum and maximum values of the parameters $MESHCV$ in the first 8 cases, respectively, while in the subsequent 8 cases, I employed 1 and 3.

Finally, in order to increase the total number of tests - thus improving the statistics of the results - I performed a supplementary series of 16 calculations with a matrix containing the opposite signs. In this way, I preserved the orthogonality of the tests, while the total number of tests was raised to 32.

**Conclusions of the first intragranular phase** From the precision tests in the first phase of the optimisation of the intragranular numerical parameters, the dichotomic mesh type emerged as the best choice in terms of precision and required running time. An equidistant mesh type would require too much grid points in order to achieve the required precision near the grain face (e.g. [58] $\Delta r = \delta_R/4 \simeq 5.5 \times 10^{-3}\ \mu m$).

The results also revealed the predominant role played by the time constants (i.e. the relative diffusion coefficient or the number of Fourier, and the decay constant) in comparison with the other physical parameters, for the optimisation of the numerical parameters.

#### 8.4.2.2 Phase 2

**Objective** Having fixed the type of mesh in the first phase, the objective of the second phase consists of determining the optimum value of the two remaining numerical parameters, namely $NRV$ and $DT$. The former is a fixed parameter and will be determined first. The optimum value of $DT$, denoted by $DT_{max}$, corresponds to the upper limit of the time-step length in order to ensure that the precision remains below 1 %. $DT_{max}$ is a function of the time constants $D_v^{'}$ and $\lambda$, hence it is very likely to vary during the irradiation history.

**Criteria for the optimisation** For the determination of the optimal number of meshes ($NRV$), the same optimisation criteria have been used as in the previous phase. For the subsequent determination of $DT_{max}$, however, an improved criterion has been applied: rather than considering the precision at the end of a certain number of time steps, I monitored the worst precision during the entire irradiation period. This was necessary since the precision may evolve over time (cf. third phase in § 8.4.2.3).

In a first attempt, I used 1000 time steps which proved to be sufficient for the stable fission products in the third phase [291]. For the radioactive fission products it turned out that I needed 10000 time steps. However, the total time step length is limited to $10^8$ s ($\simeq 3.2$ years). Whenever the total time step length with NT = 10000 exceeds this maximum, I limit NT so as to assure that $NT \times DT \leq 10^8$ s. The number of time steps used in the second phase has been justified in the third phase (cf. § 8.4.2.3).

**Parameters under consideration** In addition to the two numerical parameters, $NRV$ and $DT$, there remain only two (predominant) physical parameters: the number of Fourier ($\beta$) and the decay constant of radioactive species ($\lambda$).

It should be pointed out that I make use of $\beta = D_v^{'} \times t$ for the determination of $NRV$, whereas for the determination of $DT$, I employ the relative diffusion coefficient ($D_v^{'}$) instead. This is one of the modifications made in the course of the iterations between the three phases of the precision tests. Nevertheless, this change does not affect the optimum number of meshes, since I have varied both the relative diffusion coefficient and the time step length (cf. test matrix for $NRV$).

The results in the first phase revealed that the other physical parameters, $S_v$ (or $\dot{F}$) and $\theta_v$, did not affect the precision nor the calculation time substantially. Accordingly, I have disregarded their variation and applied nominal values ( $\theta_v = 10\,\mu m^3_{gas}/\mu m^3_{ox}$ and $S_v = 1.116 \times 10^{-7}\,\mu m^3_{gas}/\mu m^3_{ox}/s$ [291]). Given the reduced number of variable parameters, I was

| Case | $\beta$ | $\lambda\,(s^{-1})$ | $D_v\,(\mu m^2/s)$ | $NT$ | $DT\,(s)$ | $\Delta\beta$ |
|---|---|---|---|---|---|---|
| 1a | $10^{-10}$ | $10^{-1}$ | $10^{-13}$ | $10^4$ | 6.4 | $10^{-14}$ |
| 1b | | $10^{-3}$ | | | | |
| 1c | | $10^{-4}$ | | | | |
| 1d | | $10^{-5}$ | | | | |
| 1e | | $10^{-7}$ | | | | |
| 2a | $10^{-6}$ | $10^{-1}$ | $10^{-9}$ | $10^4$ | 6.4 | $10^{-10}$ |
| 2b | | $10^{-3}$ | | | | |
| 2c | | $10^{-4}$ | | | | |
| 2d | | $10^{-5}$ | | | | |
| 2e | | $10^{-7}$ | | | | |
| 3a | $10^{-4}$ | $10^{-1}$ | $5 \times 10^{-8}$ | $2 \times 10^4$ | 6.4 | $5 \times 10^{-9}$ |
| 3b | | $10^{-3}$ | | | | |
| 3c | | $10^{-4}$ | | | | |
| 3d | | $10^{-5}$ | | | | |
| 3e | | $10^{-7}$ | | | | |
| 4a | 1 | $10^{-1}$ | $10^{-6}$ | $10^5$ | 640 | $10^{-5}$ |
| 4b | | $10^{-3}$ | | | | |
| 4c | | $10^{-4}$ | | | | |
| 4d | | $10^{-5}$ | | | | |
| 4e | | $10^{-7}$ | | | | |

Table 8.4: First test matrix for $NRV$ in the second phase of the optimisation procedure for the intragranular parameters

able to refine the tests, as explained in the following section.

**Test matrix for $NRV$** For the determination of the optimum value for $NRV$, I have used two successive test series. In the first series of calculations $NRV$ varied between 2 and 32, whereas the other variables are tabulated in Table 8.4 . The results suggested an optimum value between 8 and 16.

In the second series, I refined the loop on $NRV$ by using $NRV = 8 + i \quad (i = 0, 2, \ldots 8)$. I also included the stable fission products ($\lambda = 0$) as cases 1f, 2f, 3f and 4f. Furthermore, I compared the results obtained by means of the dichotomic and the sinusoidal mesh type in order to corroborate the choice of the mesh type in the first phase. Finally, despite the fact that the time-step length is the subject of a more detailed analysis below, I assessed the effect of multiplying $DT$ by a factor 100 in order to ascertain whether the optimum value of $NRV$ remained valid.

**Conclusions from the tests for $NRV$** From all the loops on $NRV$, encompassing both dichotomic and sinusoidal mesh types with two different values of $DT$, I could draw the following conclusions:

- The dichotomic mesh type with $NRV = 10$ constitutes a good compromise for stable fission products, that is we can assure a precision better than 0.1 % on the balance of fission products in a grain, with the lowest running time.
- For radioactive species we can use the dichotomic mesh type with $NRV = 10$ as well, although the time step length should be adjusted in order to reach a precision $\leq 0.1$ % in some cases. This is the subject of the tests on $DT$ in the following section.
- With this optimum mesh it is necessary to redistribute the re-solution effect of fission products near the grain face over several meshes, since the outer layer thickness is smaller than the width of the zone in which fission products are redissolved (cf. $2\delta_R \sim 40$ nm in Fig. 8.2 on p. 149).

**Test matrix for $DT$** The assessment of the most favourable value of the microscopic time step-length ($DT_{max}$) involved several iterative phases. At each iteration, I used the previous approximation and multiplied/divided this value by several factors. The range of these factors decreased as the number of iterations increased. The iterations were stopped as soon as the precision remained below 0.1% for all cases.

The range of the decay constant for radioactive fission products has been extended according to the table of half-lives: from $\lambda = 10^{-9}\, s^{-1}$ (e.g. for $^{134}$ Cs: half-life = 2.06 y) to $\lambda = 10^{-2}\, s^{-1}$ (e.g. for $^{90}$ Kr: half-life = 32.2 s). Fission products with a decay constant smaller than $10^{-9}\, s^{-1}$ are considered to be stable. Stable and radioactive fission products have been considered separately.

**Test matrix for stable fission products** For stable fission products, I determined the worst precision observed during 1000 time steps, as a function of the relative diffusion coefficient $D_v^{'}$ only. (The number of time steps has been adapted in a few exceptional cases so as to assure that $\Delta t = NT \cdot Dt \simeq 10^8 s$ [291]). The worst precision should be $\leq 0.1\%$.

The range of $D_v^{'}$ has been extended in order to cover normal and off-normal irradiation conditions in nuclear fuel. More precisely, I considered linear heat generation rates between 15 kW/m and 40 kW/m, entailing temperatures between 320 °C and 1800 °C and fission rate densities on the order of 7 $/\mu m_{ox}^3/s$ to 19 $/\mu m_{ox}^3/s$ [291]. In addition, I increased the range of the average grain size ($3\ \mu m \leq R_{gr} \leq 20\ \mu m$). These modifications resulted in an extended range for the diffusion time-constant: $\log D_v^{'}$ = -6, -7, ..., -16.

**Test matrix for radioactive fission products** For radioactive fission products, I determined the worst precision after 10000 time steps as a function of the diffusion time-constant ($D_v^{'}$) and the decay time-constant ($\lambda$). The higher number of time-steps in comparison with the stable fission products turned out to be necessary from the results in the third phase (cf. § 8.4.2.3).

| coefficient | value |
|---|---|
| $c_0^{'}$ | −9.285772207129352E+0 |
| $c_1^{'}$ | −3.431221707808452E+0 |
| $c_2^{'}$ | −5.047761333560376E−1 |
| $c_3^{'}$ | −4.338539004830606E−2 |
| $c_4^{'}$ | −1.305526806383873E−3 |

Table 8.5: Table of coefficients for the fitted polynomial curve in Eq.(8.14), providing $DT_{max}$ for stable fission products as a function of $D_v^{'}$

The range for $D_v^{'}$ is the same as for the stable fission products. The range of the decay constant has been extended as indicated above. The choice of the intermediate values for $\lambda$ are also chosen so as to ensure a uniform distribution over the whole range: $\log \lambda$ = -2, -3, ... -9.

**Summary of the results from the tests for $DT_{max}$**

***$DT_{max}$* for stable fission products** For each value of $D_v^{'}$, I determined the maximum time-step length ($DT_{max}$) for which the precision on the balance of fission gas atoms in a grain remains lower than 0.1% during 1000 time steps. Various types of regression functions were then experimented with in order to fit these data points. The polynomial regression function of fourth order appeared to provide the best fit [291]:

$$y = \log DT_{max} = \sum_{n=0}^{k} c_n \cdot x^n \,, \tag{8.14}$$

where $x = \log D_v^{'}$. The coefficients have been reduced by a uniform factor, $c_i = f \cdot c_i^{'}$ $(i = 0, 1, \ldots 4)$ with $f = 0.956$, in order to ensure a predicted $DT_{max}$ which is lower than or equal to all the data points. The coefficients $c_i^{'}$ are tabulated in Table 8.5 and the resulting expression of $DT_{max}$ for stable fission products is represented in Fig. 8.3.

***$DT_{max}$* for radioactive fission products** In the case of radioactive species, I analysed the data points by means of a multivariate polynomial regression, resulting in an $8^{th}$ order polynomial in two dimensions:

$$z = \log DT_{max} = z\,(x, y) - \Delta \,, \tag{8.15}$$

where

$$\begin{aligned} z\,(x,y) \;=\; & \left\{ \left[ (c_0 x + c_1 y + c_2) \cdot y + c_3 + c_4 x + c_5 x^2 \right] \cdot y + c_6 + c_7 x + c_8 x^2 + c_9 x^3 \right\} \cdot y + \ldots \\ & \ldots + c_{36} + c_{37} x + c_{38} x^2 + c_{39} x^3 + c_{40} x^4 + c_{41} x^5 + c_{42} x^6 + c_{43} x^7 + c_{44} x^8 \end{aligned} \tag{8.16}$$

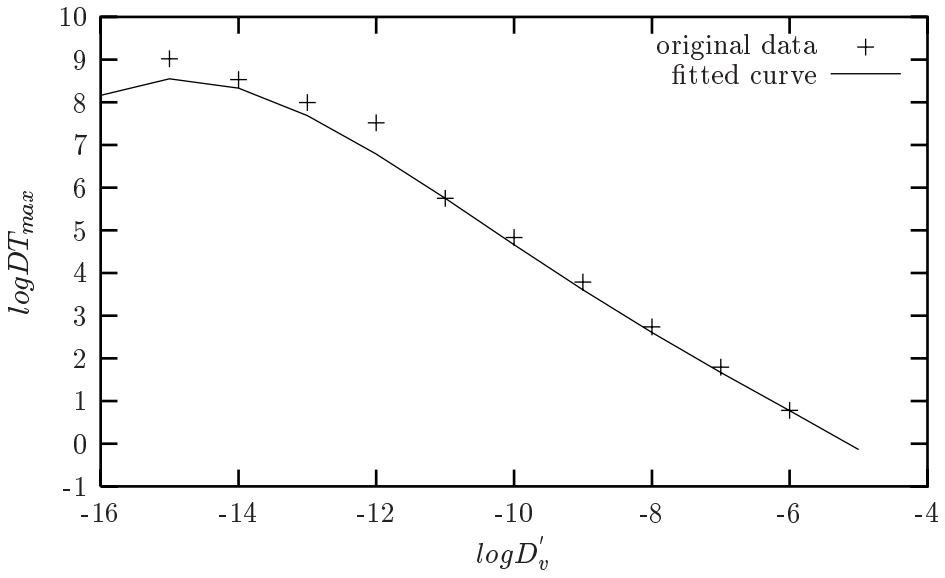


Figure 8.3: The maximum time-step length ($DT_{max}$) for the intragranular calculation of stable fission products as a function of the relative volume diffusion coefficient ($D_v^{'}$). The crosses correspond to the original data points, the line corresponds to the fitted curve calculated by means of Eq.(8.14).

and $x = \log D_v^{'}$, $y = \log \lambda$ and the coefficients are listed in Table 8.6. Rather than reducing the coefficients by a constant like for the stable species, I substracted a constant $\Delta = 0.13$ in order to guarantee that the predicted values of $DT_{max}$ according Eq.(8.15) are smaller than or equal to the corresponding data points on which the fit was based. The surface of $DT_{max}$ for radioactive species as a function of $D_v^{'}$ and $\lambda$ is depicted in Fig 8.4.

**Conclusions of the second intragranular phase** I have carried out a large number of refined tests on $NRV$, encompassing both dichotomic and sinusoidal mesh types with two different values of $NT$, in order to determine the number of meshes in the intragranular module of the FGR model. I conclude that the dichotomic mesh type with $NRV = 10$ constitutes the best compromise. With such a mesh, I can assure a precision better than 0.1% on the balance of fission products in each grain ($Q_{num}$) with the lowest calculation time, provided that the microscopic time-step length is limited. To this end, I have performed a large number of refined tests on $DT$ as well. From these results, I inferred an empirical relationship for $DT_{max}$ as a function of the intragranular time constants ($D_v^{'}$ and $\lambda$), both for stable and radioactive fission products. The upper limit for $DT$ guarantees a relative error on $Q_{num} \leq 0.1\%$ during 1000 or 10000 time steps for stable or radioactive fission products respectively.

| coefficient | value | | coefficient | value |
|---|---|---|---|---|
| $c_0$ | −9.726356292150720E−5 | | $c_{23}$ | 2.703155453612770E+0 |
| $c_1$ | −2.642530444429950E−4 | | $c_{24}$ | 2.622043136481450E−2 |
| $c_2$ | −1.205993579701880E−2 | | $c_{25}$ | −2.143757735736280E−3 |
| $c_3$ | −2.298000777595980E−1 | | $c_{26}$ | −1.021041972822180E−4 |
| $c_4$ | −2.970206138267060E−3 | | $c_{27}$ | −5.667568025591090E−6 |
| $c_5$ | 1.499046865674880E−5 | | $c_{28}$ | −2.560926531870830E+0 |
| $c_6$ | −2.228745343619100E+0 | | $c_{29}$ | −9.860196324326560E+0 |
| $c_7$ | 1.151328503944800E−2 | | $c_{30}$ | −1.796716800284540E+1 |
| $c_8$ | 4.949238610871230E−3 | | $c_{31}$ | −3.682743034482680E+0 |
| $c_9$ | 1.343778692272090E−4 | | $c_{32}$ | −3.582547671058840E−1 |
| $c_{10}$ | 1.109993604804510E+1 | | $c_{33}$ | −1.987556180171330E−2 |
| $c_{11}$ | 8.230359973095480E−1 | | $c_{34}$ | −5.966441634799570E−4 |
| $c_{12}$ | 9.266495044369160E−2 | | $c_{35}$ | −7.078147210950530E−6 |
| $c_{13}$ | 1.577576255885780E−3 | | $c_{36}$ | 9.143938773098550E+0 |
| $c_{14}$ | −4.420185760511950E−5 | | $c_{37}$ | −8.352821012503730E+0 |
| $c_{15}$ | −2.329520619083500E+1 | | $c_{38}$ | −7.860247838212520E+0 |
| $c_{16}$ | 8.208849095553270E+0 | | $c_{39}$ | −4.356138077349660E−1 |
| $c_{17}$ | 7.452838465877210E−1 | | $c_{40}$ | 1.588847983546950E−1 |
| $c_{18}$ | 1.375607851771750E−2 | | $c_{41}$ | 2.863832492136440E−2 |
| $c_{19}$ | 4.193498587228680E−5 | | $c_{42}$ | 2.089810585105110E−3 |
| $c_{20}$ | 1.818372680590780E−5 | | $c_{43}$ | 7.372098612948640E−5 |
| $c_{21}$ | 7.875099833577020E+0 | | $c_{44}$ | 1.017131873909760E−6 |
| $c_{22}$ | 3.419088915288380E+1 | | | |

Table 8.6: Table of coefficients for the fitted polynomial curve in Eq.(8.15), providing $DT_{max}$ for radioactive fission products as a function of $D_v^{'}$ and $\lambda$

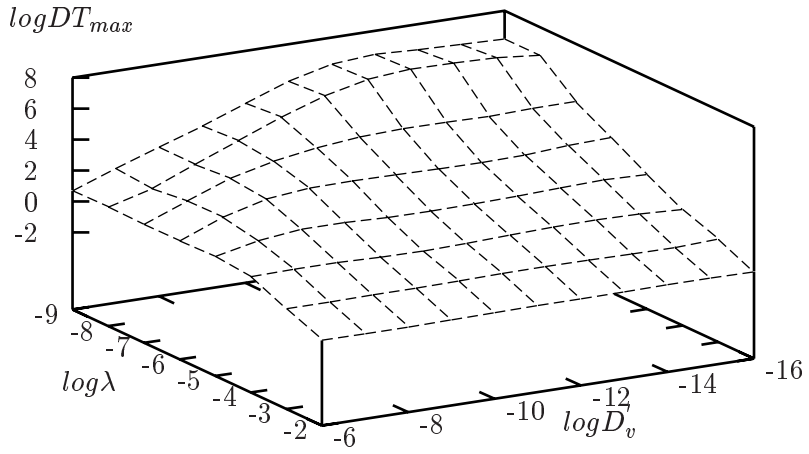


Figure 8.4: The maximum time-step length ($DT_{max}$) for the intragranular calculation of radioactive fission products, as a function of the relative volume diffusion coefficient ($D_v^{'}$) and the decay constant ($\lambda$), according to Eq.(8.15)

#### 8.4.2.3 Phase 3

**Objective** Unlike the two previous phases, the third phase does not aim at optimising the values of the remaining numerical parameters since they affect the intergranular part of the fission gas release model as well. Instead, the objective of the present section is to assess their influence on the intragranular module and to point out the dominant parameters.

**Parameters under consideration** There are four physical parameters under consideration: $D_v^{'}$, $\lambda$, $\Gamma_r$ and $\delta_R$. The variable numerical parameters in the third phase amount to two: the width of the supplementary imaginary layer ($\delta_s$) and the criterion for the convergence on the grain boundary concentration ($CRIT_{conv}$).

**Approach** The influence of the parameters on the intragranular module is assessed by monitoring the evolution of the relative error on the total balance of fission products in a closed system. The system consists of one spherical grain ($R_{gr} = 8\,\mu m$), surrounded by a closed grain boundary layer ($\delta_{gb} = 0.5$ nm). None of the fission products are allowed to escape; they can only disappear by radioactive decay.

Fission products generated in the grain will diffuse to the grain boundary. The fission products accumulating in the grain boundary are subjected to a flux of fission fragments. As a result, they have a certain probability per unit of time, denoted by $\Gamma_r$, to re-enter the grain. This mechanism entails a supplementary source term in a zone adjacent to the grain face and

has been implemented by means of the smeared model (cf. § 7.1.4 and § 8.2).

The total amount of fission products created during the irradiation in the single grain ($Q_{prod}$) is governed by a simple balance equation[a]:

$$\frac{dQ_{prod}}{dt} = y \cdot \dot{F} \cdot V_{gr} - \lambda \cdot Q_{prod}\,, \tag{8.17}$$

where $V_{gr} = \frac{4\pi}{3} R_{gr}^3$. Integrating Eq.(8.17) over time yields

$$Q_{prod}\,(t) = \begin{cases} Q_{prod}\,(0) \cdot e^{-\lambda t} + \frac{S_{fis}}{\mu} \cdot V_{gr} \cdot \frac{1-e^{-\lambda t}}{\lambda} & \lambda \neq 0 \\ Q_{prod}\,(0) + \frac{S_{fis}}{\mu} \cdot V_{gr} \cdot t & \lambda = 0 \end{cases} \tag{8.18}$$

where $S_{fis} = y \cdot \mu \cdot \dot{F}$. The value of $Q_{prod}$ is compared with the sum of the fission products remaining in the grain, provided by the subroutine PARDI, and those remaining in the closed grain boundary layer [291]:

$$\frac{dC_{gb}}{dt} \simeq -\lambda_0 \cdot C_{gb} + \lambda_1 \cdot C_v\,(R_{gr})\,, \tag{8.19}$$

where

$$\lambda_0 = \frac{D_v}{\delta_s \cdot \delta_{gb}} + \frac{\Gamma_r}{2} + \lambda\,, \tag{8.20}$$

$$\lambda_1 = \frac{D_v}{\delta_s \cdot \delta_{gb}}\,. \tag{8.21}$$

The computation of the relative error on the balance of fission products is performed after each time-step. However, the results are printed in the output file only after $N_{res}$ time-intervals:

$$N_{res} = \begin{cases} 10^0 & 10^0 \leq NT < 10^3 \\ 10^1 & 10^3 \leq NT < 10^4 \\ 10^2 & 10^4 \leq NT < 10^5 \\ 10^3 & 10^5 \leq NT < 10^6 \\ 10^4 & 10^6 \leq NT < 10^7 \\ 10^5 & 10^7 \leq NT \end{cases}$$

$N_{res}$ thus corresponds to a "sampling frequency" of the output signals, which is determined by the total number of time steps.

**Test matrix** The parameters to be investigated are limited to six: $D_v^{'}$, $\lambda$, $\Gamma_r$, $\delta_R$, $\delta_s$ and $CRIT_{conv}$. Taking for each parameter five different values we would have $5^6 = 15625$ calculations to be performed with a full factorial method. In order to reduce the number of

[a]The units of $Q_{prod}$ differ from those of the concentrations in that $Q_{prod}$ is expressed in a number of fission products rather than in a volume of gas

| case | $D_v^{'}$ | $\lambda$ | $\Gamma_r$ | $\delta_R$ | $\delta_s$ | $CRIT_{conv}$ |
|---|---|---|---|---|---|---|
| 1 | 1 | 1 | 1 | 1 | 1 | 1 |
| 2 | 1 | 2 | 2 | 2 | 2 | 2 |
| 3 | 1 | 3 | 3 | 3 | 3 | 3 |
| 4 | 1 | 4 | 4 | 4 | 4 | 4 |
| 5 | 1 | 5 | 5 | 5 | 5 | 5 |
| 6 | 2 | 1 | 2 | 3 | 4 | 5 |
| 7 | 2 | 2 | 3 | 4 | 5 | 1 |
| 8 | 2 | 3 | 4 | 5 | 1 | 2 |
| 9 | 2 | 4 | 5 | 1 | 2 | 3 |
| 10 | 2 | 5 | 1 | 2 | 3 | 4 |
| 11 | 3 | 1 | 3 | 5 | 2 | 4 |
| 12 | 3 | 2 | 4 | 1 | 3 | 5 |
| 13 | 3 | 3 | 5 | 2 | 4 | 1 |
| 14 | 3 | 4 | 1 | 3 | 5 | 2 |
| 15 | 3 | 5 | 2 | 4 | 1 | 3 |
| 16 | 4 | 1 | 4 | 2 | 5 | 3 |
| 17 | 4 | 2 | 5 | 3 | 1 | 4 |
| 18 | 4 | 3 | 1 | 4 | 2 | 5 |
| 19 | 4 | 4 | 2 | 5 | 3 | 1 |
| 20 | 4 | 5 | 3 | 1 | 4 | 2 |
| 21 | 5 | 1 | 5 | 4 | 3 | 2 |
| 22 | 5 | 2 | 1 | 5 | 4 | 3 |
| 23 | 5 | 3 | 2 | 1 | 5 | 4 |
| 24 | 5 | 4 | 3 | 2 | 1 | 5 |
| 25 | 5 | 5 | 4 | 3 | 2 | 1 |

Table 8.7: Test matrix for the third phase of the intragranular parameter optimisation according to the $L_{25}\left(5^6\right)$ Taguchi procedure. The numbers indicate the levels of each parameter in each case.

tests it is recommended to apply the Taguchi method $L_{25}\left(5^6\right)$ with 25 orthogonal arrays (cf. Table 8.7).

The five different levels for each parameter enabled me to perform an analysis of means, i.e. to compute the average response (e.g. precision or calculation time) for each parameter (e.g. $D_v^{'}$) at each level (e.g. level 4). Such an analysis of means, in turn, allowed me to point out the dominant parameter(s).

The choice of the different levels for each parameter is chosen so as to ensure a uniform distribution over the whole range. The range of each parameter is indicated in Table 8.8. Like in the previous section, the range of the physical parameters is representative of normal and off-normal irradiation conditions in LWR fuel. The re-solution parameters are chosen according to values mentioned in the literature [1, 58, 67], except for the range of the re-solution probability at the grain boundary ($\Gamma_r$), which has been extended by one order of

| parameter | unit | level 1 | level 2 | level 3 | level 4 | level 5 |
|---|---|---|---|---|---|---|
| $D_v^{'}$ | $s^{-1}$ | $10^{-16}$ | $10^{-13}$ | $10^{-11}$ | $10^{-9}$ | $10^{-7}$ |
| $\lambda$ | $s^{-1}$ | 0 | $10^{-9}$ | $10^{-6}$ | $10^{-4}$ | $10^{-2}$ |
| $\Gamma_r$ | $s^{-1}$ | $10^{-6}$ | $5 \times 10^{-6}$ | $10^{-5}$ | $5 \times 10^{-5}$ | $10^{-4}$ |
| $\delta_R$ | $\mu m$ | $10^{-2}$ | $5 \times 10^{-2}$ | $10^{-1}$ | $5 \times 10^{-1}$ | 1 |
| $\delta_s$ | $\mu m$ | $10^{-4}$ | $2 \times 10^{-4}$ | $3 \times 10^{-4}$ | $4 \times 10^{-4}$ | $5 \times 10^{-4}$ |
| $CRIT_{conv}$ | - | $10^{-8}$ | $10^{-7}$ | $10^{-6}$ | $10^{-5}$ | $10^{-4}$ |

Table 8.8: Different levels of the parameters for the third phase of the intragranular parameter optimisation

magnitude. (The re-solution parameters are not very well characterised since they can not be measured directly).

The range of the numerical parameters has been established as follows. The upper limit of the criterion for convergence is determined by the required precision. The lower limit of $CRIT_{conv}$ is limited by the best precision which can be obtained, and has been adapted during several successive tests. The range of the supplementary imaginary layer is chosen so as to assure that 1 Å $\leq \delta_s \leq \delta_{gb} (= 5 \times 10^{-4} \mu m)$.

**Conclusions of the third intragranular phase** The main objective of the third phase was to examine the effect of those parameters that may not be assessed by means of an analytical solution in the grain alone ($\lambda$, $\Gamma_r$, $\delta_R$, $\delta_s$ and $CRIT_{conv}$). They influence the intergranular module as well. Therefore, I studied their effect on the balance of fission products in a closed system consisting of one spherical grain surrounded by a grain boundary.

From the analysis of means, the influence of $\delta_s$ and $CRIT_{conv}$ on both the precision and the running time (or number of required iterations) turn out to be limited. However, their optimum values have to be determined by assessing their effect on the FGR model since they influence the intergranular module as well. This is the subject of section 8.6.

The most important physical parameters are $D_v^{'}$ and $\lambda$, in other words the microscopic time-step length $DT$. This parameter affects the precision of the grain boundary concentration through the boundary condition, since I assume that $C_v$ ($R_{gr}$) evolves linearly[b] during $DT$ in Eq.(8.19).

The precision of the grain boundary concentration is important for the precision on the balance of fission products in the grain, especially at large values for $D_v^{'}$. This results from the coupling, in particular from the boundary condition and the re-solution effect at the grain face. For this reason it appears necessary to analyse the influence of the intergranular parameters through their effect on the fission gas release model. Additionally, I should verify the appropriateness of the intragranular time-step control in the FGR model. Indeed, the

[b]Note that a similar assumption is made in the fission gas release model; not only in the third phase of the intragranular parameter optimisation.

subroutine used to solve the intergranular module subdivides $DT_{max}$ internally as a function of the required precision, which is provided on input as well (cf. § 8.5). The outcome of this routine, however, may depend on $DT_{max}$.

Finally, it should be underlined that the precision tests in the third phase were performed in a closed system. Consequently, the fission products accumulate in the grain boundary without being released. This entails an overprediction of the grain boundary concentration ($C_{gb}$), which in turn engenders an overestimation of the importance of the precision of $C_{gb}$ as well as the re-solution effect[c].

## 8.5 Implementation of the intergranular module

There are two possible situations for the intergranular module, depending on the state of the grain boundary bubbles; either they are still in the nucleation phase, either they are established and may undergo growth or shrinkage. In the first situation, the grain boundary concentrations of fission gas atoms are given in analytic form (cf. Appendix E). In the second situation, the grain boundary concentrations are governed by a coupled set of ordinary differential equations (cf. § 7.2.2.1). In order to implement these equations, I have to address the generic questions listed in § 8.4.

In addition to the questions brought about by the implementation of the set of ODE, there is the problem of implementing the transition between both phases of the intergranular module. This is the subject of the following section. The choice of the routine for the implementation of the set of ODE will be discussed in the subsequent section.

### 8.5.1 The switch between the two phases

There are two types of switches between the "nucleation" and the "growth/shrinkage" phase of the grain boundary bubbles that guarantee the reversibility of the intergranular module. Their implementation is schematically represented in Fig. 8.5.

The first type of transition occurs when the amount of gas accumulated in the gas-vacancy clusters reaches a critical value, $\hat{C}_{gbb}^{cr}$, during the nucleation phase (cf. § 7.2.1.3). In practice, I introduce a margin on the condition for the switch, i.e. instead of the value computed in Eq.(7.74), I use $\hat{C}_{gbb}^{cr}\left(1+\Delta\hat{C}_{gbb}\right)$. This margin is necessary in order to overcome a numerical problem in the bubble growth phase, more precisely to prevent never-ending switching back and forth between the two phases. Its influence on the balance of fission products has been assessed but turned out to be negligible (cf. § 8.6).

In order to find out whether the transition occurs during a time-step between $t_s$ and $t_e$, I compare $\hat{C}_{gbb}\left(t_e\right)$ with $\hat{C}_{gbb}^{cr}\left(1+\Delta\hat{C}_{gbb}\right)$. When the critical value is reached or exceeded,

[c]This is especially valid for stable fission products when the intragranular diffusion coefficient is high.

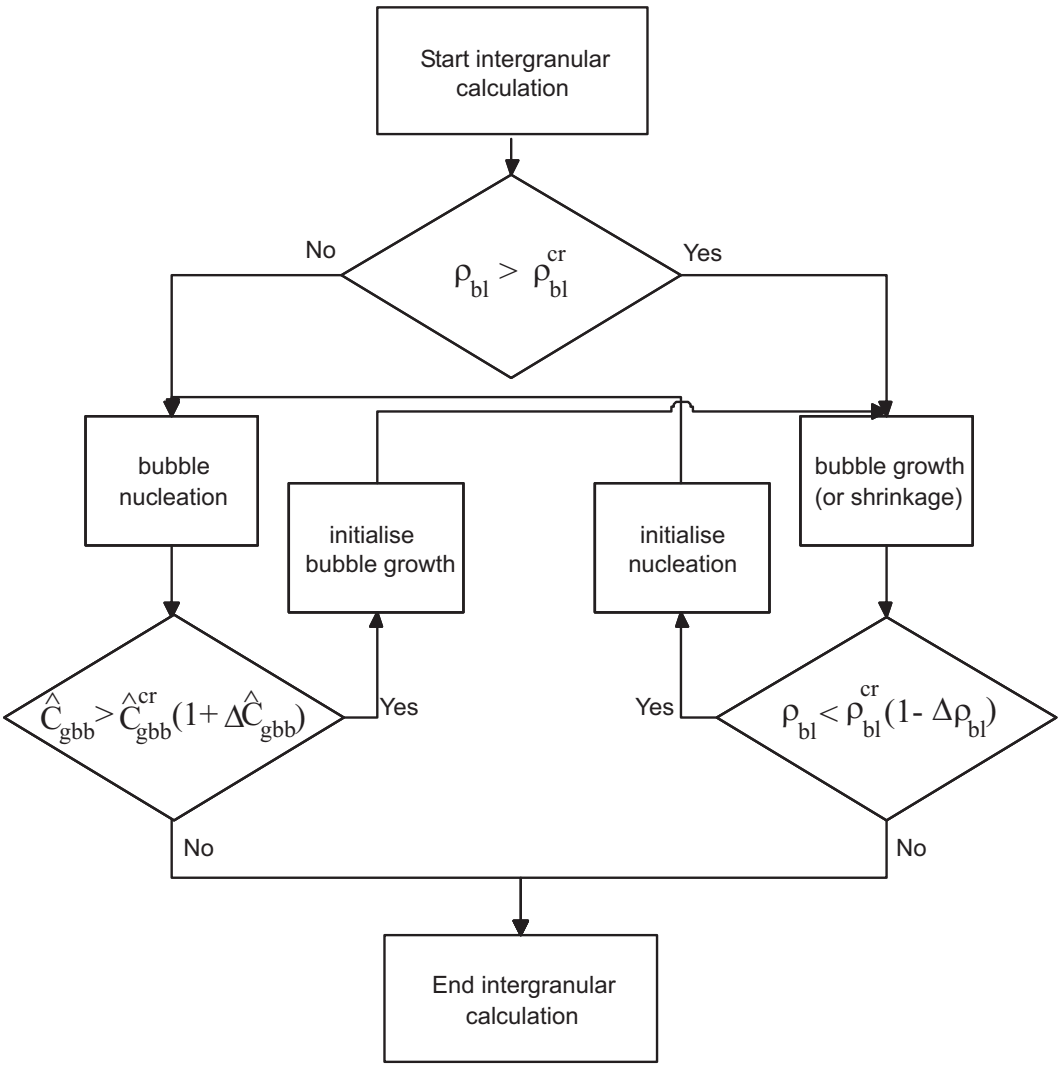


Figure 8.5: Global flowchart of the intergranular module, featuring the transitions between the nucleation and the growth/shrinkage phase of the grain boundary bubbles during a microscopic time-step.

I determine the time at which this occurs. To this end, I compute the root of the non-linear function $F(t) = \hat{C}_{gbb}(t) - \hat{C}^{cr}_{gbb}\left(1 + \Delta\hat{C}_{gbb}\right)$ in the interval $t_s \leq t_{cr} \leq t_e$, by means of a combination of the Newton-Raphson and the bisection method. The Newton-Raphson method provides fast convergence and the analytic expression for the time-derivative of the function is known (cf. Appendix E):

$$\frac{dF(t)}{dt} = \frac{d\hat{C}_{gbb}}{dt} = a_b + b_b t + r\hat{C}_{gbv}(t) - q\hat{C}_{gbb}F(t) \; . \tag{8.22}$$

The initial value for the iteration is estimated by assuming a linear evolution of the concentration in the grain boundary bubbles between $\hat{C}_{gbb}(t_s)$ and $\hat{C}_{gbb}(t_e)$ over the time interval:

$$t_{cr}|_{initial} = t_s + (t_e - t_s)\,\frac{\hat{C}^{cr}_{gbb}\left(1 + \Delta\hat{C}_{gbb}\right) - \hat{C}_{gbb}(t_s)}{\hat{C}_{gbb}(t_e) - \hat{C}_{gbb}(t_s)} \, . \tag{8.23}$$

Once I have determined $t_{cr}$, I compute $\hat{C}_{gbv}(t_{cr})$ by means of an analytical expression (cf. Eq.(E.34)). Both figures are supplied on input for the bubble growth phase, together with $\hat{C}^{cr}_{gbb}\left(1 + \Delta\hat{C}_{gbb}\right)$, and $\rho_{bl} = \rho^{cr}_{bl}$.

The second type of transition occurs during the bubble growth/shrinkage phase. When the radius of curvature of the bubbles, calculated by means of Eq.(7.38), reaches a certain lower limit, I assume that the nucleation phase starts over again. The lower limit for the grain boundary bubble radius of curvature is set to $\rho^{cr}_{bl}(1 - \Delta\rho_{bl})$, where I have introduced a margin. This margin is also necessary in order to overcome a numerical problem in the bubble nucleation phase, more precisely to avoid that $\hat{C}_{gbb} \geq \hat{C}^{cr}_{gbb}\left(1 + \Delta\hat{C}_{gbb}\right)$ when entering the nucleation phase. The influence of $\Delta\rho_{bl}$ on the balance of fission products has been assessed but turned out to be negligible as well (cf. § 8.6).

When $\rho_{bl} = \rho^{cr}_{bl}(1 - \Delta\rho_{bl})$ is fulfilled, the numerical routine used to solve the set of ODE returns the time at which this occurs, together with the corresponding values for the concentrations. This information is required on input for the nucleation phase.

### 8.5.2 Determination of the numerical routine and the corresponding parameters

The routine applied to solve the equations of the intergranular module when the bubbles are in the growth/shrinkage phase is LSODAR [301]. The choice was relatively straightforward for several reasons. First of all, it is part of a widely used package of FORTRAN routines for ordinary differential equations, ODEPACK [302], which is freeware. Accordingly, it has undergone extensive performance testing and optimisation. Furthermore, the routine solves simultaneously a coupled set of ODE and algebraic equations. The latter represent constraint functions, such as a limit on $\rho_{bl}$, therefore LSODAR is perfectly suited for the equations involved

in the intergranular module. Finally, the solver switches automatically between stiff and non-stiff methods. This means that the user does not have to determine whether the problem is stiff or not, and the solver will automatically choose the appropriate method.

LSODAR requires on input a number of numerical parameters, some of which simply describe the numerical problem at hand (e.g. number of equations, time-step length, etc. ), while the others determine the desired precision of the results. Except for the type of mesh, I have determined the intergranular numerical parameters by analysing their effect on the fission gas release model, because they affect the precision of the intragranular module as well (cf. § 8.4.2.3). Their optimisation is described in the following section.

For the spatial discretisation of the pellet in the FGR calculation, I have adopted the equivolume type of grid. This mesh type associates an equal weight to each macroscopic ring, and accounts for the gradient in the retention profile of fission products towards the pellet periphery. Furthermore it is applied in the COMETHE code from BELGONUCLEAIRE, with which my FGR model should be coupled (cf. § 8.3). A dichotomic type of mesh would provide too large central rings, irrespective of the number of rings. An equidistant type of mesh does not account for the gradients near the pellet edge, thus requiring a higher number of rings, or calculation time, in order to obtain the same mesh size (i.e. precision) in that region.

## 8.6 Determination of the remaining numerical parameters in the fission gas release model

The remaining numerical parameters of the fission gas release model that need to be determined amount to nine: the number of meshes in the grain boundary concentration profiles ($NRJ$); the number of groups in the grain size distribution ($NRK$); the criterion for the convergence of the grain boundary concentrations ($CRIT_{conv}$); the width of the imaginary supplementary layer at the grain boundary ($\delta_s$); the relative tolerance parameters for the transitions between the nucleation phase and the bubble growth/shrinkage phase in the intergranular module ($\Delta\hat{C}_{gbb}$, $\Delta\rho_{bl}$); and the relative tolerance parameters used in the subroutine LSODAR ($RTOL(i), \quad i = 1, 2, 3$).

Even those parameters that, a priori, only affect the precision of the intergranular module (e.g. $NRJ$), have an influence on the precision of the intragranular module as well, albeit indirectly (cf. § 8.4.2.3). All the remaining parameters can thus be termed global in the sense that they affect both modules of the fission gas release model simultaneously. As a result, I need to apply the FGR model to well defined irradiation histories in order to assess their sensitivity, and determine their optimum values.

In view of the interrelationship with other phenomena (e.g. the heat transport), it is necessary to couple the FGR model with a fuel performance code. For all the simulations in this section, I have used the FTEMP2 code to provide on input the radial temperature

distribution (cf. § 8.3). The normalised fission rate distribution in the pellets is taken to be independent of burnup and is given by Eq.(8.6).

The determination of the remaining parameters involves three phases. The first step aims at the elimination of the less significant parameters as well as the determination of the spatial discretisation, i.e. $NRK$ and $NRJ$. In the second step, I perform more refined calculations in order to choose the other parameters. The third step is devoted to the modification of the microscopic time-step length ($DT_{max}$), required by the precision on the grain boundary concentration.

Each step will be described separately in the following sections. For the sake of conciseness, however, I limit myself to highlight the methodology and summarise the outcome. More detailed results have been reported separately [303].

### 8.6.1 Phase 1

#### 8.6.1.1 Objective

The first step aims at finding out the most significant parameters as well as determining the spatial discretisation, i.e. the number of macroscopic rings ($NRJ$) together with the number of grain size classes ($NRK$). For the sensitivity analysis, I look concurrently at the accumulated fission gas release fraction and the required CPU time.

#### 8.6.1.2 Test Matrix

For the application of my FGR model, I have chosen two hypothetical cases from a round robin exercise, FUMEX [13]. Given the absence of experimental data and their associated uncertainties, the two cases enable a straightforward intercomparison with model predictions from 19 other codes, along with testing the sensitivity to changes in experimental and numerical variables, as well as the stability of the calculation.

The first case consisted of a fuel rod running at a constant power level of 20 kW/m to a final burnup of 50 MWd/kg$UO_2$. In the second case, the power was held constant at 20 kW/m to a burnup of 30 MWd/kg$UO_2$ when there was a ramp to 40 kW/m in half an hour. This high power was held to an end-of-life (EOL) burnup of 50 MWd/kg$UO_2$. The general fuel rod characteristics used in the calculations are indicated in [303].

In line with the optimisation procedure of the intragranular parameters (cf. § 8.4.2), I make use of a Taguchi procedure [298–300] for the sensitivity analysis of the global parameters. However, such analysis is most successful for independent parameters. In view of this, and in order to reduce the total number of variable parameters, I group a few of them. More precisely, I impose $CRIT_{conv} = RTOL(2) = RTOL(3)$ in the present analysis, since the criterion for convergence on the grain boundary concentrations should be in the order of (or larger than) the relative tolerance parameter used by the subroutine LSODAR. As a result, I

| variable | unit | level 1 | level 2 |
|---|---|---|---|
| $NRJ$ | - | 5 | 15 |
| $NRK$ | - | 1 | 8 |
| $\delta_s$ | $\mu m$ | $5 \times 10^{-4}$ | $2 \times 10^{-4}$ |
| $\Delta\hat{C}_{gbb}$ | - | $10^{-2}$ | $10^{-5}$ |
| $\Delta\rho_{bl}$ | - | $10^{-2}$ | $10^{-5}$ |
| $RTOL(1)$ | - | $10^{-3}$ | $10^{-6}$ |
| $CRIT_{conv}$ | - | $10^{-3}$ | $10^{-6}$ |

Table 8.9: Different levels of the parameters for the first phase of the global numerical parameter optimisation

have to consider 7 parameters: $NRJ$, $NRK$, $\delta_s$, $\Delta\hat{C}_{gbb}$, $\Delta\rho_{bl}$, $RTOL(1)$, and $CRIT_{conv} = RTOL(2) = RTOL(3)$.

Assessing the influence of the 7 parameters by means of a full factorial design, assuming that they can take only two different values would require $2^7 = 128$ tests. Like in the first phase of the optimisation of the intragranular parameters (cf. Table 8.2 on p. 8.2), I reduce the total number of runs and determine the most important parameters by applying the $L_8\left(2^7\right)$ Taguchi procedure [303]. The two levels of each parameter are given in Table 8.9 .

#### 8.6.1.3 Conclusions from the first phase

From the first phase in the optimisation procedure of the global parameters, I choose $NRJ = 10$, providing a good compromise in terms of calculation time and precision.

For the grain size distribution, I choose $NRK = 3$: it provides one class above, equal to and below the mean grain size, while the running time remains limited. For higher values of $NRK$, the calculation time will increase without influencing the fraction of released fission products significantly since the volume fraction of the supplementary classes is below 1 %. Nevertheless, the effect of $NRK$ on the predicted fraction of gas release shows that it is necessary to include the grain size distribution in the FGR model in order to avoid overpredictions since, for example, with $NRK$ equal to 1 and 8 the average FGR fraction at end-of-life was 2.33 % and 0.36 % respectively [303]. This confirms the findings of Olander and co-workers [30, 96].

For the second phase of the optimisation procedure, I have to take into account that $CRIT_{conv}$ is predominant for the precision on the fission gas release fraction and the calculation time. In addition, I should couple the values of $\Delta\hat{C}_{gbb}$ and $\Delta\rho_{bl}$ with $CRIT_{conv} = RTOL\,(2) = RTOL\,(3)$ and $RTOL\,(1)$ respectively. In particular, I should impose that $\Delta\rho_{bl} > RTOL\,(1)$ and $\Delta\hat{C}_{gbb} > RTOL\,(2) = RTOL\,(3) = CRIT_{conv}$ so as to avoid numerical problems that may arise during the switch from the grain boundary bubble growth/shrinkage phase to the nucleation phase [303].

### 8.6.2 Phase 2

#### 8.6.2.1 Objective

The goal in the second phase of the global parameter optimisation consists in determining the remaining numerical parameters, more precisely $\Delta\hat{C}_{gbb}$, $\Delta\rho_{bl}$, $RTOL(i)$ $(i = 1, 2, 3)$, $CRIT_{conv}$, and $\delta_s$. The criteria used for the optimisation, as well as the irradiation histories, are identical to those applied in the previous phase.

#### 8.6.2.2 Test Matrix

Taking into consideration the previous results, some of the variable parameters can be grouped. First of all, the margin for the switch from the nucleation phase to the growth phase, $\Delta\hat{C}_{gbb}$, should be larger than the relative tolerance parameters used for the concentrations in the intergranular module, $RTOL(2)$ and $RTOL(3)$. In addition, the criterion for convergence of the grain boundary concentrations should be of the same order of magnitude, whence I impose $CRIT_{conv} = RTOL(2) = RTOL(3)$ and $\Delta\hat{C}_{gbb} = 10 \cdot CRIT_{conv}$. In a similar way, I enforce $\Delta\rho_{bl} = 10 \cdot RTOL(1)$, where $RTOL(1)$ corresponds to the required precision for the bubble radius of curvature in the subroutine LSODAR.

Given the reduced number of parameters, I simulate the same hypothetical FUMEX cases as before, although with a refined test scheme. To this end, I double the number of levels for each parameter in a $L_{16}\left(4^3\right)$ Taguchi approach [303]. The range of the parameters is the same as in the first phase.

Since there are four different levels for each numerical parameter, I determine the magnitude of the effect of each parameter by means of an analysis of means, using several response tables. In particular, I assess the influence of each level of each parameter by determining the average response (fission gas release fraction and CPU time).

#### 8.6.2.3 Conclusions from the second phase

I examined the influence of the numerical parameters in the FGR model on the amount of released gases and the running time. The analysis covered extreme irradiation conditions, that is a low temperature irradiation for a long time, a ramp test and irradiation at high temperature up to a high discharge burnup. The influence of the numerical parameters is negligible at high linear heat rates ($\sim 40$ kW/m) in contrast with the low temperature irradiation ($\sim 20$ kW/m).

On the basis of these results, I determined the optimum values for the global numerical parameters: $CRIT_{conv} = RTOL(2) = RTOL(3) = RTOL(1) = 10^{-5}$, $\Delta\hat{C}_{gbb} = \Delta\rho_{bl} = 10^{-4}$, and $\delta_s = 3 \times 10^{-4}\mu m$.

| Parameter | value | unit |
|---|---|---|
| pellet inside diameter | 0 | mm |
| pellet outside diameter | 10.36 | mm |
| cladding inside diameter | 10.56 | mm |
| cladding outside diameter | 12.28 | mm |
| pellet height | 10.3 | mm |
| pellet chamfer width | 0.33 | mm |
| pellet chamfer length | 0.23 | mm |
| dishing | - | - |
| fuel column length | 27.81 | cm |
| fuel density | 95.5 | % TD♣ |
| enrichment $U^{235}$ | 4.94 | % |
| grain radius | 8 | $\mu m$ |
| fuel surface roughness | 3.5 | $\mu m$ |
| clad surface roughness | 1.5 | $\mu m$ |
| fill gas | He | - |
| fill gas pressure | 5 | bar |

Table 8.10: Main parameters used in the COMETHE code calculations for the simulation of the empirical threshold for release.

♣% of theoretical density, which amounts to 10.96 g/cm$^3$

### 8.6.3 Phase 3

#### 8.6.3.1 Objective

Having fixed the numerical parameters, I verify the influence of the optimum time-step length ($DT_{max}$), calculated by means of Eqs. (8.14) and (8.15), on the predicted fission gas release fractions. Indeed, in the third phase of the intragranular parameter optimisation it appeared necessary to ascertain whether $DT_{max}$ is still appropriate and, if required, to adapt it in order to meet the requirements on precision and calculation time. This is the objective of the present section.

#### 8.6.3.2 Test Matrix

The simulation of the empirical Halden threshold for the onset of fission gas release is quite sensitive to the precision of the results, hence it is very appropriate to fine-tune $DT_{max}$ over a wide range of conditions. For the simulation of this release threshold, I determine the central temperature and the average burnup in the pellet when the fraction of the released gases reaches 1 % during an irradiation at constant linear heat rate (25 kW/m, 30 kW/m, 35 kW/m, and 38 kW/m). The main fuel rod parameters used in the calculation are indicated in Table 8.10.

The approach for fine-tuning the microscopic time-step length is very simple: I reduce

$DT_{max}$ by a constant factor until the variations on the predictions remain smaller than the experimental uncertainties. More precisely, I simulate the empirical curve with decreasing values of $DT_{max}$ and verify whether the variations of the predicted burnup, at which 1 % of the produced fission gases are released, remains below the experimental error on the burnup value ($\sim$ 5 %). This approach has two main advantages: I cover a wide range of temperatures and burnup values, and the burnup value (or time) at which 1% fission gas release is reached is very sensitive to the slope of the release curve, which in turn is strongly influenced by the numerical parameters, especially at low linear heat rates [303]. The empirical release curve is simulated with three different values for the microscopic time-step length: I divide $DT_{max}$ by 1, 5 and 10.

#### 8.6.3.3 Conclusions from the third phase

In order to guarantee predictions that are independent of the microscopic time-step length, it is necessary to divide $DT_{max}$, computed from Eqs. (8.14) or (8.15), by a constant factor. A factor of 5 provides a good compromise between precision and running time.

## 8.7 Balance calculation and output

At the end of each macroscopic time interval, $\Delta t_{macr} = NT \times DT_{max}$, the main programme invokes a subroutine called BALANCE, provided that convergence has been achieved on the grain boundary concentrations, or when the number of trials to achieve convergence exceeds 100 (cf. Fig. 8.1). The BALANCE subroutine computes the total gas inventory remaining in the pellets, together with the cumulated number of fission gas atoms produced by the fission process. The relative difference between both numbers yields the released fraction.

The calculation of the number of fission gas atoms in the grains, $Q_v$, is straightforward since the routine that solves the intragranular diffusion equation numerically, PARDI, provides the average concentration in each annulus, $n$, of the grain of class $(k,l,m)$, $C_{klm,n}$:

$$\begin{aligned} Q_v &= \sum_{k,l,m} N_{klm} \left[ \sum_{n=1}^{NRV} \frac{C_{klm,n}}{\mu} \cdot \frac{4\pi}{3} \left( r_{klm,n+1}^3 - r_{klm,n}^3 \right) \right] \\ &= \sum_{k,l,m} \frac{f_{klm} V_m}{R_{klm}^3} \left[ \sum_{n=1}^{NRV} \frac{C_{klm,n}}{\mu} \cdot \left( r_{klm,n+1}^3 - r_{klm,n}^3 \right) \right] , \end{aligned} \tag{8.24}$$

where

$$V_m = \frac{4\pi}{3} \left( R_{m+1}^3 - R_m^3 \right) , \tag{8.25}$$

corresponds to the volume of the $m$-th macroscopic ring in the pellet, $\mu$ converts the concentration ($\mu m_{gas}^3 / \mu m_{ox}^3$) to the number of gas atoms ($\#/\mu m_{ox}^3$), $N_{klm}$ represents the number of grains of class $(k,l,m)$, which is related to the volume fraction of grains in that class, $f_{klm}$

(cf. Eq.(8.2)), by

$$N_{klm}\frac{4\pi}{3}R_{klm}^3 = f_{klm}V_m\,. \tag{8.26}$$

The calculation of the gas inventory in the grain boundary is also straightforward since $\hat{C}_{gbv}$ and $\hat{C}_{gbb}$ correspond to the average gas concentration in the bulk of the grain boundary and in the grain boundary bubbles of each macroscopic ring, respectively:

$$Q_{gb} = \left(\hat{C}_{gbv} + \hat{C}_{gbb}\right)\frac{V_m}{\mu}\,. \tag{8.27}$$

Finally, the cumulated number of fission gas atoms produced by the fission process during the macroscopic time-step in the pellet is given by

$$dQ_{prod} = y \cdot \dot{F} \cdot V_m \cdot \Delta t_{macr}\,. \tag{8.28}$$

After the balance calculation, the main programme calls the subroutine STEPOUTPUT wherein output is provided for two separate files. The first file contains the computed fractional release at the end of every macroscopic time interval, along with the time, the pellet average burnup and the average linear heat rate. The second file contains detailed information regarding intra- and intergranular concentration profiles. Note that at the very end of the irradiation history, there is an optional generation of a third output file in order to re-start the calculation.

## 8.8 Summary and conclusions

I have discussed the implementation of the fission gas release model that was presented in the previous chapter. The analysis covered the structure, solution scheme, and the major subroutines involved in the solution scheme.

The most important issue for the programme implementation is the reduction of the calculation time while assuring sufficient precision. Most of my efforts have been devoted to the implementation of the intragranular module, since it is invoked a large number of times and the majority of the fission gas atoms remain in the grains under normal operating conditions.

The non-linear diffusion problem in the grains is solved by means of the PARDI routine developed at BELGONUCLEAIRE. The variational technique applied in PARDI is simple and provides a solution in analytic form with short computational times. Moreover, a careful choice of trial functions allows to obtain the local concentrations, together with the average values in each finite element. This simplifies the balance calculation after each macroscopic time interval. Finally, the implicit Euler technique for the time-integration requires minimal computer memory, while it assures unconditional stability for every time-step length.

The optimisation of the numerical parameters used in PARDI involves three steps. The first

phase aims at the determination of the predominant parameters as well as the mesh type. The sensitivity analysis rests on the Taguchi approach, which provides a limited number of tests with a judicious combination of all parameters under consideration. The optimisation criteria are the precision on the balance of fission products in a grain, obtained by comparing the numerical solution with an analytical solution under simplifying conditions, and the required CPU time.

The dichotomic grid emerges as the best choice in terms of precision and running time. In addition, it allows an elegant implementation of the re-solution process in some layers near the grain boundary (cf. § 8.2). This would be impossible to realize with the same accuracy in the model of Kogai [181], for he employed the two-zone scheme of Matthews et al. [160], which leads to errors of $\sim 2$ % release in small-release experiments. Denis et al. [58] avoid this problem by employing a very fine equidistant mesh: $r_i - r_{i-1} = \delta_R/4 \simeq 5 \times 10^{-3} \mu m$. Nevertheless, such a grid would require much longer running times.

During the second phase of the intragranular optimisation phase, I started with a series of tests in order to determine the number of rings in each grain $NRV$. The dichotomic mesh type with $NRV = 10$ constitutes the best compromise. With such a discretisation, I can assure a precision better than 0.1% on the balance of fission products in every grain ($Q_{num}$) with the lowest calculation time, provided that the microscopic time-step length ($DT$) is limited. To this end, I have performed a large number of refined tests on $DT$ as well. From these results, I inferred an empirical relationship for the upper limit of $DT$ as a function of the intragranular time constants (the reduced volume diffusion coefficient, $D_v^{'}$, and the radioactive decay constant, $\lambda$) for both stable and radioactive fission products. The upper limit, $DT_{max}$, guarantees a relative error on $Q_{num} \leq 0.1\%$ during 1000 or 10000 time steps for stable or radioactive fission products, respectively under the test conditions[d].

In the third phase of the intragranular optimisation phase, I examine those parameters for which the effect may not be assessed by means of an analytical solution in the grain alone (the re-solution rate, $\Gamma_r$; the re-solution depth, $\delta_R$; the width of the imaginary supplementary layer at the grain face, $\delta_s$; and the convergence criterion for the grain boundary concentrations, $CRIT_{conv}$). They influence the intergranular module as well. Therefore, I study their effect on the balance of fission products in a closed system consisting of one spherical grain surrounded by a grain boundary layer.

The main conclusion from the third phase is that the precision of the grain boundary concentration is important for the precision on the balance of fission products in the grain. This results from the coupling between the intra- and intergranular modules, i.e. from the boundary condition and the re-solution effect at the grain face. Therefore it is necessary to analyse the influence of the intergranular parameters through their effect on the fission gas

[d] In practical FGR calculations, the precision on the intragranular inventory of fission products is *in the order of* 0.1 %, not necessarily *smaller than* 0.1 %, since the precision tests for the intragranular module were carried out under simplifying conditions.

release model, and to verify the suitability of the intragranular time-step control in the FGR model.

The implementation of the intergranular module warrants special care for the transitions between the nucleation and the growth/shrinkage phase of the grain boundary bubbles. In order to overcome numerical problems it is necessary to introduce margins on the criteria for the switches ($\Delta\hat{C}_{gbb}$ and $\Delta\rho_{bl}$). Their effect on the precision and running time has been analysed and turned out to be negligible.

For the solution of the equations in the grain boundary bubble growth/shrinkage phase, I make use of the LSODAR routine. This software has undergone extensive performance testing and optimisation, solves simultaneously a coupled set of ODE and algebraic equations, and switches automatically between stiff and non-stiff methods.

The numerical parameters required on input of LSODAR are determined in conjunction with the other global parameters in the FGR model, except for the spatial discretisation of the pellet. For the latter, I adopt the equivolume type of grid. This mesh type associates an equal weight to each macroscopic ring, and accounts for the steep gradient in the retention profile of fission products towards the pellet periphery. The choice of the remaining numerical parameters is based on a sensitivity study of the released fraction of fission gases and the calculation time, for well defined irradiation histories.

Given the interrelationship with other phenomena, the FGR model has to coupled with a fuel performance code. I use the FTEMP2 code to provide on input the radial temperature distribution. The normalised fission rate distribution in the pellets is taken to be independent of burnup in the optimisation procedure.

The determination of the remaining parameters involves three phases. In the first two phases, I employ a Taguchi approach and simulate two simplified FUMEX cases that cover extreme irradiation conditions. The results reveal that the influence of the numerical parameters is negligible at high linear heat rates ($\sim$ 40 kW/m) in contrast with the low temperature irradiation ($\sim$ 20 kW/m). Furthermore, they point out the predominant effect of the convergence criterion on the grain boundary concentrations and allow me to choose 10 macroscopic rings (i.e. $NRJ = 10$). Finally, the results confirm the findings of Olander and co-workers [30, 96], more precisely that it is necessary to include the grain size distribution in order to avoid the overprediction of the fission gas release fraction. A separate analysis of the discretised grain size distribution of Hillert [118] pointed to the optimum value of $NRK = 3$.

In the second phase, I perform more refined calculations in order to choose the last parameters: $CRIT_{conv} = RTOL\,(2) = RTOL\,(3) = RTOL\,(1) = 10^{-5}$, $\Delta\hat{C}_{gbb} = \Delta\rho_{bl} = 10^{-4}$, and $\delta_s = 3 \times 10^{-4}\mu m$. ($RTOL(i)$, with $i = 1, 2, 3$ , correspond to the relative tolerance parameters used in the subroutine LSODAR).

In the last phase, I simulate the empirical Halden threshold at which 1 % of the fission products are released. The reproduction of the Halden threshold is very sensitive to the

numerical parameters and covers a wide range of irradiation conditions. The objective is to ascertain the appropriateness of $DT_{max}$ derived in the intragranular optimisation procedure. For that purpose, I use decreasing values of $DT$, i.e I divide $DT_{max}$ by a constant factor. In order to guarantee predictions that are independent of the microscopic time-step length, it is necessary to divide $DT_{max}$ by 5. This factor provides a good compromise between precision and running time.

Despite all my efforts to limit the calculation time, the FGR model remains quite time-consuming in comparison with the total CPU time required by a fuel performance code (by a factor $\sim$ 10 to 100). This is an inherent problem of mechanistic models that solve differential equations. For this reason, such models are generally developed in a stand-alone version only, whereas the fuel performance codes compute the fractional release by means of analytical approximations.

# Chapter 9

# Model application

## Contents

## 9.1 Introduction

The fission gas release model contains many physical variables and constants. Some of these, such as decay constants, fission yields and atomic volumes are reasonably well characterised. Others, however, such as diffusion coefficients, re-solution parameters and surface energies are hard to measure and prone to large uncertainties. This lack of confidence also reflects uncertainties in other areas, for example, in the distribution of temperature, power rating, hydrostatic stress, etc. . Ultimately, of course, the uncertainties may be used advantageously as "tuning" devices with which to tailor the model to reproduce experimental data. The resulting quantities will serve as "median" or average values for further model applications.

The objective of the present chapter is twofold. The first goal is to analyse the sensitivity of my fission gas release model to the (uncertain) physical parameters. The second aim is to validate the model by comparing the predictions with well characterised experimental data. However, the interrelationship of the FGR process with the other phenomena occurring in the fuel during irradiation renders the coupling of the model with a general fuel performance code indispensable for its application. The code should provide the radial temperature, stress and fission-rate distributions in the pellets during the entire irradiation history (cf. § 8.3).

In order to test the model, I couple it with a code in two stages. At first, the thermal fission gas release model has been tested [288,290]. This model consists of the intra- and intergranular modules described in the previous chapter, except that the athermal mechanisms (cf. § 7.2.2) are not (yet) incorporated. From the preliminary sensitivity studies, the hydrostatic stress and the re-solution rate constant emerge as key parameters. More importantly, it appears imperative to account for the athermal open porosity fraction, resulting for example from the fabrication process, in order to reproduce low temperature observations properly.

In the second step, I include the athermal release mechanisms and test the complete model in conjunction with the COMETHE code from BELGONUCLEAIRE [304]. For the sake of brevity, only the sensitivity analysis of the complete model is reported in the following section. In the subsequent section I compare the model predictions with well characterised experimental data from the open literature.

## 9.2 Sensitivity analysis of the model

### 9.2.1 Test matrix

Like for the determination of the global numerical parameters in the FGR model (cf. § 8.6), I need a well defined and simple irradiation history for the sensitivity study of the physical constants. However, because the sensitivity is likely to be dependent on the irradiation conditions, several irradiation conditions are indispensable. Therefore, I consider constant linear heat rates between 20 kW/m and 40 kW/m, covering a broad range of operating conditions.

By determining the central temperature and the average burnup in the pellet when the fraction of the released gases reaches 1 or 2 %, I simulate the empirical release threshold. The main fuel rod parameters used in the COMETHE calculations are indicated in Table 8.10 on p. 174.

The fixed numerical parameters applied in the FGR model have been determined in § 8.8 and are summarised in Table 9.1.

There are many physical parameters in my FGR model for which there is a general applied value in the open literature. The fission yield for the fission gas atoms ($y$) is approximately taken to be 0.29, in accordance with recent measurements [269]. An angle of 50° is currently accepted between the grain boundary and the intergranular bubble surface ($\theta$) [1, 58, 59, 181]. The mean distance at which gas atoms are knocked back into the grains by the re-solution process at the grain boundary is $\simeq 22 \times 10^{-3} \mu m$ [58, 161], corresponding to the range of primary knock-ons [68]. In general, one assumes that there is approximately one intergranular bubble per square micron at the onset of interlinkage, i.e. $C_{bl} \simeq 1/\mu m^2$ [1, 58, 181].

The physical constants in my FGR model, to which large uncertainties pertain, amount to 7: the re-solution rate coefficient near the grain boundary ($\Gamma_r$); the free surface energy of $UO_2$ ($\gamma$); the volume ($D$) as well as the grain boundary ($D_{gb}$) diffusion coefficient for single gas atoms in $UO_2$; the conductance of the gas in the tube representing the escape tunnels for release along the grain boundaries (cf. Eq.(7.64)), which is determined by the normalisation factor $V_t^0$ and the sigmoidal function $f\,(\phi_{bl})$; and the nucleation radius of curvature of intergranular bubbles ($\rho_{bl}\,(t=0) = \rho_{bl}^0$).

In addition to the effect of those uncertain parameters on the release process, I focus my attention on several input parameters. Those which have been put forward as important with respect to the release rate are the temperature, the hydrostatic pressure ($P_h$), the average grain radius ($\overline{R_{gr}}$), and the initial open porosity fraction $(\Delta V/V)_{open}^0$. (The influence of the uncertainty on the local temperature is also underlined in § 9.3).

An exhaustive study of the effects of changing the various parameters would perhaps serve only to confuse. For this reason, it is better to limit the analysis to changes in one key parameter whilst maintaining the other parameters fixed at the "most likely" values. The

| parameter | value | | parameter | value |
|---|---|---|---|---|
| $NRV$ | 10 | | $\Delta \hat{C}_{cgb}$ | $10^{-4}$ |
| $MESHCV$ | 2 (dichotomic) | | $\Delta \rho_{bl}$ | $10^{-4}$ |
| $NRJ$ | 10 | | $RTOL(i)$ $(i = 1, 2, 3)$ | $10^{-5}$ |
| $MESHGB$ | 0 (equivolume) | | $CRIT_{conv}$ | $10^{-5}$ |
| $NRK$ | 3 | | $\delta_s$ | $3 \times 10^{-4} \mu m$ |

Table 9.1: Table summarising the fixed numerical parameters used in the sensitivity analysis of the FGR model.

most likely values for the physical constants correspond to those of the open literature that provided good results in the model calibration (cf. § 9.3). The range for each parameter is based on the data found in the open literature as well:

- The initial open porosity fraction is closely related to the density of the pellets (cf. Fig. 7.7). A typical value for a fuel pellet with a density around 95.5 % of the theoretical density (TD = 10.96 g/cm$^3$ for $UO_2$) is in the order of 0.1 %, but rises rapidly to a few percent when the density decreases below 94 % of TD [278, 305]. As a fixed value I therefore apply $(\Delta V/V)^0_{open} = 0.1$ %, and I increase this number to 2.5 %. The hypothetical case of $(\Delta V/V)^0_{open} = 0$ % is included as well.

- One of the least well characterised input parameters is $P_h$ [59, 219]. Following Bernard et al. [59], $P_h$ varies between -0 MPa and -120 MPa, where -90 MPa is taken as the fixed value. The upper limit corresponds to the fracture threshold of $UO_2$ [306] (in uni-axial traction).

- The fixed average grain radius is indicated in Table 8.10: $\overline{R_{gr}} = 8\,\mu m$. Its influence is analysed by varying the parameter by a factor 2.

- The re-solution rate coefficient is assumed to be proportional with the local fission rate density (cf. Eq.(7.53)). The re-solution rate at 20 kW/m, $\Gamma^*_r$, is taken as the reference value and varies between $10^{-5}\,s^{-1}$ and $4 \times 10^{-7}\,s^{-1}$ [1, 58, 59]. The fixed value is in the middle of this range, i.e. $2 \times 10^{-6}\,s^{-1}$, as adopted by Bernard et al. [59].

- The free surface energy, $\gamma$, varies between 0.3 J/m$^2$ and 1 J/m$^2$ according to values reported in the literature [1, 2]. Most authors seem to apply the highest value [59, 161, 181], and so do I.

- For the volume diffusion coefficient, I apply the composite expression ($D = D_a + D_b + D_c$) used by Denis et al. [58], and compare the predictions with those obtained by using Kogai's expression [181] (cf. § 7.1.3). The difference in the composite expression is a factor 4 for $D_b$ and $D_c$. In order to complement the sensitivity study, I therefore increased and decreased $D_a$ by a factor 2.

- In view of the absence of any measurement of $D_{gb}$ of Xe in $UO_2$, I have to resort to using the value for $U^{4+}$ proposed by Reynolds and Burton [86], as did Kogai [181]. More recently, Olander and myself re-examined experimental data on Xe release from trace-irradiated $UO_2$ disks [257] (cf. § 6.2.2). The fitting procedure fairly accurately fixed $D_{gb}$ at 1500 °C, but was unable to determine a reliable activation energy for this property. The value of $D_{gb}$ at 1500 °C varied between $1.6 \times 10^{-14}$ m$^2$/s and $1.1 \times 10^{-15}$ m$^2$/s, in comparison with $2.2 \times 10^{-13}$ m$^2$/s according to Kogai. This suggests that I have applied

an overestimation for $D_{gb}$. Therefore, I divide $D_{gb}$ by a factor 2 and 4 to assess its influence on the fractional release.

- In general, one assumes that there is approximately one intergranular bubble per square micron at the onset of interlinkage, i.e. $C_{bl} \simeq 1/\mu m^2$. Nevertheless, I modify this number by a factor 2 up or down, in order to ascertain the consequences on the predictions.
- Following Kogai [181], I apply a fixed value of $\phi^* = \pi/4$ as the centre for the sigmoidal curve $f(\phi_{bl})$ defined in Eq.(7.65). Nevertheless, in order to analyse its influence, I apply $\phi^*$= 50 % as employed by Denis et al. [58] and Nakajima et al. [189].
- For the normalisation factor of the gas conductance in the escape tunnels (cf. Eq.(7.64)), I apply $V_t^0 = 10^{-12}\mu m^3$ like Kogai [181]. The factor is varied by a factor 2 to test its influence on the predictions.
- Finally, in accordance with Kogai [307], I apply a nucleation radius of curvature for the intergranular bubbles of $\rho_{bl}^0 = 1 \times 10^{-3}\ \mu m$. I vary this radius by a factor 2 up or down to gauge its effect on the FGR fraction.

The choice of the fixed values for each parameter is not crucial for the present sensitivity analysis. This is corroborated by the previous parametric studies, where the same conclusions hold although I have applied somewhat different values [288, 290, 304].

### 9.2.2 Results and discussion

Prior to discussing the influence of the various parameters, it should be underlined that the empirical Halden threshold corresponds to a correlation between small and large gas releases, taken to be 0.5 % to 2 %, with the peak fuel centre temperature. This explains part of the dispersion of experimental data points on which the empirical curve is based (cf. Fig. 3.4 on p. 47), and should be kept in mind when comparing my predictions for a single pellet with that of a whole fuel rod[a].

An important implication of the Halden threshold definition is that it corresponds to the onset of *thermal* release. For this reason, I indicate the central temperature together with the average pellet burnup when the fraction of released fission gas atoms reaches 2 %, rather than 1 %, in most of the figures. The 1 %-curve is mainly relevant for the *athermal* release, and is only shown to highlight the effect of some parameters on the athermal release component of the FGR model (e.g. the effect of the initial open porosity fraction in Fig. 9.1).

#### 9.2.2.1 The effect of the initial open porosity

The effect of the initial open porosity fraction on the threshold for fission gas release is summarised in Figs. 9.1 and 9.2.

[a] In other words, I consider a uniform axial power profile in the fuel rod.

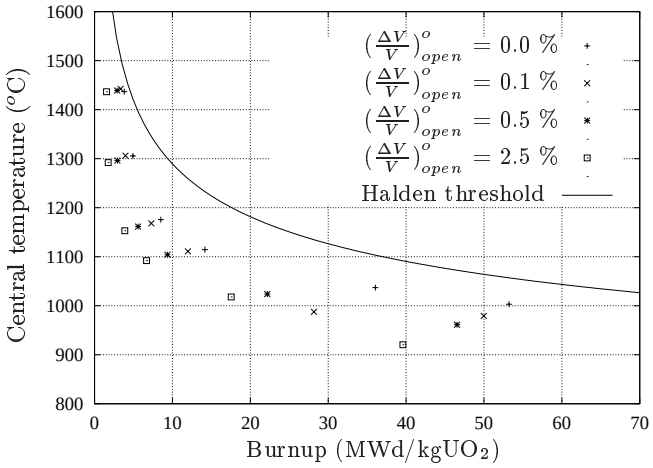


Figure 9.1: The effect of the initial open porosity fraction, $(\frac{\Delta V}{V})^o_{open}$, on the threshold for 1 % FGR.

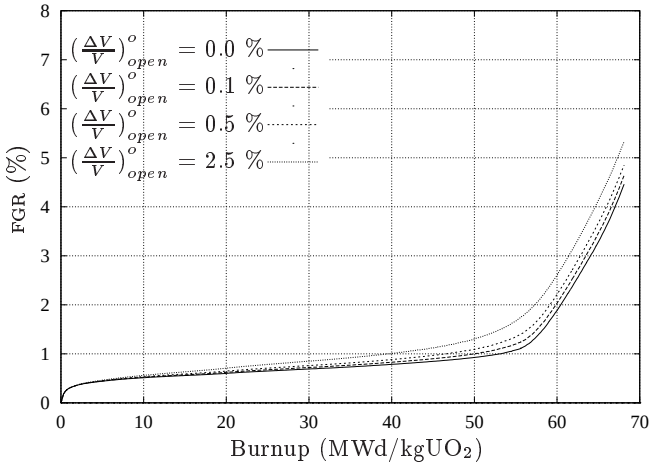


Figure 9.2: The effect of the initial open porosity fraction, $(\frac{\Delta V}{V})^o_{open}$, on the fission gas release fraction during irradiation at 20 kW/m.

As indicated in Fig. 9.1, the influence of the initial open porosity fraction on the threshold for FGR is most manifest at high burnup and low temperature, that is were athermal release (cf. $\phi_a \times J_1$ in § 7.2.2.1) predominates. Fig. 9.2 reveals that the release at 20 kW/m increases gradually below 1 %. The release mechanism is mainly athermal. There is only a sudden increase of the fractional release due to the thermal component in the pellet centre at high burnup, i.e. when gas filled bubbles cover a sufficient areal fraction of the grain boundary. The bubble interconnection at high burnup is promoted by the temperature rise, which in turn stems from the thermal conductivity degradation (like in Fig. 9.5) in combination with the thermal barrier effect of the porous rim at high burnup. The hypothetical case with $(\Delta V/V)^0_{open} = 0$ in Fig. 9.2 provides an idea of the numerical error at beginning-of-life, i.e. $\simeq 0.3$ %, since one would expect zero release at those temperature levels.

The growing importance of the athermal release contribution with burnup, as revealed in Fig. 9.1, provides an alternative explanation for the reduction of the threshold for release at burnups $\geq 50$ MWd/kgUO$_2$. It does not require an increase of the bulk diffusion coefficient [171,173], and/or a reduction of the re-solution rate at the grain boundaries [192] with burnup.

At low burnup values we have $\phi_a \simeq \phi^0_{af}\,[1 - f_{dens}\,(T, bu, R_{gr})]$, where $\phi^0_{af}$ is determined by the initial open porosity fraction, $(\Delta V/V)^0_{open}$ (cf. § 7.2.2.2). Accordingly, the athermal release can only contribute at low burnup, when $\phi^0_{af}$ is significant and the densification - or the local temperature - remains moderate. This can be inferred from the radial distributions of the FGR, $\phi_a$ and $\phi_{bl}$ at the onset of fission gas release in the case of an irradiation at a constant linear heat rate of 40 kW/m with different values of $(\Delta V/V)^0_{open}$ in Fig. 9.3. Since the release is mainly thermally driven, the fraction of FGR is closely related to the areal fraction of the gas filled bubbles ($\phi_{bl}$). The radial gradient of the athermal open porosity fraction ($\phi_a$) reflects the densification, which is strongly temperature dependent.

The models for fission gas release of various authors [58, 59, 161, 181, 240] disregard the influence of the initial open porosity fraction entirely. Furthermore, except for Koo et al. [240], they suppose that release can only occur when intergranular bubbles form an interconnected tunnel network. This is unlikely to happen during an irradiation with a central temperature below 900 °C, such as in the first FUMEX case (cf. § 9.3.1.2).

#### 9.2.2.2 The effect of the hydrostatic pressure

Fig. 9.4 shows that increasing the hydrostatic pressure exercised on the grain boundary bubbles ($P_h$) defers the onset of thermal release, due to the inhibiting effect on the bubble development. This is confirmed in Fig. 9.5, showing the accumulated fraction of FGR along with the central temperature, provided on input by the COMETHE code, as a function of the pellet average burnup during irradiation at a constant linear heat rate of 24 kW/m, for various values of $P_h$. This picture also reveals that the hydrostatic pressure does not affect the athermal release component.

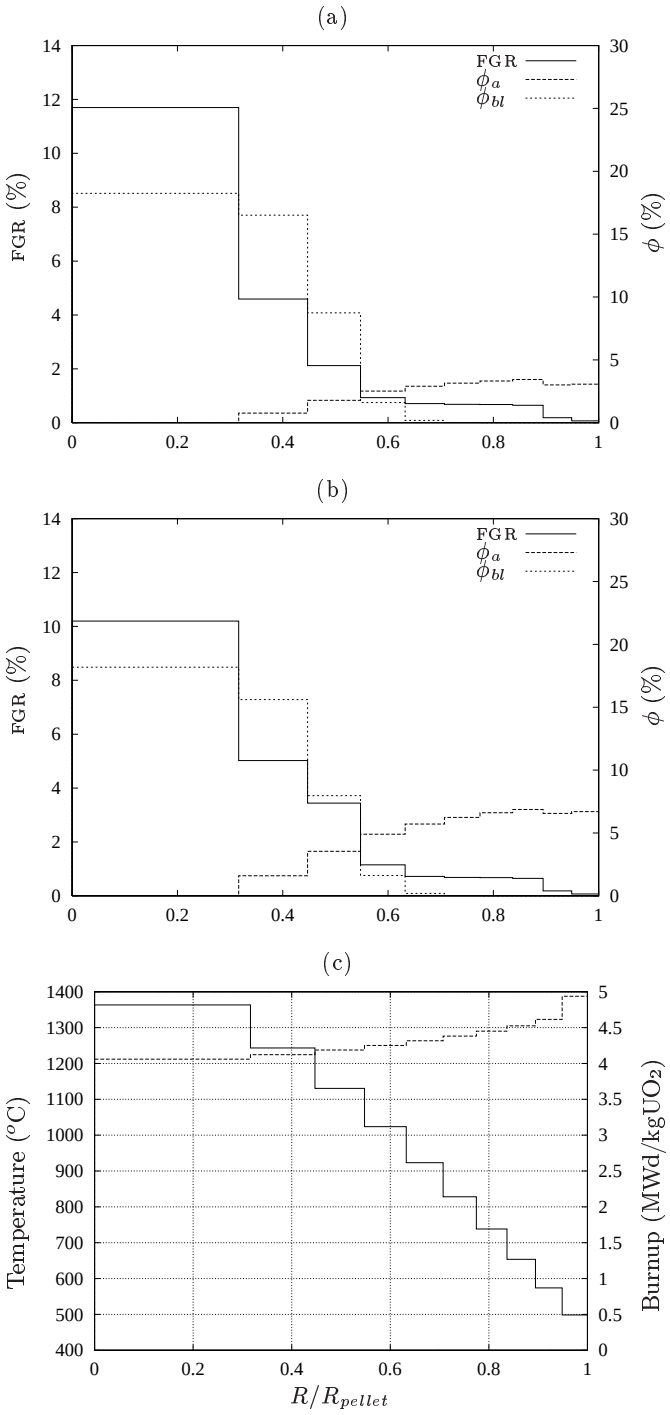


Figure 9.3: The effect of the initial open porosity fraction, $(\frac{\Delta V}{V})^o_{open}$, on the radial distribution of the fission gas release fraction, FGR, the bubble surface fraction, $\phi_{bl}$, and the athermal open porosity fraction, $\phi_a$, at the onset of release during irradiation at 40 kW/m for (a) $(\frac{\Delta V}{V})^o_{open}$ = 0.1% and (b) $(\frac{\Delta V}{V})^o_{open}$ = 2.5%. (c) Radial temperature and burnup distribution, provided by the COMETHE code, at the onset of thermal release with $(\frac{\Delta V}{V})^o_{open}$ = 0.1%.

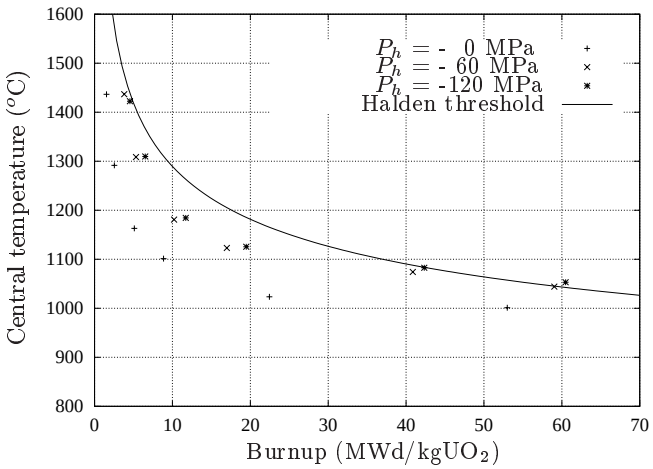


Figure 9.4: The effect of the hydrostatic pressure, $P_h$, on the threshold for 2 % FGR.

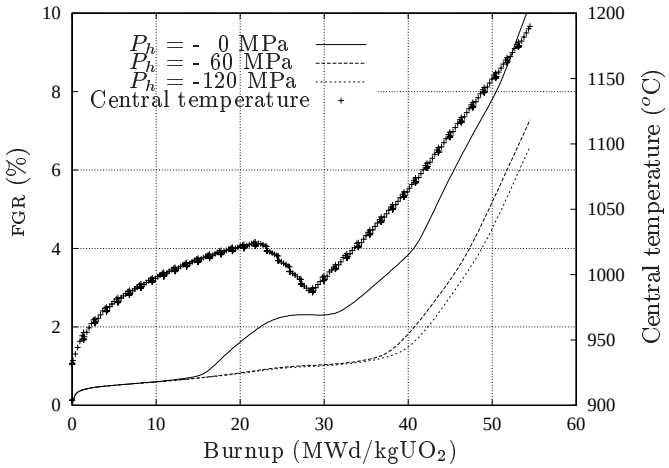


Figure 9.5: The effect of the hydrostatic pressure, $P_h$, on the fission gas release fraction during irradiation at 24 kW/m. Evolution of the central temperature (+), provided on input by the COMETHE code.

The significant effect of $P_h$ on the fission gas release process is in accordance with data, both from in-pile and out-of-pile experiments [113,186,211,215,216]. It is, however, in contradiction with the observations of Tempest et al. [217], who concluded that there was no delaying effect on interlinkage from internally pressurising the rods to 40 bar. Nevertheless, their conclusion is likely due to the range of the hydrostatic pressure applied in their experiments, which is more than one order of magnitude smaller in comparison with the range of the hydrostatic pressure in the above-mentioned experiments.

The effect of the hydrostatic pressure on the thermal release component is also reflected in the bubble pressures at the onset of release. For example, in the case of irradiation at 40 kW/m, the intergranular bubble pressure at the onset of thermal release varies between 7 MPa and 98 MPa for hydrostatic pressures between 0 MPa and -90 MPa, respectively. These calculated bubble pressures are in line with the observations of Verwerft [308].

According to Fig. 9.4, the effect of $P_h$ appears to be more important at 24 kW/m. This is just an artefact though, which can be explained by means of the curves in Fig. 9.5. The temperature drop in the pellet between 22 MWd/kgUO$_2$ and 28 MWd/kgUO$_2$ is due to the closure of the gap between the fuel and the cladding material, and causes the reduction of the release rate in the curve at 0 MPa. The temperature rise following the gap closure reflects the thermal conductivity degradation with burnup.

Finally, the slope of the curves in Fig. 9.5 change a second time above 40 MWd/kgUO$_2$, although this is only clearly visible at 0 MPa. The first alteration, around 15 MWd/kgUO$_2$ for the release at 0 MPa and 37 MWd/kgUO$_2$ for the other two curves, corresponds to the onset of thermal release in the central (first) ring of the pellet. The second change in the slope stems from the onset of release in the second ring. Such an outward shift of the onset of release with burnup has been observed experimentally by a shift of a dark ring in electron probe micro-analysis [309].

#### 9.2.2.3 The effect of the grain boundary bubble concentration

Increasing the number of grain boundary bubbles per unit of surface reduces the bubble radius at which interconnection starts off according to Eq.(7.41). The effect on the incubation period during irradiation at constant power is illustrated in Fig. 9.6. The influence is important, although it has never been reported; most authors assumed $C_{bl} \simeq 1/\mu m^2$ at the onset of release. The scatter in the published data on grain boundary bubble concentrations, however, is largely masked by the uncertainties pertaining to other parameters in Eq. (7.38), not the least being the grain boundary diffusion coefficient (cf. § 9.2.2.5).

#### 9.2.2.4 The effect of the centre of the sigmoidal function

The influence of the centre of the sigmoidal function, $\phi^*$, on the onset of release is shown in Fig. 9.7. It can be explained via its effect on the grain boundary bubble radius at which

interconnection starts off, $R^*_{bl}$. By reducing $\phi^*$ from $\pi/4$ to $1/2$, Eq.(7.41) is replaced by

$$R^*_{bl} = \frac{1}{\sqrt{2\pi C^0_{bl}}}, \tag{9.1}$$

whereas Eq.(7.42) becomes

$$\phi_{bl} = \begin{cases} \pi R^2_{bl} C^0_{bl} & R_{bl} < R^*_{bl} \\ \frac{1}{2} & R_{bl} \geq R^*_{bl} \end{cases} . \tag{9.2}$$

As a direct consequence, the gas flow through the interconnected tunnel network (cf. $J_5$ in Eq.(7.68)), rises because of the increase of the sigmoidal function, $f(\phi_{bl})$, as depicted in Fig. 9.8. Nevertheless, the effect of $\phi^*$ on the onset of release is small in comparison with the influence of the intergranular bubble density, the diffusion coefficients (cf. § 9.2.2.5), and the re-solution rate at the grain boundaries (cf. § 9.2.2.7).

#### 9.2.2.5 The effect of the diffusion coefficients

The effect of both the bulk and the grain boundary diffusion coefficient is illustrated in Figs. 9.9 and 9.10, respectively. The difference between the composite expressions for the volume diffusion coefficients applied by Denis et al. [58] and Kogai [181] is that $D_b$ and $D_c$, i.e. those that dominate below 1400 °C, are multiplied by a factor 4 (cf. § 7.1.3). This is very well reflected in Fig. 9.9. In contrast, the total variation of the thermal diffusion coefficient, $D_a$, by a factor 4 does not affect the release threshold at all. This is because only a small central portion of the pellet is at temperatures above 1400 °C during irradiation at high linear heat generating rates (in the present case LHR $\geq$ 40 kW/m).

The uncertainty on the grain boundary diffusion coefficient bears also important consequences on the kinetics of fission gas release. Despite this effect, I continue to use the expression applied by Kogai, until more accurate and reliable data become available. Besides, a possible overestimation of $D_{gb}$ may be compensated for by an underestimation of $C_{bl}$ (cf. above), or by an uncertainty on the grain boundary width [83] in the bubble growth rate equation (Eq.(7.38)). This is confirmed by a simulation with $C_{bl} = 2/\mu m^2$ and $D_{gb}/4$ in Fig. 9.10.

#### 9.2.2.6 The effect of the average grain size

In Figs. 9.11 and 9.12 there appears to be a more pronounced influence of the average grain size on the release threshold as the burnup increases. More surprisingly, the effect on the 1 %-release threshold appears to be in contradiction with that on the 2 %-threshold at high burnup and low temperatures ($\leq$1100 °C). Both observations can be explained by analysing the release curves at 20 kW/m in Fig. 9.13.

The effect of the grain size on the 1 %-release threshold reflects the sensitivity of the

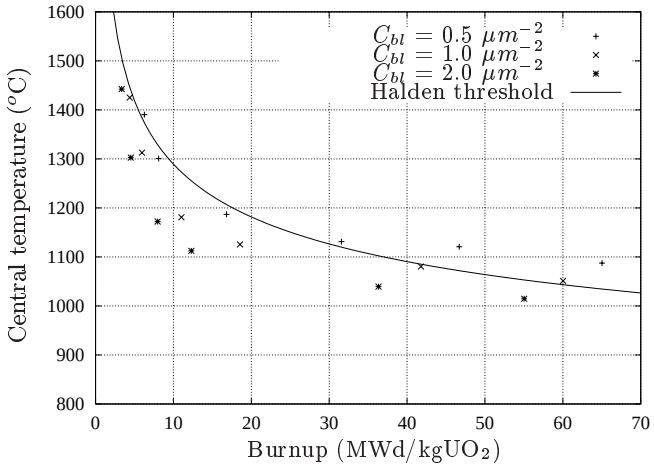


Figure 9.6: The effect of the intergranular bubble conc., $C_{bl}$, on the threshold for 2 % FGR.

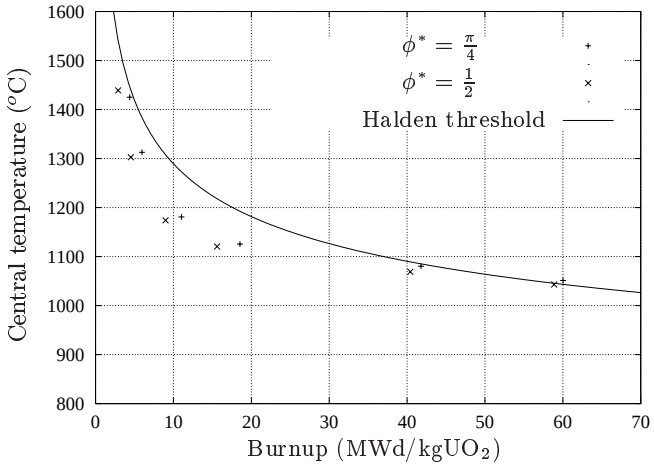


Figure 9.7: The effect of the centre of the sigmoidal function, $\phi^*$, on the threshold for 2 % FGR.

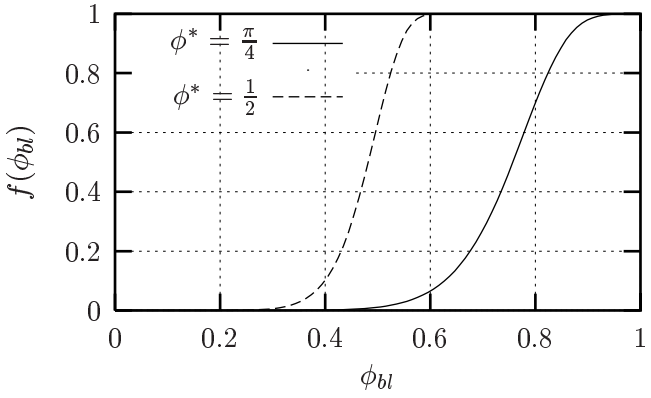


Figure 9.8: The evolution of the sigmoidal function, $f\left(\phi_{bl}\right)$, as a function of the areal coverage fraction of intergranular bubbles, $\phi_{bl}$, for two different values of $\phi^*$ according to Eq.(7.65).

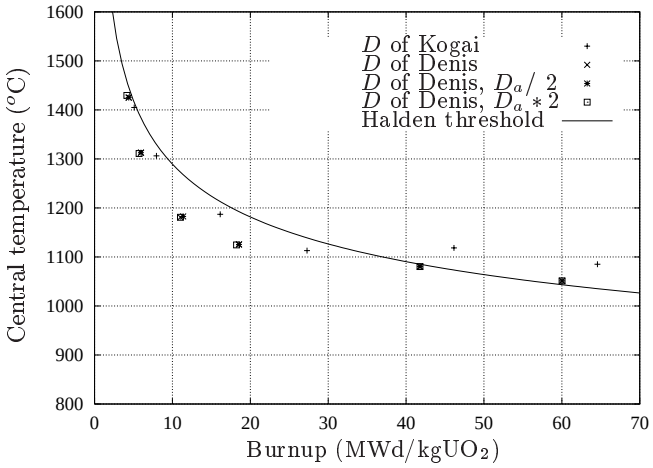


Figure 9.9: The effect of the bulk diffusion coefficient, $D$, on the threshold for 2 % FGR.

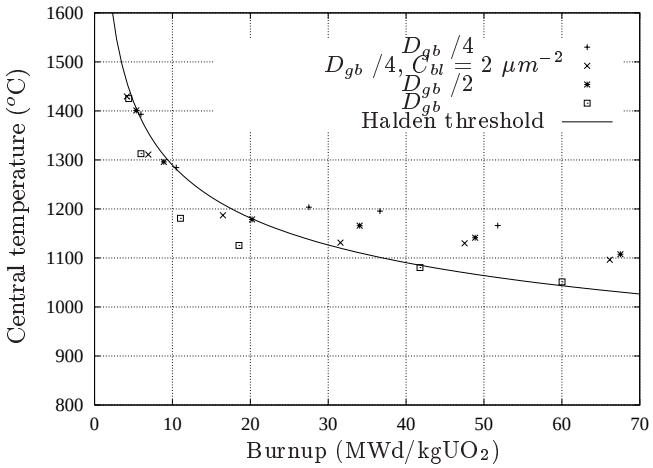


Figure 9.10: The effect of the grain boundary diff. coeff., $D_{gb}$, on the threshold for 2 % FGR.

athermal release component. The latter is the product of $\phi_a (= \phi_{af} + \phi_{at})$ and $J_1$, which depends on $\overline{R_{gr}}$ in two opposing ways. Firstly, the densification is reduced in large grain fuel according to Eq.(7.82), hence $\phi_{af} = \phi_{af}^0 \left[1 - f_{dens}\left(T, bu, \overline{R_{gr}}\right)\right]$ will enlarge. This effect predominates in the beginning of the irradiation - say below $\leq$3 MWd/kgUO$_2$ - where $f_{dens}$ changes most rapidly. Conversely, the flux leaving the grains ($J_1$) is inversely proportional with the grain radius. Increasing $\overline{R_{gr}}$ therefore reduces the athermal flux along with the grain edge tunnel formation ($\phi_{at}$). The second phenomenon determines the slope of the release curve when the densification level reaches a constant level, around 3 MWd/kgUO$_2$. Nevertheless, the release curve crosses the 1 %-threshold earlier in the large grain size fuel due to the initial densification effect.

The effect of $\overline{R_{gr}}$ on the incubation period for the 2 %-release threshold in Fig. 9.12 is due to the (thermal) release rate after the establishment of bubble interconnection around 55 MWd/kgUO$_2$ (cf. Fig. 9.13). The onset of thermal release, which starts in the pellet centre, corresponds to a saturation concentration of fission gas atoms in the grain boundaries. It is independent of the grain size [288, 310], because the specific surface of the grains and the amount of gas reaching the grain boundaries by diffusion are both inversely proportional to $\overline{R_{gr}}$. In the present calculations, the grain boundary saturation concentration is in the order of $4 \times 10^{19}$ atoms/m$^2$, matching experimental data [112, 192] quite well.

#### 9.2.2.7 The effect of the re-solution rate at grain boundaries

The influence of $\Gamma_r^*$ is depicted in Figs. 9.14, 9.15 and 9.16. An increase of the re-solution rate coefficient produces a delay in the onset of thermal release, as well as in the release rate after the establishment of the interconnected tunnel network.

At 20 kW/m, however, the effect of $\Gamma_r^*$ on the 1 %-release threshold is reversed (cf. Figs. 9.14 and 9.16). Like for the grain size effect, this can be attributed to the contribution of the athermal release. At high temperatures, the thermal release component predominates and will be mitigated by the irradiation induced re-solution at the grain boundaries. At low temperatures, the re-solution still prevents the grain boundary bubble development. However, under these circumstances the small bubbles hardly contribute to the venting of gas atoms. They mainly inhibit the athermal release by capturing those gas atoms that could be released through the athermal open porosity. Accordingly, increasing the re-solution rate will boost the athermal release component at low temperatures (by reducing $\phi_{bl}$), until the thermal release contribution prevails (cf. Fig. 9.16). Nevertheless, Fig. 9.16 also reveals that during irradiation at low temperature ($\leq$1100 °C) and low burnup levels ($\leq$10 MWd/kgUO$_2$), the re-solution process impedes the athermal release rate as well. This is because grain boundary bubbles are still in the nucleation phase (i.e. $\phi_{bl}$ is constant), hence they cannot affect the athermal release process as indicated above.

An important implication of the results in Figs. 9.14, 9.15 and 9.16 is that the local fission

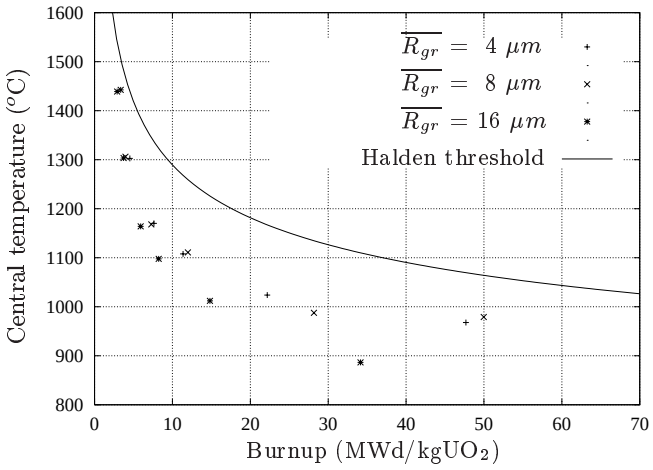


Figure 9.11: The effect of the average grain radius, $\overline{R_{gr}}$, on the threshold for 1 % FGR.

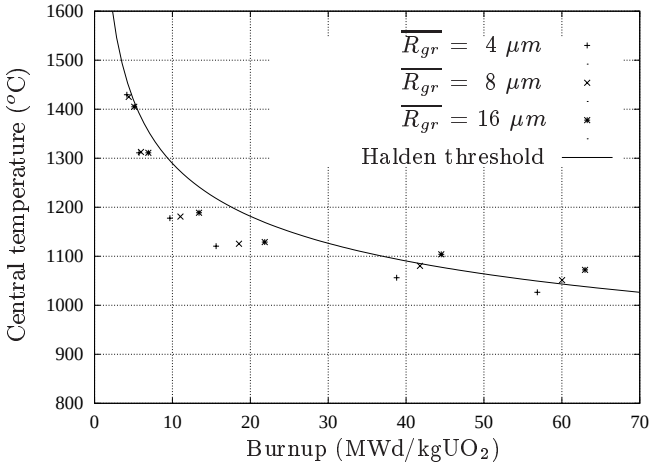


Figure 9.12: The effect of the average grain radius, $\overline{R_{gr}}$, on the threshold for 2 % FGR.

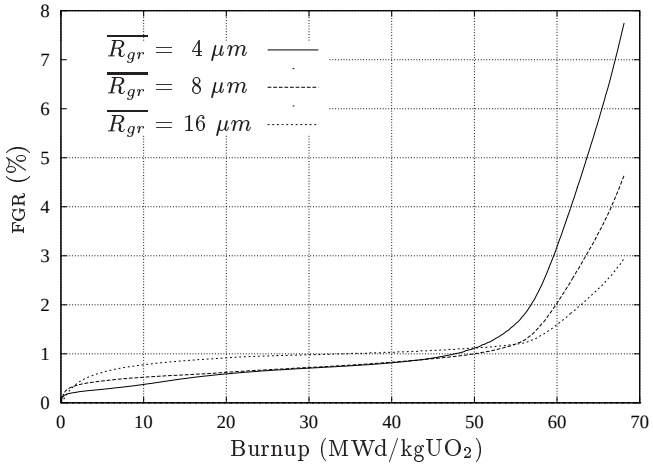


Figure 9.13: The effect of the average grain radius, $\overline{R_{gr}}$, on the fission gas release fraction during irradiation at 20 kW/m.

rate density ($\dot{F}$) plays a key role in the FGR process. Not only does it determine the bulk diffusion coefficient in the athermal regime but, more importantly, it determines the local re-solution rate according to Eq.(7.53). Therefore, it is important to choose experimental data for the model validation with well characterised fission rate densities (cf. § 9.3).

The re-solution process at the grain boundaries is disregarded in Kogai's model [181]. Besides, incorporating this effect in the intragranular module of Kogai's model is impossible since he implemented the two-zone scheme of Matthews et al. [160] (cf. § 8.8). This leads to poor predictions of the onset of release during irradiation, as the numerical technique provides a predicted "release" around 1.7 % at zero burnup [160].

#### 9.2.2.8 Parameters with a negligible effect

Among the parameters considered in the present sensitivity study, only three have a negligible effect on the onset of release. First of all, an increase in surface energy is expected to delay the onset of release through the increase of the grain boundary storage capacity. Fig. 9.17, however, shows that the effect is negligible. The relatively large bubble radius of curvature ($\sim 0.3\,\mu m$) at the onset of thermal release, in combination with the large hydrostatic pressure (e.g. 90 MPa) in the bubble growth law (cf. Eq.(7.38)) explains why the role of the surface energy is so small. Yet, even with a zero hydrostatic pressure was the effect of $\gamma$ found to be insignificant [288].

Second, the initial value of the grain boundary bubbles has no influence on the predicted release fractions when $\rho_{bl}^0$ varies between $5 \times 10^{-4} \mu m$ and $2 \times 10^{-3} \mu m$ (cf. Fig. 9.18), as expected. The choice of $\rho_{bl}^0 = 1\,nm$ is thus irrelevant.

The third parameter having a negligible influence on the onset of release is the normalisation factor of the gas conductance in the escape tunnels, $V_t^0$, as revealed in Fig. 9.19. The choice of $V_t^0 = 10^{-12} \mu m^3$ in Eq.(7.64) following Kogai [181] is therefore of no importance.

### 9.2.3 Conclusions of the parametric study

Prior to comparing the FGR model predictions with well qualified experimental data in the following section, I performed a parametric simulation of the empirical threshold for fission gas release. The model predicts the decrease of the incubation period with burnup fairly good, although it is extremely difficult to predict accurately [13]. Several other experimental observations are also reproduced, such as the outward shift of the onset of release with increasing burnup [309], and the saturation concentration or the bubble pressures at the grain boundaries [308].

The sensitivity analysis revealed the key physical parameters in the model, namely $C_{bl}$, $D_{eff}$, $D_{gb}$, $\Gamma_r$, and to a limited extent $\phi^*$. From the input parameters under consideration, mainly $P_h$ and $(\Delta V/V)_{open}^0$ proved to influence the thermal and athermal release, respectively. The onset of thermal release is not dependent on $\overline{R_{gr}}$, unlike the release rate after bubble

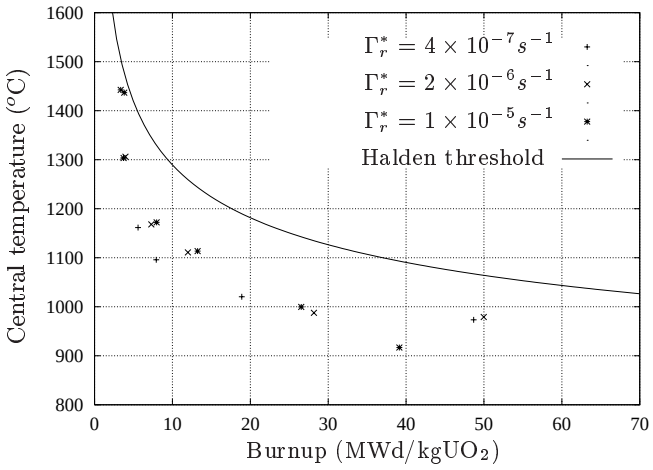


Figure 9.14: The effect of the re-solution rate coeff., $\Gamma_r^*$, on the threshold for 1 % FGR.

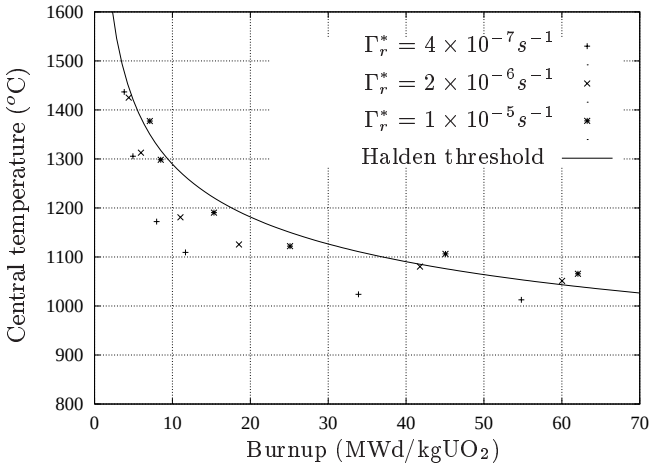


Figure 9.15: The effect of the re-solution rate coeff., $\Gamma_r^*$, on the threshold for 2 % FGR.

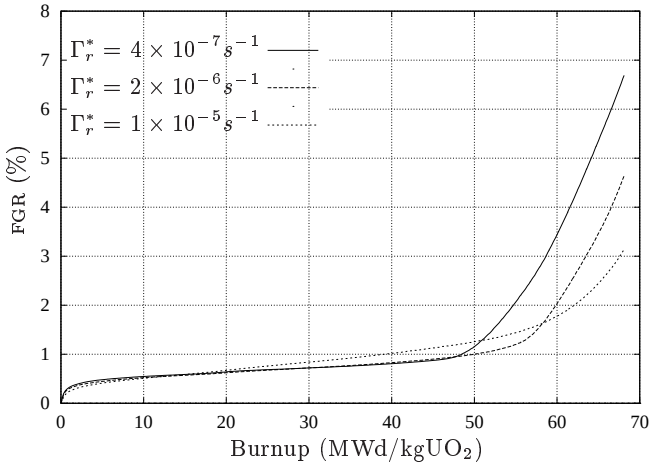


Figure 9.16: The effect of the re-solution rate coeff., $\Gamma_r^*$, on the fission gas release fraction during irradiation at 20 kW/m.

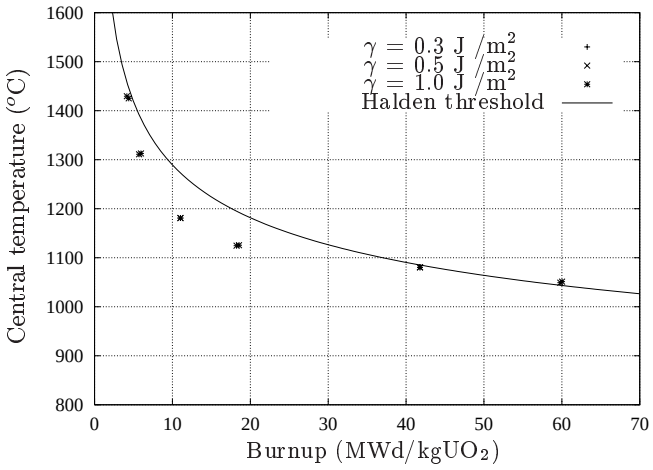


Figure 9.17: The effect of the free surface energy of $UO_2$, $\gamma$, on the threshold for 2 % FGR.

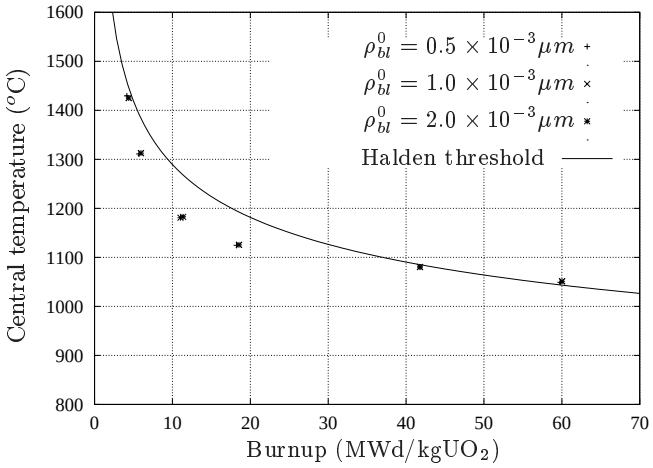


Figure 9.18: The effect of the inital radius of curvature of grain boundary bubbles, $\rho_{bl}^0$, on the threshold for 2 % FGR.

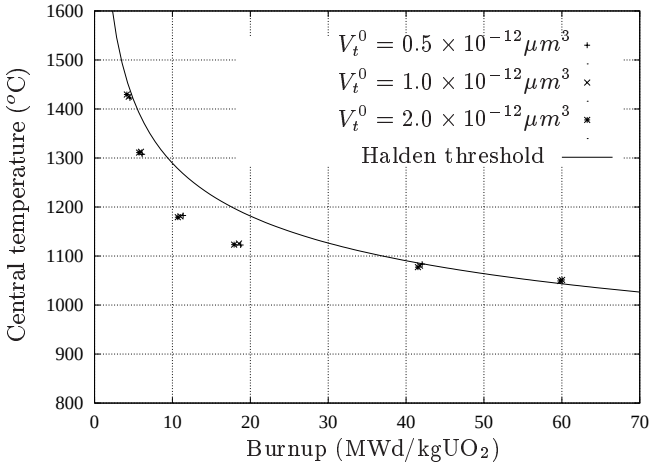


Figure 9.19: The effect of the normalisation factor of the gas conductance in the escape tunnels, $V_t^0$, on the threshold for 2 % FGR.

interconnection and the athermal release component. These results provide guidelines for choosing well characterised experimental data with which to compare model predictions in the following section.

## 9.3 Comparison of model predictions with experimental data

### 9.3.1 Experimental data

#### 9.3.1.1 Isothermal release data of small samples

In view of the sensitivity of the model predictions to certain parameters, it is recommended to choose experimental data where they are well characterised. An excellent case in point is the data-set of Zimmermann [215, 311]. He irradiated isothermally $UO_2$ samples of high density to various degrees of burnup. The fuel characteristics are presented in Table 9.2 together with the operating parameters.

| | Unit | Unrestrained sample | Restrained sample |
|---|---|---|---|
| Fuel density | % TD$^{\clubsuit}$ | 98.2 | 96.7 |
| $^{235}$U enrichment | % | 15 | 20 |
| Mean grain diameter | $\mu m$ | 10 | 7 |
| Fuel stoichiometry | - | $2.00 < O/U < 2.005$ | |
| Pellet diameter | mm | 2.2 / 5.5$^{\diamondsuit}$ | 3.0 |
| Height | mm | 1 | 5.7 |
| Burnup | %$^{\heartsuit}$ | 0.4 - 12.6 | 2.0 - 9.8 |
| Fission rate density | f/cm$^3$s | $3.1 \times 10^{13} - 1.4 \times 10^{14}$ | $4.5 \times 10^{13} - 6.3 \times 10^{13}$ |
| Mean fuel temperature | K | 1300 - 2020 | 1450 - 1920 |
| Compressive stress | MPa | 0 | 2 - 50 |

Table 9.2: $UO_2$ characteristics and irradiation data of the samples used by Zimmermann [215].

$^{\clubsuit}$% of theoretical density, which amounts to 10.96 g/cm$^3$
$^{\diamondsuit}$annular pellets
$^{\heartsuit}$a burnup level of 1 % of the initial U-atoms corresponds roughly to 8.27 MWd/kg$UO_2$

There were two different types of irradiation capsules. The first was used to evaluate the release and swelling in unrestrained samples. The irradiation specimen is a stack of annular $UO_2$ and molybdenum pellets. The alternating arrangement and the small dimensions of the $UO_2$ pellets ensure a low temperature gradient in the fuel. The fuel temperature is measured by a thermocouple in the central hole of the sample.

A different capsule was employed for the determination of the release in restrained samples. The fuel column with a length of 40 mm is irradiated in a thick-walled can of a molybdenum

| sample (nr.) | time (days) | $\dot{F}$ (f/$\mu m^3$/s) | burnup (at %) | $T_{avg}$ (K) | $T_{max}$ (K) | $P_h$ (MPa) | FGR (%) |
|---|---|---|---|---|---|---|---|
| 20 | 351 | 31 | 3.9 | 1300 | 1410 | 0 | 37.0 |
| 26 | 136 | 60 | 2.9 | 1290 | 1350 | -2 | 1.0 |
| 10 | 38 | 50 | 0.8 | 1390 | 1430 | 0 | 5.0 |
| 12 | 183 | 43 | 2.9 | 1420 | 1490 | 0 | 49.0 |
| 13 | 183 | 51 | 3.4 | 1490 | 1550 | 0 | 52.5 |
| 21 | 351 | 37 | 4.6 | 1420 | 1460 | 0 | 29.3 |
| 28 | 141 | 57 | 2.9 | 1530 | 1560 | -50 | 25.7 |
| 33 | 293 | 50 | 5.2 | 1490 | 1530 | -2 | 68.8 |
| 36 | 387 | 49 | 6.8 | 1460 | 1490 | -30 | 69.4 |
| 39 | 570 | 49 | 9.8 | 1450 | 1580 | -2 | 84.3 |
| 40 | 570 | 47 | 9.4 | 1470 | 1570 | -40 | 87.1 |
| 41 | 570 | 45 | 8.9 | 1490 | 1550 | -40 | 87.6 |
| 11 | 44 | 57 | 1.0 | 1780 | 1840 | 0 | 34.5 |
| 14 | 183 | 56 | 3.8 | 1680 | 1800 | 0 | 62.0 |
| 16 | 274 | 39 | 3.8 | 1700 | 1750 | 0 | 85.2 |
| 17 | 274 | 46 | 4.5 | 1780 | 1820 | 0 | 74.6 |
| 23 | 351 | 43 | 5.4 | 1690 | 1820 | 0 | 67.5 |
| 27 | 136 | 63 | 3.1 | 1600 | 1780 | -2 | 45.3 |
| 31 | 259 | 51 | 4.7 | 1620 | 1690 | -50 | 62.7 |
| 32 | 259 | 54 | 5.0 | 1830 | 1950 | -50 | 69.3 |
| 37 | 387 | 52 | 7.1 | 1620 | 1710 | -2 | 83.9 |
| 19 | 274 | 55 | 5.3 | 1940 | 2050 | 0 | 85.0 |
| 22 | 351 | 40 | 5.0 | 2020 | 2140 | 0 | 87.0 |
| 35 | 293 | 55 | 5.7 | 1900 | 1990 | -2 | 93.5 |
| 38 | 387 | 54 | 7.4 | 1920 | 2060 | -2 | 94.3 |

Table 9.3: Summary of the experimental data-set of Zimmermann [311] used for my FGR model validation.

alloy. The pressure loading of the fuel is provided by a piston which is loaded pneumatically by a fixed gas pressure in an outer pressure capsule. The temperature was monitored with three thermocouples in the molybdenum can wall.

Zimmermann performed a radiochemical evaluation of the burnup and, of course, an assessment of the fractional fission gas release in several samples at end-of-life. (More detailed information on the equipment and the measurement techniques may be found in [215, 311]). I employ the results of those samples for which the FGR fraction is measured to validate my model. The experimental results are listed in Table 9.3.

Zimmermann completed these results with data from other irradiation experiments, including $UO_2$ fuel pins with a low density (87% - 90 % TD), $UO_2$-Cr and $UO_2$-V cermets, and specimens of creep experiments. Nevertheless, these results are not representative for LWR fuel and, most importantly, they are not well characterised in terms of grain size, temperature,

open porosity fraction, and hydrostatic pressure. (This explains part of the large dispersion observed in his experimental data, as revealed in Fig. 9.22). For these reasons, I do not include these "supplementary" results in the validation procedure of my model for fission gas release.

The data-set in Table 9.3 provides an excellent basis for the validation of my FGR model for several reasons. First of all, the key input parameters for my model are well characterised. In particular, the temperature is monitored and uniform, the fission rate density and the burnup are measured, and the open porosity fraction is negligible. The uniformity of the temperature distribution ensures a negligible thermal stress, hence the hydrostatic stress is only determined by the externally applied pressure, which is well known. A second advantage of the data-set is that it does not require to couple the FGR model with a general fuel performance code. This rules out any discussion about uncertainties on the input variables such as the radial distribution of the hydrostatic pressure, the temperature, etc. . A third advantage of the data-set from Zimmermann is that it covers a broad range of release fractions: between 1 % and 95 % release. Finally, I can compare my predictions with those of others who relied on the same data for their model validation [58, 161, 181, 240].

#### 9.3.1.2 In-pile data from an instrumented fuel rod

In addition to the release in the samples of Zimmermann, I have simulated the fission gas release in an instrumented fuel rod, more precisely the first FUMEX case [13]. This case represents the irradiation of PWR type fuel under normal operating conditions. The measured parameters for this experiment were the fuel centerline temperature, the total rod average fission gas release during post-irradiation examination, and the cladding elongation. The main characteristics of the instrumented fuel rod - used for the COMETHE code calculations - are summarised in Table 9.4.

The simulation of the first FUMEX case is interesting since it was part of a benchmark for 19 other codes from 15 countries [13]. Furthermore, it extends the simulation of the release in small samples, described in the previous section, to that in a whole fuel rod. It also provides an extra data point in the low-temperature and low-release area, which is of most practical interest. Finally, the hydrostatic pressure is less important in the athermal regime (cf. § 9.2.2.2), which is beneficial given the uncertainties pertaining to this parameter.

### 9.3.2 Model results and discussion

#### 9.3.2.1 Isothermal release data of small samples

The predicted release fractions in the 25 samples irradiated under isothermal conditions compare very favourably with the measured values of Zimmermann in Fig. 9.20. The comparison is good since all the predicted values with the average temperature deviate less than a fac-

| Parameter | value | unit |
|---|---|---|
| pellet inside diameter | 0 | mm |
| pellet outside diameter | 8.09 | mm |
| cladding inside diameter | 8.22 | mm |
| cladding outside diameter | 9.50 | mm |
| pellet height | 10.0 | mm |
| number of dishes | 2 | - |
| relative dish radius | 0.852 | - |
| land width | 0.6 | mm |
| fuel column length | 81.0 | cm |
| fuel density | 94.1 | % |
| open porosity | 62 | ♠% |
| enrichment $U^{235}$ | 3.5 | % |
| grain radius | 5 | $\mu m$ |
| fuel surface roughness | 2.0 | $\mu m$ |
| clad surface roughness | 0.5 | $\mu m$ |
| fill gas | He | - |
| fill gas pressure | 10 | bar |

Table 9.4: Main parameters used in the COMETHE code calculations for the simulation of the first FUMEX case.

♠% of the total porosity fraction

tor 2 from the experimental results, corresponding to the generally accepted band of error. The differences may be either attributed to measurement uncertainties, such as temperature or stoichiometry deviations, either to model imperfections such as an error in the diffusion coefficients.

In order to assess the influence of temperature fluctuations, I have simulated the release in the samples with $T_{avg} \pm \Delta T$, where $\Delta T = T_{max} - T_{avg}$, which is a good measure of the deviation. The average temperature ($T_{avg}$) is indicated in Table 9.3 along with the maximum sample temperature ($T_{max}$). The corresponding results are used to plot the error-bars in Fig. 9.20. From this figure it transpires that the temperature fluctuations can explain a large part of the deviations. In addition, the large error-bars for samples 10 and 26 underline the importance of temperature variations around the threshold for thermal release. Caution should also be paid to the interpretation of the results in samples 19, 35, 38 and 22, because the average temperature exceeded 1600 °C, hence one may expect a grain growth effect.

The results obtained with the temperature variations in Fig. 9.20 suggest that any discrepancy remaining between the model and experiment must arise from other causes. It is considered that the main cause lies in uncertainties in the diffusion coefficients and/or the

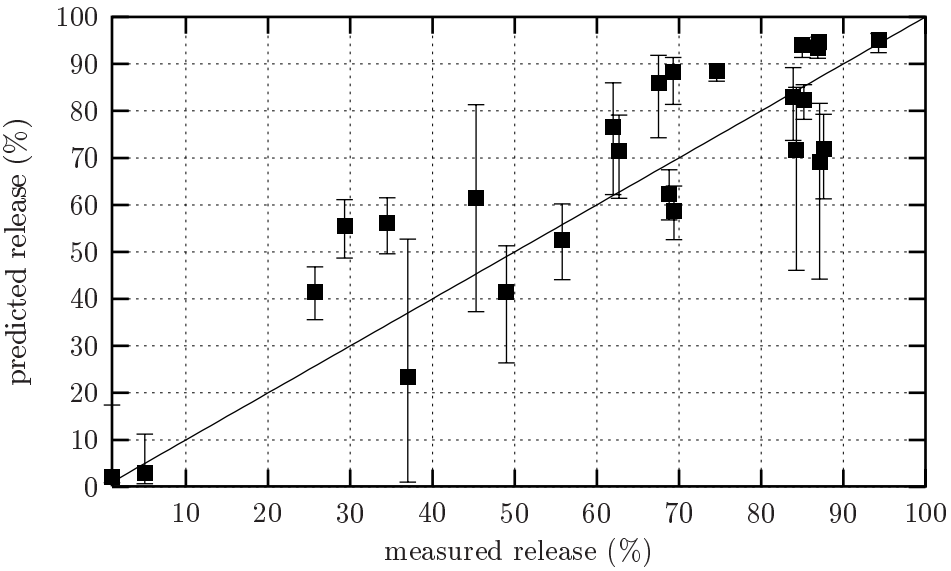


Figure 9.20: Comparison of predicted with measured fractions of fission gas release in the samples of Zimmermann [311]. The error-bars correspond to the simulation with $T_{avg} \pm \Delta T$, where $\Delta T = T_{max} - T_{avg}$, and where $T_{avg}$ and $T_{max}$ are indicated in Table 9.3.

re-solution rate coefficient. Indeed, significant uncertainties on the bulk diffusion coefficient persist (cf. § 7.1.3), and direct measurement of the re-solution rate coefficients are unavailable.

Since the samples provide release fractions for various levels of burnup and temperatures, I have plotted the corresponding fractional retention against the temperature in Fig. 9.21. This figure depicts (schematically) a radial retention distribution in a pellet with a given radial temperature and burnup distribution, as presented by Verwerft [308]. The most interesting feature in this plot is the temperature threshold at which release starts off. According to my calculations this temperature is between 1000 °C and 1100 °C, corresponding very well with that derived by Verwerft. The scatter for each temperature level arises mainly from the different burnup levels among the samples.

When comparing my predictions with those of others who relied on the same data for their model validation [58, 161, 181, 240], one could have the impression that my results are less favourable. However, the data of Zimmermann were misused by all of them. More precisely, none of them has simulated each experimental point individually. Instead, they considered average values for the grain size, fuel density, hydrostatic pressure, fission rate density, and compared their calculations with the *predictions* of Zimmermann [215] for four different temperature levels (1250 K, 1500 K, 1750 K and 2000 K) as a function of burnup (cf. Fig. 9.22). These lines, however, correspond to the simulation of Zimmermann in order to fit the experimental data points, rather than to measured release fractions in a specific

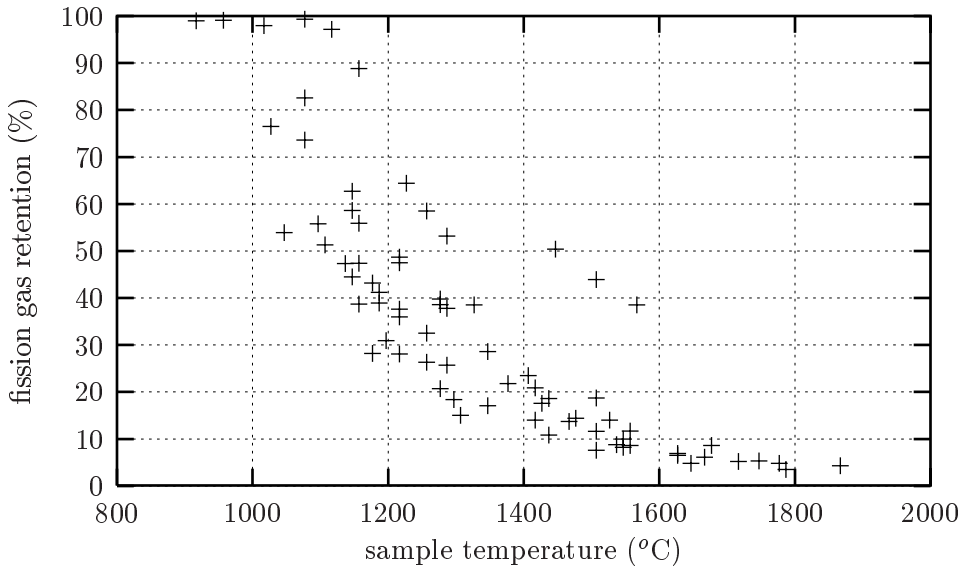


Figure 9.21: Predicted fractional retention of fission gas as a function of the temperature in the samples of Zimmermann [311], according to the fission gas release model. The calculations were performed with $T_{avg} \pm \Delta T$, where $\Delta T = T_{max} - T_{avg}$, and where $T_{avg}$ and $T_{max}$ are indicated in Table 9.3.

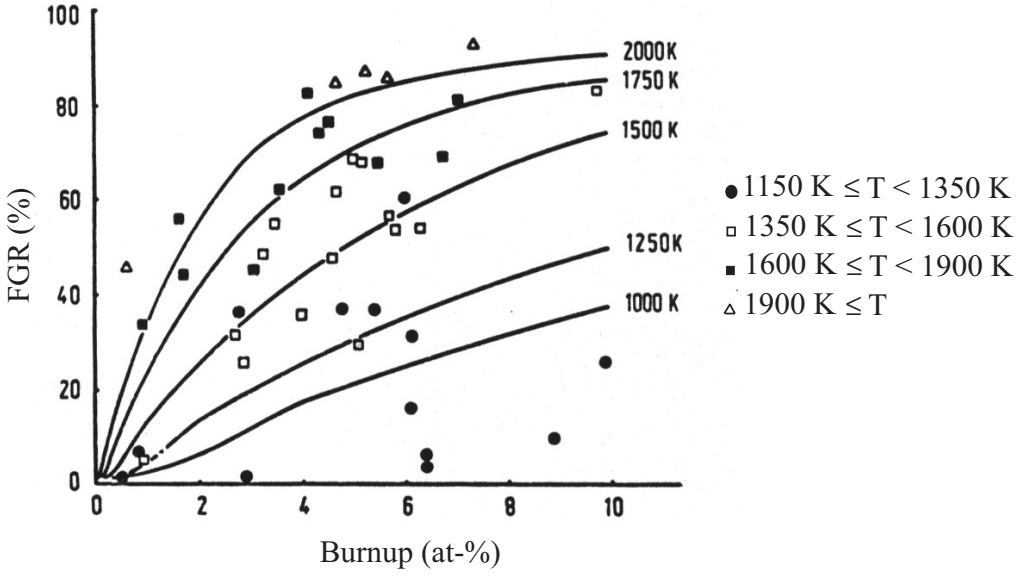


Figure 9.22: All original data points of Zimmermann [311]. The experimental results are grouped according to the temperature range, and for each range he provided a simulation at an average temperature level as a function of burnup.

sample at a particular temperature in the course of irradiation. Furthermore, Zimmermann categorized the complete data-set in four groups, according to four temperature ranges, for his simulation [311]:

- group 1: $1150\,K \leq T < 1350\,K$,
- group 2: $1350\,K \leq T < 1600\,K$,
- group 3: $1600\,K \leq T < 1900\,K$,
- group 4: $T \geq 1900\,K$.

Given the sensitivity of the predictions to the sample temperature, and in view of the large spread in the experimental data corresponding to each temperature range (group), it is misleading to draw curves like Zimmermann [215] did.

#### 9.3.2.2 First FUMEX case

The first FUMEX case is a particularly difficult case for accurate predictions since it lies near the threshold for 1 % release. The difficulty is reflected in the underprediction of the majority of the codes in the FUMEX exercise [13] (cf. Fig. 3.5).

The simulation of the fission gas release in the first FUMEX case with the present model is depicted in Fig. 9.23. The central temperature prediction according to the COMETHE code is shown in Fig. 9.24. The central temperature remained below 850 °C throughout the entire irradiation period and the measured fission gas release fraction on discharge after 33 MWd/kg$UO_2$ was 1.8 % [13]. Both the calculated fission gas release fraction in Fig. 9.23 and the central temperature in Fig. 9.24 compare favourably well with the experimental data. The modest shortfall of the predicted release fraction points to an underpredicted athermal diffusion coefficient and/or an underestimation of the athermal open surface fraction.

Although I have only considered a single axial zone in the calculations, instead of the actual axial power distribution, it does not affect the outcome. This is confirmed by the results in Fig. 9.23, where I have simulated the release for a linear heat generation rate about 7 % lower than the nominal value. The reason for the insensitivity is that the fuel rod operates in the athermal regime, where the axial power (or temperature) variations are unimportant, i.e. hardly affect the diffusion properties (cf. Fig. 7.2).

Given the low temperatures and moderate burnup level, it is unlikely that the relatively large release fraction measured on discharge stems from the interconnection of grain boundary bubbles. Besides, according to the empirical Halden threshold (cf. Eq.(3.5)) the central temperature for the onset of thermal release is $\sim$ 1100 °C, which is well above the maximum temperature recorded during the entire irradiation period. The most plausible explanation for the observed FGR fraction is the rather high proportion of initial open porosity, $(\Delta V/V)^0_{open}$, estimated to be $\sim$ 3.66 %. This is in line with previous observations [14, 152].

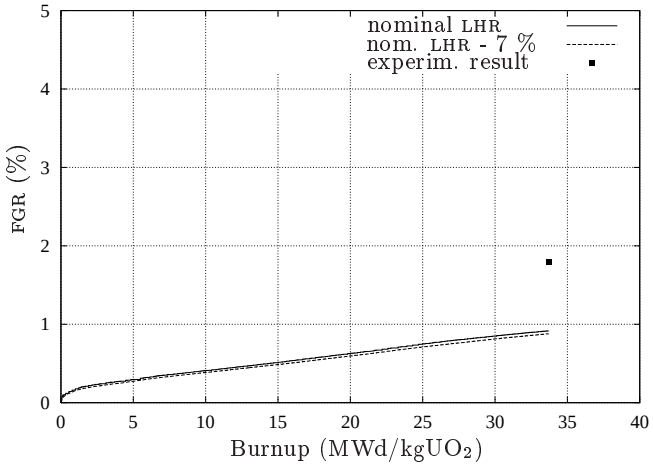


Figure 9.23: Comparison of the predicted fission gas release fraction (FGR) with the experimental result in the first FUMEX case [13] for two values of the linear heat rate (LHR).

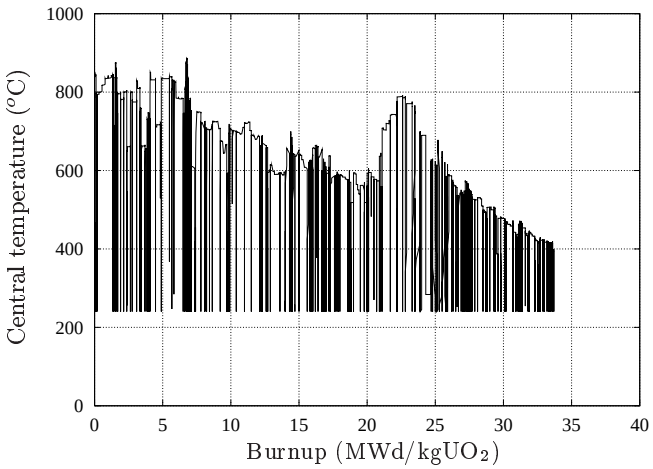


Figure 9.24: Evolution of the central temperature in the first FUMEX case [13], according to the COMETHE code.

## 9.4 Summary and conclusions

The new fission gas release model contains many physical variables and constants. Some of these are reasonably well characterised. Others, however, such as diffusion coefficients, re-solution parameters and surface energies are hard to measure and prone to large uncertainties.

Before tuning the unknown parameters in order to reproduce experimental data, it is necessary to assess quantitatively the importance of each parameter individually. To this end, I have performed a parametric simulation of the empirical threshold for fission gas release. The sensitivity study shows in the first place that the FGR model provides an excellent tool to analyse the contribution of each mechanism, as well as the influence of each parameter individually. Furthermore, it transpires that the model reproduces the decrease of the incubation period with burnup fairly well, although it is extremely difficult to predict accurately. Several other experimental observations are also reproduced, such as the outward shift of the onset of release with increasing burnup, and the saturation concentration or the bubble pressures at the grain boundaries.

The sensitivity analysis also revealed the key physical parameters in the model, namely the bubble concentration ($C_{bl}$); the effective volume diffusion coefficient ($D_{eff}$) the grain boundary diffusion coefficient ($D_{gb}$); the re-solution rate ($\Gamma_r$); and to a limited extent the centre of the sigmoidal function determining the gas conductance in the escape tunnels ($\phi^*$). Except for $C_{tr}$, however, these parameters are poorly characterised. From the input parameters under consideration, mainly the hydrostatic pressure ($P_h$) and the initial volume fraction of open porosity ($(\Delta V/V)^0_{open}$) proved to influence the thermal and athermal release, respectively. Nevertheless, $P_h$ requires more research, but this is beyond the scope of the present thesis. The onset of thermal release is not dependent on the average grain radius ($\overline{R_{gr}}$), unlike the release rate after bubble interconnection and the athermal release component.

The results of the parametric study provide guidelines for choosing qualified experimental data with which to compare model predictions. The experimental data-set of Zimmermann [311] is an excellent basis for the model validation as the crucial input parameters are well characterised. For this reason, many other authors used the same data for their model qualification [58, 161, 181, 240]. Nevertheless, all of them erroneously compared their predictions with those of Zimmermann [215], rather than with the experimental data. In addition, they applied average values for several sensitive parameters, not the least being the sample temperature. The simulation of the individual data points with my model is better, and takes into account the temperature fluctuations. In addition, the temperature threshold at which the release begins lies between 1000 °C and 1100 °C and corresponds very well with that reported by Verwerft [308].

In order to extend the model validation by means of in-pile observations, I have reproduced the first FUMEX case, which is also a difficult case for accurate predictions since it lies near the threshold for 1 % release. The simulation is satisfactory, and points out the importance

of the open porosity fraction for the athermal release.

It is thus fair to conclude that the comparison of the FGR model with experimental data, characterising normal steady state operating conditions, is satisfactory when applying for all the parameters a combination of the values that are reported in the literature. Yet, there are deviations that appear to arise from uncertainties on diffusion coefficients and re-solution parameters. Following this conclusion, it is recommended to perform extensive measurements on trace-irradiated $UO_2$ samples (cf. chapter 6). This kind of investigation should provide precious information about the diffusion coefficients. One could then implement the results in the present FGR model and re-examine experimental data, e.g. those of Zimmermann [311], to yield revised estimates of the trapping and re-solution parameters when bubbles are present.

# Part IV

# Conclusions and recommendations

# Conclusions

The general objective of this work is to improve the predictive capabilities of the fission gas release (FGR) model in fuel performance codes for light water reactors. More precisely, a FGR model has to be developed that must be able to cope with the incubation behaviour, especially with the reduction of the release threshold at high burnup, as well as with the burst phenomenon during smooth power variations in $UO_2$ fuel. These objectives are achieved by means of two complementary contributions; (a) by elucidating underlying basic mechanisms, in particular those governing the intergranular behaviour, and (b) by improving the mathematical description of the FGR process as a whole.

## Original contributions to the description of the mechanisms governing the intergranular behaviour

The onset of release is extremely difficult to predict accurately, and this just happens to be the most important region above which gas release can exacerbate. Since the onset of (thermal) release is correlated with the establishment of an interconnected network of grain boundary bubbles, it is important to have a precise description of the corresponding kinetics.

### Modelling the variable precipitation of fission products at grain boundaries

In general, the precipitation or trapping of fission products is dependent on the temperature and burnup, on the species under consideration, on stoichiometry deviations and additives, as well as on the geometrical parameters such as the number density and the size of the trapping centres. The existing models for the precipitation of volatile fission products, however, considered the traps to be perfect absorbers or black spheres, in the sense that traps did not (re-)emit fission products to the grain boundary. Accordingly, they did not account for the variable efficiency of the traps at trapping fission products impinging on their surface. In view of this, I have developed a model for precipitation of fission products in a grain boundary that embodies the variable efficiency of the traps at trapping fission products impinging on their surface, in addition to the overlapping diffusion fields between traps and the source term under continuous irradiation conditions [251].

I have assessed the influence of the trapping parameters on the precipitation rate according to different models from the open literature, which have been extended in order to incorporate the variable intrinsic reaction rate. The interrelationships among the models have been established while their limitations and range of validity have been discussed. The results reveal that there is a critical value above which the influence of the intrinsic reaction rate coefficient, between a fission product and an intergranular trap, on the global precipitation rate coefficient becomes negligible. This is beneficial given the uncertainty pertaining to this parameter. In addition, it justifies the assumption of an infinite intrinsic reaction rate coefficient for intergranular bubbles in fission gas release models, and it could explain the similar behaviour of different species for which the reduced intrinsic reaction rate coefficient is larger than 1.

### The role of grain boundary diffusion in fission gas release

There appeared to be a contradiction about the role of the grain boundary with respect to inert fission gas atoms: either it was considered to be a perfect sink where gas atoms are immobile and precipitate to form bubbles (in high burnup fuel), or the grain boundary served as a high diffusivity pathway for the release of fission products (in trace-irradiated fuel). In both approaches the grain boundary was considered to be a homogeneous phase.

I proposed [255, 256] to reconcile both points of view by accounting for the inhomogeneous characteristics of the grain boundaries in ceramics. In particular, I considered grain boundary diffusion along with trapping and irradiation induced re-solution at grain boundary traps. Consequently, grain boundary diffusion should be operative in trace-irradiated fuel, while there would be a switch to growth and interlinkage of grain boundary bubbles in controlling intergranular fission gas migration under certain conditions. This idea, however, raises several questions, among which:

1. Is there experimental evidence for grain boundary diffusion to assist the release of inert gas atoms in trace-irradiated fuel, in a similar way as for the volatile fission products Te and I?

2. What are the conditions for the transition from release assisted by grain boundary diffusion to growth and interlinkage of intergranular bubbles in controlling fission gas release?

3. How can we explain the different behaviour of inert gas atoms and the other volatile fission products (e.g. Te, I) in grain boundaries of $UO_2$?

In order to answer the first question, I have re-analysed experimental data on Xe release in trace-irradiated $UO_2$ [257]. The measurements indicated that the liberation involves more than only lattice diffusion at the specimen surface, and that the data are consistent with

sequential lattice and grain boundary diffusion unimpeded by intergranular traps. The fitting procedure also provided rough estimates of the grain boundary diffusion coefficient in $UO_2$.

In order to address the second issue, I have assessed the mean migration distance of a fission gas atom in a grain boundary decorated with a population of circular traps [256, 257]. The results provide quantitative conditions for the transition and are independent of the grain boundary diffusion coefficient, whereas the influence of the intrinsic reaction rate coefficient on the intergranular diffusion length is strongly limited under most common circumstances. It is thus fair to conclude from the computations, that for values of the geometric parameters that roughly encompass the intergranular bubble populations observed in irradiated fuel, a fission gas atom will be trapped after a migration distance in the grain boundary equal to the size of a grain or less. This result simply provides a theoretical justification for the universal rejection of grain boundary transport as a release mechanism for fission gas in irradiated $UO_2$.

Finally, the calculations also offer a qualitative explanation for the dissimilar release rates observed in trace-irradiated $UO_2$ for Te and I in comparison with Xe. More precisely, the reduced trap efficiency for the ionic species is well reflected in the variable intrinsic reaction rate ($k_{in}^{'}$), as well as the (effective) trap surface fraction ($\phi_{eff}$).

## Original contributions to the modelling of the overall FGR process

### The mathematical concept

I have developed a new mechanistic model for the release of fission gas to the free volume in LWR fuel rods [288, 290, 304]. The concept is based on Kogai's model, which appeared in the course of this investigation, but includes various improvements:

- the effective bulk diffusion coefficient accounts explicitly for the trapping and re-solution associated with intragranular bubbles, as commonly applied in other models;
- the kinetics of the intra- and intergranular behaviour of the gas atoms are coupled in both directions;
- the intergranular precipitation rate constant accounts for the competition effect between neighbouring traps;
- grain boundary bubble sweeping is accounted for during bubble growth;
- the influence of the hydrostatic pressure on the thermal release component has been corrected;
- the model accounts for two important fabrication parameters, namely the grain size distribution and the open porosity fraction.

According to the present model, the release of fission gas is determined by two different components.

The thermal release component is controlled by the formation of an interconnected tunnel network of grain boundary bubbles. These channels are established as soon as the temperature and the burnup are high enough so that a sufficient amount of gas atoms have precipitated into the intergranular cavities. The growth of these bubbles takes into account the effect of the hydrostatic stress on the grain boundary bubble size. Therefore, my model is able to handle burst release due to the lowering of the pellet clad mechanical interaction and/or the thermal stresses during power reductions.

The athermal release component is determined by the athermal diffusion coefficient together with the athermal open porosity fraction. It enables release at low temperatures where fission gas filled bubbles at grain boundaries, resulting from diffusion controlled precipitation, are not yet developed. Consequently, the athermal release provides an alternative explanation for the decrease of the release threshold at high burnup, rather than introducing an increase of the bulk diffusion coefficient, or a reduction of the re-solution rate at the grain boundaries.

### The model implementation

For the numerical implementation of the FGR model, I have written a new programme, although various subroutines come from the open literature. The key issue for the model implementation is the reduction of the calculation time while assuring sufficient precision. Most of my efforts have been devoted to the implementation of the intragranular module, since it is invoked a large number of times and the majority of the fission gas atoms remains in the grains under normal operating conditions [291,303]. The optimisation of the intragranular numerical parameters involves several steps and relies on the Taguchi technique, which provides a limited number of tests with a judicious combination of all parameters under consideration.

From the optimisation procedure, the dichotomic grid emerges as the best choice in terms of precision and running time. In addition, it allows an elegant implementation of the re-solution process near the grain boundary. This would be impossible to realise with the same accuracy in the model of Kogai, for he employed a two-zone scheme that leads to errors of $\sim 2$ % release in small-release experiments. Others overcome this problem by employing a very fine equidistant mesh, but such a grid would require much longer running times. The optimisation procedure also assures a precision on the balance of fission products in each grain in the order of 0.1 %.

Although the new FGR model has been developed in a stand-alone version, it can be coupled with any fuel performance code. This is demonstrated by the successful coupling of the FGR model with the FTEMP2 code of the OECD Halden Reactor Project [288], as well as with the COMETHE-IV code from BELGONUCLEAIRE [290, 304].

### The model application

Some of the physical variables and constants in the fission gas release model are hard to measure and prone to large uncertainties. Before fixing all the parameters and comparing the model predictions with experimental data, it is thus necessary to assess their influence on the outcome. To this end, I performed a parametric simulation of the empirical threshold for fission gas release [288, 290, 304].

The sensitivity study not only underlines the crucial parameters, it also shows that the FGR model provides an excellent tool to analyse the contribution of each mechanism to the overall release process. Furthermore, it transpires that the model reproduces

- the decrease of the incubation period with burnup fairly well, although it is extremely difficult to predict accurately;
- the outward shift of the onset of release in the pellets with increasing burnup;
- the saturation concentration or the bubble pressure at the grain boundaries.

The parametric study provides guidelines for choosing qualified experimental data with which to compare model predictions. The data-set of Zimmermann is an excellent basis for the model validation, and has been used by many others for their model qualification. Nevertheless, all of them erroneously compared their predictions with those of Zimmermann, rather than with the experimental data. In addition, they applied average values for several sensitive parameters. The simulation of the individual data points with my model is better, and takes into account the temperature fluctuations. In addition, the temperature threshold at which the release begins lies between 1000 °C and 1100 °C and corresponds very well with that reported by Verwerft.

In order to extend the model validation by means of in-pile observations, I have reproduced the first FUMEX case, which is also a difficult case for accurate predictions as the fractional release is close to the onset of release. The simulation is satisfactory, and points out the importance of the open porosity fraction for the athermal release.

It is thus fair to conclude that the comparison of the FGR model with experimental data, characterising normal steady state operating conditions, is satisfactory when applying for all the parameters a combination of the values that are reported in the literature.

# Recommendations for further research

Further research for improving the modelling of fission gas release in light water reactor fuel should be carried out in two principal directions.

On one hand, the validity domain of the model could be extended to include transient conditions (e.g. micro-cracking, grain growth), the rim effect at very high burnup (beyond 60 MWd/kg$UO_2$), MOX fuel, and the (chemically active) volatile fission products such as I and Cs. The most important issue for the Belgian nuclear industry is of course the MOX fuel. Besides modifications to the neutronic and thermal aspects of the fuel performance, there are differences in the behaviour of the fission gas atoms. Those dissimilarities not only arise from differences in the material properties; several people also attribute it to a certain degree of heterogeneity in the microstructure of certain types of MOX fuel. Several international research programmes have been launched to address this issue, among which OMICO by SCK•CEN.

On the other hand, there is a need for acquiring accurate experimental data for the diffusion coefficients, the re-solution parameters, and the grain boundary bubble characteristics in both the nucleation and the interconnection phase. For the diffusion coefficients, it is recommended to perform extensive measurements on trace-irradiated $UO_2$ samples. One could then implement the results in the present FGR model and re-examine experimental data to yield revised estimates of the trapping and re-solution parameters when bubbles are present. For the characteristics of grain boundary bubbles, White from BNFL promised to release some of their data into the public domain soon. Those experimental data should be complemented with a theoretical study; for instance by means of the Fokker-Planck theory for the bubble nucleation problem, and by means of percolation theory for the bubble interconnection. With regard to the latter, I have performed a number of preliminary Monte Carlo calculations that prove this approach to be very promising. This type of calculations should provide a sound basis for the sigmoidal functions, introduced in Kogai's model to describe the degree of bubble interconnection.

Finally, there is also room for improvement on some of the input parameters of the FGR model. The hydrostatic pressure, for example, deserves more theoretical and, if possible, experimental investigations. Following my own stress calculations in pellet segments, I have proposed a theoretical analysis in collaboration with people from CEA-Saclay, as soon as the data of Nakamura and co-workers (JAERI) will be made available.

# Appendices

# Appendix A

# List of participants in the FUMEX exercise

| Code number | Country | Organisation | Code |
|---|---|---|---|
| | Norway/OECD | HRP | Experiment |
| 1 | Argentina | CNEA | BACO |
| 2 | Bulgaria | INRNE | PIN micro |
| 3 | Canada | AECL | ELESIM.MOD11 |
| 4 | Finland | VTT | ENIGMA 5.8 |
| 5 | France | EDF | TRANSURANUS-EDF 1.01 |
| 6 | France | CEA/DRN | METEOR-TRANSURANUS |
| 7 | CEC | ITU | TRANSURANUS |
| 8 | India | BARC | PROFESS |
| 9 | India | BARC | FAIR |
| 10 | India | NPC | FUDA |
| 11 | Japan | NNFD | TRUST 1b |
| 12 | Japan | CRIEPI | EIMUS |
| 13 | China | CIAE | FRAPCON-2 |
| 14 | Romania | INR | ROFEM-1b |
| 15 | Switzerland | PSI | TRANSURANUS-PSI |
| 16 | Czech Republic | NRI Rez | PIN/W |
| 17 | United Kingdom | BNFL | ENIGMA 5.2 |
| 18 | United Kingdom | NE | ENIGMA 5.8 |
| 19 | Russia | IIM | START 3 |

More detailed information may be found in Ref. [13] .

# Appendix B

# The models for the intergranular precipitation of fission products

## B.1 The Smoluchowsky approach

Rather than using the concentration of fission products dissolved in the grain boundary, the correlation derived from the Smoluchowsky theory considers the pair-probability function for fission products and sinks or the distribution function of the fission products $U(R,t)$ [228, 229, 241]. The distribution function is a solution of the Smoluchowsky equation:

$$\frac{\partial U\left(R,t\right)}{\partial t} = D_{gb}\Delta U\left(R,t\right), \tag{B.1}$$

subject to the uniform initial condition

$$U\left(R,t=0\right) = 1, \tag{B.2}$$

and to the SBC (5.1) or RBC (5.2) at the reaction surface, while the concentration should remain finite for large values of $R$. The distribution function can be derived from the concentration profile in an infinite region bounded internally by the cylinder $R = R_{tr}$, defined by

$$V\left(R,t\right) = 1 - U\left(R,t\right), \tag{B.3}$$

with a zero initial concentration

$$V\left(R,t=0\right) = 0, \tag{B.4}$$

and a surface at constant concentration

$$V\left(R_{tr},t\right) = 1. \tag{B.5}$$

The corresponding concentration profile reads [262]

$$V(R,t) = 1 + \frac{2}{\pi}\int_0^\infty e^{-D_{gb}\lambda^2 t}\frac{C(\lambda,R)}{F(\lambda)}\frac{d\lambda}{\lambda}, \tag{B.6}$$

where

$$C(\lambda,R) = J_0(\lambda R)\,Y_0(\lambda R_{tr}) - Y_0(\lambda R)\,J_0(\lambda R_{tr}), \tag{B.7}$$

and

$$F(\lambda) = J_0^2(\lambda R_{tr}) + Y_0^2(\lambda R_{tr}). \tag{B.8}$$

The pair-probability distribution function $U(R,t)$ can be computed easily, given the definition of $V(R,t)$:

$$U(R,t) = -\frac{2}{\pi}\int_0^\infty e^{-D_{gb}\lambda^2 t}\frac{C(\lambda,R)}{F(\lambda)}\frac{d\lambda}{\lambda}. \tag{B.9}$$

In the case of a general radiation boundary condition at the reaction surface, the solution reads [262]:

$$U(R,t) = -\frac{2k_{in}^{'}}{\pi}\int_0^\infty e^{-D_{gb}\lambda^2 t}\frac{C\left(\lambda,k_{in}^{'},R\right)}{F\left(\lambda,k_{in}^{'}\right)}\frac{d\lambda}{\lambda}, \tag{B.10}$$

where

$$C\left(\lambda,k_{in}^{'},R\right) = J_0(\lambda R)\left[\lambda R_{tr}Y_1(\lambda R_{tr}) + k_{in}^{'}Y_0(\lambda R_{tr})\right] - Y_0(\lambda R)\left[\lambda J_1(\lambda R_{tr}) + k_{in}^{'}J_0(\lambda R_{tr})\right], \tag{B.11}$$

and

$$F\left(\lambda,k_{in}^{'}\right) = \left[\lambda R_{tr}J_1(\lambda R_{tr}) + k_{in}^{'}J_0(\lambda R_{tr})\right]^2 + \left[\lambda R_{tr}Y_1(\lambda R_{tr}) + k_{in}^{'}Y_0(\lambda R_{tr})\right]^2, \tag{B.12}$$

with $J_\nu$ and $Y_\nu$ representing the Bessel functions of the first and second kind of order $\nu$ ($\nu = 0, 1$) respectively [247]. The time dependent rate coefficient is obtained by integrating the normal component of the flux over the surface of the trap [229, 241]:

$$k(t) = \oint_{trap} D_{gb}\nabla U \cdot dA \tag{B.13}$$

$$= 2\pi R_{tr}D_{gb}\left[-\frac{2k_{in}^{'}}{\pi}\int_0^\infty e^{-D_{gb}\lambda^2 t}\frac{\left.\frac{\partial C\left(\lambda,k_{in}^{'},R\right)}{\partial R}\right|_{R_{tr}}}{F\left(\lambda,k_{in}^{'}\right)}\frac{d\lambda}{\lambda}\right]. \tag{B.14}$$

Making use of the derivatives and the Wronskian of Bessel functions [263]

$$Y_0(z)\,J_1(z) - J_0(z)\,Y_1(z) = \frac{2}{\pi z}, \tag{B.15}$$

we obtain in the case of radiation boundary conditions

$$\left.\frac{\partial C\left(\lambda, k_{in}^{'}, R\right)}{\partial R}\right|_{R_{tr}} = -\frac{2k_{in}^{'}}{\pi R_{tr}}, \tag{B.16}$$

and for perfect sink conditions

$$\left.\frac{\partial C\left(\lambda, k_{in}^{'}, R\right)}{\partial R}\right|_{R_{tr}} = -\frac{2}{\pi}.$$

Inserting this in (B.14), the time dependent rate coefficient for intergranular trapping in the case of a general rate limited reaction on the trap surface becomes

$$k(t) = \frac{8\left(k_{in}^{'}\right)^2 D_{gb}}{\pi}\int_0^\infty \frac{e^{-D_{gb}\lambda^2 t}}{F\left(\lambda, k_{in}^{'}\right)}\frac{d\lambda}{\lambda}, \tag{B.17}$$

whereas for perfect sinks this simplifies to

$$k(t) = \frac{8D_{gb}}{\pi}\int_0^\infty \frac{e^{-D_{gb}\lambda^2 t}}{F(\lambda)}\frac{d\lambda}{\lambda}, \tag{B.18}$$

as obtained by Szabo [229]. Finally, under quasi-steady-state conditions one obtains the following approximation [229, 262, 312]:

$$lim_{\tau\to\infty} k_{qs}(\tau) = 4\pi D_{gb}\left[\frac{1}{\ln(4\tau) - 2\gamma} - \frac{\gamma}{\left[\ln(4\tau) - 2\gamma\right]^2} - \cdots\right]$$

where $\tau = \frac{D_{gb}t}{R_{tr}^2}$ and $\gamma = 0.57722\cdots$ is Euler's constant.

## B.2 The mean field approach

In the mean field approximation, one assumes that the deviation from the bulk value of the pair-distribution function

$$\delta C(R) = C(R) - C_{bulk}, \tag{B.19}$$

satisfies

$$D_{gb}\triangle\delta C(R) = k_{ss}C_{tr}\delta C(R) \tag{B.20}$$

This equation is solved subject to either a perfect sink boundary condition (5.1) or a general rate limited boundary condition (5.2). In the general case of a radiation boundary condition, the solution can be written as:

$$C(R) = C_{bulk}\left[1 - \frac{k_{in}^{'} K_0(qR)}{qR_{tr}K_1(qR_{tr}) + k_{in}^{'}K_0(qR_{tr})}\right] \tag{B.21}$$

where $q = \sqrt{\frac{k_{ss}C_{tr}}{D_{gb}}}$.

The steady-state rate constant is obtained by dividing the fission product flux into the trap

$$4\pi R_{tr}^2 D_{gb} \left.\frac{\partial C}{\partial R}\right|_{R_{tr}} \tag{B.22}$$

by $C_{bulk}$ and multiplying by the trap density $C_{tr}$. Since $C(R)$ is a function of $k_{ss}$, this procedure leads to an implicit equation for $k_{ss}$, which is characteristic for the MFA

$$k_{ss}' = \frac{k_{in}^{'}\sqrt{2k_{ss}'\phi}K_1\left(\sqrt{2k_{ss}'\phi}\right)}{\sqrt{2k_{ss}'\phi}K_1\left(\sqrt{2k_{ss}'\phi}\right) + k_{in}^{'}K_0\left(\sqrt{2k_{ss}'\phi}\right)}, \tag{B.23}$$

where $k_{ss}^{'} = \frac{k_{ss}}{2\pi D_{gb}}$, and $\phi = C_{tr}\pi R_{tr}^2$ represents the fraction of the grain boundary covered by the traps and $K_\nu$ are the modified Bessel's functions of the second kind of order $\nu$ ($\nu = 0, 1$). Taking the limit for $k_{in}^{'} \to \infty$, corresponding to perfect sinks conditions, we obtain the same result as obtained by Szabo [229]. Taking the limit for $\phi \to 0$ and making use of the modified Bessel function's properties [247] we obtain

$$k_{ss}' = \frac{k_{in}^{'}}{1 - k_{in}^{'}\left(\gamma + \ln\sqrt{\frac{k_{ss}'\phi}{2}}\right)}] \tag{B.24}$$

## B.3 The cell model without source term

In the absence of any source term, that is under annealing conditions, the diffusion equation governing the concentration profile of fission products in a Wigner-Seitz cell surrounding each trap (cf. Fig. 5.2) in the grain boundary can be formulated in cylindrical geometry:

$$\frac{\partial C_{gbv}(R,t)}{\partial t} = \frac{D_{gb}}{R}\frac{\partial}{\partial R}\left[R\frac{\partial C_{gbv}(R,t)}{\partial R}\right] \tag{B.25}$$

The choice of the capture surface implies that an equal number of fission products crosses the border in each direction, hence

$$\left.\frac{\partial C_{gbv}(R,t)}{\partial R}\right|_{R=R_s} = 0 \tag{B.26}$$

This results from the symmetry of the concentration profile which in turn is due to the regular disposition of traps. The initial concentration profile of fission products in the cell is taken to be uniform: $C_{gbv}\left(R, t=0\right)=\theta$.

When the gas atom concentration at the surface of the trap satisfies the Smoluchowsky boundary condition (5.1), we can infer the concentration from a complementary mathematical problem. To this end we define

$$V\left(R,t\right)=C_{gbv}\left(R,t\right)-\theta \tag{B.27}$$

, with a zero initial value

$$V\left(R,t=0\right)=0, \tag{B.28}$$

and a surface at constant concentration

$$V\left(R_{tr},t\right)=-\theta. \tag{B.29}$$

The solution for this complementary problem reads [262]:

$$V\left(R,t\right)=-\left[\theta+\pi\theta\sum_{n-1}^{\infty}\exp\left(-D_{gb}\lambda_n^2 t\right)C\left(\lambda_n R\right)\frac{J_1^2\left(\lambda_n R_s\right)}{J_0^2\left(\lambda_n R_{tr}\right)-J_1^2\left(\lambda_n R_s\right)}\right] \tag{B.30}$$

where $\lambda_n$ is a root of

$$J_0\left(\lambda_n R_{tr}\right)Y_1\left(\lambda_n R_s\right)=Y_0\left(\lambda_n R_{tr}\right)J_1\left(\lambda_n R_s\right), \tag{B.31}$$

and

$$C\left(\lambda_n,R\right)=J_0\left(\lambda_n R\right)Y_0\left(\lambda_n R_{tr}\right)-Y_0\left(\lambda_n R\right)J_0\left(\lambda_n R_{tr}\right) \tag{B.32}$$

When the gas atom concentration at the surface of the trap obeys the more general radiation boundary conditions (5.2), we use Green's function for diffusion in a hollow cylinder with unit instantaneous surface source at $t=0$ and $R=R^{'}$ [262]:

$$G\left(R,R^{'},t\right)=\frac{\pi}{4}\sum_{n=1}^{\infty}\frac{\lambda_n^4 J_1^2\left(\lambda_n R_s\right)}{H_n\left(\lambda_n,k_{in}^{'}\right)}C\left(\lambda_n,k_{in}^{'},R\right)C\left(\lambda_n,k_{in}^{'},R^{'}\right)\exp\left(-D_{gb}\lambda_n^2 t\right), \tag{B.33}$$

where

$$\begin{aligned}C\left(\lambda_n,k_{in}^{'},R\right) &= J_0\left(\lambda_n R\right)\left[\lambda_n R_{tr}Y_1\left(\lambda_n R_{tr}\right)+k_{in}^{'}Y_0\left(\lambda_n R_{tr}\right)\right]\\ &\quad -Y_0\left(\lambda_n R\right)\left[\lambda_n R_{tr}J_1\left(\lambda_n R_{tr}\right)+k_{in}^{'}J_0\left(\lambda_n R_{tr}\right)\right],\end{aligned} \tag{B.34}$$

$$H\left(\lambda_n, k_{in}^{'}\right) = \lambda_n^2 \left\{ \left[\lambda_n R_{tr} J_1\left(\lambda_n R_{tr}\right) + k_{in}^{'} J_0\left(\lambda_n R_{tr}\right)\right]^2 \left(\lambda_n^2 R_{tr}^2 + k_{in}^{'2}\right) J_1^2\left(\lambda_n R_s\right) \right\}, \quad \text{(B.35)}$$

and where $\lambda_n$ are the positive roots of (5.19):

$$\begin{aligned} &\left[\lambda_n R_{tr} J_1\left(\lambda_n R_{tr}\right) + k_{in}^{'} J_0\left(\lambda_n R_{tr}\right)\right] Y_1\left(\lambda_n R_s\right) \\ &= \left[\lambda_n R_{tr} Y_1\left(\lambda_n R_{tr}\right) + k_{in}^{'} Y_0\left(\lambda_n R_{tr}\right)\right] J_1\left(\lambda_n R_s\right). \end{aligned} \quad \text{(B.36)}$$

The concentration profile in the Wigner-Seitz cell in case of a RBC can then be inferred from

$$C_{gbv}\left(R,t\right) = \int_{R_{tr}}^{R_s} G\left(R, R^{'}, t\right) 2\pi R^{'} dR^{'}. \quad \text{(B.37)}$$

Making use of the Wronskian relationship for Bessel functions (B.15) and (5.19), we obtain

$$\int_{R_{tr}}^{R_s} C\left(\lambda_n, k_{in}^{'}, R^{'}\right) R^{'} dR^{'} = \frac{-2k_{in}^{'}}{\pi\lambda_n^2}, \quad \text{(B.38)}$$

whence

$$C_{gbv}\left(R,t\right) = -\pi k_{in}^{'} \theta \sum_{n=1}^{\infty} \left[\frac{C\left(\lambda_n, k_{in}^{'}, R\right)}{F\left(\lambda_n, k_{in}^{'}\right)}\right] e^{-D_{gb}\lambda_n^2 t}, \quad \text{(B.39)}$$

where

$$F\left(\lambda_n, k_{in}^{'}\right) = \left[\frac{\lambda_n R_{tr} J_1\left(\lambda_n R_{tr}\right) + k_{in}^{'} J_0\left(\lambda_n R_{tr}\right)}{J_1\left(\lambda_n R_s\right)}\right]^2 - \left(\lambda_n^2 R_{tr}^2 + k_{in}^{'2}\right). \quad \text{(B.40)}$$

## B.4 The cell model with source term

Under continuous irradiation conditions, the diffusion equation in the Wigner-Seitz cell surrounding a trap (cf. Eq.(B.25)) contains a source term and the initial concentration is taken to be zero. When the radiation boundary condition applies at the trap surface, the solution to this problem can be written in the form:

$$C_{gbv}\left(R,t\right) = C_{\infty}\left(R\right) + C_t\left(R,t\right), \quad \text{(B.41)}$$

where $C_{\infty}\left(R\right)$ represents the stationary concentration profile, which satisfies

$$\triangle C_{\infty}\left(R\right) + S = 0 \quad \text{(B.42)}$$

along with

$$\left.\frac{\partial C_\infty(R)}{\partial R}\right|_{R_{tr}} = \frac{k_{in}^{'}}{R_{tr}} C_\infty(R_{tr}), \tag{B.43}$$

$$\left.\frac{\partial C_\infty(R)}{\partial R}\right|_{R_s} = 0. \tag{B.44}$$

The stationary concentration profile in the Wigner-Seitz cell in the case of general radiation boundary conditions reads:

$$C_\infty(R) = \frac{S}{4D_{gb}}\left[\left(R_{tr}^2 - R^2\right) + R_s^2 \ln\left(\frac{R}{R_{tr}}\right)^2 + \frac{2}{k_{in}^{'}}\left(R_s^2 - R_{tr}^2\right)\right], \tag{B.45}$$

where $C_t(R,t)$ corresponds to the transitory part of the concentration and is the solution of a simplified problem:

$$\frac{\partial C_t(R,t)}{\partial t} = \Delta C_t(R,t), \tag{B.46}$$

with initial condition $C_t(R, t=0) = -C_\infty(R)$, and boundary conditions

$$\left.\frac{\partial C_t(R,t)}{\partial R}\right|_{R_{tr}} = \frac{k_{in}^{'}}{R_{tr}} C_t(R_{tr}, t) \tag{B.47}$$

$$\left.\frac{\partial C_t(R,t)}{\partial R}\right|_{R_s} = 0. \tag{B.48}$$

Again we use Green's function (B.33) for diffusion in a hollow cylinder with unit instantaneous surface source at $t = 0$ and $R = R^{'}$:

$$C_t(R,t) = -\int_{R_{tr}}^{R_s} G\left(R, R^{'}, t\right) 2\pi R^{'} C_\infty\left(R^{'}\right) dR^{'} \tag{B.49}$$

The integral on the right hand side can be computed by making use of the Wronskian relationship of Bessel functions (B.15) and (5.19). The total concentration profile in the cellular model with radiation boundary conditions can thus be obtained:

$$C_{gbv}(R,t) = C_\infty(R) - \frac{S}{D_{gb}} \sum_{n=1}^{\infty} \left[\Psi_n\left(\lambda_n, k_{in}^{'}\right) C\left(\lambda_n, k_{in}^{'}, R\right)\right] e^{-D_{gb}\lambda_n^2 t} \tag{B.50}$$

where $C\left(\lambda_n, k_{in}^{'}, R\right)$ is given by (5.17), $\lambda_n$ are the positive roots of (5.19), $F\left(\lambda_n, k_{in}^{'}\right)$ is given by (5.18) and

$$\Psi_n\left(\lambda_n, k_{in}^{'}\right) = \frac{1}{F\left(\lambda_n, k_{in}^{'}\right)} \left\{ \frac{R_s\left[\lambda_n R_{tr} Y_1(\lambda_n R_{tr}) + k_{in}^{'} Y_0(\lambda_n R_{tr})\right]}{\lambda_n Y_1(\lambda_n R_s)} - R_s^2 - \frac{k_{in}^{'}}{\lambda_n^2} \right\}. \tag{B.51}$$

The concentration profile in the case of perfect sink conditions can simply be inferred by taking the limit for $k_{in}^{'} \rightarrow \infty$.

# Appendix C

# Analytical solution for the indirect release in trace-irradiated samples

Neglecting the areal fraction of traps ($\phi$) compared to unity in the source term of the conservation equation for mobile Xe in the grain boundaries of trace-irradiated samples, Eq.(6.9) becomes

$$\frac{1}{\kappa}\frac{\partial U}{\partial \tau} = \frac{\partial^2 U}{\partial X^2} + \left(\frac{1}{\sqrt{\pi\tau}} - 1\right) - G\,U. \tag{C.1}$$

The initial condition is

$$U = 0 \quad at \quad \tau = 0,\ \forall\, X, \tag{C.2}$$

which assumes that all Xe is in the grains prior to the high-temperature anneal. The boundary conditions are:

$$\begin{aligned} U &= 0 \quad at \quad X = 0 \\ \partial U/\partial X &= 0 \quad at \quad X \to \infty \end{aligned} \tag{C.3}$$

The conservation equation (C.1) is first transformed using the new variables:

$$\theta \equiv \kappa\tau\,, \tag{C.4}$$

$$V \equiv \frac{e^{G\theta}}{\sqrt{\kappa}}U\,, \tag{C.5}$$

which leads to:

$$\frac{\partial V}{\partial \theta} = \frac{\partial^2 V}{\partial X^2} + \frac{e^{G\theta}}{\sqrt{\pi\theta}} - \frac{e^{G\theta}}{\sqrt{\kappa}}\,. \tag{C.6}$$

Equation (C.6) is solved by the Laplace transform method with the same initial and boundary conditions as U (Eqs. (C.2) and (C.3)). The subsidiary equation for (C.6) is:

$$\frac{d^2\tilde{V}}{dX^2} - p\tilde{V} = -\frac{1}{\sqrt{p-G}} + \frac{1}{\sqrt{\kappa}\,(p-G)}\,. \tag{C.7}$$

Solving for the transform of $V$ and taking the gradient at $X = 0$ gives:

$$\left(\frac{d\tilde{V}}{dX}\right)_{X=0} = \frac{1}{\sqrt{p}\sqrt{p-G}} - \frac{1}{\sqrt{\kappa}}\frac{1}{\sqrt{p}\,(p-G)}\,. \tag{C.8}$$

The Bateman tables [313] provide the inverse transform of the second term on the right of Eq. (C.8):

$$L^{-1}\left(\frac{1}{\sqrt{\kappa}}\frac{1}{\sqrt{p}\,(p-G)}\right) = \frac{1}{\sqrt{\kappa}}\exp\left(G\theta\right)\frac{erf\left(\sqrt{G\theta}\right)}{\sqrt{G}}\,. \tag{C.9}$$

For the first term on the right of Eq. (C.8), invoking the convolution property of the Laplace transform again yields:

$$\begin{aligned} L^{-1}\left(\frac{1}{\sqrt{p}\sqrt{p-G}}\right) &= L^{-1}\left[\frac{1}{\sqrt{\left(p-\frac{G}{2}\right)^2 - \left(\frac{G}{2}\right)^2}}\right] \\ &= \exp\left(\frac{1}{2}G\theta\right) I_0\left(\frac{1}{2}G\theta\right) \end{aligned} \tag{C.10}$$

where $I_0$ is the modified Bessel function of the first kind of zero order. Assembling these results gives:

$$\begin{aligned} \left(\frac{\partial U}{\partial X}\right)_{X=0} &= \sqrt{\kappa}\exp\left(-G\theta\right)\left(\frac{dV}{dX}\right)_{X=0} \\ &= \sqrt{\kappa}\exp\left(-\frac{1}{2}G\theta\right) I_0\left(\frac{1}{2}G\theta\right) - \frac{erf\left(\sqrt{G\theta}\right)}{\sqrt{G}}\,. \end{aligned} \tag{C.11}$$

# Appendix D

# The average number of jumps in a random array of bubbles

Consider a solute atom arriving at the grain boundary from one of the adjacent grains. The injected atom will be absorbed directly if it falls within the circle of a trap, or if it lands on a lattice site neighbouring the trap (imperfect trapping is treated below). The probability of absorption of the injected atom, $p_0$, is calculated as follows. A unit area of grain boundary contains $N_{ls} = 1/a_0^2$ lattice sites; $N_{st} = \pi \left(R_{tr}/a_0\right)^2 C_{tr}$ represents the number of lattice sites internal to the traps; and the number of peripheral sites is given by $N_{ps} = 2\pi \left(R_{tr}/a_0\right) C_{tr}$. The probability of absorption of the injected atom can then be calculated as follows:

$$p_0 = \frac{N_{st} + N_{ps}}{N_{ls}} = 2\pi R_{tr} a_0 C_{tr} \left(1 + \frac{R_{tr}}{2a_0}\right) \tag{D.1}$$

If the atom is not absorbed on injection, it proceeds to undergo a random walk process on the lattice sites available to it. Since the internal sites are forbidden to the atom, the number of sites available for jumping is $N_{ls} - N_{st}$. Absorption occurs only if the atom jumps into one of the sites peripheral to the trap. Since the jumps are in random directions and the traps are randomly placed, the probability of absorption per jump, $p$, is just the ratio of the number of peripheral sites divided by the number of available sites:

$$p = \frac{N_{ps}}{N_{ls} - N_{st}} = \frac{2\pi R_{tr} a_0 C_{tr}}{1 - \pi R_{tr}^2 C_{tr}} \tag{D.2}$$

The probability that a jumping gas atom survives $j$ jumps in its random walk is:

$$P_j = (1 - p_0)(1 - p)^j \quad j = 1, 2, \ldots \tag{D.3}$$

Until now, we have assumed that once a solute atom reached a trap, it was absorbed by it. This is equivalent to the Smoluchowsky boundary condition. However, we can extend the

model to the more general partial reflection condition corresponding to imperfect trapping. To this end, we define the probability, $p_a$, that a solute atom in a site adjacent to a trap is absorbed by the trap. (For the Smoluchowsky condition $p_a = 1$). As a result, the probability of absorption of an atom per jump in Eq. (D.3) becomes $p_a p$ instead of $p$. The average number of jumps that an atom makes before absorption occurs is given by:

$$\begin{aligned} \overline{j} &= \sum_{j=1}^{\infty} j P_j \\ &= (1-p_0) \sum_{j=1}^{\infty} j \left(1-p_a p\right)^j \\ &= (1-p_0) \frac{(1-p_a p)}{(p_a p)^2} \end{aligned} \tag{D.4}$$

In order to relate $p_a$ to the dimensionless intrinsic trapping rate constant $k_{in}^{'}$, we recall the analogy between diffusion to the circular trap in the grain boundary and diffusion of point defects to the core of a dislocation. The flux per unit length of dislocation line is given by Olander [68]:

$$\oint_{trap} \overrightarrow{J} \cdot \overrightarrow{n}\, dS = Z D_{gb} \left[C\left(R_s\right) - C\left(R_{tr}\right)\right] \tag{D.5}$$

where

$$Z = \frac{2\pi}{ln\left(\frac{R_s}{R_{tr}}\right)} \tag{D.6}$$

Equating this flux to the corresponding expression in Eq. (5.2) yields:

$$C\left(R_{tr}\right) = \frac{1}{1+\beta} C\left(R_s\right) \tag{D.7}$$

where

$$\beta = \frac{2\pi k_{in}^{'}}{Z} = -\frac{1}{2} k_{in}^{'} ln\phi \tag{D.8}$$

Substituting equation (D.7) into equation (D.5) yields:

$$\oint_{trap} \overrightarrow{J} \cdot \overrightarrow{n} dS = Z D_{gb} \left(\frac{\beta}{1+\beta}\right) C\left(R_s\right) \tag{D.9}$$

Under Smoluchowsky boundary conditions the flux per unit length of dislocation line reads:

$$\oint_{trap} \overrightarrow{J} \cdot \overrightarrow{n}\, dS = Z D_{gb} C\left(R_s\right) \tag{D.10}$$

Accordingly, the flux under radiative boundary conditions reduces to this expression if $\beta \to \infty$

whence we obtain a reasonable approximation to $p_a$:

$$p_a = \frac{\beta}{1+\beta} = \frac{k'_{in} ln\phi}{k'_{in} ln\phi - 2} \tag{D.11}$$

Inserting this expression into Eq. (D.4), using the result in Eq. (6.33), and dividing by $R_s$ of Eq. (5.14) yields the dimensionless migration distance $l$ in Eq.(6.34).

# Appendix E

# Analytical solution for the intergranular module in the nucleation phase

During the nucleation phase of the intergranular bubbles, the radius of the gas-vacancy cluster is supposed to remain constant until the critical amount of gas atoms is built up. Until then, the concentrations of the gas atoms dissolved in the grain boundary ($\hat{C}_{gbv}$) and those accumulated in the gas-vacancy clusters ($\hat{C}_{gbb}$) are governed by the following coupled set of ODE:

$$\frac{d\hat{C}_{gbv}}{dt} = (1-\phi_{bl}-\phi_a)J_1 - J_2 - J_3^v - \lambda\hat{C}_{gbv} \tag{E.1}$$

$$\frac{d\hat{C}_{gbb}}{dt} = \phi_{bl}J_1 + J_2 - J_3^b - \lambda\hat{C}_{gbb} \tag{E.2}$$

The expressions for the flux terms in each macroscopic ring with index $m$ are provided in section 7.2.1.2. The intergranular source term is given by

$$J_{1,m} = A_m - B_m\hat{C}_{gbv}$$

where

$$A_m(t) = \frac{3}{\delta_s}\sum_{k,l}\frac{f_{klm}}{R_{klm}}D_{klm}C_{klm}(R_{klm},t)\,, \tag{E.3}$$

$$B_m = \frac{3}{\delta_{gb}S_{gb}\delta_s}\sum_{k,l}\frac{f_{klm}}{R_{klm}}D_{klm}\,. \tag{E.4}$$

The flux of gas atoms entering the grain boundary bubbles by diffusion controlled precipitation

is computed by means of

$$J_2 = \left[\frac{8D_{gb}\phi_{bl}\left(1-\phi_{bl}\right)}{\left(1-\phi_{bl}\right)\left(\phi_{bl}-3\right)-2\ln\phi_{bl}}\right]\frac{\hat{C}_{gbv}}{R_{bl}^2}, \tag{E.5}$$

whereas the flux of atoms knocked back in the two adjacent grains by irradiation induced re-solution is expressed as

$$J_3^v = \Gamma_r \hat{C}_{gbv}\,, \tag{E.6}$$

$$J_3^b = \Gamma_r \hat{C}_{gbb}\,, \tag{E.7}$$

where

$$\Gamma_r = \Gamma_r^* \frac{\dot{F}}{\dot{F}_{ref}}\,, \tag{E.8}$$

and the reference fission rate density ($\dot{F}_{ref}$) is taken at a linear heat generation rate of 20 kW/m.

During the nucleation phase of the grain boundary bubbles, both the number density as well as the size (or the surface fraction) of the vacancy-gas-atom cluster are assumed to remain constant. In addition, the temperature is supposed to stay constant during each microscopic time step, which implies that the grain boundary diffusion coefficient is invariable. The coupled system of ODE in each macroscopic annulus of the pellet with index $m$ can therefore be re-written as

$$\frac{d\hat{C}_{gbv}(t)}{dt} = a_v + b_v t - p\hat{C}_{gbv}(t) \tag{E.9}$$

$$\frac{d\hat{C}_{gbb}(t)}{dt} = a_b + b_b t + r\hat{C}_{gbv}(t) - q\hat{C}_{gbb}(t) \tag{E.10}$$

where all the coefficients are constant between $t_s$ and $t_e$:

$$a_v = \frac{A_m\left(t_s\right)t_e - A_m\left(t_e\right)t_s}{t_e - t_s}\left(1-\phi_{bl}-\phi_a\right) \tag{E.11}$$

$$a_b = \frac{A_m\left(t_s\right)t_e - A_m\left(t_e\right)t_s}{t_e - t_s}\phi_{bl} \tag{E.12}$$

$$b_v = \frac{A_m\left(t_e\right) - A_m\left(t_s\right)}{t_e - t_s}\left(1-\phi_{bl}-\phi_a\right) \tag{E.13}$$

$$b_b = \frac{A_m\left(t_e\right) - A_m\left(t_s\right)}{t_e - t_s}\phi_{bl} \tag{E.14}$$

$$p = B_m\left(1-\phi_{bl}-\phi_a\right) + \left[\frac{8D_{gb}\phi_{bl}\left(1-\phi_{bl}\right)}{\left(1-\phi_{bl}\right)\left(\phi_{bl}-3\right)-2\ln\phi_{bl}}\right]\frac{1}{R_{bl}^2} + \Gamma_r + \lambda \tag{E.15}$$

$$q = \Gamma_r + \lambda \tag{E.16}$$

$$r = \left[\frac{8D_{gb}\phi_{bl}\left(1-\phi_{bl}\right)}{\left(1-\phi_{bl}\right)\left(\phi_{bl}-3\right)-2\ln\phi_{bl}}\right]\frac{1}{R_{bl}^2} - B_m\phi_{bl} \tag{E.17}$$

The simplified set of ODE may be integrated analytically over the interval $t_s \leq t \leq t_e$, during which all coefficients are constant. The homogeneous solution has the form

$$\begin{pmatrix} \hat{C}_{gbv} \\ \hat{C}_{gbb} \end{pmatrix} = \begin{pmatrix} x \\ y \end{pmatrix} e^{st}, \tag{E.18}$$

where the 2 eigenfunctions $(s_1, s_2)$ , for which the set of ODE has a non-trivial solution, are obtained from the following determinant

$$\begin{vmatrix} -p-s & o \\ r & -q-s \end{vmatrix} = 0, \tag{E.19}$$

hence $s_1 = -p$ and $s_2 - -q$. The corresponding eigenvectors $(\vec{V}_1, \vec{V}_2)$ are defined by the conventional relationship:

$$\begin{aligned} \frac{d\vec{V}_1}{dt} &= \begin{pmatrix} -p & 0 \\ r & -q \end{pmatrix}\begin{pmatrix} x_1 \\ y_1 \end{pmatrix} \\ &= s_1\vec{V}_1 \\ &= -p\begin{pmatrix} x_1 \\ y_1 \end{pmatrix} \end{aligned} \tag{E.20}$$

from which we obtain

$$\vec{V}_1 = x_1\begin{pmatrix} 1 \\ \frac{r}{q-p} \end{pmatrix}, \tag{E.21}$$

and, similarly

$$\begin{aligned} \frac{d\vec{V}_2}{dt} &= \begin{pmatrix} -p & 0 \\ r & -q \end{pmatrix}\begin{pmatrix} x_2 \\ y_2 \end{pmatrix} \\ &= s_2\vec{V}_2 \\ &= -q\begin{pmatrix} x_2 \\ y_2 \end{pmatrix} \end{aligned} \tag{E.22}$$

from which we obtain

$$\vec{V}_2 = \begin{pmatrix} 0 \\ y_2 \end{pmatrix}. \tag{E.23}$$

This yields the homogeneous solution of the set of ODE:

$$\begin{pmatrix} x_h \\ y_h \end{pmatrix} = x_1 \begin{pmatrix} 1 \\ \frac{r}{q-p} \end{pmatrix} e^{-pt} + \begin{pmatrix} 0 \\ y_2 \end{pmatrix} e^{-qt} \tag{E.24}$$

For the particular solution I propose a linear form:

$$\begin{pmatrix} x_p \\ y_p \end{pmatrix} = \begin{pmatrix} \alpha_v \\ \alpha_b \end{pmatrix} + \begin{pmatrix} \beta_v \\ \beta_b \end{pmatrix} t\,. \tag{E.25}$$

Inserting Eq.(E.24) and Eq.(E.25) in the set of ODE yields:

$$\frac{d}{dt}\begin{pmatrix} x_p \\ y_p \end{pmatrix} = \begin{pmatrix} -p & 0 \\ r & -q \end{pmatrix}\begin{pmatrix} x_p \\ y_p \end{pmatrix} + \begin{pmatrix} a_v \\ a_b \end{pmatrix} + \begin{pmatrix} b_v \\ b_b \end{pmatrix} t \tag{E.26}$$

$$= \begin{pmatrix} \beta_v \\ \beta_b \end{pmatrix} t \tag{E.27}$$

Identifying the terms independent and linear in $t$ provides 4 equations for the 4 constants in the particular solution:

$$\beta_v = -p\alpha_v + a_v \tag{E.28}$$

$$\beta_b = r\alpha_v - q\alpha_b + a_b \tag{E.29}$$

$$0 = -p\beta_v + b_v \tag{E.30}$$

$$0 = r\beta_v - q\beta_b + b_b \tag{E.31}$$

The particular solution can thus be written as

$$\begin{pmatrix} x_p \\ y_p \end{pmatrix} = \begin{bmatrix} -\frac{b_v - a_v p}{p^2} \\ -\frac{r}{q}\left(\frac{b_v - a_v p}{p^2}\right) - \left(\frac{r b_v + p b_b}{q p^2}\right) + \frac{a_b}{q} \end{bmatrix} + \begin{pmatrix} \frac{b_v}{p} \\ \frac{r b_v + p b_b}{pq} \end{pmatrix} t\,. \tag{E.32}$$

I determine the coefficients in the homogeneous solution from the two initial conditions:

$$\begin{bmatrix} \hat{C}_{gbv}(t_s) \\ \hat{C}_{gbv}(t_s) \end{bmatrix} = \begin{pmatrix} \theta_v \\ \theta_b \end{pmatrix}$$

$$= x_1 \begin{pmatrix} 1 \\ \frac{r}{q-p} \end{pmatrix} e^{-pt_s} + \begin{pmatrix} 0 \\ y_2 \end{pmatrix} e^{-qt_s}$$

$$+ \begin{bmatrix} -\frac{b_v - a_v p}{p^2} \\ -\frac{r}{q}\left(\frac{b_v - a_v p}{p^2}\right) - \left(\frac{r b_v + p b_b}{q p^2}\right) + \frac{a_b}{q} \end{bmatrix} + \begin{pmatrix} \frac{b_v}{p} \\ \frac{r b_v + p b_b}{pq} \end{pmatrix} t_s \tag{E.33}$$

which yields the analytical solution of the grain boundary concentrations in each macroscopic

ring of the pellet during the time-interval $t_s \leq t \leq t_e$:

$$\begin{aligned}
\hat{C}_{gbv}(t) &= \theta_v e^{-p(t-t_s)} - \frac{b_v - a_v p}{p^2}\left[1 - e^{-p(t-t_s)}\right] \\
&\quad + \frac{b_v}{p}\left[t - t_s e^{-p(t-t_s)}\right] \qquad \text{(E.34)} \\
\hat{C}_{gbb}(t) &= \frac{r}{q-p}\left[\theta_v + \frac{b_v - a_v p}{p^2} - \frac{b_v}{p} t_s\right]\left[e^{-p(t-t_s)} - e^{-q(t-t_s)}\right] \\
&\quad - \left[\frac{r}{q}\left(\frac{b_v - a_v p}{p^2}\right) + \frac{r b_v + p b_b}{p q^2} - \frac{a_b}{q}\right]\left[1 - e^{-q(t-t_s)}\right] \\
&\quad + \left(\frac{r b_v + p b_b}{pq}\right)\left[t - t_s e^{-q(t-t_s)}\right] + \theta_b e^{-q(t-t_s)} \qquad \text{(E.35)}
\end{aligned}$$

# Bibliography


[1] R.J. White and M.O. Tucker. A new fission gas release model. *J. Nucl. Mater.*, 118:1–38, 1983.

[2] E.N. Hodkin and M.G. Nicholas. Surface and interfacial properties of non-stoichiometric uranium dioxide. *J. Nucl. Mater.*, 67:171–180, 1977.

[3] P. Van Uffelen. An overview of fission product release mechanisms. Technical Report R-3144, SCK•CEN, 1997. Internal report of Belgian National Nuclear Research Center.

[4] D.R. Olander. *Fundamental aspects of nuclear reactor fuel elements*, chapter 15. Technical Information Center - Energy Research and Development administration, University of California, Berkeley, 1976. TID-26711-P1 or ISBN 0-87079-031-5.

[5] C. Wise. Recoil release of fission products from nuclear fuel. *J. Nucl. Mater.*, 136:30–47, 1985.

[6] B.J. Lewis. Fission product release from nuclear fuel by recoil and knock-out. *JNM*, 148:28–42, 1987.

[7] OECD. Scientific issues in fuel behaviour. Technical report, NEA Nuclear Science Committee Task Force, 1995.

[8] R.J. White, A. Haaland, and E. Skattum. The power and burn-up dependence of thermal and fission product release phenomena deduced from fuel irradiation in the gas flow rigs IFA-430 and IFA-504. Technical Report HWR-119, OECD Halden Reactor Project, 1984.

[9] H. Wallin and J.A. Turnbull. IFA-563 isothermal wafer fuel test : irradiation history and fission gas release measurements up to 25 MWd/kg$UO_2$. Technical Report HWR-411, OECD Halden Reactor Project, 1994.

[10] G. Nilsson. Ejection of uranium atoms from sintered $UO_2$ by fission fragments in different gases and at different pressures. *J. Nucl. Mater.*, 20:215–230, 1966.

[11] G.T. Lawrence. A review of the diffusion coefficient of fission-product rare gases in uranium dioxide. *J. Nucl. Mater.*, 71:195–218, 1978.

[12] K. Forsberg, F. Lindström, and A.R. Massih. Modelling of some high burnup phenomena in nuclear fuel. In IAEA [314], pages 251–275. Windermere, United Kingdom.

[13] IAEA. Fuel modelling at extended burnup. Technical Report IAEA-TECDOC-998, 1998.

[14] M. Møgensen, C. Bagger, H. Toftegaard, and P. Knudsen. Fission gas release below 20 kW/m in transient tested water reactor fuel at extended burnup. [315], pages 32–37. Pembroke, Ontario, Canada.

[15] R.W. Grimes. Simulating the behaviour of inert gases in $UO_2$. In Donnelly and Evans [316], pages 415–429.

[16] Hj. Matzke. Gas release mechanisms in $UO_2$ - a critical review. *Rad. Effects*, 53:219–242, 1980.

[17] Hj. Matzke. *Diffusion in ceramic oxide systems*, pages 1–56. Volume 17 of Hastings [317], 1986.

[18] Hj. Matzke. Fundamental aspects of inert gas behaviour in nuclear fuels : oxides, carbides and nitrides. In Donnelly and Evans [316], pages 401–414.

[19] J.H. Davies and F.T. Ewart. The chemical effects of composition changes in irradiated oxide fuel materials. *J. Nucl. Mater.*, 41:143–155, 1971.

[20] H. Kleykamp. The chemical state of LWR high-power rods under irradiation. *J. Nucl. Mater.*, 84:109–117, 1979.

[21] J.-P. Piron. Fuel properties at high burnup - part ii. Technical Report HBC/91/30, S.A. BELGONUCLEAIRE - SCK•CEN, 1991. Topical report of the High Burnup Chemistry (HBC) Program.

[22] Hj. Matzke. Oxygen potential in the rim region of high burnup $UO_2$ fuel. *J. Nucl. Mater.*, 208:18–26, 1994.

[23] C.E.L. Hunt, D.S. Cox, and F.C. Iglesias. Fission-product release during accidents - an accident management perspective. *Nuclear Engineering and Design*, 148:205–216, 1994.

[24] K. Une, M. Amaya, M. Imamura, and Y. Korei. Fission gas release from defective BWR fuels. *J. Nucl. Mater.*, 226:323–326, 1995.

[25] B.J. Lewis, R.D. MacDonald, N.V. Ivanoff, and F.C. Iglesias. Fuel performance and fission product release studies for defected fuel elements. *Nucl. Technol.*, 103:220–245, aug 1993.

[26] W. Miekeley and F.W. Felix. Effect of stoichiometry on diffusion of xenon in $UO_2$. *J. Nucl. Mater.*, 42:297–306, 1972.

[27] M.A. Mansouri. *Release of fission products from lightly-irradiated* $UO_{2+x}$. PhD thesis, University of California, Berkeley, 1995.

[28] M.A. Mansouri and D.R. Olander. Fission product release from trace irradiated $UO_{2+x}$. *J. Nucl. Mater.*, 254:22–33, 1998.

[29] B. Grapengriesser and D. Schrire. Impact of systematic stoichiometry differences among BWR rods on fission gas release. [315], pages 103–110. Pembroke, Ontario, Canada.

[30] S.G. Prussin and D.R. Olander. Migration of fission products in $UO_2$. Technical Report DOE/ER/13033–T1, University of California, Berkeley, 1995.

[31] D. Freson. Fuel properties at high burnup - part ii: Fission gas release and fuel swelling. Technical Report HBC/96/52, S.A. BELGONUCLEAIRE - SCK•CEN, 1996. Topical report of the High Burnup Chemistry (HBC) Program.

[32] P.S. Copeland and R.C. Smith. Experiments to investigate the effects of small changes in fuel stoichiometry on fission gas release. In IAEA [314], pages 443–454. Windermere, United Kingdom.

[33] M. Hirai, J.H. Davies, and R. Williamson. Diffusivities of fission gas species in $UO_2$ and (U,Gd)O $_2$ nuclear fuels during irradiation. *J. Nucl. Mater.*, 226:238–251, 1995.

[34] A.B. Lidiard. Self-diffusion of uranium in $UO_2$. *J. Nucl. Mater.*, 19:106–108, 1966.

[35] S.E. Lemekhov. Towards mechanistic understanding of FGR and related processes at extended burnup and specified conditions. [318], pages 220–228. West Palm Beach, Florida.

[36] K. Park and D.R. Olander. A defect model for the oxygen potential of urania. *High Temperature Science*, 29:203–222, 1990.

[37] Y. Iwano. A defect study of nonstoichiometric uranium dioxide by statistical-mechanical models. *J. Nucl. Mater.*, 209:79–91, 1994.

[38] S. Nicoll, Hj. Matzke, and C.R.A. Catlow. A computational study of the effect of Xe concentration on the behaviour of single Xe atoms in $UO_2$. *J. Nucl. Mater.*, 226:51–57, 1995.

[39] K. Shiba, A. Itoh, and M. Akabori. The mechanisms of fission gas release from (Th,U)$O_2$. *J. Nucl. Mater.*, 126:18–24, 1984.

[40] K. Une, I. Tanabe, and M. Oguma. Effects of additives and the oxygen potential on the fission gas diffusion in $UO_2$ fuel. *J. Nucl. Mater.*, 150:93–99, 1987.

[41] S. Kashibe and K. Une. Effect of additives ($Cr_2O_3$, $Al_2O_3$, $SiO_2$, MgO) on diffusional release of $^{133}$Xe from $UO_2$ fuels. *J. Nucl. Mater.*, 254:234–242, 1998.

[42] J.C. Killeen. Fission gas release and swelling in $UO_2$ doped with $Cr_2O_3$. *J. Nucl. Mater.*, 88:177–184, 1980.

[43] Y. Harada. Sintering behaviour of niobia-doped large grain $UO_2$ pellet. *J. Nucl. Mater.*, 238:237–243, 1996.

[44] P.T. Sawbridge, C. Baker, R.M. Cornell, K.W. Jones, D. Reed, and J.B. Ainscough. The irradiation performance of magnesia-doped $UO_2$ fuel. *J. Nucl. Mater.*, 95:119–128, 1980.

[45] S. Gamaury, B. Morel, and Ph. Dehaudt. Advanced fuel with improved cesium retention. a study using simulated fuel. volume 2, pages 85–90. German Nuc. Soc., European Nuc. Soc., INFORUM, mar 1995.

[46] P. Shewmon. *Diffusion in solids.* The Minerals, Metals & Materials Society, second edition, 1989.

[47] S.W. Tam, J.K. Fink, and L. Leibowitz. Theory of high-temperature phase transitions in actinide oxides. *J. Nucl. Mater.*, 130:199–206, 1985.

[48] S. Van Den Berghe. *The uranium valence in the Cs-U-O system: crystal structures and thin layers. Contribution to the physico-chemical study of the grain boundaries in irradiated fuel.* PhD thesis, Université de Limoges, 2001.

[49] J.A. Turnbull, C.A. Friskney, J.R. Findlay, F.A. Johnson, and A.J. Walter. The diffusion coefficients of gaseous and volatile species during the irradiation of uranium dioxide. *J. Nucl. Mater.*, 107:168–184, 1982.

[50] P.A. Tempest. The reliability of on-line fission gas release measurements in the study of fuel interlinkage and resintering phenomena. Technical Report HWR-275, OECD Halden Reactor Project, 1991.

[51] J.H. Evans. Recent experimental studies on thermal and irradiation-induced resolution of gas atoms from bubbles in solids. In Donnelly and Evans [316], pages 307–319.

[52] Hj. Matzke, C. Ronchi, and C. Baker. Precipitation of Xe and Cs into bubbles, kinetics of bubble migration and alternative release processes. *Eur. Appl. Res. Repts.*, 5(6):1105–1157, 1984.

[53] R.A. Verrall, Hj. Matzke, T. Ogawa, and B.J.F. Palmer. Iodine, rubidium, and krypton release and bubble formation in oxide fuels. In I.A. Hastings, editor, *Proc. Intern. Conf. CANDU Fuel*, number AECL-9475, 1986.

[54] Hj. Matzke, I.L.F. Ray, and R.A. Verrall. Diffusion and behaviour of iodine and rubidium in $UO_2$ and $ThO_2$. In *Water reactor fuel behaviour and fission product release in off-normal and accident conditions*, number IWGFPT/27, pages 183–195. IAEA, 1986.

[55] W.H. Hocking, R.A. Verrall, P.G. Lucuta, and Hj. Matzke. Depth-profiling studies of ion-implanted cesium and rubidium in SIMFUEL and uranium dioxide. *Rad. Effects*, 125:299–321, 1993.

[56] Y.H. Kalnin and E.A. Kotomin. A comparison of the effective medium and modified smoluchowski equations for the reaction rate of the diffusion-controlled reactions. *J. Nucl. Mater.*, 232:253–255, 1996.

[57] M.V. Speight. A calculation on the migration of fission gas in material exhibiting precipitation and re-solution of gas atoms under irradiation. *Nucl. Sc. Eng.*, 37:180–185, 1969.

[58] A. Denis and R. Piotrkowski. Simulation of isothermal fission gas release. *J. Nucl. Mater.*, 229:149–154, 1996.

[59] L.C. Bernard and E. Bonnaud. Finite volume method for fission gas release. *J. Nucl. Mater.*, 244:75–84, 1997.

[60] J.R. MacEwan and W.H. Stevens. Xenon diffusion in $UO_2$. Some complicating factors. *J. Nucl. Mater.*, 11:77–93, 1964.

[61] R.A. Jackson and C.R.A. Catlow. Trapping and solution of fission Xe in $UO_2$. Part 1: Single gas atoms and solution from underpressurized bubbles. *J. Nucl. Mater.*, 127:161–166, 1985.

[62] A.R. Whapman. Electron microscopy observation of the fission gas bubble distribution in $UO_2$. *Nucl. Appl.*, 2:123, 1966.

[63] A.J. Manley. Transmission electron microscopy of irradiated $UO_2$ fuel pellets. *J. Nucl. Mater.*, 27:216–224, 1968.

[64] R.S. Nelson. The stability of gas bubbles in an irradiation environment. *J. Nucl. Mater.*, 31:153–161, 1969.

[65] J.A. Turnbull. The distribution of intragranular fission gas bubbles in $UO_2$ during irradiation. *J. Nucl. Mater.*, 38:203–212, 1971.

[66] R.M. Cornell. An electron microscope examination of matrix fission-gas bubbles in irradiated uranium dioxide. *J. Nucl. Mater.*, 38:319–328, 1971.

[67] J.A. Turnbull. A review of irradiation induced re-solution in oxide fuels. *Rad. Effects*, 53:243–250, 1980.

[68] D.R. Olander. *Fundamental aspects of nuclear reactor fuel elements*, chapter 13. Technical Information Center - Energy Research and Development administration, University of California, Berkeley, 1976. TID-26711-P1.

[69] H. Blank and Hj. Matzke. The effect of fission spikes on fission gas re-solution. *Rad. Effects*, 17:57–64, 1973.

[70] C. Ronchi and P.T. Elton. Radiation re-solution of fission gas in uranium dioxide and carbide. *J. Nucl. Mater.*, 140:228–244, 1986.

[71] R.J. White. A new mechanistic model for the calculation of fission gas release. [318], pages 196–202. West Palm Beach, Florida.

[72] R.A. Jackson and C.R.A. Catlow. Trapping and solution of fission Xe in $UO_2$. Part 2: Solution from small overpressurized bubbles. *J. Nucl. Mater.*, 127:167–169, 1985.

[73] J.H. Evans, A. Van Veen, and K.T. Westerduin. A tem and tds study of gas release from bubbles in krypton-implanted uranium dioxide. *J. Nucl. Mater.*, 195:250–259, 1992.

[74] M.S. Veshchunov. On the theory of fission gas bubble evolution in irradiated $UO_2$ fuel. *J. Nucl. Mater.*, 277:67–81, 2000.

[75] I.R. Brearly and D.A. Macinnes. Modelling of fission-gas release from fuel undergoing isothermal heating. *J. Nucl. Mater.*, 118:68–72, 1983.

[76] D.R. Olander. *Fundamental aspects of nuclear reactor fuel elements*, chapter 7. Technical Information Center - Energy Research and Development administration, University of California, Berkeley, 1976. TID-26711-P1 or ISBN 0-87079-031-5.

[77] K. Lassmann. The oxired model for redistribution of oxygen in nonstoichiometric uranium-plutonium oxides. *J. Nucl. Mater.*, 150:10–16, 1987.

[78] F. D'Annucci and C. Sari. Oxygen diffusion in uranium-plutonium oxide fuels at low temperatures. *J. Nucl. Mater.*, 68:357–359, 1977.

[79] J. Janek and H. Timm. Thermal diffusion and Soret effect in (U,Me)$O_{2+\delta}$: the heat of transport of oxygen. *J. Nucl. Mater.*, 255:116–127, 1998.

[80] D.R. Olander. *Fundamental aspects of nuclear reactor fuel elements*, chapter 11. University of California, Berkeley, 1976. TID-26711-P1.

[81] Thermal diffusion in $UO_2$-$PuO_2$ mixtures. In H. Beisswenger, M. Bober, and G. Schumacher, editors, *Proc. of IAEA Symp. on the use of plutonium as a reactor fuel*, pages 273–282, 1967. Brussels.

[82] G.L. Hofman, S.L. Hayes, and M.C. Petri. Temperature gradient driven constituent redistribution in U-Zr alloys. *J. Nucl. Mater.*, 227:277–286, 1996.

[83] I. Kaur, Y. Mishin, and W. Gust. *Fundamentals of grain and interphase boundary diffusion.* John Wiley & Sons, third edition, 1995.

[84] N.L. Peterson. *Diffusion mechanisms in grain boundaries in solids*, volume 6 of *Advances in ceramics*, page 236. The American Ceramic Society, Inc., Columbus, Ohio, 1985.

[85] A. Atkinson. Diffusion along grain boundaries and dislocations in oxides, alkali halides and carbides. *Solid State Ionics*, 12:309–320, 1984.

[86] G.L. Reynolds and B. Burton. Grain-boundary diffusion in uranium dioxide: the correlation between sintering and creep and a reinterpretation of creep mechanism. *J. Nucl. Mater.*, 82:22–25, 1979.

[87] N. Kourti and I. Shepherd. Modelling intergranular fuel swelling in severe accidents. *J. Nucl. Mater.*, 277:37–44, 2000.

[88] A.C.S. Sabioni, W.B. Ferraz, and F. Millot. Effect of grain-boundaries on uranium and oxygen diffusion in polycrystalline $UO_2$. *J. Nucl. Mater.*, 278:364–369, 2000.

[89] K. Une and S. Kashibe. Corrosion behavior of irradiated fuel pellets in high temperature water. *J. Nucl. Mater.*, 232:240–247, 1996.

[90] A.J. Flipot, H. Van Den Broeck, A. Delbrassine, and R. Gilissen. Burnable poison dispersion in $UO_2$ fuel. *Nuclear Engineering Int.*, 15(167):345–349, 1970.

[91] P. Van Uffelen. Modèle d'évolution de l'homogénéité du plutonium dans le combustible MOX. Master's thesis, Université Libre de Bruxelles, Faculté des Sciences Appliquées, 1994.

[92] M.V. Speight and J.A. Turnbull. Enhanced fission-product release by grain-boundary diffusion. *J. Nucl. Mater.*, 68:244–249, 1977.

[93] J.A. Turnbull and C.A. Friskney. The release of fission products from nuclear fuel during irradiation by both lattice and grain boundary diffusion. *J. Nucl. Mater.*, 58:31–38, 1975.

[94] J.A. Turnbull, C.A. Friskney, F.A. Johnson, A.J. Walter, and J.R. Findlay. The release of radioactive gases from uranium dioxide during irradiation. *J. Nucl. Mater.*, 67:301–306, 1977.

[95] D.R. Olander. *Combined grain-boundary and lattice diffusion in fine-grained ceramics*, pages 271–293. Volume 17 of Hastings [317], 1986.

[96] U.M. El-Saied and D.R. Olander. Fission gas release during grain growth in a microstructure with a distribution of grain sizes. *J. Nucl. Mater.*, 207:313–326, 1993.

[97] M. Akabori and K. Fukuda. Release behavior of cesium in irradiated (Th,U)$O_2$. *J. Nucl. Mater.*, 186:47–53, 1991.

[98] Y. Guérin, J. Noirot, D. Lespiaux, C. Struzik, P. Garcia, P. Blanpain, and G. Chaigne. Microstructure evolution and in-reactor behaviour of MOX fuel. [319], pages 1023–1036. Park City, Utah, USA.

[99] M. Peehs, G. Kaspar, and K.H. Neeb. Cs and I release source terms from irradiated LWR fuel. *J. Nucl. Mater.*, 119:284–290, 1983.

[100] G. Schumacher and S.A. Wright. Modeling cesium behavior in nuclear reactor fuels at high temperature. *J. Nucl. Mater.*, 130:21–35, 1985.

[101] M. Peehs, G. Kaspar, and F. Sontheimer. Cs and I source terms of irradiated $UO_2$. Number IWGFPT/25, pages 121–130. IAEA, 1986.

[102] P. Dehaudt, G. Eminet, M. Charles, and C. Lemaignan. Microstructure of $UO_2$ in a wide range of burnups and temperatures. Impacts on fission gas release mechanisms. [318], pages 140–149. West Palm Beach, Florida.

[103] V.F. Chkuaseli and Hj. Matzke. Volatile fission product bubble behaviour in uranium dioxide. *J. Nucl. Mater.*, 223:61–66, 1995.

[104] C.T. Walker, C. Bagger, and M. Møgensen. Observations on the release of cesium from $UO_2$ fuel. *J. Nucl. Mater.*, 240:32–42, 1996.

[105] S.G. Prussin, D.R. Olander, W.K. Lau, and L. Hansson. Release of fission products (Xe, I, Te, Cs, Mo and Tc) from polycrystalline $UO_2$. *J. Nucl. Mater.*, 154:25–37, 1988.

[106] T. Kubo, T. Hosokawa, K. Une, S. Kashibe, K. Takei, Y. Ishii, T. Ikeda, M. Oguma, K. Ito, H.S. Rosenbaum, and T.C. Rowland. Fission gas behaviour in advanced $UO_2$ with controlled microstructures. [318], pages 196–202. West Palm Beach, Florida.

[107] Y.H. Koo, D.S. Sohn, and Y.K. Yoon. An analysis method for the fuel rod gap inventory of unstable fission products during steady-state operation. *J. Nucl. Mater.*, 209:62–78, 1994.

[108] P. Lösönen. Modeling steady state fission gas release at high burnup. [319], pages 289–303. Park City, Utah, USA.

[109] C.T. Walker, P. Knappik, and M. Møgensen. Concerning the development of grain face bubbles and fission gas release in $UO_2$ fuel. *J. Nucl. Mater.*, 160:10–23, 1988.

[110] C.T. Walker and M. Møgensen. On the rate determining step in fission gas release from high burn-up water reactor fuel during power transients. *J. Nucl. Mater.*, 149:121–131, 1987.

[111] M.O. Tucker. Grain boundary porosity and gas release in irradiated $UO_2$. *Rad. Effects*, 53:251–256, 1980.

[112] K. Une and S. Kashibe. Fission gas release during post irradiation annealing of BWR fuels. *J. Nucl. Sc. Techn.*, 27(11):1002–1016, 1990.

[113] M. Møgensen, C. Bagger, and C.T. Walker. An experimental study of the distribution of retained xenon in transient-tested $UO_2$ fuel. *J. Nucl. Mater.*, (199):85–101, 1993.

[114] R. Hargreaves and D.A. Collins. A quantitative model for fission gas release and swelling in irradiated uranium dioxide. *J.Br.Energy Soc.*, 15(4):311–318, oct 1976.

[115] D.R. Olander. *Fundamental aspects of nuclear reactor fuel elements*, chapter 14. Technical Information Center - Energy Research and Development administration, University of California, Berkeley, 1976. TID-26711-P1 or ISBN 0-87079-031-5.

[116] R.J. White. Equi-axed and columnar grain growth in $UO_2$. [314], pages 419–427. Windermere, United Kingdom.

[117] R.A. Vandermeer. Microstructural path concept applied to normal grain growth. *Acta metall. mater.*, 40(6):1159–1166, 1992.

[118] M. Hillert. On the theory of normal and abnormal grain growth. *Acta Metallurgica*, 13:227–238, mar 1965.

[119] L.B. Ainscough, B.W. Oldfield, and J.O. Ware. Isothermal grain growth kinetics in sintered $UO_2$ pellets. *J. Nucl. Mater.*, 49:117–128, 1974.

[120] H.V. Atkinson. Overview no. 65: Theories of normal grain growth in pure single phase systems. *Acta Metall.*, 36(3):469–491, 1988.

[121] M.C. Paraschiv, A. Paraschiv, and F. Glodeanu. On the fission gas release from oxide fuels during normal grain growth. *J. Nucl. Mater.*, 246:223–231, 1997.

[122] O.V. Khoruzhii, S.Y. Kourtchatov, and V.V. Likhanskii. New model of equiaxed grain growth in irradiated $UO_2$. *J. Nucl. Mater.*, 265:112–116, 1999.

[123] H. Kleykamp. The chemical state of fission products in oxide fuels. *J. Nucl. Mater.*, 131:221–246, 1985.

[124] M.A. Gulden. Migration of gas bubbles in uranium dioxide. *J. Nucl. Mater.*, 23:30–36, 1967.

[125] F.A. Nichols. Transport phenomena in nuclear fuels under severe temperature gradients. *J. Nucl. Mater.*, 84:1–25, 1979.

[126] F.A. Nichols. Pore migration in ceramic fuel elements. *J. Nucl. Mater.*, 27:137–146, 1968.

[127] F.A. Nichols. Kinetics of diffusional motion of pores in solids - a review. *J. Nucl. Mater.*, 30:143–165, 1969.

[128] F.A. Nichols and C. Ronchi. *On the mobility of fission-gas bubbles*, pages 85–93. Volume 17 of Hastings [317], 1986.

[129] J.H. Evans. Bubble diffusion to grain boundaries in $UO_2$ and metals during annealing: a new approach. *J. Nucl. Mater.*, 210:21–29, 1994.

[130] J.H. Evans. The role of directed bubble diffusion to grain boundaries in post-irradiation fission gas release from $UO_2$: a quantitative assessment. *J. Nucl. Mater.*, 238:175–182, 1996.

[131] J.H. Evans. Post-irradiation fission gas release from high burn-up $UO_2$ fuel annealed under oxidising conditions. *J. Nucl. Mater.*, 246:121–125, 1997.

[132] D.R. Olander. Interaction of stresses with inclusions in solids - A review. *J. Nucl. Mater.*, 92:163–183, 1980.

[133] C. Baker. The migration of intragranular fission gas bubbles in irradiated uranium dioxide. *J. Nucl. Mater.*, 71:117–123, 1977.

[134] J.A. Turnbull. The mobility of intragranular bubbles in uranium dioxide during irradiation. *J. Nucl. Mater.*, 62:325–328, 1976.

[135] R.M. Cornell, M.V. Speight, and B.C. Masters. The role of bubbles in fission gas release from uranium dioxide. *J. Nucl. Mater.*, 30:170–178, 1969.

[136] P. Combette and I. Zacharie. Reply to the comments by J.H. Evans about two papers "Thermal treatment of $UO_2$ irradiated in a pressurised water reactor: swelling and release of fission gases" and "Microstructural analysis and modelling of intergranular swelling of an irradiated $UO_2$ fuel treated at high temperature". *J. Nucl. Mater.*, 275:112–114, 1999.

[137] P. Lösönen. On the behaviour of intragranular fission gas in $UO_2$ fuel. *J. Nucl. Mater.*, 280:56–72, 2000.

[138] G.P. Tiwari. Behaviour of inert gas bubbles under chemical concentration gradients. *J. Nucl. Mater.*, 232:119–124, 1996.

[139] G.P. Tiwari. Reply to 'Comments on "Behaviour of inert gas bubbles under chemical concentration gradients" '. *J. Nucl. Mater.*, 252:162–167, 1998.

[140] J.H. Evans and A. van Veen. Comments on "Behaviour of inert gas bubbles under chemical concentration gradients". *J. Nucl. Mater.*, 252:156–161, 1998.

[141] C. Vitanza, U. Graziani, N.T. Fordestrommen, and K.O. Vilpponen. Fission gas release from in-pile measurements. Technical Report HPR-221.10, OECD Halden Reactor Project, 1978.

[142] W.H. Stevens, J.R. MacEwan, and A.M. Ross. The diffusion behaviour of fission xenon in uranium dioxide. In *Nuclear reactor chemistry - First conference*, number TID-7610, pages 7–22. US atomic energy commission - Office of technical information, 1960.

[143] R.H. Barnes, M. Kangilasky, J.B. Melehan, and F.A. Rough. Xenon diffusion in single-crystal and sintered $UO_2$. Technical Report BMI-1533, Battelle Memorial Institute, 1961.

[144] R.M. Caroll, J.G. Morgan, R.B. Perez, and O. Sisman. Fission density, burnup, and temperature effects on fission-gas release from $UO_2$. *Nucl. Sc. Eng.*, 38:143–155, 1969.

[145] N. Cayet. Investigation of delayed fission gas release. Technical Report HWR-488, OECD Halden Reactor Project, 1996.

[146] K. Une and S. Kashibe. Fission gas release during postirradiation annealing of $UO_2$ - 2 wt% $Gd_2O_3$ fuels. *J. Nucl. Mater.*, 189:210–216, 1992.

[147] S. Kashibe and K. Une. Effects of temperature cycling and heating rate on fission gas release of BWR fuels. *J. Nucl. Sc. Techn.*, 28(12):1090–1099, 1991.

[148] M.C. Naik. *Diffusion controlled and burst release of gaseous and volatile fission products from $UO_2$ and $ThO_2$*, pages 99–126. North-Holland, 1992.

[149] J. Rest and S.M. Gehl. The mechanistic prediction of transient fission gas release from LWR fuel. *Nucl. Eng. Des.*, 56:233–256, 1980.

[150] K. Yanagisawa. Non-destructive evaluation of transient fission gas release from a pulse-irradiated PWR segment fuel by counting Krypton 85. *J. Nucl. Sc. Techn.*, 29(9):909–918, 1992.

[151] S. Valain. *Etude des mécanismes microstructuraux liés au relâchement des gaz de fission du dioxyde d'uranium irradié.* PhD thesis, Inst. Nat. Pol. de Grenoble, 1999.

[152] W. Hering. The KWU fission gas release model for LWR fuel rods. *J. Nucl. Mater.*, 114:41–49, 1983.

[153] J. Rest. An improved model for fission product behavior in nuclear fuel under normal and accident conditions. *J. Nucl. Mater.*, 120:195–212, 1984.

[154] Y.H. Koo, B.H. Lee, and D.S. Sohn. COSMOS: a computer code to analyze LWR $UO_2$ and MOX fuel to high burnup. *Ann. Nucl. En*, 26:47–67, 1999.

[155] M. Tayal, L.D. Macdonald, E. Kohn, and W.P. Dovigo. A model for the transient release of fission products from $UO_2$ fuel: GASOUT code description. *Nucl. Techn.*, 85:300–313, 1999.

[156] C. Forat. New FRAGEMA developments for fuel temperature and fission gas release modelling. [320], pages 152–159. Preston, England.

[157] W. S. Andrews, B.J. Lewis, and D.S. Cox. Artificial neural network models for volatile fission product release during severe accident conditions. *J. Nucl. Mater.*, 270:74–86, 1999.

[158] A.H. Booth. A method of calculating fission gas diffusion from $UO_2$fuel and its application to the x-2-f loop test. Technical Report CRDC-721, Atomic Energy of Canada Ltd., Chalk River, Ontario, Canada, 1957.

[159] A.H. Booth. A suggested method for calculating the diffusion of radioactive rare gas fission products from $UO_2$ fuel elements and a discussion of proposed in-reactor experiments that may be used to test its validity. Technical Report DCI-27, Atomic Energy of Canada Ltd., Chalk River, Ontario, Canada, 1957.

[160] J.R. Matthews and M.H. Wood. An efficient method for calculating diffusive flow to a spherical boundary. *Nucl. Eng. Des.*, 56:439–443, 1980.

[161] K. Ito, R. Iwasaki, and Y. Iwano. Finite element model for analysis of fission gas release from $UO_2$ fuel. *J. Nucl. Sc. Techn.*, 22(2):129–138, 1985.

[162] T. Nakajima. FEMAXI-IV: a computer code for the analysis of fuel rod behavior under transient conditions. *Nucl. Eng. Des.*, 88:69–84, 1985.

[163] K. Forsberg and A.R. Massih. Fission gas release under time-varying conditions. *J. Nucl. Mater.*, 127:141–145, 1985.

[164] P.T. Elton and K. Lassmann. Calculational methods for diffusional gas release. *J. Nucl. Mater.*, 101:259–265, 1987.

[165] P. Lösönen. Methods for calculating diffusional gas release from spherical grains. *Nucl. Eng. Des.*, 196:161–173, 1999.

[166] K. Lassmann and H. Benk. Numerical algorithms for intragranular fission gas release. *J. Nucl. Mater.*, 280:127–135, 2000.

[167] C.A. Friskney and M.V. Speight. A calculation on the in-pile diffusional release of fission products forming a general decay chain. *J. Nucl. Mater.*, 6:89, 1976.

[168] M.C. Paraschiv and A. Paraschiv. A theoretical study of fission products release from oxide fuels taking into account both grain growth and precursors effect. *J. Nucl. Mater.*, 218:66–84, 1994.

[169] M.C. Paraschiv, A. Paraschiv, and V.V. Grecu. A theoretical study of fission products release from oxide fuels. *J. Nucl. Mater.*, 275:164–185, 1999.

[170] G.V. Kidson. A generalized analysis of the cumulative diffusional release of fission product gases from an "equivalent sphere" of $UO_2$. *J. Nucl. Mater.*, 88:299–308, 1980.

[171] G.A. Berna, C.E. Beyer, K.L. Davis, and D.D. Lanning. FRAPCON-3: A computer code for the calculation of the steady-state, thermal-mechanical behavior of oxide fuel rods for high burnup. Technical Report NUREG/CR-6534, USNRC, 1997.

[172] N. Cayet, D. Baron, and S. Béguin. CYRANO3: EdF's fuel rod behaviour code: presentation and overview of its qualification on HRP and various experiments. [321], pages 323–358. Cadarache, France.

[173] N. Hoppe, M. Billaux, J. van Vliet, and S. Shihab. COMETHE4.4-021: General description. Technical Report BN 9409844/220 - A, BELGONUCLEAIRE, 1995.

[174] V.I. Arimescu and W.R. Richmond. Modelling CANDU-type fuel behaviour during extended burnup irradiations using a revised version of the ELESIM code. [315], pages 183–193. Pembroke, Ontario, Canada.

[175] M. Oguma. Cracking and relocation behavior of nuclear pellets during rise to power. *Nucl. Eng. Des.*, 76:35–45, 1983.

[176] J.R. Hofmann and C.C. Meek. Internal pressurisation in solid mixed-oxide fuel due to transient fission gas release. *Nucl. Sc. Eng.*, 64:713–723, 1977.

[177] P.C. Carman. *L'écoulement des gaz à travèrs les milieux poreux.* Presses Universitaires de France, 1961.

[178] H. Bailly, D. Ménessier, and C. Prunier, editors. *Le combustible nucléaire des réacteurs à eau sous pression et des réacteurs à neutrons rapides.* Eyrolles, 1996.

[179] C. O'Caroll and K. Lassmann. Numerical solution for the nonlinear diffusion equation describing the transport of volatile fission products in nuclear fuels. *Nucl. Technol.*, 99:268–273, 1992.

[180] A.S. Ivanov. The model of the fission gas release out of porous fuel. *Ann. Nucl. Energy*, 25(15):1275–1280, 1998.

[181] T. Kogai. Modelling of fission gas release and gaseous swelling of light water reactor fuels. *J. Nucl. Mater.*, 244:131–140, 1997.

[182] J.R. Matthews and G.J. Small. Towards a mechanistic understanding of transient fission gas release. [320], pages 195–203. Preston, England.

[183] M. Charles, J. Simmons, and C. Lemaignan. Analysis of the mechanisms involved in fission gas release during power transients at high burnup. [320], pages 221–228. Preston, England.

[184] P. Brohan. Grain boundary swelling and gas release in $UO_2$. [319], pages 786–795. Park City, Utah, USA.

[185] L. Landau and E. Lifchitz. Physique théorique. In MIR, editor, *Mécanique Des Fluides*, chapter II. MIR, 1971.

[186] T. Kogai, K. Ito, and Y. Iwano. The effect of cladding restraint on fission gas release behavior. *J. Nucl. Mater.*, 158:64–70, 1988.

[187] K. Forsberg and A.R. Massih. Diffusion theory of fission gas migration in irradiated nuclear fuel $UO_2$. *J. Nucl. Mater.*, 135:140–148, 1985.

[188] D.M. Dowling, R.J. White, and M.O. Tucker. The effect of irradiation-induced re-solution on fission gas release. *J. Nucl. Mater.*, 110:37–46, 1982.

[189] T. Nakajima and H. Saito. A comparison between fission gas release data and FEMAXI-IV code calculations. *Nucl. Eng. Des.*, 101:267–279, 1987.

[190] K. Malen. Migration of I-131 in fuel rods with burnups of 5-30 MWd/kgU reirradiated at powers of 40-60 kW/m for up to five days. In *Proc. Techn. Com. Meet. on fuel rod chemistry.* IAEA, 1979. Erlangen, Germany.

[191] M.J.F. Notley and I.J. Hastings. A microstructure-dependent model for fission product gas release and swelling in $UO_2$ fuel. *Nucl. Eng. Des.*, 56:163–175, 1980.

[192] J.A. Turnbull. An assessment of fission gas release and the effect of microstructure at high burnup. Technical Report HWR-604, OECD Halden Reactor Project, 1999.

[193] P. Shewmon and P. Anderson. Void nucleation and cracking at grain boundaries. *Acta mater.*, 46(14):4861–4872, 1998.

[194] P.J. Clemm and J.C. Fisher. The influence of grain boundaries on the nucleation of secondary phases. *Acta Metallurgica*, 3:70–73, jan 1955.

[195] R.J. White. The kinetics of fission gas release venting from saturated grain boundaries in irradiated $UO_2$. 1994. Bolkesjö, Norway.

[196] C. Forat, P. Blanpain, B. Kapusta, P. Guedeney, and P. Permezel. Fission gas release enhancement at extended burnup. [315], pages 68–75. Pembroke, Ontario, Canada.

[197] C. Bagger and M. Møgensen. Experimental assessment of a temperature threshold for thermally induced fission gas release in transient tested water reactor fuel with extended burnup. [315], pages 38–44. Pembroke, Ontario, Canada.

[198] W. Wiesenack. Experimental techniques and results related to high burn-up investigations at the OECD Halden Reactor Project. [315], pages 118–123. Pembroke, Ontario, Canada.

[199] R. Manzel, R.P. Bodmer, and G. Bart. Fission gas release in high burnup fuel. [315], pages 63–67. Pembroke, Ontario, Canada.

[200] P. Knudsen, C. Bagger, M. Møgensen, and H. Toftegaard. Fission gas release and fuel temperature during power transients in water reactor fuel at extended burnup. [315], pages 25–31. Pembroke, Ontario, Canada.

[201] K. Nogita and K. Une. Irradiation-induced recrystallization in high burnup $UO_2$ fuel. *J. Nucl. Mater.*, 226:302–310, 1995.

[202] J. Rest and G.L. Hofman. Dynamics of irradiation-induced grain subdivision and swelling in $U_3Si_2$ and $UO_2$ fuels. *J. Nucl. Mater.*, 210:187–202, 1994.

[203] M. Kinoshita, T. Kameyama, S. Kitajima, and Hj. Matzke. Temperature and fission rate effects on the rim structure formation in a $UO_2$ fuel with a burnup of 7.9 % FIMA. *J. Nucl. Mater.*, 252:71–78, 1998.

[204] J. Spino, D. Baron, M. Coquerelle, and A.D. Stalios. High burn-up rim structure: evidences that xenon-depletion, pore formation and grain subdivision start at different local burn-ups. *J. Nucl. Mater.*, 256:189–196, 1998.

[205] M. Møgensen, J.H. Pearce, and C.T. Walker. Behaviour of fission gas in the rim region of high burn-up $UO_2$ fuel pellets with particular reference to results from an XRF investigation. *J. Nucl. Mater.*, 264:99–112, 1999.

[206] K. Lassmann, C.T. Walker, and J. van de Laar. Thermal analysis of ultra-high burn-up irradiations employing the TRANSURANUS code. [321], pages 359–368. Cadarache, France.

[207] M. Lippens, D. Boulanger, and L. Mertens. Industry challenges and expectations with respect to Fission Gas Release. [322], pages ?–? Cadarache, France.

[208] D. Baron, J. Spino, and D. Papaioannou. Rim formation and fission gas behaviour: some structure remarks. [322], pages ?–? Cadarache, France.

[209] D. Baron, aug 2000. Private communication.

[210] L.A.Nordström and C. Ott. An approach to modelling fuel behaviour using data from some international high burnup fuel programmes. [315], pages 219–224. Pembroke, Ontario, Canada.

[211] J. Nakamura, M. Suzuki, and H. Uetsuka. Re-irradiation tests of LWR spent fuel at JMTR. In *Proc. Enlarged Halden Programme Group Meeting*, volume 1. OECD Halden Reactor Project, 1999. Loen, Norway.

[212] T. Kogai. A simple fission gas release/swelling model. [315], pages 211–218. Pembroke, Ontario, Canada.

[213] L.D. MacDonald, D.B. Duncan, B.J. Lewis, and F.C. Iglesias. FREEDOM: a transient fission product release model for radiactive and stable species. [320], pages 203–208. Preston, England.

[214] D.R. Olander. *Fundamental aspects of nuclear reactor fuel elements*, chapter 21. Technical Information Center - Energy Research and Development administration, University of California, Berkeley, 1976. TID-26711-P1 or ISBN 0-87079-031-5.

[215] H. Zimmermann. Investigations on swelling and fission gas behaviour in uranium dioxide. *J. Nucl. Mater.*, 75:154–161, 1978.

[216] S. Kashibe and H. Une. Effect of external restraint on bubble swelling in $UO_2$ fuels. In *Proc. Enlarged Halden Programme Group Meeting*, volume 2. OECD Halden Reactor Project, 1996. Loen, Norway.

[217] P. Tempest and R.J. White. The effect of fill gas pressurisation on fission gas release and thermal behaviour in IFA-558 and its prediction by the fuel modelling code ENIGMA. In

*Proc. Enlarged Halden Program Group Meeting*. OECD Halden Reactor Project, 1993. Storefjell, Norway.

[218] M.V. Speight and W. Beere. Vacancy potential and void growth on grain boundaries. *Metal science*, 9:190–191, 1975.

[219] M. Ichikawa, C. Fenzlein, D. Baron, and P. Van Uffelen. Conclusions of the session on the improvement of the fuel element. IAEA Techn. Com. Meet. on technical and economical limits to fuel burnup extension, San Carlos de Bariloche, Argentina, November 15-19, 1999.

[220] J.R. Matthews and M.H. Wood. A simple operational gas release and swelling model II. Grain boundary gas. *J. Nucl. Mater.*, 91:241–256, 1980.

[221] M.R. Hayns and M.W. Finnis. The response of grain boundary cavities to stress and temperature changes under conditions of continuous gas generation. *Nuclear Science Technology*, 1:255–260, 1979. European Applied Research Report.

[222] M.S. Yang and J.R. Weertman. A test of grain boundary void growth theories by small angle neutron scattering. *Scripta metallurgica*, 18:543–548, 1984.

[223] S. Kashibe and H. Une. Densification and swelling in $UO_2$ pellets under hydrostatic pressure condition. *J. Nucl. Sc. Techn.*, 35(11):796–800, 1998.

[224] S. Kashibe and H. Une. Effect of external restraint on density change and fission gas release in $UO_2$ fuels. In *Proc. Enlarged Halden Programme Group Meeting*, volume 1. OECD Halden Reactor Project, 1998.

[225] R.J. White. The development of grain face porosity in irradiated oxide fuel. [322], pages ?–? Cadarache, France.

[226] M.D. Freshley, D.W. Brite, J.L. Daniel, and P.E. Hart. Irradiation induced densification of $UO_2$ pellet fuel. *J. Nucl. Mater.*, 62:138–166, 1976.

[227] J.A. Turnbull, P. Van Uffelen, and S. Béguin. The influence of fuel-to-clad gap and $UO_2$ grain size on fission gas release in high burnup fuel PWR design fuel rods. In *Proc. Enlarged Halden Program Group Meeting*, number HWR-548. OECD Halden Reactor Project, 1998. Lillehammer, Norway.

[228] E. Kotomin and V. Kuzovkov. Phenomenological kinetics of Frenkel defect recombination and accumulation in ionic solids. *Rep. Prog. Phys.*, pages 2079–2188, 1992.

[229] A. Szabo. Theory of diffusion-influenced fluorescence quenching. *J. Phys. Chem.*, 93:6929–6939, 1989.

[230] R.I. Cukier. On the quencher concentration dependence of fluorescence quenching: the role of solution dielectric constant and ionic strength. *J. Am. Chem. Soc.*, 107:pp 4115–4117, 1985.

[231] D.Y. Yang and R.I. Cukier. Concentration dependent fluorescence quenching with ionic reactants. *J. Chem. Phys.*, 86(5):pp 2833–2838, mar 1987.

[232] F.S. Ham. Theory of diffusion-limited precipitation. *J. Phys. Chem. Solids*, 6:335–351, 1958.

[233] F.S. Ham. Stress-assisted precipitation on dislocations. *J. Appl. Phys.*, 30(6):915–926, 1959.

[234] M.H. Wood. Sink strengths for grain-boundary cavities. *J. Nucl. Mater.*, 119:67–72, 1983.

[235] A.D. Brailsford, R. Bullough, and M.R. Hayns. Point defect sink strengths and void-swelling. *J. Nucl. Mater.*, 60:246–256, 1976.

[236] R. Bullough, M.R. Hayns, and M.H. Wood. Sink strengths for thin film surfaces and grain boundaries. *J. Nucl. Mater.*, 90:44–59, 1980.

[237] Hj. Matzke. Recent studies on the formation of the rim structure and on polygonization in LWR fuel. IAEA Techn. Com. Meet. on technical and economical limits to fuel burnup extension, San Carlos de Bariloche, Argentina, November 15-19, 1999.

[238] M.O. Tucker. The spacing of intergranular fission gas bubbles in irradiated $UO_2$. *J. Nucl. Mater.*, 74:34–40, 1978.

[239] M.O. Tucker. The transfer of fission gas between grain faces and edges in $UO_2$. *J. Nucl. Mater.*, 75:282–287, 1978.

[240] Y.H. Koo, B.H. Lee, and D.S. Sohn. Analysis of fission gas release and gaseous swelling in $UO_2$ fuel under the effect of external restraint. *J. Nucl. Mater.*, 280:86–98, 2000.

[241] U. Gösele. Concentration dependence of rate constants for diffusion- or reaction-controlled void-point-defect reactions. *J. Nucl. Mater.*, 78:83–95, 1978.

[242] Y.R.H. Kalnin and E.A. Kotomin. Many-particle peculiarities in the $A + B \rightarrow B$ bimolecular reaction kinetics. The effect of sink spatial distribution. *J. Phys.: Condensed Matter*, 8:6729–6735, 1996.

[243] T.R. Waite. Theoretical treatment of the kinetics of diffusion-limited reactions. *Physical Review*, 107(2):463–470, 1957.

[244] A.D. Brailsford and R. Bullough. The rate theory of swelling due to void growth in irradiated metals. *J. Nucl. Mater.*, 44:121–135, 1972.

[245] K.C. Russell. Phase instability under cascade damage irradiation. *J. Nucl. Mater.*, 206:129–138, 1993.

[246] U. Gösele. Comment on "Diffusion theory of luminescent emission from a doped organic solid". *Phys. Stat. Sol. (b)*, 75:K129, 1976.

[247] British association for the advancements of science, editor. *Bessel Functions. Part I: Functions of order zero and unity*, volume 6 of *Mathematical Tables*. University Press Cambridge, first edition, 1958.

[248] M. Fixman. Competitive diffusion sinks and precipitation on dislocations. *Physical Review B*, 15(12):5741–5747, 1977.

[249] G.I. Bell and S. Glasstone. *Nuclear reactor theory*. Van Nonstrand Reinhold Company, 1970.

[250] I.R. Brearley and D.A. Macinnes. Modelling of fission-gas release from fuel undergoing isothermal heating. *J. Nucl. Mater.*, 118:68–72, 1983.

[251] P. Van Uffelen. Modelling the variable precipitation of fission products at grain boundaries. *J. Nucl. Mater.*, 280:275–284, 2000.

[252] G.R. Chilton and J. Edwards. The solid state diffusion of plutonium in uranium dioxide. *J. Nucl. Mater.*, 78:182–191, 1978.

[253] M. Gardani and C. Ronchi. Transport and release of radioactive fission products in nuclear fuels: the new analytical method of the MITRA code. *Nucl. Sc. Eng.*, 107:315–329, 1991.

[254] D.R. Olander and V. Mubayi. Review of the materials-chemistry models in the VICTORIA code. *J. Nucl. Mater.*, 270:1–10, 1999.

[255] P. Van Uffelen. Developments of a new fission gas release and fuel swelling model. In *Proc. Enlarged Halden Program Group Meeting*, volume 1. OECD Halden Reactor Project, 1998. Lillehammer, Norway.

[256] P. Van Uffelen. Assessing the contribution of grain boundary diffusion to fission gas release in nuclear fuel. In *Proc. Enlarged Halden Program Group Meeting*, volume 1. OECD Halden Reactor Project, 1999. Loen, Norway.

[257] D.R. Olander and P. Van Uffelen. On the role of grain boundary diffusion in fission gas release. *J. Nucl. Mater.*, 288(2-3):137–147, 2001.

[258] R.W. Grimes and G. Busker. Predicting the behaviour of fission products in the uranium-oxygen system. 1996.

[259] D. Davies and G. Long. The emission of xenon - 133 from lightly irradiated uranium dioxide spheroids and powders. Technical Report AERE-R-4347, Harwell, UK, 1963.

[260] J. Doherty. *PEST: Model-independent parameter estimation.* Watermark Computing, 1998.

[261] J.R. Lamarsh. *Introduction to nuclear reactor theory.* Addison-Wesley Publishing Company, 1965.

[262] H.S. Carslaw and J.C. Jaeger. *Conduction of heat in solids.* Oxford University Press, second edition, 1959.

[263] M. Abramowitz and I.A. Stegun, editors. *Handbook of mathematical functions with formulas, graphs and mathematical tables.* Dover Publications, 1965.

[264] D.R. Olander, aug 1999. Private communication.

[265] I. Zacharie, S. Lansiart, P. Combette, M. Trotabas, M. Coster, and M. Groos. Microstructural analysis and modelling of intergranular swelling of an irradiated $UO_2$ fuel treated at high temperature. *J. Nucl. Mater.*, 255:92–104, 1998.

[266] Hj. Matzke, mar 2000. Private communication.

[267] T.J. Bjorlo, E. Kolstad, and C. Vitanza. FUEL-TEMP-2 computer programme for analysis of the steady state behaviour of oxide fuel rods. Technical Report HPR-211, OECD Halden Reactor Project, 1977.

[268] M. Billaux and A. Massih. Summary of sessions and panels - Fission gas release. In IAEA [314], pages 7–13. Windermere, United Kingdom.

[269] R.J. White and J.A. Turnbull. The measurement of fission product release using the gas flow rigs: A review of experiments, methodology and results from 1980-1997. Technical Report HWR-553, OECD Halden Reactor Project, 1998.

[270] H.S. Levine and C.J. MacCallum. Grain boundary and lattice diffusion in polycrystalline bodies. *Journal of Applied Physics*, 31(3):595–599, mar 1960.

[271] N.M. Ghoniem. Nucleation and growth theory of cavity evolution under conditons of cascade damage and high helium generation. *J. Nucl. Mater.*, 174:168–177, 1990.

[272] A.E. Volkov and A.I. Ryazanov. Theory of gas bubble nucleation in supersaturated solution of vacancies, interstitials and gas atoms. *J. Nucl. Mater.*, 273:155–163, 1999.

[273] H. Trinkaus. Modeling of helium effects in metals: high temperature embrittlement. *J. Nucl. Mater.*, 133:105–112, 1985.

[274] H. Trinkaus. Mechanisms controlling high temperature embrittlement due to helium. *Radiation effects*, 101:91–107, 1986.

[275] J.R. Cost and K.Y. Chen. The number of gas atoms per bubble of inert gas in a solid. *J. Nucl. Mater.*, 67:265–272, 1977.

[276] L.C. Burmeister. *Convective Heat Transfer.* John Wiley & Sons, 1983.

[277] W.M. Rohsenow and J.P. Hartnett, editors. *Handbook of Heat Transfer.* McGraw-Hill, 1973.

[278] K.W. Song, K.S. Kim, Y.M. Kim, K.W. Kang, and Y.H. Jung. Reduction of the open porosity of $UO_2$ pellets through pore structure control. *J. Nucl. Mater.*, 279:253–258, 2000.

[279] L. Sannen. Density and open porosity in $UO_2$ fuel. Technical Report TEC95/29/LS, SCK•CEN, 1995.

[280] R.L. Coble. Sintering crystalline solids. I. intermediate and final state diffusion models. *J. Appl. Phys.*, 32(5):787–792, 1961.

[281] B. Wong and J.A. Pask. Models for kinetics of solid state sintering. *J. Am. Ceram. Soc.*, 62(3-4):138–145, 1979.

[282] H. Assman and H. Stehle. Thermal and in-reactor densification of $UO_2$. Mechanisms and experimental results. *Nucl. Eng. Des.*, 48:49–67, 1978.

[283] H.C. Suk, W. Hwang, B.G. Kim, K.S. Kim, and Y.H. Heo. Improvement of ELESIM-CANDU fuel performance analysis code. [315], pages 193–201. Pembroke, Ontario, Canada.

[284] I.J. Hastings and L.E. Evans. Densification algorithm for irradiated $UO_2$ fuel. *J. Am. Ceram. Soc.*, 62(3-4):217–218, 1979.

[285] P.A. Jackson, J.A. Turnbull, and R.J. White. A description of the ENIGMA fuel performance code. Number IAEA-TECDOC-659, pages 28–38. IAEA, 1989.

[286] D. Baron. Does rim microstructure formation degrade the fuel rod perfomance? IAEA Techn. Com. Meet. on technical and economical limits to fuel burnup extension, San Carlos de Bariloche, Argentina, November 15-19, 1999.

[287] C.T. Walker, W. Goll, and T. Matsumura. Effect of inhomogeneity on the level of fission gas and caesium release from OCOM MOX fuel during irradiation. *J. Nucl. Mater.*, 228:8–17, 1996.

[288] P. Van Uffelen. Modelling isothermal fission gas release. IAEA Techn. Com. Meet. on technical and economical limits to fuel burnup extension, San Carlos de Bariloche, Argentina, November 15-19, 1999.

[289] A. Delbrassine, apr 1999. Private communication.

[290] P. Van Uffelen. Parametric study of a fission gas release model for light water reactor fuel. [319], pages 276–288. Park City, Utah, USA.

[291] P. Van Uffelen. Optimisation of the numerical parameters in the fission gas release model for LWR fuel. Technical Report R-1330, SCK•CEN, December 2000.

[292] J. van Vliet. Development of transient heat transfer models for COMETHE III-K First interim report. Technical Report 980.00/630/n/122, BELGONUCLEAIRE, August 1979.

[293] G. Lebon and J. Lambermont. Generalization of Hamilton's principle to continuous dissipative systems. *J. Chem. Phys.*, 59:2929–2936, 1973.

[294] G. Lebon, Ph. Mathieu, and J. van Vliet. Modeling of the transient heat transfer in a nuclear reactor fuel rod using a variational procedure. *Nucl. Eng. Des.*, 51:133–142, 1979.

[295] G. Lebon and Ph. Mathieu. A numerical calculation of nonlinear transient heat conduction in the fuel elements of a nuclear reactor. *Int. J. Heat Mass Transfer*, 22:1187–1198, 1979.

[296] P. Verbeek. Méthodes numériques simples de résolution de l'équation de la diffusion dans une géométrie cylindrique. Technical Report BN 980.00/630/ni/035, BELGONUCLEAIRE, September 1976.

[297] J. van Vliet. Comparaison de quelques méthodes de résolution de l'équation non stationaire de diffusion de la chaleur à une dimension. Technical Report BN 980.00/630/n/061, BELGONUCLEAIRE, December 1976.

[298] E.P. Box and S. Bisgaard. The scientific context of quality improvement. *Quality Progress*, page 54, 1987.

[299] De Nil. Statistisch proefopzetten, 1996. Training course.

[300] M. Lossie. Experimental design and analysis, 1996. Training course.

[301] L.R. Petzold. Automatic selection of methods for solving stiff and nonstiff systems of ordinary differential equations. *SIAM J. Sci. Stat. Comput.*, 4:136–148, 1983.

[302] A.C. Hindmarsh. *ODEPACK, a systematized collection of ODE solvers*. North-Holland, 1983.

[303] P. Van Uffelen. Optimisation of the global numerical parameters in the fission gas release model for LWR fuel. Technical Report R-3486, SCK•CEN, January 2001.

[304] P. Van Uffelen. Modelling the influence of the athermal open porosity on fission gas release in LWR fuel. In OECD/NEA [322]. Cadarache, France.

[305] M. Lippens. Influence de la microstructure des combustibles $UO_2$ et MOX sur leur comportement en réacteur. Technical Report BN 87025/221 ND 2151, BELGONUCLEAIRE, 1993.

[306] D.R. Olander. *Fundamental aspects of nuclear reactor fuel elements*, chapter 16. Technical Information Center - Energy Research and Development administration, University of California, Berkeley, 1976. TID-26711-P1 or ISBN 0-87079-031-5.

[307] T. Kogai. mar 1999. Private communication.

[308] M. Verwerft. Multiple voltage probe analysis of fission gas bubbles in irradiated nuclear fuel. *J. Nucl. Mater.*, 282:97–111, 2000.

[309] F. Sontheimer and H. Landskron. Puzzling features of EPMA radial fission gas release profiles: The key to realistic modeling of fission gas release up to ultra high burnup. In *Proc. Enlarged Halden Program Group Meeting*, volume 1. OECD Halden Reactor Project, 1999. Loen, Norway.

[310] J.A. Turnbull and C.A. Friskney. The relation between microstructure and the release of unstable fission products during high temperature irradiation of uranium dioxide. *J. Nucl. Mater.*, 71:238–248, 1978.

[311] H. Zimmermann. Untersuchungen zum schwellen und spaltgasverhalten in oxidischem kernbrennstoff unter neutronenbestrahlung. Technical Report KFK 2467, Kernforschungszentrum Karlsruhe, June 1977.

[312] U. Gösele and F.A. Huntley. Two-dimensional bimolecular diffusion limited reaction kinetics. *Physics Letters*, 55 A(5):291–292, dec 1975.

[313] H. Bateman. *Tables of integral transforms*. McGraw-Hill, 1954.

[314] *Proc. IAEA Techn. Com. Meet. on Water Reactor Fuel Element Modelling at High Burnup and its Experimental support*. IAEA, sep 1994. Windermere, United Kingdom.

[315] *Proc. Techn. Com. Meet. on fission gas release and fuel rod chemistry related to extended burnup*, number IAEA-TECDOC-697. IAEA, apr 1992. Pembroke, Ontario, Canada.

[316] S. E. Donnelly and J. H. Evans, editors. *Fundamental aspects of inert gases in solids*, number ISBN 0-306-44051-2. NATO Advanced Science Institute, Plenum Press, 1991.

[317] I.J. Hastings, editor. *Fission-product behavior in ceramic oxide fuel*, volume 17 of *Advances in Ceramics*. The American Ceramic Society, Inc., 1986.

[318] *Proc. Int. Top. Meet. on LWR fuel performance*. IAEA, 1994. West Palm Beach, Florida.

[319] *Proc. Int. Top. Meet. on Light-Water-Reactor-Fuel-Performance*. American Nucl.Soc., apr 2000. Park City, Utah, USA.

[320] *Proc. Techn. Com. Meet. on water reactor fuel element computer modelling in steady-state, transient and accident conditions*, number IWGFPT/32. IAEA, sep 1988. Preston, England.

[321] *Proc. Int. Sem. on thermal performance of high burnup LWR fuel*, number ISBN 92-64-16957-1. OECD-NEA, mar 1998. Cadarache, France.

[322] *Proc. Int. Sem. on fission gas behaviour in water reactor fuels*. OECD/NEA, sep 2000. Cadarache, France.